Ductile-Brittle Transition Behaviour and its Underlying Mechanisms in Steel: Effects of Cementite Morphology



Hirokazu Usuki

Supervisor: Prof Angus J Wilkinson
Prof Roger C Reed

Department of Materials
University of Oxford

This dissertation is submitted for the degree of
Doctor of Philosophy

St Anne's College

Submitted October 2024

To my mother and late father.

Acknowledgements

First and foremost, I would like to express my sincere gratitude to my academic supervisor, Professor Roger C Reed. With his constructive and positive mindset as well as keen insights, he always encouraged, inspired, and gave me the strength to push things forward. I would also like to show my profound appreciation to my academic supervisor, Professor Angus J Wilkinson. His warm and thoughtful support, including sharp and productive discussions, helped me countless times.

I would like to make a huge acknowledgement to Professor Sergio Lozano-Perez and Professor Sir Harry Bhadeshia for helping me brush up and finalise this thesis through constructive discussions and comments in the Viva examination.

I would like to thank especially Prof Yuanbo Tang, a colleague and a friend, for supporting me with all matters related to research activity, from technical discussions to miscellaneous consultations, and Dr Phani Karamched and Dr Junliang Liu for providing me with sophisticated guidance on characterisation techniques with electron microscopes and many fruitful discussions.

I am immensely grateful to the members of the research group with whom I spent a lot of time in the course of my DPhil research in Oxford - Mrs Karen Bamford, Dr Joseph Ghoussoub, Dr Yilun Gong, Dr Fauzan Adziman, Dr Jieming Zhang, Celâl Polatoğlu, Prof Chinnapat Panwisawas, Prof Daniel Barba, Dr Steve Kench, Prof D Graham McCartney, Dr Koji Kageyama, Dr Enrique Alabort, Dr Satoshi Utada, and Hisham Elamin. I received a lot of friendship and support.

My gratitude also goes to the members of the Micromechanics Group in Department of Materials and the Solid Mechanics Group in Department of Engineering Science - Mrs Rebecca Bradford, Dr Li Bo-Shiuan, Dr Jack Haley, Dr Jicheng Gong, Christopher Magazzeni, Abdalrhaman Koko, Xuewei Li, Yi Xiong, Prof Edmund Tarleton, Dr Suchandrima Das, Dr Antonio Pellegrino, Prof Clive Siviour, Dr David Chapman, Dr David Townsend, Dr LongHui Zhang, Maureen Aceves, Yuan Xu, and João Citor Sahadi - and to the Department technical staff - Stuart Carter, Jeffery Fullerton, Greg Cook, Chris Salter, Jennifer Holter, Tony Wheeler, Dr Kalin Dragnevski, and Dr Marzena Tkaczyk.

I want to give huge thanks to my friends who made my two-year Oxford stay so fulfilling - Kai Ng, Utku Ali, Stephen Turrell, Matthew Mai, Zilin Gao, Zonghao Guo, Ryuji Fujita, Siripong Cheanklin, Rafael Carrascosa Marzo, Yasuhiro Kubota, Ayako Kubota, Tori Kubota, Fumiaki Sagisaka, Moeha Ido, Takuma Morimoto, Suguru Endo, Satoshi Kishigami, and Ryosuke Hirai.

This research project was financially supported by Nippon Steel Corporation. I would like to show my gratitude to Nippon Steel Corporation and all those involved in this project. I would like to thank particularly Prof Manabu Takahashi and Kenichiro Matsumura for opening the door to this valuable opportunity, Dr Yasuhiro Shinohara for showing me a hint on how to take the initiative for this chance in addition to technical discussions, and Dr Nobuyuki Yoshimura for sample preparation.

I would never have been able to reach this DPhil study without my time at Tohoku University. I would like to thank Professor Tadashi Furuhara and Professor Goro Miyamoto for instructing me on their research approach and how deep and fun steel research can be.

My two years at Oxford coincided with the historic global pandemic, causing much confusion, inconvenience, and sadness. I wonder if I could have accomplished this without the support of everyone who was involved with me, regardless of naming here

or not. I firmly believe the difficult times and experiences in the past will be something meaningful for the rest of my life in the future.

Finally, I would like to give my sincerest gratitude to my parents, Yoshikazu Usuki and Keiko Usuki, my sister, Tomoko Kitano, and my grandparents. Those are the loved ones who have shaped who I am and where all stories began. Then, I would like to thank my wife, Kaori, and my daughter, Sakura, from the bottom of my heart for their unconditional love and dedicated support. I am so proud to have finished the DPhil research project with you both.

Abstract

Steel is irreplaceable and crucial structural material. The ductile-brittle transition behaviour is one of the most essential mechanical properties. This research aims to elucidate the effect of cementite morphology, spheroidised and pearlitic lamellar, on the ductile-brittle transition behaviour of structural steel, and to deepen our basic knowledge on an experimental basis. The key questions to have been tackled and answered in this research are the following: 1) how cementite morphology influences the ductile-brittle transition behaviour, 2) how the difference in the transition behaviour is understood in terms of deformation micromechanism, and 3) what potential plasticity and fracture of cementite are like.

Tensile tests over a wide range of temperatures and strain rates, followed by thorough post-mortem characterisation with high-resolution electron microscope techniques, as well as *in-situ* tensile testing, were conducted.

The spheroidised cementite microstructure showed relatively clear and steep change in fracture strain transition curves with temperature and strain rate, while the pearlitic lamellar microstructure was less sensitive to them meaning a gradual variation with a wider transition range. This may ensure in a certain degree of plastic deformation at lower temperatures in lamellar cementite form than in spherical form, given that the cementite fraction and ferrite grain size are the same.

The significant difference in the deformation micromechanism is that pearlitic crack initiation can proceed in a ductile manner. This step helps pearlite have the ability to

undergo continuous local plastic deformation rather than unstable crack initiation and its propagation unless tensile tests are conducted under completely brittle conditions.

In the spheroidised cementite microstructure, the ferrite matrix can deform more freely and uniformly around cementite particles to the extent of keeping compatibility between ferrite and cementite. The length for dislocations in ferrite to pile-up reached at least tens of micrometres order. The micrometre-size sharp crack formed on cementite particles is more likely to satisfy the local fracture stress condition. Brittle cracks propagate throughout the steel, resulting in the relatively steep ductile-brittle transition.

In contrast, the pearlitic lamellar cementite microstructure has a sub-micrometre lamellar structure. Additionally, the particular Pitch-Petch orientation relationship between ferrite and cementite was observed in this study, which restricts it from deforming freely and significantly. Hence, lamellar cementite cracks soon after ferrite slip occurs in pearlite. The size of the crack is lamella-thickness order, and the pile-up length for dislocations in ferrite is significantly small due to its lamellar structure. This type of crack makes it hard to propagate unstably to ferrite/cementite boundary, which suppresses macroscopic brittle fracture. Instead, it promotes further plastic deformation owing to stress and strain concentration caused by the cracking. Until a critical shearing crack, a relatively blunted and ranging over a pearlite colony, is generated, this microstructure can experience a gradual and continuous deformation that occurs simultaneously in the steel, resulting in the broader transition temperature range. The root cause of the broader and more gradual transition range in lamellar pearlitic microstructure is the hierarchical microstructure of pearlite itself. The degree of plastic deformation varies corresponding to its substructure, pearlite colony. This prevents deformation from concentrating in one spot, which is all about a high anti-brittle fracture property. In short, the process helps avoid significant strain and stress concentration, suppresses unstable crack nucleation and growth on the one hand, and thus fosters simultaneous and continuous local plastic deformation on the other hand,

as long as it is not under completely brittle conditions. This explains why the pearlitic lamellar cementite microstructure has a wider and more gradual transition range.

In the spheroidised cementite microstructure, the fracture plane of the cementite particles observed in this study was consistent with $(010)_\theta$ plane most frequently, and then $\{101\}_\theta$. In the pearlitic lamellar microstructure, the fracture plane of the cementite lamellae was $\{101\}_\theta$.

The findings of this research are of significance because they can help design the microstructure of engineering steels better. Although it is difficult to state clear guidelines for microstructural control based on only what has been uncovered from this study and further work is necessary, it is noteworthy that introducing cementite in a lamellar form results in a wider ductile-brittle transition, which may ensure plastic deformation at lower temperatures than the carbon is introduced in a spherical form. One of the most important things to avoid in steel structures under low-temperature circumstances is sudden and unstable fracture. In addition, from the perspective of countermeasures to earthquakes, having a certain degree of energy absorption capacity is desirable. In these aspects, it is suggested that lamellar microstructures such as pearlite should be selected, given that the cementite fraction and ferrite grain size are constant.

Table of contents

Nomenclature **xvii**

1 Introduction **1**
1.1 Steel: indispensable structural material and its reliability 1
1.2 Aim of the research 5
1.3 Structure of the thesis 7

2 Literature Review **11**
2.1 Ductile-brittle transition in steel 11
2.1.1 Low temperature brittleness 11
2.1.2 Ductile-brittle transition 13
2.2 Influencing factors on the DBT in steel 16
2.2.1 Mechanical factors 16
2.2.2 Microstructural factors 19
2.3 Cementite 29
2.3.1 Crystal structure and anisotropy of cementite 29
2.3.2 Slip system and fracture plane of cementite 32
2.4 Empirical findings 36
2.4.1 Failure with spheroidised cementite microstructure 36
2.4.2 Failure with pearlitic lamellar cementite microstrucuture 39
2.5 Micromechanism and modelling 45
2.5.1 Micromechanism and modelling on cleavage fracture 45
2.5.2 Modelling in the DBT region 54
2.6 Conclusion remarks and key questions for this research 56

3 Materials, and Experimental and Characterisation Techniques **61**
3.1 Materials 61
3.2 Preparation of initial microstructure 62

3.3 Mechanical testing . . . 65
3.3.1 Uniaxial tensile testing . . . 65
3.3.2 *In-situ* tensile testing in SEM . . . 68
3.4 Characterisation . . . 69
3.4.1 Scanning electron microscope: SEM . . . 69
3.4.2 High-resolution electron backscatter diffraction: HR-EBSD . . . 71
3.4.3 SEM-based transmission Kikuchi diffraction : TKD . . . 71

4 Ductile-Brittle Transition Behaviour in Steels with Identical Chemical Composition and Different Cementite Morphology 73
4.1 Introduction . . . 73
4.2 Experimental methods . . . 76
4.2.1 Materials . . . 76
4.2.2 Mechanical testing . . . 76
4.2.3 Characterisation: SEM . . . 77
4.3 Results . . . 77
4.3.1 Transition curve of fracture strain . . . 77
4.3.2 Fractography . . . 82
4.3.3 Cross-sectional observation . . . 87
4.4 Discussion . . . 96
4.4.1 Deformation and fracture process in the lower region of the DBT in the $\alpha + \theta$ microstructure . . . 96
4.4.2 Deformation and fracture process in the lower region of the DBT in the $\alpha + P$ microstructure . . . 98
4.4.3 Activation energy of the DBT in both microstructures . . . 98
4.5 Summary and Conclusions . . . 105

5 Local Plasticity Preceding Macroscopic Fracture in the Lower Region of the DBT Detected by High-Resolution Characterisation Techniques 107
5.1 Introduction . . . 107
5.2 Experimental methods . . . 110
5.2.1 Materials . . . 110
5.2.2 Characterisation . . . 110
5.3 Results . . . 112
5.3.1 HR-EBSD analysis for spheroidised cementite microstructure . . . 112
5.3.2 TKD analysis for pearlitic lamellar cementite microstructure . . . 116

5.4 Discussion . . . 129
5.4.1 Internal stress of cementite particles . . . 129
5.4.2 Cementite particle cracking . . . 131
5.4.3 Lamellae fracture at the early stage of the deformation process . 133
5.4.4 Forming pearlitic cracking . . . 134
5.4.5 Orientation relationship in pearlite . . . 136
5.4.6 The effect of cementite morphology on the DBT behaviour . . . 137
5.5 Summary and Conclusions . . . 138

6 *In-situ* Observation of Local Plasticity on Spheroidised and Pearlitic Lamellar Cementite Microstructures 141
6.1 Introduction . . . 141
6.2 Experimental methods . . . 143
6.2.1 Materials . . . 143
6.2.2 *In-situ* tensile test . . . 143
6.2.3 Characterisation . . . 144
6.3 Results . . . 146
6.3.1 *In-situ* tensile test . . . 146
6.3.2 Microstructural evolution with spheroidised cementite . . . 146
6.3.3 Microstructural evolution with lamellar cementite . . . 156
6.4 Discussion . . . 157
6.4.1 The effect of microstructural factors on cementite cracking . . . 157
6.4.2 The effect of lamellar orientation on local plasticity in pearlite . 164
6.4.3 Comparison with two microstructures . . . 168
6.5 Summary and Conclusions . . . 171

7 Conclusions and Future Work 173
7.1 Conclusion remarks . . . 173
7.2 Future Work . . . 180
7.2.1 Improvement of the experimental methodology to determin and consider T_{DBT} . . . 180
7.2.2 Examination of the effects of other metallurgical factors . . . 180
7.2.3 Extension to other microstructures . . . 182
7.2.4 Generalisation by modelling of the DBT behaviour . . . 182

References 185

Nomenclature

Acronyms / Abbreviations

BCC	Body-centred cubic
BSE	Backscattered electron
CCUS	Carbon capture, utilisation and storage
COP	Conference of the parties
CR	Controlled rolling
CTOD	Crack tip opening displacement
DBT	Ductile-brittle transition
DBTT	Ductile-brittle transition temperature
DIC	Digital image correlation
DP	Dual-phase
EBSD	Electron backscatter diffraction
ECD	Equivalent circular diameter
EDM	Electrical discharge machining
FEG-SEM	Field emission gun scanning electron microscope
FEM	Finite element method
FIB	Focused ion beam
GND	Geometrically necessary dislocation
HAZ	Heat affected zone
HR-EBSD	High-resolution electron backscatter diffraction
HRR	Hutchinson-Rice-Rosengren
HTUFF	Super high HAZ toughness technology with fine microstructure imparted by fine particles
IPF	Inverse pole figure

KAM	Kernel average misorientation
MA	Martensite-Austenite constituent
RKR	Ritchie–Knott–Rice
ROI	Region of interest
SE	Secondary electron
SEM	Scanning electron microscope
TKD	Transmission Kikuchi diffraction
TRIP	Transformation induced plasticity

Nomenclature

A_α	Areal intercept of a ferrite grain
$\overline{A_\alpha}$	Average areal intercept of ferrite grains
A_θ	Areal intercept of a cementite particle
a	Fitting constant in the hyperbolic tangent function for transition curve
α	A coefficient indicating the power, -1 or -1/2
B	Specimen thickness for Beremin model
C_{ij}	Elastic constants of single crystal cementite
C_{mn}	A numerical factor dependent on work-hardening exponent and the Weibull shape factor for Beremin model
C_0	Crack length / Cementite size
γ_{c}	Surface energy of carbide
$\gamma_{\mathrm{c/f}}$	Surface energy of cementite and ferrite interface
$\gamma_{\mathrm{f/f}}$	Surface energy of ferrite grain boundaries
γ_{gb}	Plastic work per unit area for crack to propagate into adjacent grains
γ_i	Shear strain component of single crystal cementite (i = 4, 5, 6)
γ_{p}	Effective surface energy / Plastic work required to create a unit area of fracture surface
γ_{s}	Surface energy per unit area
d	Ferrite grain size
d_{g}	Grain diameter relating characteristic distance
d_α	Apparent average ferrite grain size

d_θ	Cementite particle size from areal intercept of a cementite particle
$\overline{d_\theta}$	Apparent average cementite particle size
d_{ECD}	Equivalent circular diameter of a cementite particle
ΔG	Activation energy of the DBT relating Arrhenius-type plot
E	Young's modulus
ε_{eqv}	Equivalent strain
ε_1	Maximum principal strain
ε_2	Minimum principal strain
ε_i	Normal strain component of single crystal cementite (i = 1, 2, 3)
ε_p	Equivalent plastic strain
ε_{xx}	Macroscopic tensile strain
ε_y	Yield strain
ε_0	A constant for Arrhenius-type plot of transition curve
$\dot{\varepsilon}$	Strain rate
J_{TC}	Critical total J integral under mixed-mode I and III conditions
K_{Ic}	Critical stress intensity factor
k	Hall-Petch constant
$k_{\mathrm{Y}}^{\mathrm{S}}$	Constant related to shear stress state
k_{B}	Boltzmann constant
$l_0{}^*$	Characteristic distance
m	Weibull shape factor
μ	Shear modulus
ν	Poisson's ratio
P_R	Probability of failure for Beremen model
r_c	Probability of cementite cracking
r_{E}	Young's modulus of cementite
S_p	Lamellar spacing of pearlite
σ_f	Cleavage fracture stress / Critical fracture stress for crack to propagate into adjacent ferrite grain
σ_y	Yield stress
σ_{yy}	Local tensile opening stress relating characteristic distance

σ_{max}	Maximum principal stress
σ_0	Friction stress (constant) / Flow stress relating characteristic distance
σ_i	Normal stress component of single crystal cementite (i = 1, 2, 3)
σ_{W}	Weibull stress for Beremin model
σ_u	Measured fracture stress for Beremin model
σ_{11}	Elastic stress normal component
σ_{22}	Elastic stress normal component
σ_{12}	Elastic stress shear component
S	Fracture strain for transition curve
S_0	Fitting constant in the hyperbolic tangent function for transition curve
τ_i	Shear stress component of single crystal cementite (i = 4, 5, 6)
τ_{eff}	Effective local shear stress
τ_{max}	Maximum in-plane shear stress
T_{GY}	Temperature at which cleavage fracture is coincident with general yield
T	Temperature
T_{DBT}	Ductile-brittle transition temperature
t	Thickness of cementite
V_{u}	Volume element unit for Beremin model
$\alpha + \theta$ microstructure	Ferrite and sheroidised cementite microstructure
$\alpha + P$ microstructure	Ferrite and pearlitic lamellar cementite microstructure

Chapter 1

Introduction

1.1 Steel: indispensable structural material and its reliability

Steel is essential for innovation, value creation and sustainability as part of our concerted efforts to maintain a safe and reliable society. It is by far and away the most widely used family of metals owing to its superior yet wide-ranging mechanical behaviours and concomitant economic benefits. Steel plays an important role in many industries, including construction, infrastructure, shipbuilding, and energy storage and transportation. One of the most essential properties of weldable structural steel is toughness, the resistance to brittle fracture. Brittle fracture is a phenomenon in which unstable cracks propagate rapidly throughout the material. Since brittle fracture generally accompanies no macroscopic deformation, it can cause sudden catastrophic damage when it occurs. When considering the safety of steel structures, brittle fracture must be prevented. Nevertheless looking back at the past there have been serious

accidents related to this type of fractures in steel structures, such as fabrication of ships [1], oil tankers [2], pressure vessels [3, 4], and marine structures [5].

Figure 1.1 represents the application trend over a number of decades in the usage of weldable structural steel plates in terms of yield strength and thickness of steel plate, categorised in each industry [6]. This figure shows what kind of steel plates have been used in each industry with respect to strength and plate thickness from the 1970s to the 2010s. With the increasing demand for larger, lighter, easy-to-fabricate steel structures, steel plates have become thicker and stronger. It is known that the higher yield strength of high-strength steel and the increased plastic constraint caused by thicker plates would increase the ductile-brittle transition (DBT) temperature of steels. The higher the strength of structural steel, the higher the risk of embrittlement. Therefore, it is becoming more and more important to understand better, control, and predict the DBT behaviour of steel from the perspective of ensuring the safety of steel structures. Figure 1.2 [7] is another example that summarises the evolution of the strength of structural steels used in each industry. Here, too, a similar trend is revealed that higher tensile strength steels have been used with the ages.

When it comes to looking at the future, new technological developments such as the establishment of alternative energy utilization technologies and these supply chains with economic rationality, and carbon capture, utilisation and storage (CCUS) have been underway in the context of achieving carbon neutrality as an irreversible social requirement [8]. Structural steels will be required to respond to such new emerging applications. For example, liquefied hydrogen is expected to be stored and transported at extremely low temperatures for energy usage [9]. It has been becoming clear that ship cargo tanks and onshore storage tanks for liquified CO_2 in the CCUS supply

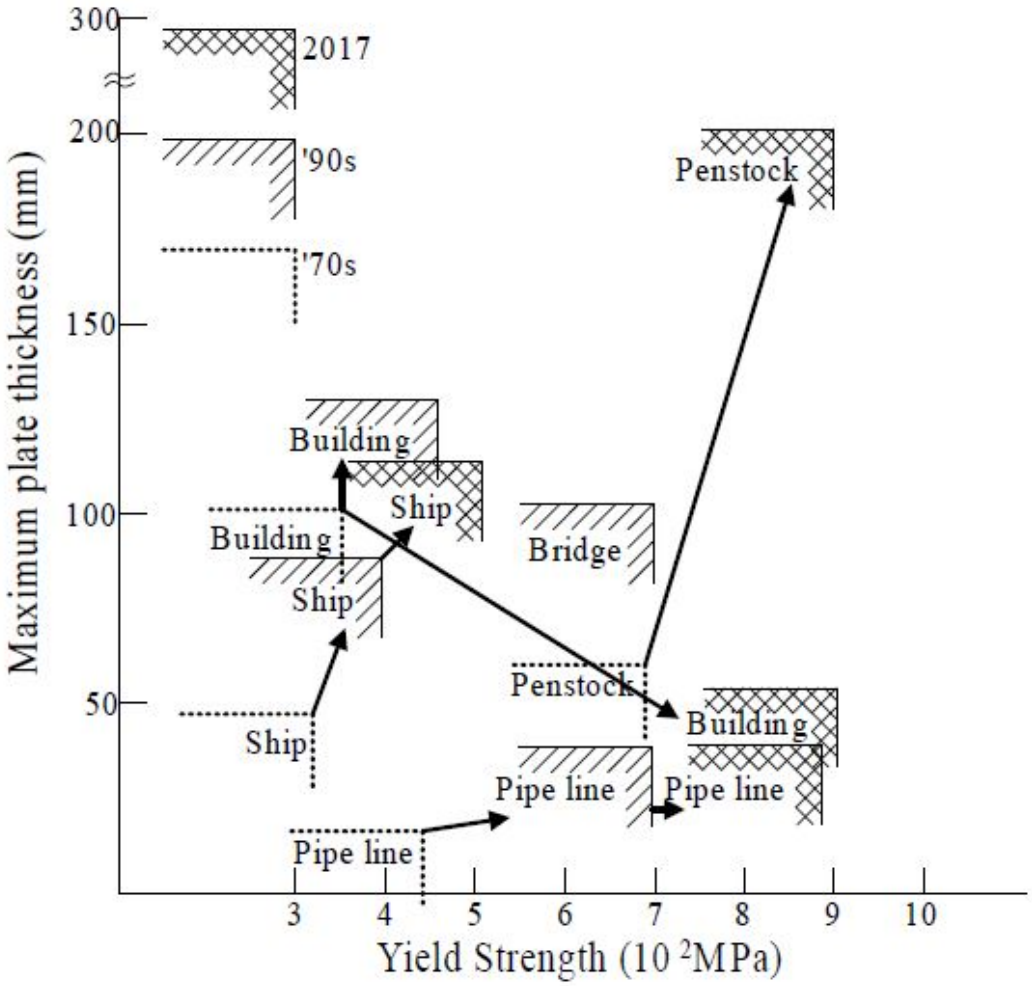


Fig. 1.1 The applicaton trend of steel plates to varoius structure from 1970s to 2010s from the viewpoint of strength and plate thickness [6].

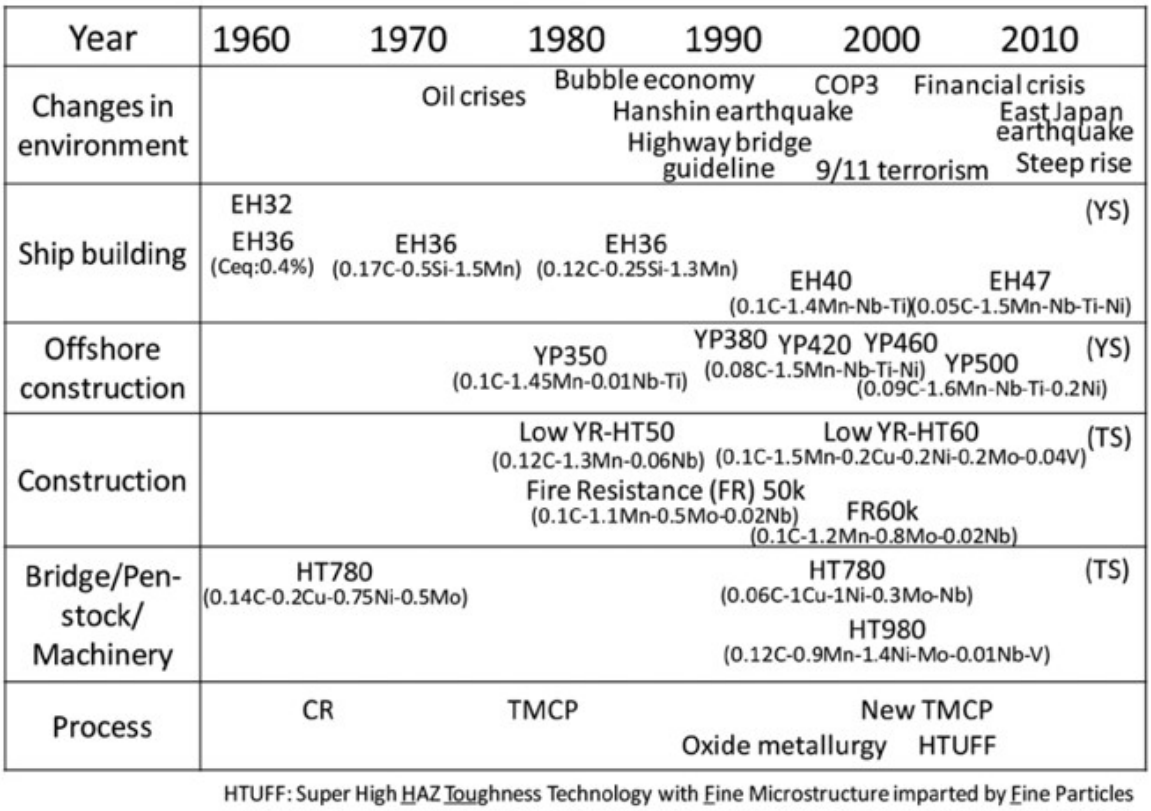


Fig. 1.2 History of steel plates for ship building, marine construction, construction and bridge focusing on their strength and usages of alloying elements [7]. The numbers before the element symbols indicate concentration in weight (wt) %.

chain will also require to have an excelent low temperature toughness [10]. Liquified ammonia as an alternative fuel and/or a hydrogen carrier will also be stored at low temperatures [11]. In addition to the low temperature toughness, when considering environmentally assisted fractures in those possible applications such as hydrogen embrittlement and ammonia stress corrosion cracking, it is vital to keep expanding our incomplete understanding of the toughness of steel for research and development in the future.

1.2 Aim of the research

Steel is a crucial structural material for the society. Brittle fracture of steel structures must be avoided. Due to this social responsibility, many studies have been conducted to understand the characteristics and mechanisms of brittle fracture in structural steels. Here, a brief outline is described and the details will be presented in the literature survey in Chapter 2. In terms of understanding the process and controlling the properties, much work has been carried out [12], especially on the initiation and propagation of unstable brittle cracks [13–16], the influence of microstructure and chemical composition [17–19] and modelling it [13, 14, 20]. Beginning with a single ferrite phase of body-centred cubic (BCC) iron [13–15] and then targeting dual phase of ferrite and cementite [16, 21, 22], research on the understanding of deformation and fracture behaviour has been conducted. The matrix varies widely from simple ferrite to bainite and martensite. Models for brittle fracture are on the way to being developed. The basic recognition of the brittle fracture process comes from early work on characterisation with optical microscope from the 1950s [17, 23] and then with electron microscope.

However, one problem in the study of the ductile-brittle transition in structural steels is the lack of comprehensive understanding of the local plastic deformation that occurs prior to macroscopic brittle fracture. Although there are models based on the influencing factors of the microstructure, there are still difficulties in describing the initiation of cracks. It is easy to speculate that the deformation and fracture process is even more difficult to treat, especially in the lower part of the DBT region, where some degree of plastic deformation precedes brittle fracture. Although the methodology has evolved from an experimental point of view, there are still limitations in detecting local strains and stresses [24]. To further complicate the issue, local development of plasticity is affected by the microstructure of the steel. Following the application trends in Figure 1.1, the microstructures applied have expanded from a single ferrite phase to ferrite and pearlite, bainite, and martensite, becoming more complicated. They differ in matrix grain size, crystal orientation relationship, and cementite size and morphology. For example, the following fundamental questions are inevitably and insufficiently answered: - How do the differences in microstructure lead to the difference in deformation and fracture processes, and how do they affect the DBT behaviour? - What is the fracture plane of cementite particles, one of the most fundamental phases in practical steels, and how does it interact with the ferrite matrix? - What is the deformation behaviour of ferrite and pearlite microstructures in the transition temperature region? etc.

To improve this situation and move it forward, that is, to deeply understand the deformation and fracture process in the DBT and control it, it is necessary to capture the development of local strain and stress in the vicinity of initial cracks, which is the driving force for propagation and further failure. Although there is some analytical work on

simplified systems [25–27], experimental knowledge is very limited, and it is difficult to say that even the fundamentals are fully understood. On one positive side, technological advances in various fields have made high-resolution electron microscopes and their related analytical equipment more available [28–31]. Microstructural observations with such advanced techniques and the experimental understanding of the deformation and fracture behaviour of structural steel in the DBT region from them are by no means a solved endeavour. In that sense, structural steel might be a so-called "traditional" material, yet it is definitely still "worth-researching-material" and can shed light on new findings.

The ultimate goal of the research is to fully understand the relationship between mechanical properties, microstructure, and production process, namely, chemical composition and manufacturing method, and to design and utilise them on an industrial and commercial scale. With this ultimate goal in mind, the purpose of this research is to improve the fundamental understanding of the first relationship, thus, mechanical properties and microstructure, regarding the DBT behaviour of steel. In this research, with carefully designed test steels and cutting-edge high-resolution characterisation techniques, much attention will be paid to elucidating the effect of cementite morphology on the DBT behaviour of structural steel, focusing on local plasticity before a macroscopic brittle fracture occurs and how the microstructure affects it.

1.3 Structure of the thesis

In this Chapter 1, a general introduction, aim of the research, and thesis structure are described.

Chapter 2 provides background information for conducting this research. Explicit recognition of what has been reported and what is still unknown is crucial in the first place. The DBT phenomenon in steel is discussed first. Then, mechanical and microstructural influencing factors on the DBT are considered. In addition, basic information on cementite, a critical phase in this research, is presented. After that, experimental findings regarding the deformation and fracture process in ferrite and spheroidised cementite microstructure, as well as ferrite and pearlitic lamellar cementite microstructure, are outlined. Lastly, a summary of the literature review and key questions that should be answered in this work are given at the end of the chapter.

Chapter 3 describes the preparation for the initial microstructures of test specimens that are suitable for a series of evaluations. One of the most important points in carrying out this research is proper preparation of initial microstructures. The influence of many metallurgical factors on the DBT of steel has been reported, including grain size, impurity elements such as phosphorus and sulfur which are unavoidably contained and could embrittle steel, and inclusions such as oxides and sulfides that can function as stress concentration points and initial cracks. It is necessary to eliminate nad minimise these influences as much as possible, and evaluate only the impact of a microstructural factor of interest. In addition, the mechanical testing and characterisation methods are also presented in detail.

In Chapter 4, the DBT behaviour of tested steel is considered, with the same chemical composition but two different cementite morphologies. Tensile tests are performed over a wide range of temperatures and strain rates to obtain several transition curves. In the tensile tests, a high-speed camera is applied for high strain rate conditions. As post-mortem characterisation, the fracture surface of the tested specimen and

the cross-sectional microstructures are observed. Based on these observations, the deformation and fracture process of ferrite and spheroidised cementite and ferrite and pearlitic lamenllar cementite microstructure are considered. Then, from the relationship between the strain rates and the ductile-brittle transition temperature (DBTT) obtained, the activation energy is calculated by Arrhenius plot analysis, and the DBT behaviour of both microstructures is grasped.

Chapter 5 presents a post-mortem analysis using advanced characterisation techniques, such as high-resolution electron backscatter diffraction (HR-EBSD) and transmission Kikuchi diffraction (TKD). By analysing the tested specimens of the lower region of the DBT, the local plastic deformation behaviour before macroscopic brittle fracture is characterised. Additionally, the fracture surface of cementite particles is investigated in the ferrite and spheroidised cementite microstructure. Using the HR-EBSD dataset, the elastic strain and stress of the spheroidised cementite and ferrite matrix, and the geometrically necessary dislocation (GND) density distribution is calculated. Then, the internal stress and fracture stress of the cementite are compared. For ferrite and pearlitic lamellar cementite microstructure - which have much finer microstructure - TKD is performed for characterisation coupled with crystallographic orientation analysis. The fracture of cementite lamellae at the very early stage of deformation, and the formation of pearlitic cracks are discussed.

In Chapter 6, *in-situ* observation for ductile deformation and subsequent digital image correlation (DIC) analysis are tackled. In the DBT region, particularly in the lower ones, localised plastic deformation occurs prior to macroscopic brittle fracture. Understanding the interaction between cementite and ferrite matrix is essential until the cementite cracks in the ferrite and spheroidised cementite microstructure. In

the ferrite and pearlitic lamellar cementite microstructure, the interaction between ferrite and pearlite, as well as the localised plastic deformation behaviour in pearlite, are emphasised. The development of the localised plastic deformation behaviour is compared in both microstructures.

In Chapter 7, the conclusions on the effect of cementite morphology on the DBT behaviour obtained in this research are summarised. Suggestions for future work are also described emphasising this aspect.

Chapter 2

Literature Review

2.1 Ductile-brittle transition in steel

2.1.1 Low temperature brittleness

Figure 2.1 illustrates three common fracture mechanisms in ferritic steel [32]. Generally, the ductile fracture (a) is composed of void nucleation, growth, and coalescence of the void that initiates at inclusion and/or second phase particles. Cleavage fracture (b) involves separation along specific crystallographic planes and much less plastic deformation and energy dissipation than ductile fracture. Its fracture path is transgranular. In addition, intergranular fracture (c) occurs when the preferred fracture path is along with grain boundaries. Cleavage fracture and intergranular fracture are called brittle fracture. Examples of fracture surfaces for ductile and cleavage fracture are shown in Figure 2.2 (a) and (b), respectively. Cleavage fracture is emphasised among the mechanisms of brittle fracture in this research project.

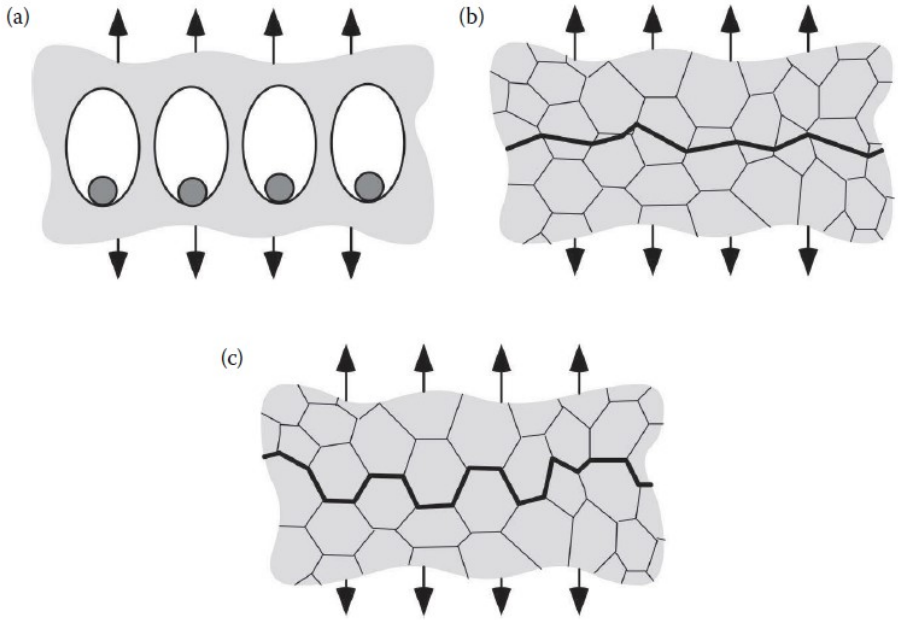


Fig. 2.1 Three micromechanisms of fracture in metals: (a) ductile fracture, (b) cleavage fracture, (c) intergranular fracture [32].

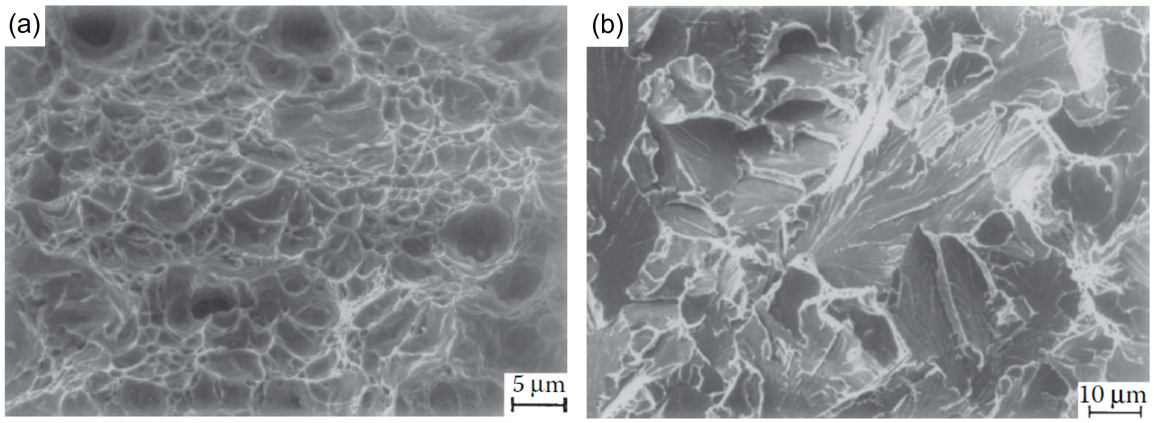


Fig. 2.2 Scanning electron microscope (SEM) images showing examples of ductile fracture surface (a) in low carbon steel, and cleavage fracture surface (b) in A508 class 3 steel, low-alloyed steel for pressure vessels with yield strength of 345 MPa class [32].

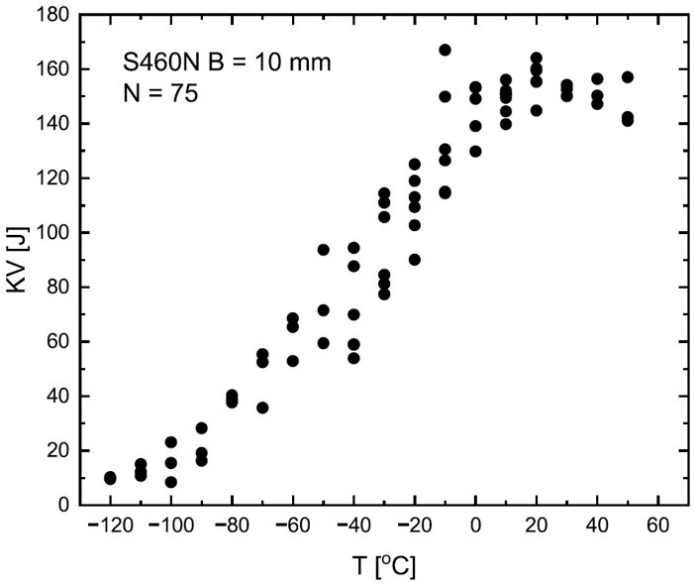


Fig. 2.3 An example of the Charpy impact test transition curve [33]. The tested steel is EN10025-3 S460N, a high strength weldable fine-grain structural steel made by normalising conditions with ultimate tensile strength of 540 MPa class. KV indicates absorbed energy for a Charpy V-notch test piece. N stands for the number of the tests. B is the width of the Charpy test specimen.

2.1.2 Ductile-brittle transition

Figure 2.3 illustrates an example of the Charpy V-notch test transition curve [33]. At high temperatures, specimens fail in a ductile manner with significant plastic deformation, and hence, the absorbed energy is relatively high. On the other hand, at low temperatures, cleavage fracture is dominant, which leads to low energy absorption. To some extent, ferritic steel comes to be brittle from ductile with decreasing temperature, and there is a particular temperature region where the ductile fracture mechanism and the cleavage fracture mechanism compete with each other. This is the DBT region. In the DBT region, failure of steel can be preceded by large-scale plasticity, ductile crack nucleation, and growth before macroscopic cleavage fracture [34].

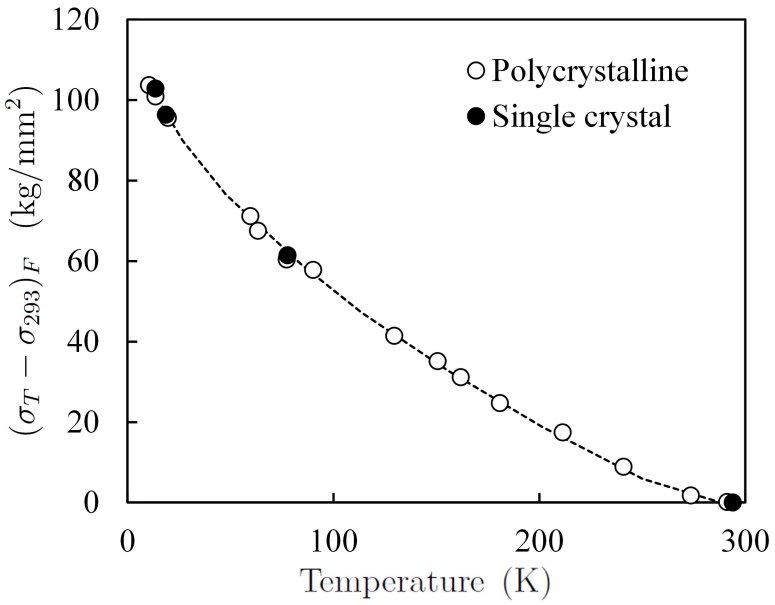


Fig. 2.4 Temperature dependence of flow stress for single crystal and polycrystalline specimens of iron tested in compression. Strain rate was 4×10^{-4}/s. The data points were taken at a strain of 10 % [35]. The vertical axis ($(\sigma_T - \sigma_{293})_F$) indicates the difference of the flow stress between each test temperature and the reference temperature of 293 K.

Iron, as well as other BCC metals, shows a marked temperature dependency of its yield stress. This means the flow stress of iron increases with decreasing temperature [35], as shown in Figure 2.4. This is because the Peierls stress, which is the stress required for dislocation glide, is significantly higher at absolute zero temperature in BCC metals [36] and decreases considerably with increasing temperature due to the much contribution of a thermal activation process.

By contrast, the cleavage fracture stress is much less sensitive to temperature [37–39]. Griffith [40] proposed cleavage fracture stress σ_f via the following formulation by postulating initial cracks in material and considering an energy balance during crack propagation. The initial crack is assumed to be elliptical with length $2C_0$ and its

thickness equal to be a plate thickness.

$$\sigma_f = \left(\frac{2E\gamma_{\mathrm{s}}}{\pi C_0}\right)^{1/2} \quad \text{in plane-stress condition} \tag{2.1}$$

$$\sigma_f = \left(\frac{2E\gamma_{\mathrm{s}}}{\pi(1-\nu^2)C_0}\right)^{1/2} \quad \text{in plane-strain condition} \tag{2.2}$$

where γ_s is the free surface energy per unit area, E is Young's modulus, and ν is Poisson's ratio. Since γ_s is thought to be largely independent to temperature, σ_f has little temperature dependency. Griffith's theory estimated the cleavage fracture stress of ferritic steel to be much lower than it is, although the theory is suitable for completely brittle materials such as glass. Irwin [41] and Orowan [42] independently took into consideration the fact that, to some extent, plastic deformation is involved in a crack tip even in the cleavage fracture process and added the effect of plastic work into the free surface energy term γ. Eventually, the work of Irwin and Orowan succeeded in evaluating the cleavage fracture stress of steel.

The DBT phenomenon can be understood in terms of the relationship between yield stress and cleavage fracture stress, as shown in Figure 2.5 [42]. The intersection point between yield stress and cleavage fracture stress can be regarded as a DBTT. Below this point, ferritic steel fails by being brittle, that is, without macroscale plasticity. According to the Equation 2.1 and Equation 2.2, the fracture stress is implied to be a function of the crack length. The crack length itself is unrelated to mechanical constraints. On the other hand, the local yield stress at the crack tip is strongly influenced by the plastic constraint and stress concentration in that area. Therefore, the DBTT can be changed depending on the size and shape of the test specimen [43].

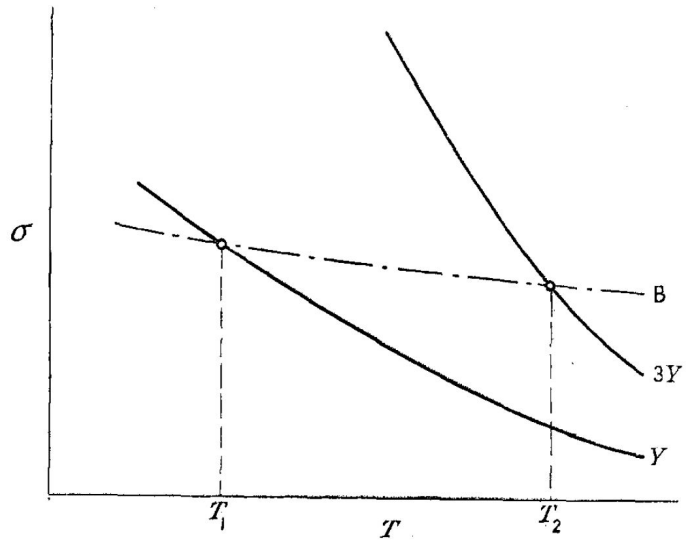


Fig. 2.5 The Orowan model for the ductile-brittle transition; the transition temperature (T_2) as the abscissa of the intersection point of the fracture stress curve (B) with the constrained yield stress curve ($3Y$) plotted against the temperature [42].

2.2 Influencing factors on the DBT in steel

Considering the relationship between cleavage fracture stress and yield stress shown in Figure 2.5, toughness, in other words, DBTT, and susceptibility of cleavage fracture are affected by all the factors that have influence on yield stress and cleavage fracture stress, such as microstructure, strain rate, and stress triaxiality as well as temperature. Here, experimental results about influencing factors on the DBT are reviewed.

2.2.1 Mechanical factors

Strain rate

As to the effect of strain rate on the DBT, increasing strain rate has the same effect as lowering temperature in terms of the contribution of thermal activation energy to dislocation movement. Therefore, a higher strain rate causes the DBTT to rise. Figure 2.6 [44] shows fracture toughness data for A572 grade 50 steel, a low-alloyed

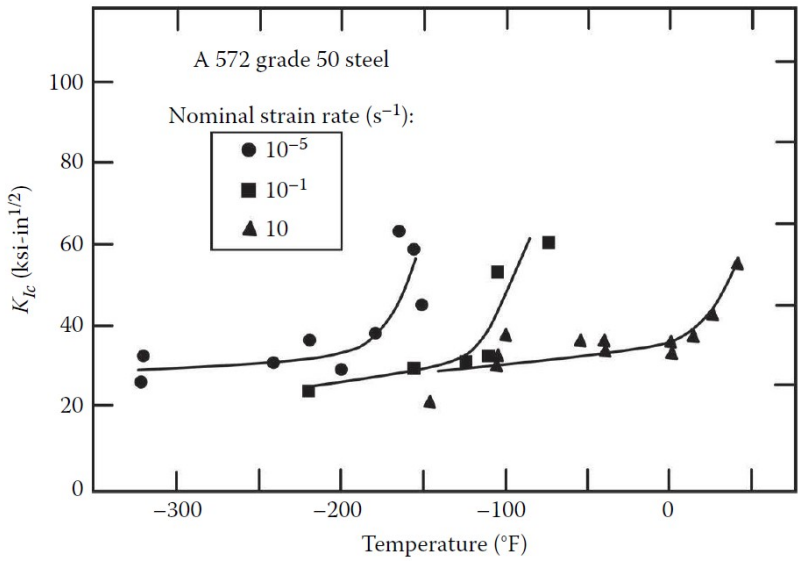


Fig. 2.6 Effect of loading rate on the cleavage fracture toughness of A572 grade 50 steel, a low-alloyed columbium-vanadium structural steel with yield strength of 345 MPa class [44].

columbium-vanadium structural steel with yield strength of 345 MPa class, at different loading rates. The critical plane-strain stress intensity factor $K_{\mathrm{I}c}$ was determined from fracture toughness testing. Fracture toughness increased significantly with the temperature from the onset of the ductile fracture. Increasing the loading rate has the effect of shifting the temperature transition to higher. Petch [45] investigated the effects of temperature and strain rate on the Charpy V-notch transition temperature and reported that it increased at high strain rate.

Loading condition

Regarding the effect of loading conditions, Li et al. [46–50] investigated the fracture toughness of F-82H steel, a ferritic/martensitic stainless steel (Fe-0.1C-8Cr-2W-0.2V-0.04Ta in wt%), under mixed-mode I and III conditions at ambient temperature. Different ratios of tension/shear stress were achieved by changing the principal axis of

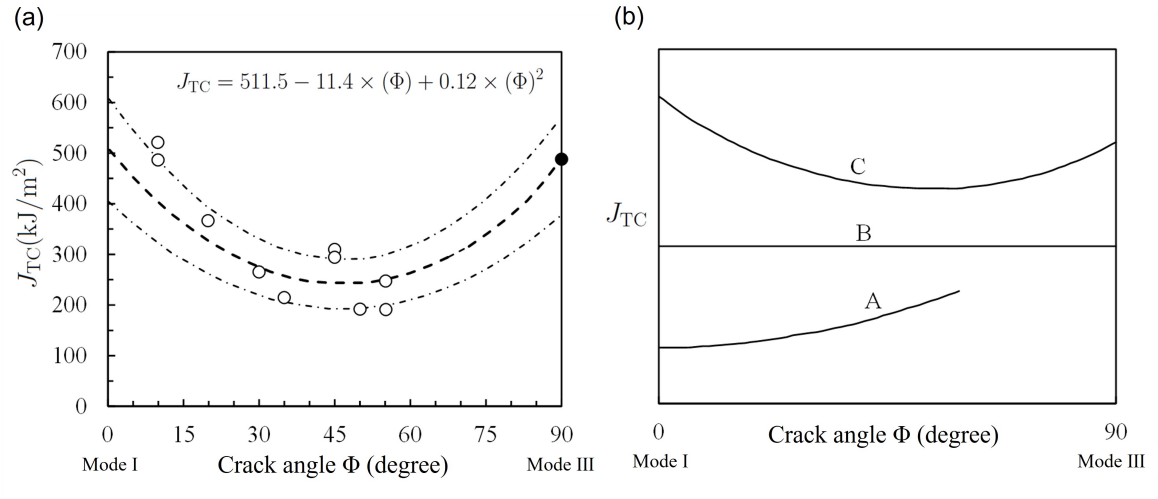


Fig. 2.7 Effect of loading mode on critical total J integrals J_{TC} of F-82H steel; (a) the dependence of the J_{TC} integrals on the crack-inclination angles, (b) dependence of the J_{TC} integral toughness for various structural materials on crack-inclination angles. Brittle, intermediate toughness, and tough materials follow curves A, B, and C, respectively [46].

the crack plane from the load line with modified compact tension specimens. They showed that the critical total J integral J_{TC} under the mixed-mode varied with the crack angles and was lower than their mode I and mode III counterparts (Figure 2.7 (a)). In addition, they discussed that the dependency of the J_{TC} integrals on loading mode was different from the level of toughness of tested materials as shown in Figure 2.7 (b).

Stress concentration and Stress triaxiality

The fracture behaviour of notched bend tests is shown in Figure 2.8 [51]. A similar tendency was observed in low-temperature tensile tests [52], and when the inclined angle of the notch root became blunt, the temperature at which cleavage fracture was coincident with general yield, T_{GY}, shifted to the lower temperature. This arises from the decrease in stress concentration at the notch root.

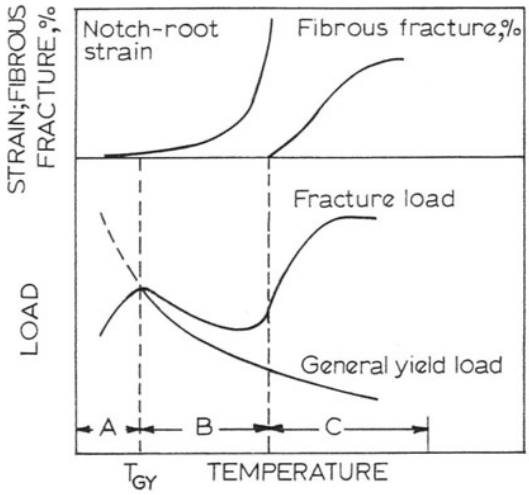


Fig. 2.8 Typical results of the temperature dependency of fracture load and general yield load in notched slow-bend tests [51].

The effect of stress triaxiality was investigated by changing the plate thickness of notched test pieces [37]. When the plate thickness was reduced, the temperature at which the fracture load began to decrease was not obviously affected, but T_{GY} shifted to lower temperatures. This is explained as follows [51] with Figure 2.9; when the plate thickness is thin enough, the notch root is in a plane-stress state, and stress equivalent to the yield stress is applied at the notch root due to plastic deformation. On the other hand, when the plate thickness is thick enough, the notch root is in a plane-strain state, resulting the stress at the notch root exceeds the yield stress due to a higher stress triaxiality, making brittle fracture more likely to happen.

2.2.2 Microstructural factors

Alloying element

The effects of alloying elements include the increase in yield strength due to solid solution strengthening, the change in microstructure, and the toughness of the ferrite matrix

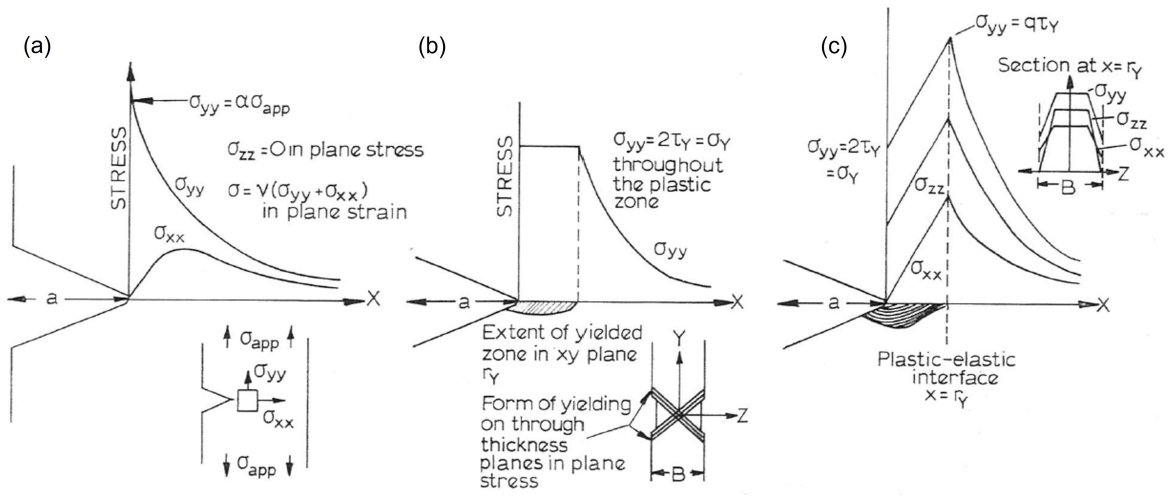


Fig. 2.9 Stress state at notch root; (a) elastic stress distribution in notched testpiece, (b) distribution of principal stress σ_{yy} in plane stress, (c) distribution of principal stresses in plane strain [51]. σ_Y is tensile yield stress. τ_Y is shear yield stress. σ_{app} is applied stress.

itself. These effects have been investigated for a long time, but most of the research thus far has focused on the relationship between the elemental concentration and mechanical properties [17]. Based on the micromechanism of deformation and fracture, the addition of alloying elements changes the microstructure, and the mechanical properties change as a result. Here, the details of its effect through microstructural change will be glossed over, although the important items will be discussed later, but rather their physical effects on yield stress and fracture stress, that is, the direct influence on the toughness of the ferrite matrix itself are described.

Solution strengthening by adding alloying elements increases yield strength [53, 54]. In particular, the amount of the increase is large for P and Si, which is advantageous for strengthening, but on the other hand, can be said to be the elements that tend to cause embrittlement due to the increase in yield strength according to the Orowan model in Figure 2.5. Various alloying elements have be investigated such as Mn [55], Si [56, 57], Ni [55, 57], Al [58], Cu [59]. Both Ni and Mn show solid solution strengthening at room

temperature, but solid solution softening at low temperatures. This is expected to enhance the decrease in transition temperature. The transition temperature decreased with Ni addition but increased with Mn. This is thought to be because the addition of Mn reduces the grain boundary energy, making grain boundary fracture more likely to occur [55]. Similarly, the increase in Al content made slip deformation less likely to occur, but rather twin deformation more likely to occur, which produced more crack intiation. That was why the transition temperature increased with Al addition [58].

Matrix grain

It is well known that yield stress σ_y can be described by the Hall-Petch equation [60, 61]:

$$\sigma_y = \sigma_0 + kd^{-1/2} \tag{2.3}$$

where σ_0 is friction stress (constant), k is Hall-Petch constant, and d is grain size. Thus as ferrite matrix grains become finer, the yield stress increases, which also seems to increase the DBT temperature. The fracture stress, however, is known to increase too due to grain refinement. This is because the dislocation stacking distance is short when the grains are small, meaning the stress concentration is not that intensive.

Griffith's theory [40] suggests that the critical process for overall cleavage fracture of fine-grained mild steel may be grain-sized microcrack propagation into the first grain boundary. In this case, the Griffith model implies that cleavage fracture stress σ_f varies according to [32]

$$\sigma_f = \left(\frac{2E\gamma_{\mathrm{gb}}}{\pi(1-\nu^2)d} \right)^{1/2} \tag{2.4}$$

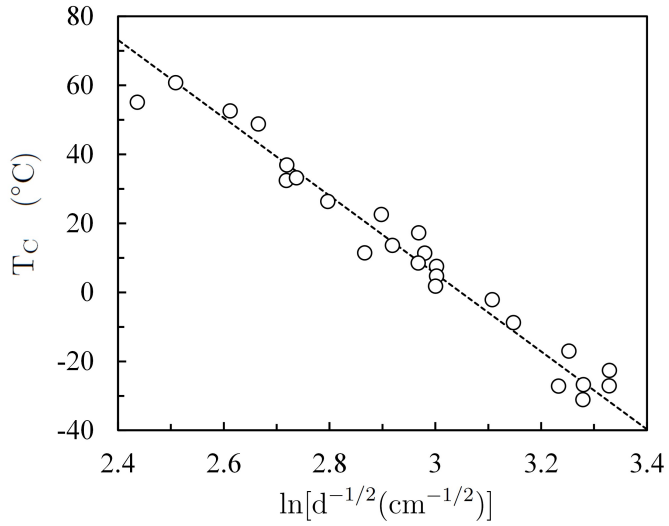


Fig. 2.10 The effect of ferrite grain size (d) on the DBT temperature (T_C) obtained from Charpy V-notched impact test in a mild steel (Fe-0.11C-0.51Mn-0.02Si–0.05S-0.03P in wt%) [62].

where γ_{gb} is the plastic work per unit area required for the microcrack to propagate into the adjacent ferrite grain, d is the grain size assumed to be equiaxed, E is the Young's modulus, and ν is the Poisson's ratio.

With respect to fracture stress, Low [23] demonstrated that cleavage fracture stress of decarburised steel varied linearly with the reciprocal square root of ferrite grain size. The same tendency was reported between ferrite grain size and transition temperature obtained from the Charpy V-notched impact test in a mild steel [62] as shown in Figure 2.10. In this way, subtracting the effects of the increase in yield stress and fracture stress, the toughness was reported to be improved in many cases [63, 64].

The cleavage fracture process of bainitic and martensitic steel is more complicated due to the complexity of their microstructures. They have hierarchical microstructures in terms of crystallography [65–69]. These consist of lath, block, and packet, which are domain units characterised by specific crystal orientation relationships. Although

a number of studies have been conducted [70–73], further analysis is needed. Bainite and martensite have crystallographic misorientations in block and packet boundaries. Hence, such boundaries can be a barrier to cleavage fractures. Therefore, the block and packet size can be considered an "effective" grain size for toughness. Dolby et al. [74] demonstrated cleavage fracture stress could be described with packet diameter. More recently, it has been reported that block plays a controlling factor as the effective grain size on the DBT in lath martensite [75].

So far the functions of the BCC matrix are summarised in terms of the mobility of dislocations by yield stress, and resistance against brittle crack initiation and propagation by fracture stress. In addition, the matrix itself can generate the crack initiation needed for brittle fracture. In carbon-free systems or ultra-low carbon steels, brittle fracture occurs due to twin deformation of the matrix. Based on experiments, several theories have been proposed regarding this mechanism, including the theory that cracks are generated from stress concentration at the intersection of two twins [76, 77], the theory that cracks are generated when twins collide with grain boundaries [78], and the theory that the twins themselves break down and generate cracks [20, 76, 79]. Figure 2.11 shows an example of cleavage crack nucleation at twin intersections in a silicon-iron single crystal.

Embrittling secondary phase

In the next two subsections, the effect of the secondary phase on cleavage fracture and the DBT is reviewed. Embrittling secondary phases function as crack initiation sites. For example, they include cementite, inclusions like nitrides or oxides, and local brittle

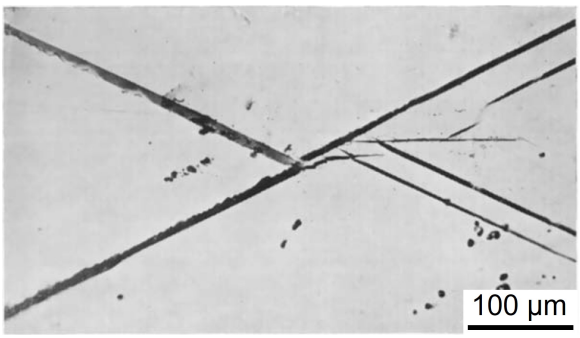


Fig. 2.11 An example of cleavage crack nucleation at twin intersections in a silicon-iron single crystal [76].

zones like martensite-austenite constituent (MA) formed during welding process. Here, the work on embrittling secondary phases other than cementite is briefly summarised.

In the DBT region, cleavage fracture is preceded by plastic deformation [34]. Metal fracture due to void formation at secondary phase particles was first established by Tipper [80]. Marino et al. [81] and Babout et al. [82, 83] studied the nucleation from large inclusions in model alloys by means of X-ray tomography. They revealed that the hardness of matrix had an influence on crack nucleation. That is, nucleation occurred by decohesion at the particle/matrix boundary in a soft matrix. By contrast, particle cracking was predominant in hard matrix (Figure 2.12). In the former case, fine-scale mechanism of decohesion may be thought of involving the coalescence of vacancy loops at the interface, followed by interface crack propagation [84]. In the latter case, the process may be viewed as a cleavage nucleation process. Pineau et al. [12] summarised the parameters in void nucleation, as shown in Table 2.1. In addition to void nucleation, particle fragmentation for elongated inclusions, and microcracks in brittle phases for multiphase steels such as DP (dual-phase) steel [85, 86] and TRIP (transformation induced plasticity) steel [87] have been reported as brittle fracture initiation sites. Taken a practical weldable structural steel, a typical example is an

inclusion such as TiN [88] as shown in Figure 2.13. It is also known that brittle fracture can occur from MA that is formed during the cooling process of the heat affected zone (HAZ) of welded joints [89].

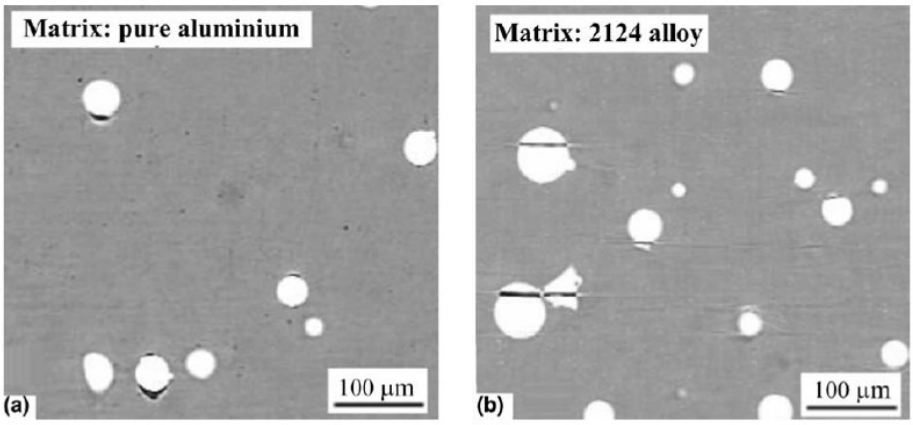


Fig. 2.12 Reconstructed images obtained by X-ray tomography during *in-situ* tensile test for different metal matrix composites reinforced by 0.04 volume fraction of ZrO_2/SiO_2 spherical particles, showing the influence of the plastic behaviour of the matrix surrounding the particles on the damage initiation mode. For the matrix made of pure aluminium (low yield stress and medium work hardening rate), decohesion prevails. In contrast, for aluminium 2124 alloy matrix with higher yield stress and work hardening rate, particle fracture is the dominant failure mechanism [83].

Table 2.1 Key parameters in void nucleation and relative trends upon increasing the parameter for the microscopic mechanism [12].

Parameter	Type	Trend	
		Decohesion	Cracking
Matrix yield strength		↘	↗
Matrix hardening exponent		↘	↗
Particle elongation		↘	↗
Particle stiffness		↗	↗
Load orientation	axial	↘	↗
	transverse	↗	↘
Load triaxiality		↗	↘

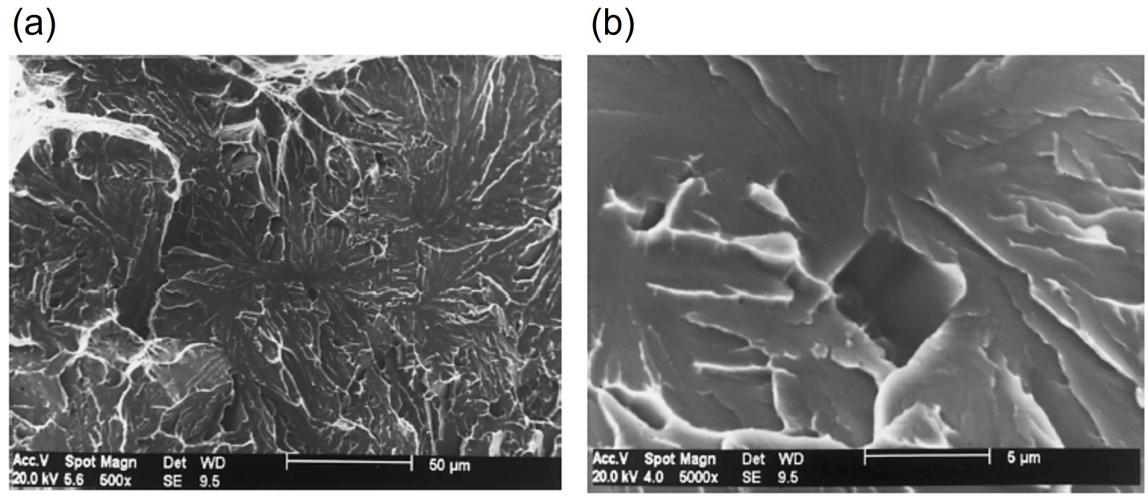


Fig. 2.13 SEM images of cleavage crack initiation point with TiN around the image centre in (a), and its magnified image in (b) [88].

Cementite as secondary phase

Here the effect of the cementite as an embrittling secondary phase on cleavage fracture and the DBT is reviewed. Cementite is crucial as a source of microcracks. Because of the carbon content for practical steels, cementite is the most common secondary phase, and hence, a great deal of research on the influence of cementite on cleavage fracture has been conducted. If considered pure iron or ultra-low carbon steel, which have almost no cementite, cleavage cracks initiate from the intersection between twin boundaries or twin/grain boundary as previously described. Considering ferrite and cementite microstructure, especially spheroidised cemenetite, substantial experimental evidence suggests that crack nucleation occurs in cementite and requires some plastic deformation of the matrix [16, 25–27, 52, 72, 90–99]. Such cracks are considered to be preferred to initiate at grain boundary cementite.

In general, grain refinement introduces many more grain boundaries, which act as a barrier for cleavage crack propagation. Smaller grains can also function to reduce crack

initiation, like grain boundary cementite cracking, by decreasing dislocation pile-up and then stress concentration [100]. In addition to this, smaller grains imply thinner grain boundary cementite. Ferrite grain size and cementite size are not mutually exclusive, meaning that if ferrite grain is coarsened (refined), cementite size also becomes large (small). Several studies have pointed out that the effect of grain refinement on toughness in low carbon steel includes the effect of cementite refinement at the same time. Curry et al. [25] investigated the relationship between ferrite grain size, cementite particle size, and fracture stress in a spheroidised high carbon steel. Their work revealed that the cleavage fracture stress was proportional to the reciprocal square root of ferrite grain size as well as cementite size as shown in Figure 2.14 (a). They also demonstrated the effect of cementite size on fracture stress (Figure 2.14 (b)) and proposed that the determinant factor for controlling cleavage fracture stress was cementite size. Allen et al. [101] showed that the refinement of carbide films by manganese addition was accompanied by a systematic lowering of the transition temperature. Bowen et al. [92] presented the relationship between maximum cementite size and cleavage fracture stress with an assumption that cleavage fracture initiates from cementite even in tempered martensite microstructure as well as in ferrite and cementite microstructure. Bowen's work showed that the cleavage fracture stress of pressure vessel steel was proportional to the reciprocal square root of carbide size.

Pearlite has a finer structure consisting of two phases: ferrite and cementite. It also has substructures, with the ferrite matrix being classified into blocks of the same crystallographic orientation, and within such a block, also categorised into by the same orientation of cementite lamellae, which are called colonies [102]. A schematic illustration of metallographic structures of pearlite is shown in Figure 2.15.

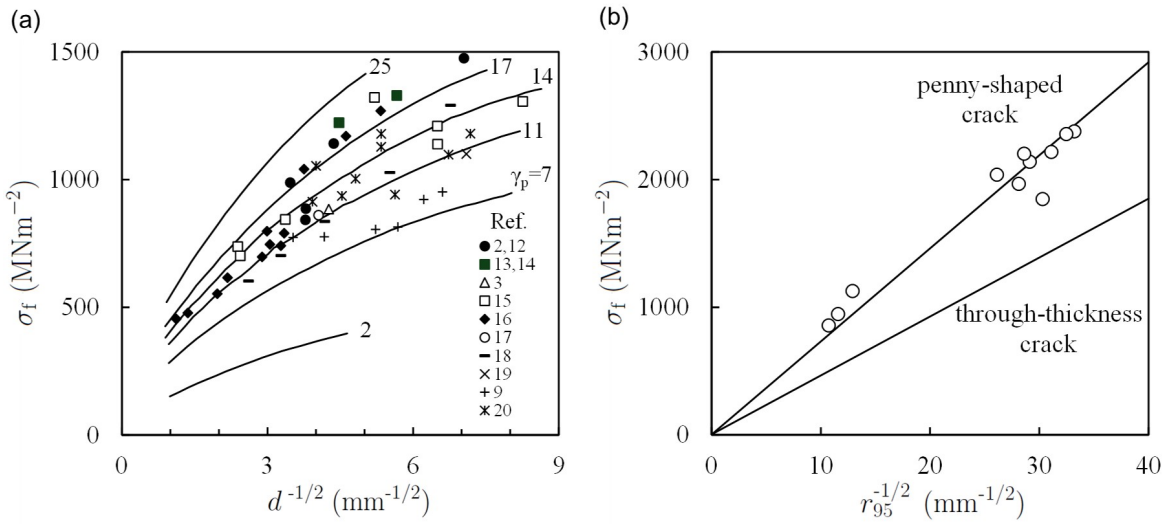


Fig. 2.14 The relationship between (a) ferrite grain size d and cleavage fracture stress σ_f, (b) cementite size as 95th percentile carbide radius r_{95} and cleavage fracture stress, in a spheroidised high carbon steel [25].

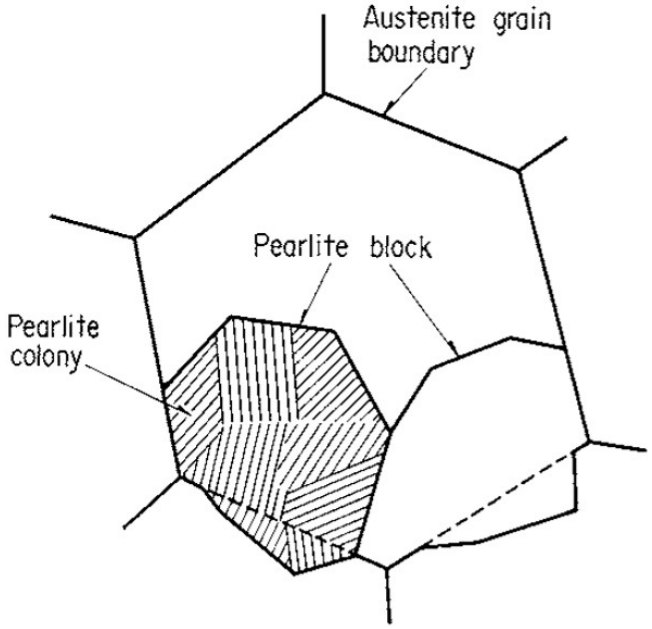


Fig. 2.15 Schematic illustration of metallographic structures of pearlite; pearlite is composed of blocks, where ferrite matrix has almost the same crystallographic orientation. In addition, a block is also categorised by the same orientation of cementite lamellae direction, which is called colony [102].

It has been reported that yield stress σ_y of pearlite and lamellar spacing satisfy the following relationship [103–105]:

$$\sigma_y = \sigma_0 + kS_p^{\alpha} \tag{2.5}$$

where σ_0 and k are constants, and S_p is the lamellar spacing of pearlite. α is a coefficient indicating the power, but both -1 and -1/2 have been reported, and the debate has still been open. The controlling factor of the toughness of pearlite was a topic to discuss for a long time, with some claiming that colony size is the dominant factor [19] and others reporting that they are not [106–108]. Over the decades, many studies have demonstrated the advantage of blocks over colonies in deflecting brittle cracks [108–113].

2.3 Cementite

2.3.1 Crystal structure and anisotropy of cementite

Although cementite is one of the most fundamental and prominent phases in practical steels, there are still many unknowns about its fundamental properties. The reason for this is that it is difficult to prepare single-phase bulk samples because the cementite is a metastable phase [114]. The stable phase is graphite, but graphitisation is very rare in steel, so carbon exists as cementite during normal and practical heat treatment. Intrinsically, the properties of cementite are subject to variation due to its anisotropy or the influence of alloying elements. In addition to this, such size and shape restrictions for samples have limited experimental methods and cause extrinsic variations in the properties of cementite obtained in experiments.

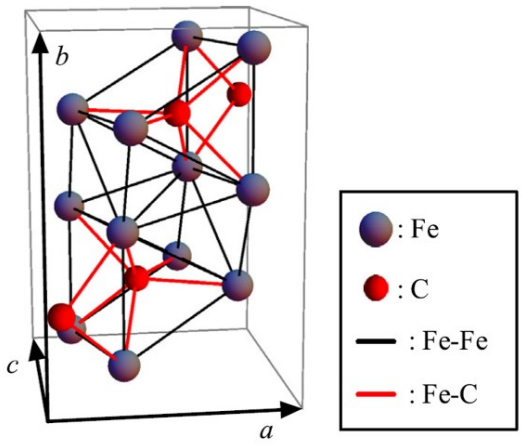


Fig. 2.16 Schematic illustration of cementite unit cell [22].

The crystal structure of cementite was studied by Fasiska et al. [115]. It is an orthorhombic unit cell containing twelve iron atoms and four carbon atoms, and its space group is *Pnma*. There are several works on the lattice parameters [116, 117]. Although there are some differences in the values, they are almost the same, for example, a=5.084 Å, b=6.747 Å, c=4.525 Å [117]. It is noted that the definition of unit cell parameters varies depending on literature. All crystallographic planes and directions in cementite in this research are described with *Pnma* space group. When referring to literature adopting a different space group, the indices have been permuted. Figure 2.16 demonstrates the unit cell of cementite [22].

Many empirical studies have been conducted on the elastic constants of cementite. Since the 1950s, Young's modulus of polycrystalline cementite at room temperature has been reported in a wide range of 140 to 300 GPa using various methods [114, 118–120]. The average and deviation of the reported experimental values 186 ± 20 GPa, which is about 10 % smaller than that of BCC iron at room temperature, which is 211 GPa [121]. Although it is more recent, a theoretical approach has also tackled this problem using first-principles calculations. In 2008, Jiang et al. [122] first used this method to

calculate the elastic constants C_{ij} of single crystal cementite, and many other reports have been published since then [123–127]. Hooke's law for an orthorhombic crystal of cementite can be written as

$$\begin{pmatrix} \sigma_1 \\ \sigma_2 \\ \sigma_3 \\ \tau_4 \\ \tau_5 \\ \tau_6 \end{pmatrix} = \begin{pmatrix} C_{11} & C_{12} & C_{13} & 0 & 0 & 0 \\ C_{21} & C_{22} & C_{23} & 0 & 0 & 0 \\ C_{31} & C_{32} & C_{33} & 0 & 0 & 0 \\ 0 & 0 & 0 & C_{44} & 0 & 0 \\ 0 & 0 & 0 & 0 & C_{55} & 0 \\ 0 & 0 & 0 & 0 & 0 & C_{66} \end{pmatrix} \begin{pmatrix} \varepsilon_1 \\ \varepsilon_2 \\ \varepsilon_3 \\ \gamma_4 \\ \gamma_5 \\ \gamma_6 \end{pmatrix} \tag{2.6}$$

where σ_i and τ_i are the normal stress and shear stress. ε_i and γ_i are the normal and shear strains, respectively. Table 2.2 summarises the elastic moduli in GPa at zero pressure and at 0 K obtained from first-principles calculations by previous papers. The value of C_{44} is extremely low compared to the other constants, and the rest are within the range of about ±20 %. Some studies indicated C_{44}'s of negative value, but in that case the elastic stability criteria for orthorhombic crystal is not satisfied [128]. With respect to the anisotropy of shear modulus, several works reported that C_{44} showed a smaller value than C_{55} and C_{66}, and some have reported that it is on the order of one-tenth of those values [123]. Pure iron also has anisotropy, but at room temperature, $C_{11} = 230, C_{12} = 134, C_{44} = 116$ GPa [129]. The difference between the maximum and minimum Young's modulus for each crystal orientation obtained from this is about a factor of two. In contrast, cementite is thought to have a greater anisotropy of more than five judged from Table 2.2 [114, 120].

Table 2.2 Elastic moduli of single crystal cementite in GPa under zero pressure and at 0 K obtained from first-principles calculations by some previous papers.

Author	Ref.	C_{11}	C_{22}	C_{33}	C_{12}	C_{23}	C_{13}	C_{44}	C_{55}	C_{66}	Conditions
Jiang	[122]	388	345	322	156	162	164	15	134	134	E-S, relaxed
		395	347	325	158	163	169	18	134	135	S-S, relaxed
		413	412	378	154	170	167	82	136	140	E-S, unrelaxed
		417	415	381	157	174	171	82	136	140	S-S, unrelaxed
Nikoussi	[123]	385	341	316	157	167	162	13	131	131	S-S, relaxed
Henriksson	[125]	394	412	360	157	166	146	83	133	136	E-S, unrelaxed
Mauger	[127]	383	344	300	162	162	156	28	134	135	S-S

E-S: calculation from energy-strain relationship, S-S: calculation from stress-strain relationship, relaxed: unit cell and internal atomic positions are allowed to vary to the favourable states, unrelaxed: internal atomic positions are fixed even after the unit cell is deformed.

2.3.2 Slip system and fracture plane of cementite

Lattice defects of cementite in steel have been observed [130–132], and slip deformation of cementite has been reported [130, 132–135]. Ker [130] reported that the slip plane is $(001)_\theta$ based on trace analysis of accumulated dislocations. Inoue et al. [133–135] indicated that the slip plane is $(001)_\theta$, $(100)_\theta$, $(010)_\theta$, and $\{110\}_\theta$. The magnitude of the Burgers vector of the system corresponds to the length of one edge of the unit cell. This is thought to be the reason for the high strength and low ductility of cementite. Regarding temperature dependence of ductility, no dislocations were found in the lamellar cementite in pearlite when deformed hypereutectoid steel at low temperatures, but dislocations appeared above room temperature. They were low at room temperature and dramatically increased above room temperature [134]. The effects of alloying elements on the ductility have also been reported. In cementite containing Cr, there are almost no dislocations in the cementite when deformed at room temperature. Still, stacking faults increased with the addition of Mn, and $(100)_\theta$ and $\{101\}_\theta$ slip was observed even at room temperature with Ni addition [133, 135].

As to the anisotropy of C_{44} mentioned in the previous section, if C_{44} is actually lower than C_{55} and C_{66}, the slip system of $(010)_\theta[001]_\theta$ should be dominant in theory. However, this was not the observed case [135]. Therefore, it was pointed out that the possibility that C_{44} is not that low at room temperature in practice [120]. This was because C_{44} is sensitive to temperature, and the first-principles calculations run at 0 K.

Table 2.3 summarises the previous research findings of the slip system and fracture plane of cementite [22, 130, 134–141]. It is recognised that various reports have been made on the slip system of cementite, and it cannot be said that the results obtained are unambiguous. This suggests that the shape of cementite, deformation process, and temperature may have an impact on the deformation process. With respect to the fracture plane of cementite, there is still little empirical work.

Finally, previous work on strength and toughness is described. Testing methods for the strength of cementite have been limited due to the restrictions on the shape of the sample. Umemoto et al. [142] conducted compression tests on bulk sintered cementite. At room temperature, it showed no ductility and broke in the elastic region, and the compressive fracture strength of pure cementite was about 2.8 GPa. This value varied between 1.8 and 3.2 GPa depending on alloying elements. At elevated temperatures, dislocation glide became active, and ductility was observed. The Vickers hardness of pure cementite has been reported to be 1130 to 1140 HV, depending on the testing load and sample preparation method [143–147]. Inoue et al. [137] measured the hardness anisotropy, showing that when the sample surface was $(010)_\theta$, the hardness increased by 10 % compared to other surfaces. In terms of the temperature variation of hardness, it decreased with increasing temperature from room temperature, and this was particularly significant above 300 °C [137, 147]. It has been reported that this

decrease is affected by alloying elements, but there are no data on its change below ambient temperature. There are a limited number of studies on the fracture toughness of cementite determined by indentation [148, 149]. The fracture toughness of sintered cementite in cast iron with 5 wt%C, 9.2 wt%Cr, 5.1 wt%Cr, and 4.5 wt%V was shown to be 2.24 to 2.74 $MPam^{1/2}$, which is in the same range as other alloy carbides [149].

Table 2.3 Compilation of previous research findings on the slip system and fracture plane of cementite.

Author	Year	Ref.	Material	Conditions	Slip system	Fracture plane
Keh	1963	[130]	0.95%C-Fe (1095 steel), spheroidised	TEM / cold-rolled, RT	(010)[001]	Not mentioned
Sevillano	1975	[136]	Eutectoid steel, lamellar	TEM / drawing, RT	(010), (100), and potentially (001), (110), (101), and (011)	Not mentioned
Inoue	1976	[134]	(0.86, 1.25)%C-Fe, lamellar	TEM / cold-rolled, RT	(001), (100), (010), possible slip direction [100] on (001), and [010] on (100), and [100] on (010)	Not mentioned
Inoue	1976	[137]	4.8%C-5.8%Cr-Fe, spheroidised	X-ray, OM / vickers, RT	(001), (100), (010), (101) at RT	occur mostly {101}, a few with {110}, {102}
Inoue	1977	[135]	1.25%C-Fe, lamellar	TEM / cold-rolled, RT	(001)[100], (010) × [100], [001], [101], (100) × [010], [001], {110} × [001], [100], [010]	Not mentioned
Inoue	1977	[138]	1.23%C-Fe, lamellar	TEM / tensile test, -196°C, -78°C, RT to 700°C	(001), (010) at RT and 300 °C, (001), (010), (100), {101} (sometime) above 400 °C	Probably (101) (001) (102) at -196°C, -78°C, RT
Tagashira	2000	[139]	0.76%C-Fe, lamellar	TEM	Slip off surface of cementite lamella is $(2\bar{1}1)$	Not mentioned
Karkina	2013	[140]	0.8%C-Fe (U8 steel), lamellar	TEM / cold-rolled, RT	(010)[100] at RT	Not mentioned
Shibanuma	2014	[22]	0.1%C-Fe, shperoidised	EBSD / tensile test, -140 to -40°C	Not mentioned	(010)
Mussi	2016	[141]	synthesised Fe_3C	TEM/ 1250°C, 10bar	(010)[100] most frequent, then (010)[001] and (100)[001]	Not mentioned

2.4 Empirical findings

2.4.1 Failure with spheroidised cementite microstructure

Interaction with ferrite matrix and cementite to crack

It is revealed that plastic deformation and yield strength play important roles in the factors that cause cementite cracks [150–152]. Grain boundary cementite is a typical embrittlement phase, but intragranular spheroidised cementite can also affect crack nucleation. Gurland [152] observed cracks in cementite particles in a 1.05 wt%C hypereutectoid steel. The number of cementite cracks increased as macroscopic plastic deformation progressed as shown in Figure 2.17 (b). The cracking occurred preferentially in particular cementite particles, which were relatively coarse and the longest axes close to parallel to the tensile direction as shown in Figure 2.17 (c).

The work of Argon et al. [153] revealed that the local tensile stress acting at the interface between a rigid particle and deformable matrix phase is amplified by the onset of local yielding of the matrix, especially in the presence of hydrostatic pressure. In their related study [154], an analytical work demonstrated that the local tensile stress required to fracture a cementite particle in a ferrite matrix is about 1500 MPa, which was significantly smaller than the theoretical value. This suggests that some factors, such as intrinsic defects in cementite or stress concentration due to the dislocation pile-up to the cementite particle, which may be at work to increase the local stress.

Shibanuma et al. [22] investigated quantitatively crack formation in spheroidised cementite. They observed cracks in various deformed microstructures with different cementite sizes and ferrite grain sizes. Although the effect of cementite distribution on cracking was not taken into account, they quantified crack nucleation in ferrite

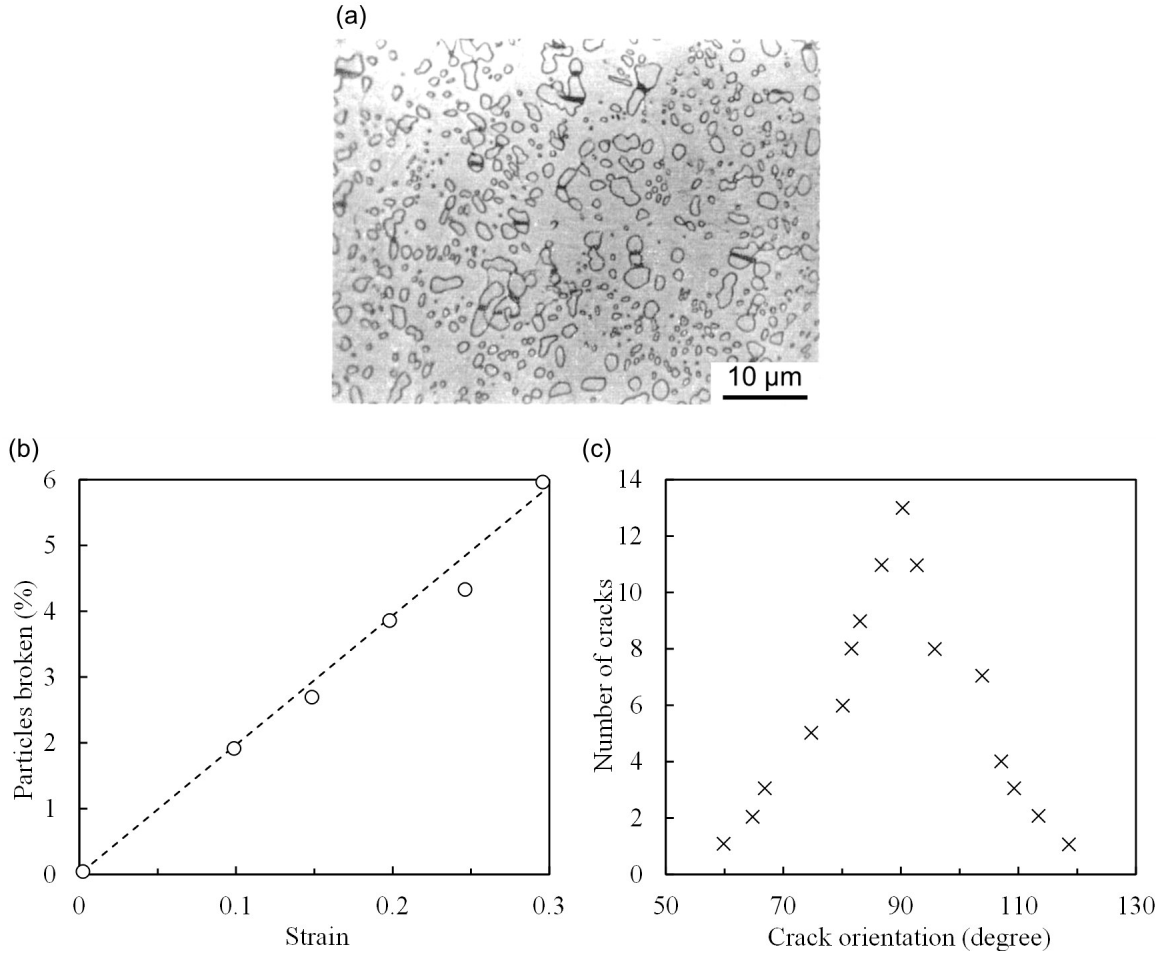


Fig. 2.17 (a) An optical microscope image showing some cementite particles are cracked. The tensile direction is up and down to the image. (b) The ratio of cracking cementite as a function of strain in tension. (c) Frequency of crack with the angle to the tensile axis.

and cementite microstructure of low carbon steels. They proposed the probability of cementite cracking r_c to the following empirical equation:

$$r_c = 6.06 \times 10^{-5} \left\{ r_{\mathrm{E}} \sigma_{max} + 0.179 \sigma_y \left(\frac{\varepsilon_p}{\varepsilon_y} \right)^{0.627} - 402 \right\} t^{2.47} \tag{2.7}$$

where r_{E} is Young's modulus of cementite, σ_{max} is maximum principal stress, σ_y is yield stress, ε_p is equivalent plastic strain, ε_y is yield strain, and t is thickness of cementite. The number of cracked cementite increased with increasing equivalent strain and principal stress.

As described in the previous section, the crystal structure of cementite is orthorhombic, with 12 iron atoms and four carbon atoms in the unit cell. Although the cleavage plane of cementite remains open to debate, it is believed that slip in cementite likely occurs on the $(010)_\theta$ plane because this is the only plane in which all the bonds within the plane are composed of Fe-Fe bonds. The Fe-Fe bond is much weaker than that of Fe-C [155]. Shibanuma et al. [22] investigated cracks in cementite using EBSD and reported that many cracks were fitted to the $(010)_\theta$ plane trace.

Lee et al. [156] investigated the effect of carbide distribution in the DBT region of SA 508 steel for nuclear reactor pressure vessel (0.18C-1.46Mn-0.10Si-0.006P-0.003S-0.86Ni-0.15Cr-0.51Mo-0.004V-0.03Cu-0.008Al in wt%) on the Charpy impact property. The critical carbide size calculated by the Griffith equation and the distance between carbides of a size larger than the critical size both increased with increasing test temperature. This can be interpreted as an improvement in toughness due to a decrease in the probability that carbides of a size larger than the critical size exist in the process zone where stress concentration occurs at the notch root.

Critical steps for macroscopic failure

Lin et al. [21] tackled the effects of ferrite grain size and cementite particle size on the toughness of sharp cracks and rounded bottom notches. Around the lower region of the DBT curve, grain-sized microcracks were observed as shown in Figure 2.18 (e). On the other hand, under fully brittle conditions, cementite cracks were dominant (Figure 2.18 (d)). As the grain-sized microcracks were thought to be formed by arresting the propagation of cementite cracks, they showed that the rate-controlling step of macroscopic cleavage fracture may change from the propagation of cementite cracks to the propagation of the microcracks of a ferrite-grain size, depending on temperature.

2.4.2 Failure with pearlitic lamellar cementite microstrucuture

Shear cracking in pearlite

Bruckner [157] was the first to report that when pearlitic steel was tensile tested, cracks inclined at 45° to the tensile direction appeared in colonies where the pearlite lamellae were parallel to the tensile direction. Followers subsequently reported similar observations [158, 159]. Miller and Smith studied the fracture mechanism of pearlite microstructure of 0.1 to 1.0 wt% carbon steel in detail using optical microscope [159], indicating the tendency of what Bruckner discovered in Figure 2.19. The fracture process is initiated by stress concentration at the plane of maximum shear stress, which in turn promotes the cracking of cementite at the plane of maximum tensile stress. As the shear stress increases, adjacent small cracks or holes grow and join together to

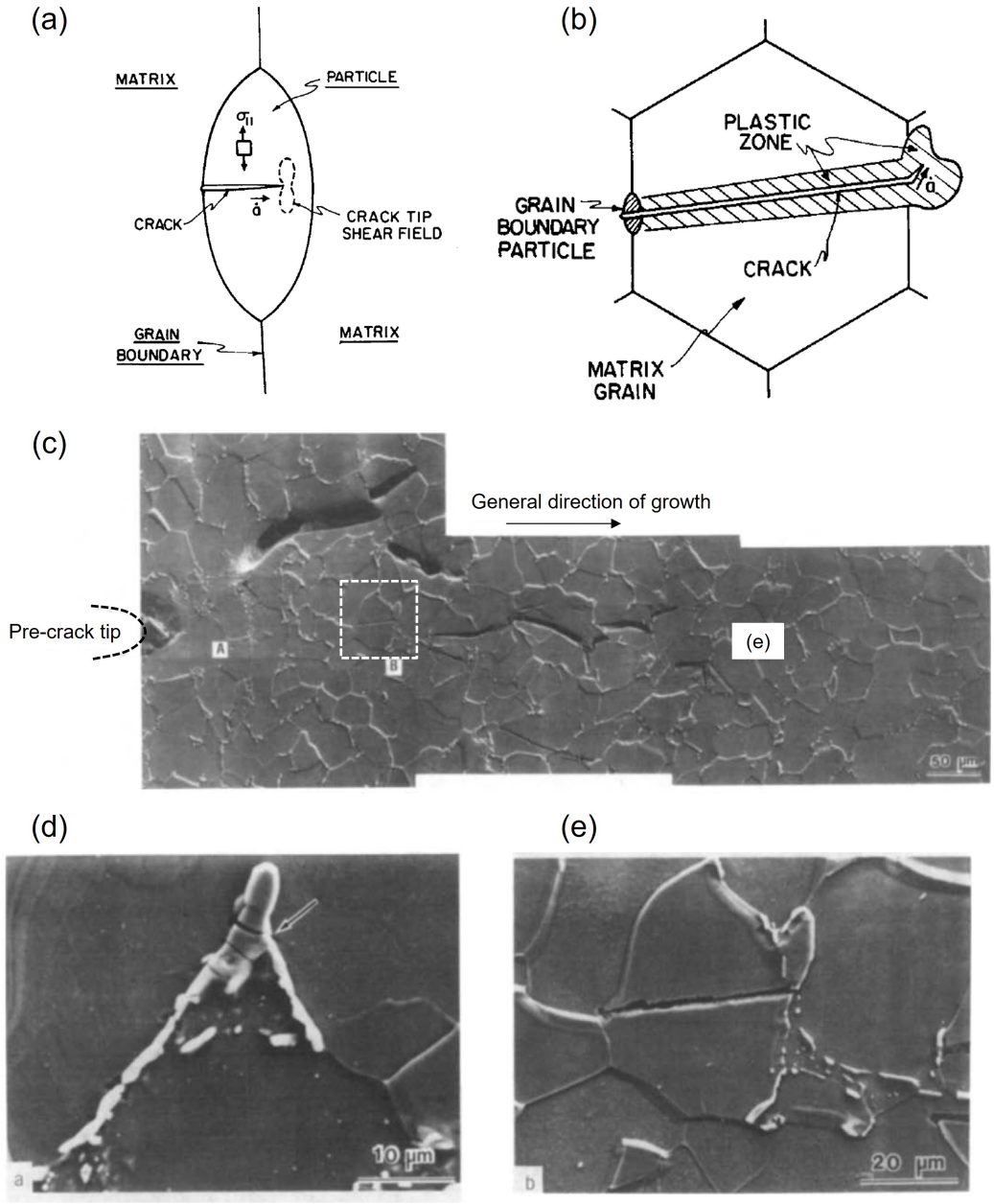


Fig. 2.18 Illustrations of possible critical steps (a) under fully brittle conditions, including cementite crack formation and its propagation into the surrounding ferrite matrix, (b) under the lower region of the DBT involving the propagation of a grain-sized microcrack through the adjacent ferrite grain. (c) is the area in the vicinity of pre-crack tip. (d) and (e) are SEM images for cementite crack and grain-sized microcrack, respectively. (e) is a magnified image of the area with dotted rectangle in (c) [21].

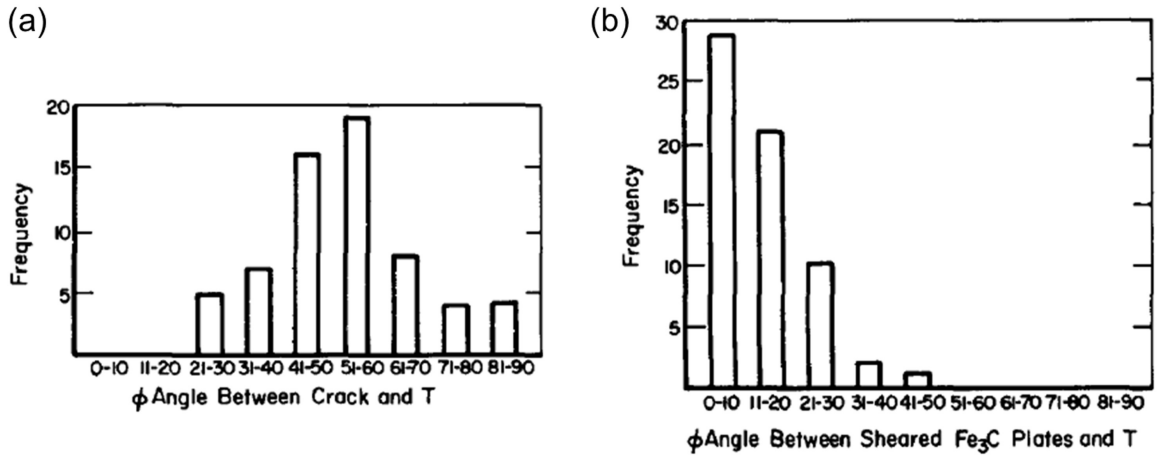


Fig. 2.19 Geometrical information of pearlitic cracks; (a) histogram showing the frequency of cracked pearlite colonies as a function of the angle between the cracks and the tensile axis, (b) histogram showing the frequency of cracked pearlite colonies as a function of the angle between the cementite lamellae and the tensile axis [159].

form larger cracks. These are the mechanisms first proposed by Miller and Smith [159] as the shear cracking process (Figure 2.20).

The mechanism of shear cracking formation in pearlite is still controversial. Some reports suggested that shear cracking could occur in a brittle manner [158, 160], while others pointed out that the shear cracking process is ductile [108, 159].

Recently, Shibanuma et al. [161] performed low-temperature quasi-static tension tests for steels with ferrite and banded pearlite microstructures at various temperatures and observed microcracks. Their microcrack trace analysis with EBSD showed that none of the cracks matched the $\{100\}_\alpha$ plane, while the $\{110\}_\alpha$ plane corresponded well with all of the microcracks observed. They concluded that this came from crack formation by the stable shear fracture on a slip plane in ferrite. The probability of microcrack occurrence could be well described as a function only of equivalent plastic strain as shown in Figure 2.21, and was independent of temperature, pearlite fraction, and loading conditions. In the process of their studies, Nemoto et al. [162]

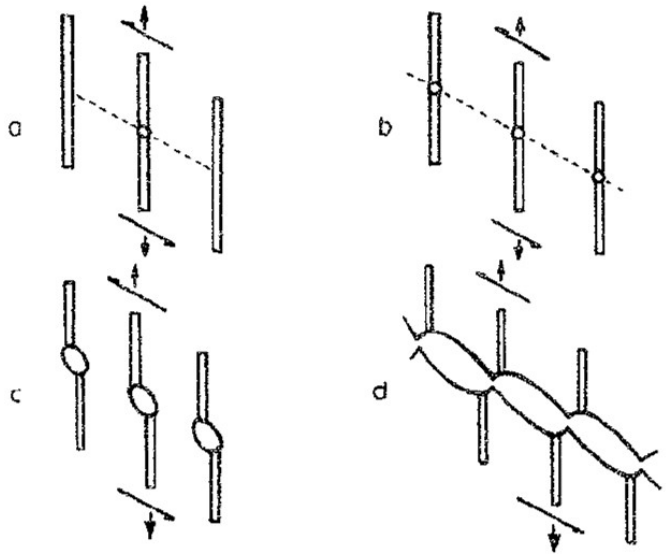
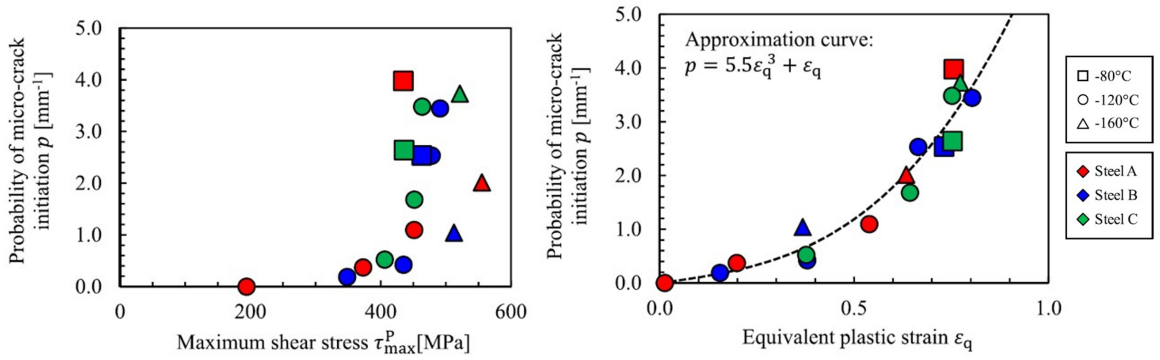


Fig. 2.20 Suggested mechanism for shear cracking in pearlite; (a) cracking of a cementite plate, (b) shear zone developing in the ferrite causing cracking of adjacent plates, (c) and (d) void formation and coalescence [159].

demonstrated serial sectioning of the microcracks and three-dimensional observations. All detected microcracks were initiated at the ferrite/pearlite interface and were observed to propagate stably into pearlite. The three-dimensional shape could be described well by an elliptical approximation, with the long axis being up to the ferrite grain size as maximum, and the short axis ranging between the pearlite band thickness and the ferrite grain size.

Fractographical fracture unit

Many studies have reported that the cleavage fracture plane of pearlite is the $\{100\}_\alpha$ plane [108–111, 113, 163]. However, Zhou et al. [113] observed that in some pearlite blocks, although the misorientation of the $\{100\}_\alpha$ planes between adjacent blocks was more than 15 degrees, which was considered to be sufficient for a crystallographic resistance for crack propagation, such the block boundaries were ineffective in changing crack propagating plane. The surface energy required for fracture of the $\{110\}_\alpha$ plane



(a) Maximum shear stress (b) Equivalent plastic strain

Fig. 2.21 The probability of cracking in pearlite microstructure against maximum shear stress and equivalent plastic strain [161].

is not significantly different from that of the $\{100\}_\alpha$ plane [164, 165]. Still, dislocation emission from the crack tip was thought to inhibit the crack propagation in the $\{110\}_\alpha$ direction [165–169]. Although $\{110\}_\alpha$ cleavage fracture planes have been reported in atomic simulations, no such simulations were performed on dislocation emission at the crack tip and the $\{110\}_\alpha$ cleavage plane in pearlite microstructure. Barik et al. [170] recently analysed thoroughly the Charpy impact fractured surfaces of eutectoid steels using EBSD and showed that the cleavage fracture surfaces are dominated, as previously reported, by $\{100\}_\alpha$, but crack propagation along the $\{110\}_\alpha$ plane was also commonly observed in some pearlite colonies or blocks (Figure 2.22). From their discussions, this is because the dislocation emission from the crack tip is suppressed due to the necessity to cross the cementite lamella and ferrite interface and its restriction of the dislocation slip activity.

Critical steps

Kavishe et al. [171] showed that the cleavage fracture behaviour of pearlite changed depending on the cleavage fracture stress. When the lamellar spacing is small - and

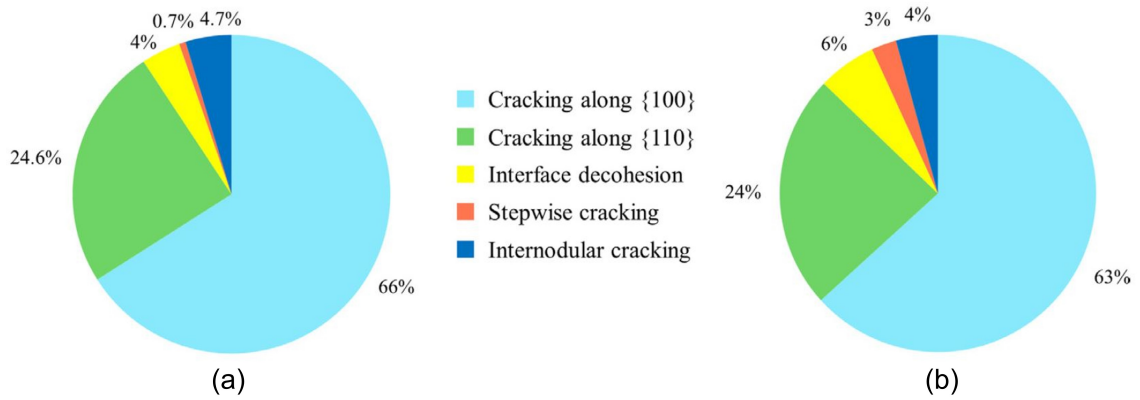


Fig. 2.22 Pie charts showing the percentage contribution of different cracking mechanisms in fully pearlitic eutectoid steels austenitised at (a) 1150 °C and (b) at 850 °C, succeeded by isothermal transformation at 550 °C, respectively [170].

then the fracture stress is high - the cracking of lamellar cementite becomes the rate-controlling step that directly leads to macroscopic brittle failure. When the lamellar spacing is large and the fracture stress is relatively low, the cracking of lamellar cementite in pearlite becomes a shear-like chain before the unstable brittle crack propagation, which becomes the dominant step for macroscopic brittle fracture. In the temperature range where the former process is rate-controlling, macroscopic fracture stress was independent of temperature, while in the latter process the fracture stress decreased with decreasing temperature. Lewandowski et al. [172] also pointed out that the lamellar spacing in pearlite affects the cleavage fracture stress and fracture process.

Park et al. [108] investigated brittle fracture surface of tensile tests conducted at room temperature and showed that river patterns of cleavage fracture surfaces were generated starting from ductile fractured features. In contrast, they reported that such ductile fracture surfaces were not observed in notched impact test specimens. Their analysis based on fracture mechanics showed that the fracture of just a few cementite lamellae can cause macroscopic brittle failure in the notched impact test. They point

out that the difference between the two types of the test came from the difference in stress concentration caused by the presence or absence of a mechanical notch and the difference in strain rate. In other words, this corresponded to a case where the fracture stress becomes relatively small compared to the yield stress due to the increase in yield stress caused by the notch and the high strain rate.

More recently, Khiratkar et al. [110] have reported through detailed analysis using EBSD that the block diameter has an effect on toughness in completely brittle conditions, and the lamellar spacing has an effect when a certain degree of deformation is allowed.

As reviewed so far, the majority of pearlite toughness studies have focused on fully pearlitic eutectoid steels. In practice, low carbon to hypoeutectoid compositions are common in structural steels, where the complicated dual-phase structure is made up of ferrite and pearlite. The cleavage fracture and the DBT behaviour of such microstructure requires enough investigation.

2.5 Micromechanism and modelling

Proposed micromechanisms based on the experimental findings over many years, as well as modelling works, are briefly reviewed.

2.5.1 Micromechanism and modelling on cleavage fracture

The early works

Stroh model The early work on the mechanism of stress intensity leading to macroscopic brittle fracture was proposed by Zener [13] and Stroh [14]. They proposed

a mechanism for the formation of cleavage crack nucleation by coalescence of edge dislocations. Their models assumed that cleavage crack was initiated when the local normal stress reached a critical value over a critical distance due to dislocation pile-up (Figure 2.23). Stroh's model is based on a criterion of cleavage nucleation. It described the cleavage fracture stress as with a temperature dependency, which does not fully agree with what was experimentally observed.

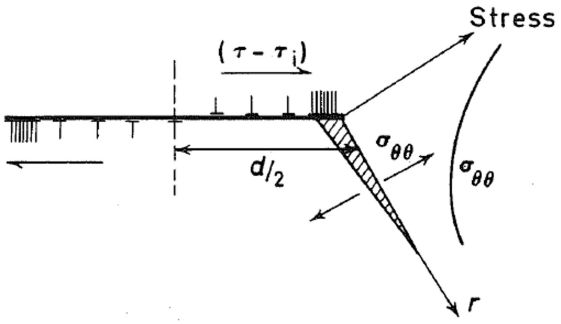


Fig. 2.23 Stroh's model for cleavage fracture [37].

Cottrell model Cottrell [15] investigated cleavage fracture of mild steel in terms of a dislocation mechanism and proposed a model allowing crack growth to be the controlling factor. The condition of propagation of the crack initiated at the intersection of two slip planes was calculated. According to this model, cleavage fracture stress σ_f can be described as

$$\sigma_f = \frac{2\mu\gamma_{\mathrm{s}}}{k_{\mathrm{Y}}^{\mathrm{S}}} d^{-1/2} \tag{2.8}$$

where μ is shear modulus, γ_s is free surface energy, $k_{\mathrm{Y}}^{\mathrm{S}}$ is a constant related to shear stress state, d is grain size of ferrite matrix.

Smith model Smith [16] modified Cottrell's model to account for the fact that in mild steel cleavage fracture initiated from carbide particles located at grain boundaries and coarse carbide promoted cleavage fracture (Figure 2.24). Grain boundary carbide

is cracked by dislocation pile-up if local shear stress τ_{eff} is satisfied with the following condition:

$$\tau_{eff} \geqq \left(\frac{4E\gamma_{\mathrm{c}}}{\pi(1-\nu^2)d} \right)^{1/2} \tag{2.9}$$

where γ_{c} is the surface energy of the carbide, E is Young's modulus, ν is Poisson's ratio, and d is ferrite grain size. Additionally, if it is assumed that the work for propagating crack from carbide into the ferrite matrix of the unyielding grain (γ_{p} as an effective surface energy) is greater than γ_{c}, fracture at yield point is a crack nucleation-controlled process if

$$\tau_{eff} \geqq \left(\frac{4E\gamma_{\mathrm{p}}}{\pi(1-\nu^2)d} \right)^{1/2} \tag{2.10}$$

By contrast, if τ_{eff} lies between the two criteria above, then the fracture becomes a crack growth-controlled process. No further crack growth happens unless the additional stress increase is produced by dislocation pile-up [51].

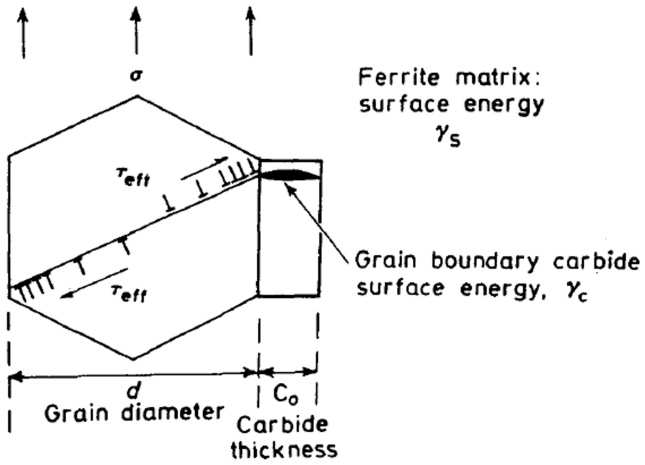


Fig. 2.24 Smith's model for cleavage fracture in mild steel. A crack nucleates at a grain boundary carbide [173].

Multi-barrier model

Following early models, cleavage fracture processes of ferrite and spheroidised cementite microstructure came to be considered a process of three elementary stages consistent with the following [21, 174–176];

1. pile-up dislocations induce stress concentration and cementite cracking in ferrite matrix,

2. crack propagation into the adjacent ferrite matrix and along a cleavage plane $(100)_\alpha$ of the ferrite matrix, and becoming a grain-sized crack,

3. crack propagation of the grain-sized crack into neighbouring grains across the grain boundary.

A schematic diagram of this process is shown in Figure 2.25. Critical carbide size and ferrite grain size for cleavage fracture can be described in terms of local fracture toughness. Therefore, in this model, the critical step can be varied case-by-case. The critical carbide particle size and ferrite grain size are derived from the local maximum principal stress by a Griffith-like expression. In addition, since carbide and ferrite grain have their distribution in size, distribution functions need to be considered from a statistical point of view.

With respect to crossing the second stage barrier, that is, the cementite/ferrite boundary, cementite is thought to be cracked because of the plastic strain in the surrounding matrix. At this point, the microcrack can be treated as a Griffith crack [40]. If a given macroscopic stress is sufficiently high, the microcrack propagates into the ferrite matrix. Moreover, if the cementite is spherical and it produces a penny-shaped

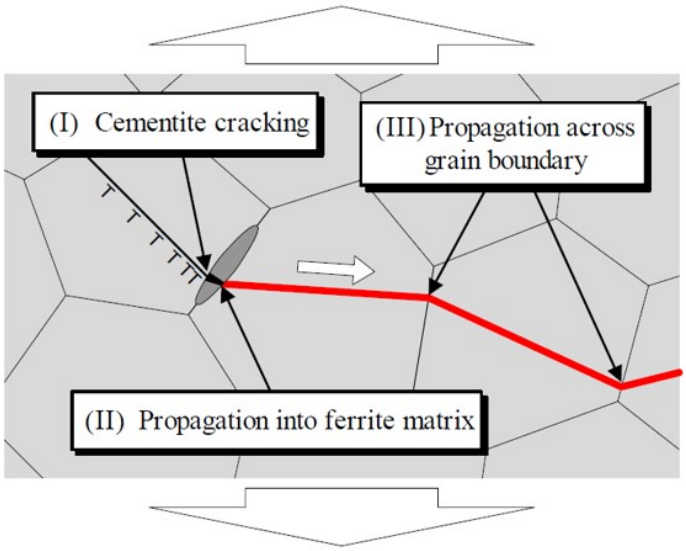


Fig. 2.25 Multi-barrier model for cleavage fracture [176].

crack, the critical fracture stress for the second stage σ_f is given by

$$\sigma_f = \left(\frac{\pi E \gamma_{\mathrm{p}}}{(1-\nu^2) C_0} \right)^{1/2} \tag{2.11}$$

where γ_{p} is the plastic work required to create a unit area of fracture surface in the ferrite matix, namely an effective surface energy, and C_0 is cementite size (crack length) [21]. For a given stress state, the strain necessary to initiate a crack in a particle increases with temperature.

About crossing the second barrier, the ferrite/ferrite grain boundary, a number of previous studies [177–184] have shown that crack is arrested at boundaries which are largely misoriented, especially with large twisted angle. Gell et al. [180] revealed that twisting rather than tilting misorientation highly contributed to the resistance of grain boundaries for cleavage crack. The study of Lambert et al. [179] in bainitic steel with acoustic emission suggested that the process-controlling step was not necessarily the same with variation of temperature and that cleavage fracture could be controlled

by the crack nucleation in carbide at very low temperature, while it was controlled by propagation of crack arrested at grain boundaries in higher temperature. This implies the cleavage fracture stress is not necessarily constant with temperature. In fact, previous studies reported that the surface energy of cementite and ferrite interface $\gamma_{c/f}$ was independent of temperature and is of the order of 7 J/m^2 [175, 185], while the surface energy of ferrite grain boundaries $\gamma_{f/f}$ is much larger and has strong temperature dependency [174–176, 185, 186]. So, grain boundaries play an important role in cleavage fracture in ferritic steels, and especially in the DBT region where the critical step for triggering overall cleavage fracture could be the propagation of grain-sized microcracks. This is consistent with the experimental work of Lin et al. [21] (Figure 2.18).

Shibanuma et al. [161] performed low-temperature quasi-static tension tests for steels with ferrite and banded pearlite microstructures at various temperatures and observed microcracks. They predicted that the effective surface energy for a microcrack in pearlite to propagate into ferrite (i.e. at the ferrite/pearlite interface) was greater than that for a cleavage crack to penetrate the ferrite/ferrite grain boundaries estimated by San Martin et al. [175].

RKR (Ritchie–Knott–Rice) model

Characteristic distance In order to explain why steel does not fracture on the application of a minimal load, Ritchie, Knott, and Rice [26] postulated an additional condition for cleavage crack propagation in addition to the HRR (Hutchinson-Rice-Rosengren) field, which describes elastic-plastic deformation ahead of the crack tip [187, 188]. The additional condition is that applied stress needs to exceed critical cleavage fracture stress over “a characteristic distance” ahead of the crack tip (Figure 2.26).

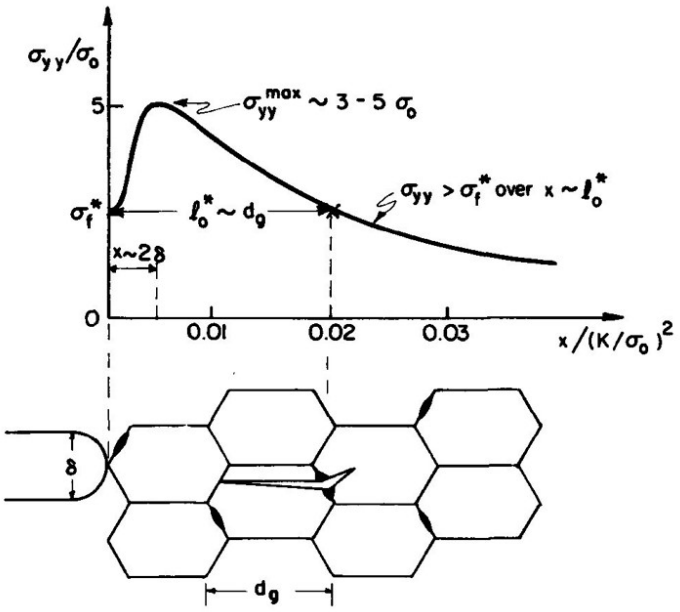


Fig. 2.26 The "characteristic distance" $l_0{}^*$ idea, as originally formulated by Ritchie et al. [26], is expected to be of the order of the grain diameter d_g for the microstructure shown, with the normalised local tensile stress σ_{yy} by the flow stress σ_0 [190].

From the bending test they conducted, it was found that the characteristic distance was equivalent to about two-grain diameters. It was further shown that the onset of fibrous fracture (void nucleation) ahead of the crack tip can be deduced from the position of the maximum achievable stress intensification. They argued that if cleavage fracture started from grain boundary carbide and propagated into ferrite matrix, the local stress applied must be sufficient to propagate cleavage cracks over the opposite grain boundary and the adjacent one; the fracture stress must be exceeded over one or two grains. However, the following works [25, 189] revealed no clear relationship, at least, between such critical distance and grain size.

Open to statistical analysis Curry and Knott [25, 90] provided a statistical view of the RKR model with characteristic distance, which should be associated to the volume of material required to obtain carbides so that a fracture condition is satisfied. A

"critical volume", which should be related to a characteristic distance, depends on the average spacing of cleavage nucleation sites. They applied this concept to evaluate the statistical fracture toughness of quenched and tempered martensite with spheroidised carbides. From their evaluation, it is important to note that the probability of "eligible" particles within the activated volume zone depends on its nucleation process and, hence, fracture toughness. Their suggestion opened the door to statistical fracture conditions. The statistical argument can also explain why cleavage fracture toughness tends to be widely scattered [99, 191].

Beremin model

It was only in the 1980s that models were proposed to account for cleavage fracture in terms of statistical effects. The approach used by Curry and Knott [25] opened the door for more formal statistical models describing cleavage fracture [21, 27, 95, 96, 99, 192]. These models all treated cleavage fracture as a weakest link phenomenon, where the probability of fracture is equal to the probability of sampling at least one critical particle triggering fracture. Therefore, the fracture toughness has intrinsic scatter. The work of Beremin [27] proposed a model to evaluate a scatter of cleavage fracture toughness by using Weibull distributions [193]. This model can evaluate fracture toughness quantitatively by determining the adjustable parameters that fit the experimental results. Based on this model, the probability of failure P_R is

$$P_R = 1 - \exp\left[- \left(\frac{\sigma_{\mathrm{W}}}{\sigma_u} \right)^m \right] \tag{2.12}$$

where σ_{W} is Weibull stress, σ_u is measured fracture stress, m is Weibull shape factor [194]. For more details of the model based on Weibull weakest link theory, Pineau's

paper [195] should be referred to. Although this model is widely accepted currently, it needs to be considered an empirical treatment. Some standards have been published to evaluate the fracture toughness with this model [196, 197]. When small-scale yielding condition applies, meaning that HRR field can be applied at the crack tip, the probability of failure P_R can be described as [27]

$$P_R = 1 - \exp\left[\frac{{K_{\mathrm{I}c}}^4 B {\sigma_y}^{m-4} C_{mn}}{V_u {\sigma_u}^m}\right] \tag{2.13}$$

where $K_{\mathrm{I}c}$ is critical stress intensity factor, B is the specimen thickness, σ_y is yield stress, and C_{mn} is a numerical factor dependent both on the work-hardening exponent and the Weibull shape factor m, V_{u} is a volume element unit, and σ_u is the measured fracture stress. This is applicable when considering small-scale yielding. The case in the middle region of the DBT is mentioned in a later section. In particular, it is noted to be difficult to predict quantitatively fracture toughness from only microstructural parameters because Beremin's model adopts fitting parameters that adjust the experimental results of fracture toughness testing.

Multiscale model synthesis approach

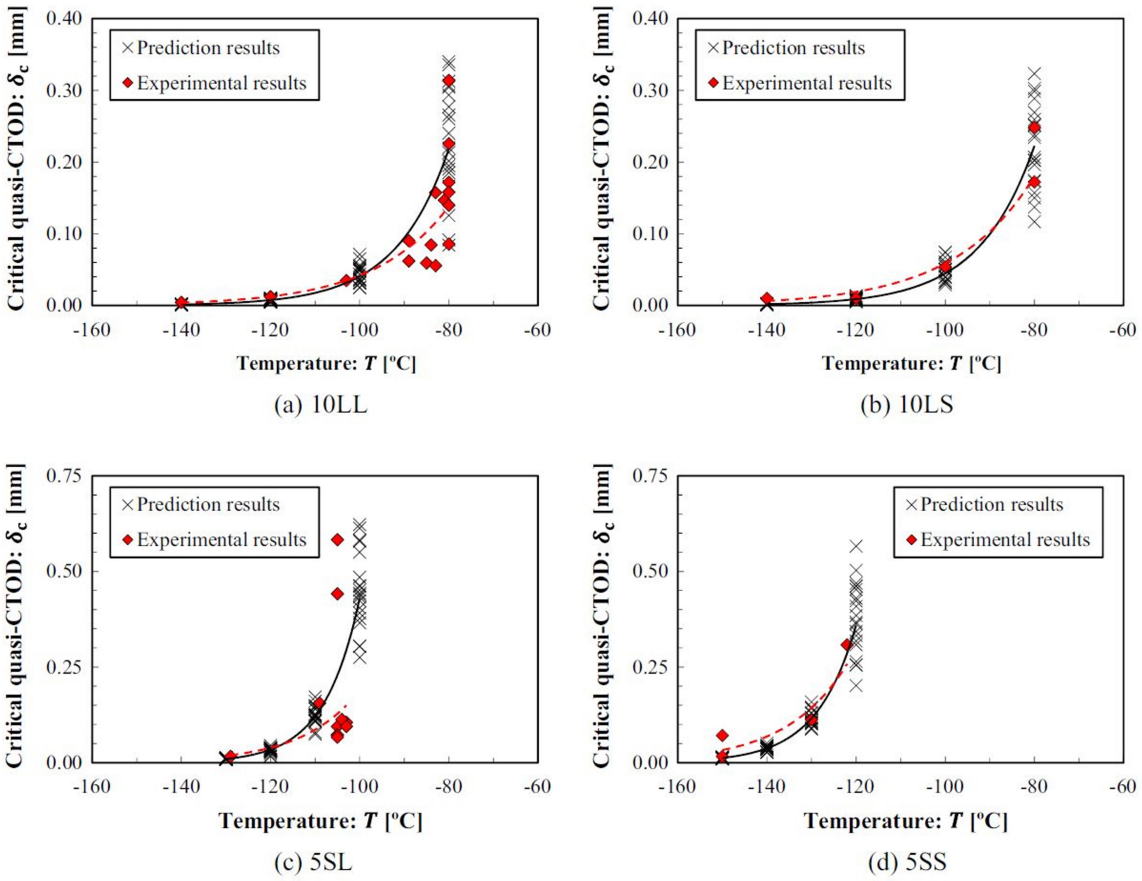
Shibanuma et al. [198, 199] proposed a theoretical model based on the Monte Carlo method, which needs no fitting parameters but only microstructural ones. A model predicting fracture toughness of ferrite and cementite microstructure was suggested. They assumed the aforementioned three cleavage fracture stages (Figure 2.25), and the fracture conditions for the respective stages were formulated as functions of ferrite grain size, cementite particle size, local stress and strain (see also Section 2.4.1). Furthermore, an active zone of fracture toughness specimen is divided into volume elements where

microstructures are assigned. Cleavage fracture is assumed to initiate at one time when all the fracture criteria are simultaneously satisfied in any one of the volume elements. Prediction results of the dependence of critical crack tip opening displacement (CTOD) were in accordance with experimental results as shown in Figure 2.27 [199]. Shibanuma et al. [200] also proposed a similar model for steels with a banded ferrite and pearlite microstructure without any parameter fitting from the experimental results. In their study, a multiscale model based on the micromechanics of brittle fracture initiation was applied, which required the ferrite grain size and pearlite band thickness distributions, a stress-strain curve, as well as specimen geometry and boundary conditions for the fracture toughness test.

2.5.2 Modelling in the DBT region

Modified Beremin models

The Beremin model [27] is based on the assumption that there are already small defects as initial cracks in microstructure, and that the cleavage fracture process is purely controlled by the stress criterion. Hence, some modifications were proposed by introducing an effect of plastic strain on cleavage crack nucleation on an embrittling secondary phase and its deactivation if it did not propagate immediately [202–204]. These works mainly focused on the competition between cleavage fracture and plasticity in the significantly lower part of the DBT region. When the temperature increases to the middle of the DBT region, the HRR field solution [187, 188], which is the approximation of a stress field around a crack tip, is no longer valid. In such cases of large-scale yielding, the Weibull stress can only be obtained by finite element method (FEM) calculations.



Representative values of the steels 10LL, 10LS, 5SL and 5SS.

Symbol		10LL	10LS	5SL	5SS
Ferrite grain diameter: d (μm)	Average	75	78	37	24
	Max	218	229	67	45
Cementite thickness: t (μm)	Average	0.55	0.19	0.45	0.13
	Max	2.02	0.66	1.15	0.44
Average aspect ratio of cementite particle		2.29	4.99	3.45	3.31
Yield stress at room temperature (MPa)		161	171	213	248

Fig. 2.27 Comparison between the experimental and prediction results for critical quasi-CTOD [199]. The tested steels have various sizes of ferrite grains and cementite particles. The quasi-CTOD is calculated by simply applying the CTOD estimation formula of BS 7448 [201]. It is noted that the quasi-CTOD does not represent the physical crack tip opening displacement, but it should be regarded as a parameter representing a degree of plastic deformation at notch root. Thus in the reference of [199] the fracture toughness is evaluated using a critical value of the quasi-CTOD.

Computational modelling on crack nucleation

Some research has tackled the modelling of the fracture process in the middle of the DBT region, where local plasticity becomes more intense and the area involved is larger. Most of them have made use of FEM, coupled with the aforementioned methods summarised in previous sections [205–212]. Some computational models can describe the crack initiation in the DBT region. Nevertheless, the models proposed so far seem to be useful only in a very simplified situation or limited cases.

2.6 Conclusion remarks and key questions for this research

In this chapter, previous studies that served as the background for this research project were summarised in an effort to understand what has been reported and what is still unknown. The scope of the review included the following topics: the DBT phenomenon in steel, the mechanical and microstructural factors that affect the DBT behaviour, the nature of cementite, experimental findings for the DBT process, and micromechanism and modelling work.

The DBT in steel can be considered a physical phenomenon determined by the relationship between the brittle fracture stress (mainly thinking of cleavage fracture here) and the yield stress at a macroscopic level. The fundamental reason for the transition is that Peierls stress for dislocation glide is highly temperature-dependent. Under the deformation at low temperatures or high strain rates or under stress concentration due to notches, the yield stress can be greater than or equal to the fracture stress, and

the brittle fracture can occur without macroscopic plastic deformation. This is the transition from ductile to brittle.

At a microscopic level, it can be regarded as a competitive phenomenon of localised deformation and stress concentration. Metallurgical factors have a significant effect on the DBT phenomenon. Alloying elements affect yield stress and fracture stress by directly changing the interfacial energy and the mobility of dislocations. They also influence localised deformation and stress concentration through the changes in microstructure. In the ferrite matrix of BCC iron, it is of great practical significance to deepen our understanding of cementite as an embrittling secondary phase that acts as a source of stress concentration and crack initiation. Regarding the effect of cementite morphology on ductile fracture, it is reported that for a given amount of cementite, the ductile fracture strain containing pearlite is lower than that of spheroidised cementite [213]. However, no detailed experimental study has been conducted on the effect of cementite morphology on the overall DBT behaviour.

The deformation and fracture process in the DBT region can be regarded as a process in which local plasticity proceeds to some extent before an unstable brittle crack initiates and propagates macroscopically. It is important to elucidate how the cementite morphology, in such circumstances, affects the micromechanism and eventually, the mechanical properties of the DBT behaviour. Furthermore, focusing on the micromechanism itself of deformation and fracture in the DBT region of spheroidised cementite and pearlitic lamellar cementite, respectively, fundamental research is needed to obtain a more detailed and clear understanding of the effect of microstructures. In particular, there are little data available on the elastic and plastic deformation of cementite, its interaction with the ferrite matrix before crack initiation, and the nature

of the fracture of cementite, which is obviously crucial but its fracture plane also remains debated. With respect to the difference in the study for each cementite morphology, the simpler ferrite and spheroidised cementite microstructure has been studied from an early stage in terms of characterisation, fracture mechanism investigation, as well as modelling work. In contrast, pearlitic steels have not been sufficiently studied. One reason for this is its complicated microstructure. Even in the situation, the majority of studies that have already been reported focus on fully pearlitic steels, and there is even much less research when it comes to hypoeutectoid dual-phase steels with ferrite and pearlite mixtures.

Based on all the reviewed material in this chapter as summarised above, the key questions to be tackled and answered in this research project are as follows:

1. How does the ductile-brittle transition behaviour change when the same volume fraction but different morphology, spheroidised and pearlitic lamellar, of cementite is introduced, with other influencing factors remaining unchanged?

2. How can the ductile-brittle transition behaviour be obtained, and can the difference between the two morphologies be understood and explained in terms of the intricate micromechanisms of deformation and fracture?

3. With respect to the deformation and fracture process in the DBT region of each microstructure, what are the plastic process of deformation of cementite and its interaction with the ferrite matrix before macroscopic crack initiation? Plus, what is the fracture plane of cementite?

All the mentioned above motivate the present work. A particular emphasis will be placed on micromechanisms and their characterisation. The aim of this research is

to achieve a microstructure-based fundamental understanding in more detail about the effect of cementite morphology on the DBT behaviour, with the combination of well-designed initial microstructures and advanced high-resolution characterisation techniques. The findings of this work are of significance because they can help design the microstructure of engineering steels better.

Chapter 3

Materials, and Experimental and Characterisation Techniques

3.1 Materials

Fe-0.2 wt%C alloy was selected in this study. To minimise the effect of any other microstructural factors affecting toughness, specific steels rather than commercial ones were designed and produced on a laboratory basis. The alloy ingots were prepared by vacuum melting and casting of 50 kg ingot. Table 3.1 shows the chemical composition of tested material, which aims for a simple binary chemical composition, and quite few impurities and inclusions. The ingots were produced by Nippon Steel Corporation.

Table 3.1 Chemical composition in wt% of tested materials.

C	Si	Mn	P	S	Al	B	N	O	Fe
0.20	0.003	<0.003	<0.002	<0.0003	0.023	<0.0003	<0.0005	0.0012	Bal.

3.2 Preparation of initial microstructure

Figure 3.1 shows a manufacturing process of the tested materials. The ingots were subsequently reheated, hot-rolled, and water-quenched to room temperature. Then, steel plates with 25 mm in thickness were obtained. Bars with 20 mm in diameter were machined from the plates. Some of the bars were tempered at 700 °C for 48 hours to obtain ferrite (α) and spheroidised cementite (θ) microstructure, denoted as the $\alpha + \theta$ microstructure hereafter. The others were austenitised at 950 °C for 1 hour and subsequently held at 740 °C for 0.5 hours for proeutectoid ferrite to be formed, followed by air cooling to room temperature for pearlite to be formed. Austenitising temperature was carefully selected to obtain nearly the same ferrite grain size distribution as the $\alpha + \theta$ microstructure. Ferrite grain size is one of the controlling factors for toughness, and hence the DBT behaviour [90]. In this way, ferrite and pearlitic lamellar cementite microstructure was obtained, denoted as the $\alpha + P$ microstructure hereafter. Figure 3.2 illustrates the initial microstructures of the tested materials. Figure 3.2 (a) and (b) are the $\alpha + \theta$ microstructure. Figure 3.2 (c) and (d) are the $\alpha + P$ microstructure.

Figure 3.3 demonstrates the distribution of apparent ferrite grain size as equivalent circle diameter (ECD), the diameter of a circle with the same area as the measured one, from areal intercept in each initial microstructure. The apparent ferrite grain size d_α was measured by electron backscatter diffraction (EBSD) analysis, calculated from the following equation:

$$d_\alpha = 2\sqrt{\frac{\overline{A_\alpha}}{\pi}} \tag{3.1}$$

where $\overline{A_\alpha}$ is the average areal intercept of ferrite grains. They are 82.1 μm, and 75.9 μm in the $\alpha + \theta$ microstructure and the $\alpha + P$ microstructure, respectively. To obtain

A_α, an areal intercept of a ferrite grain, each grain is defined as a set of measurement points of EBSD with crystal orientation difference of 15 degrees or less. The detailed EBSD operating condition is referred to in Section 3.4.2. The difference in cumulative frequency is small as shown in Figure 3.3. The similar A_α distribution in these initial microstructures implies that the effect of the difference in ferrite grain size on the DBT behaviour of the tested materials can be minimised. In the $\alpha + \theta$ microstructure, each cementite particle size d_θ was estimated [214, 215] from an areal intercept of a particle A_θ to be

$$d_\theta = \sqrt{\frac{6A_\theta}{\pi}} \tag{3.2}$$

and the apparent average cementite particle size ($\overline{d_\theta}$) was estimated by averaging d_θ, which was 2.0 μm. Image J software was used for image analysis, measuring cementite particle size and shape.

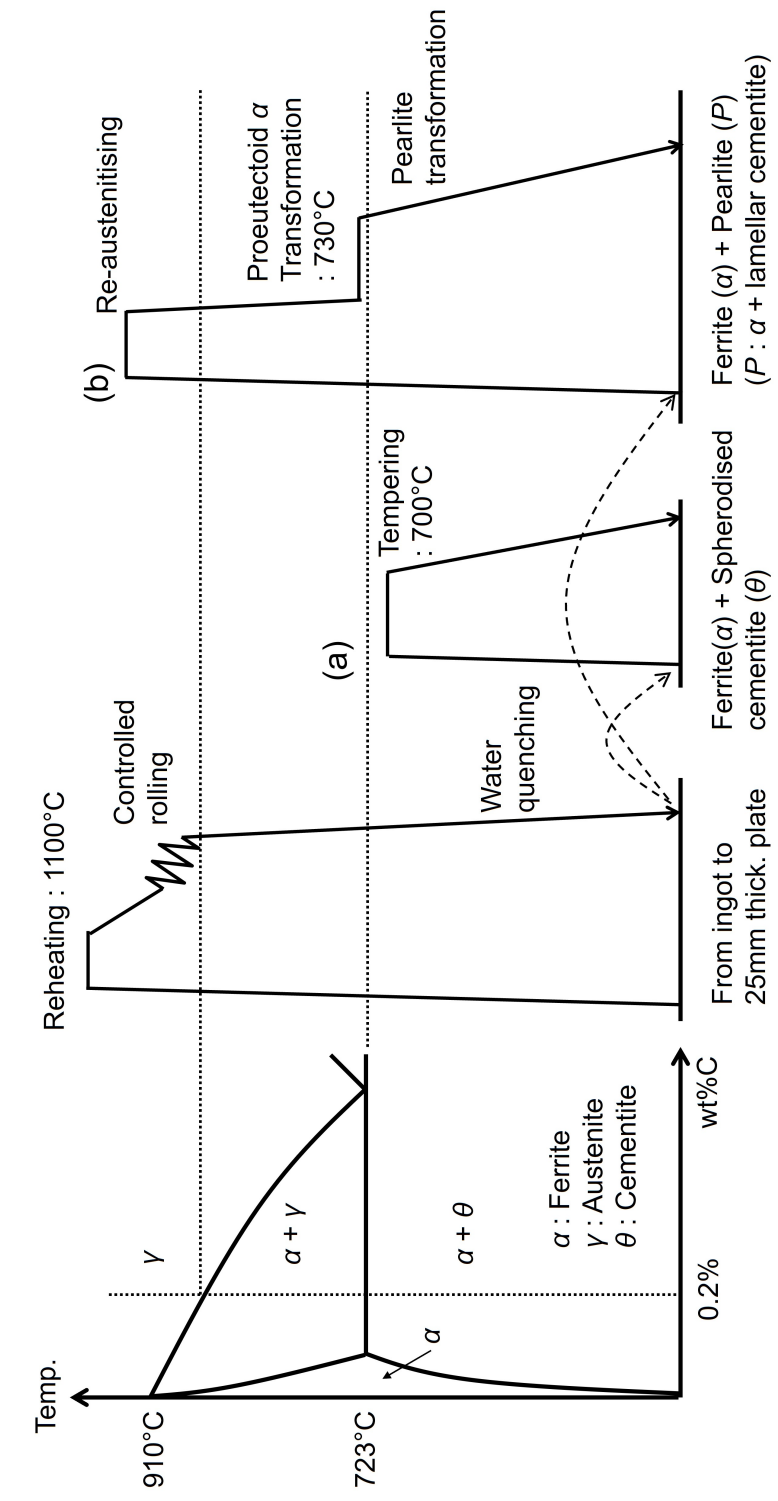


Fig. 3.1 Schematic illustration showing the manufacturing process for obtaining initial microstructures with Fe-C binary phase diagram; (a) ferrite and spheroidised cementite $(\alpha + \theta)$ microstructure, (b) ferrite and pearlitic lamellar cementite $(\alpha + P)$ microstructure.

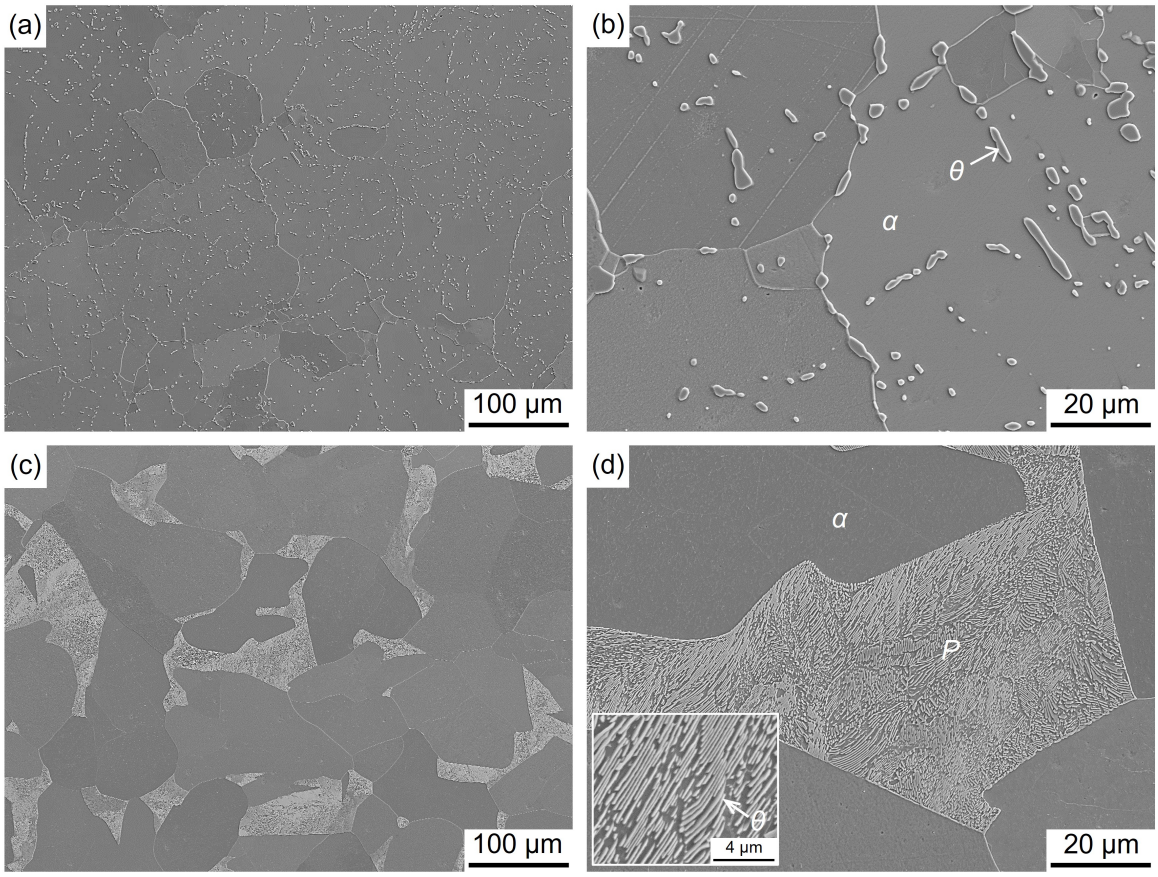


Fig. 3.2 SEM SE images indicating initial microstructures; (a) and (b) are ferrite and spheroidised cementite ($\alpha + \theta$) microstructure, (c) and (d) are ferrite and pearlitic lamellar cementite ($\alpha + P$) microstructure.

3.3 Mechanical testing

3.3.1 Uniaxial tensile testing

Uniaxial tensile tests were conducted with a wide range of temperatures and strain rates in order to investigate the DBT behaviour in each microstructure. Solid cylindrical tensile specimens were machined from heat-treated bars. The gauge part of the specimen was 8 mm in length and 3 mm in diameter. Tensile tests were performed by INSTRON 8850 Servo-Hydraulic with STS environmental chamber for tests in

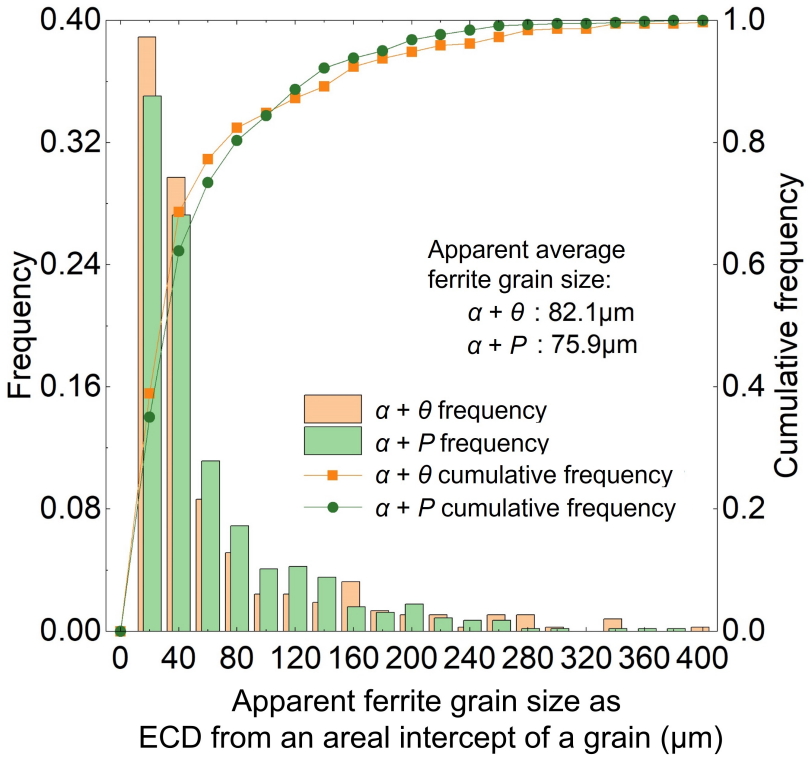


Fig. 3.3 The distribution of apparent ferrite grain size as ECD from areal intercept in each initial microstructure.

low temperatures down to -100 °C. Liquid nitrogen was used to cool down inside the chamber. The built-in hydraulic chucking grips did not work in low temperature conditions, so customised mechanical chucking grips were newly developed for this experiment. Temperature was monitored and controlled by the thermocouple attached to the specimen. Test temperature and strain rate ranged from -100 °C to 25 °C, and 1×10^{-3}/s to 1×10^{1}/s, respectively. Specimens were held for two minutes after the monitored temperature reached the target one. The test was conducted at most three times at a testing condition when it was thought to be in the DBT region since fracture strain could vary substantially. Figure 3.4 illustrates the tensile testing setup.

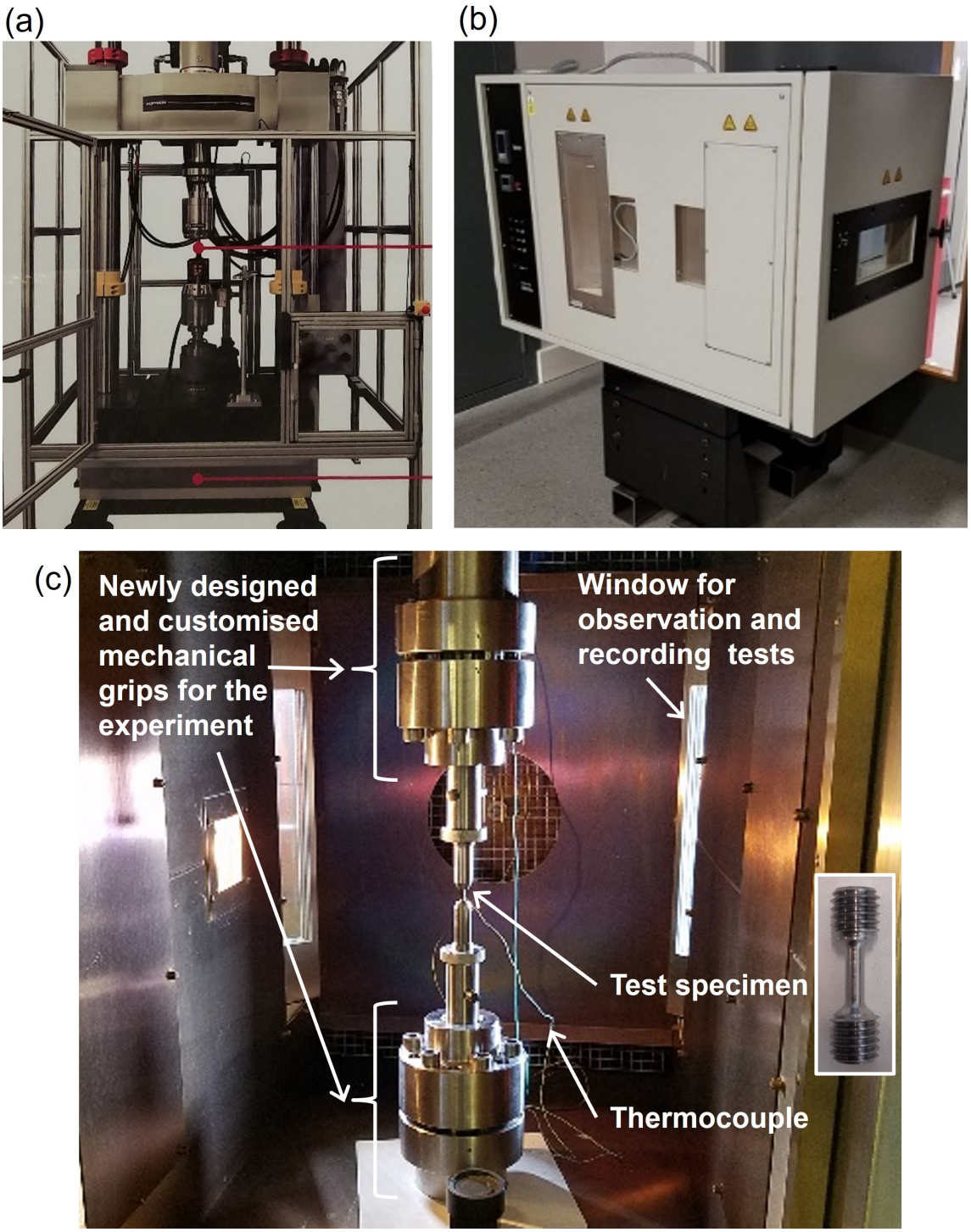


Fig. 3.4 Illustration of uniaxial tensile testing setup; (a) an overall view of the testing machine, (b) environmental chamber, (c) testing setup inside the environmental chamber.

3.3.2 *In-situ* tensile testing in SEM

Specimen preparation

Figure 3.5 represents the specimen geometry of *in-situ* tensile test, which is a double dog-bone type with a gauge part of 5 mm × 2 mm × 1.5 mm. After electrical discharge machining (EDM), specimen surfaces were polished by standard metallographic methods with 40 nm colloidal silica finishing. Then, EBSD scanning was conducted to acquire crystallographic orientation information before mechanical testing. After that, the specimens were etched with 5 % nital for about 30 seconds to get the surface microstructure to appear.

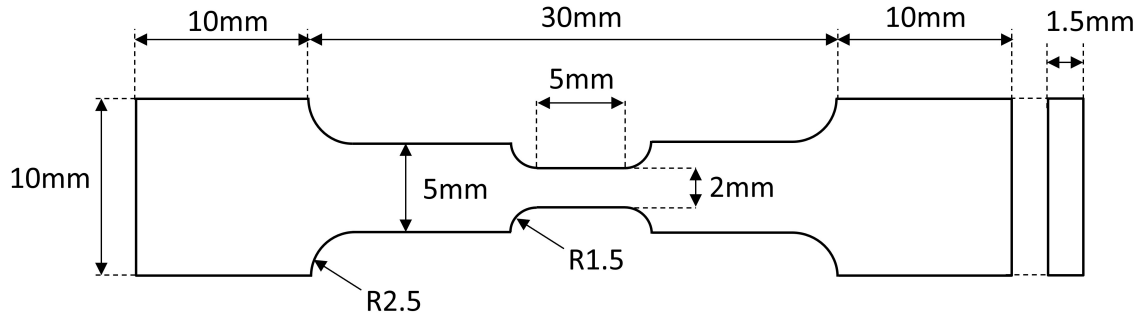


Fig. 3.5 The specimen geometry of *in-situ* tensile test.

Tensile testing

In-situ tensile tests were performed at room temperature. Tensile deformation was applied using a 5 kN Deben loading stage in the chamber of ZEISS Merlin field emission gun scanning electron microscope (FEG-SEM). The tensile tests were conducted by controlling the displacement of the loading stage at a strain rate of 1×10^{-3}/s. Figure 3.6 demonstrates the experimental setup for the *in-situ* tensile testing.

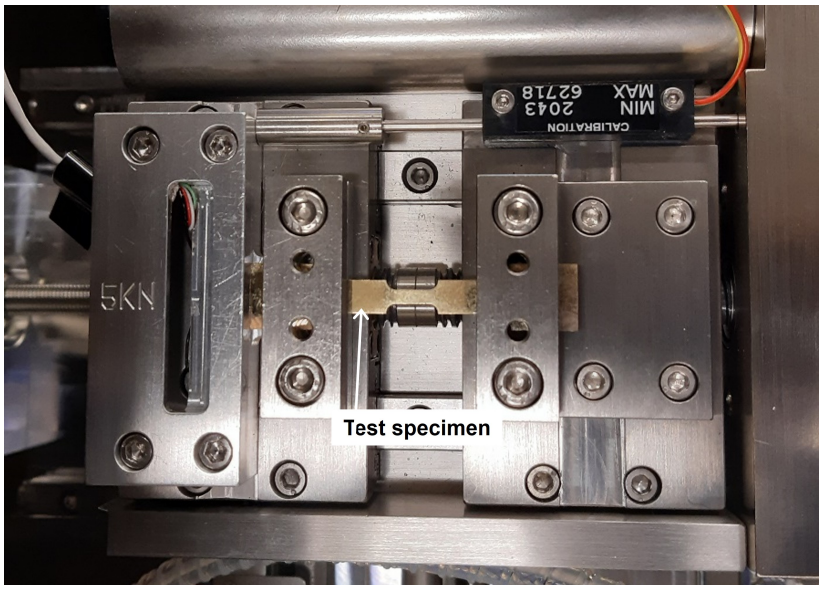


Fig. 3.6 *In-situ* tensile testing setup; the Deben loading stage and a tensile test specimen.

3.4 Characterisation

3.4.1 Scanning electron microscope: SEM

Metallographic specimens were prepared using standard procedures. The removal of materials was achieved by grinding and polishing. Grinding was performed with three pads of different sizes of resin-bonded diamond, which were No.220, 500, and 1200, respectively. Polishing was demonstrated by cloth pads with a water-soluble diamond suspension of 9, 3 and 1 μm, respectively. All samples were finished with 40 nm size colloidal silica suspension. A ZEISS Merlin FEG-SEM was applied for characterisation. Secondary electron (SE), in-lens, and backscattered electron (BSE) detectors were equipped for acquiring topological and compositional information. Fracture surfaces of the specimens tested at various temperatures and strain rates were observed (Figure 3.7 (a)). In addition, the tested specimens were cut at a plane passing through the centre of the fracture surface in the longitudinal direction of the cylindrical geometry,

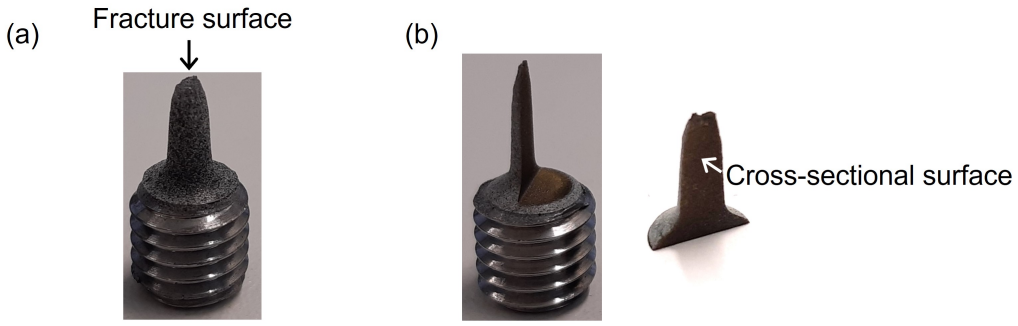


Fig. 3.7 Observation surfaces of tested specimen; (a) fracture surface, (b) cross-sectional surface.

and characterised on the cross-sectional surface, as shown in Figure 3.7 (b). For microstructural observation, the cut specimen was mounted, polished, and etched with 5 % nital at room temperature, followed by SEM observation beneath the fracture surface. In the $\alpha + \theta$ microstructure, SEM images operated at 15 kV and 10 nA were taken randomly from the picked-up areas just below the fracture surface. In the $\alpha + P$ microstructure, lower accelerating voltage and probe current - 10 kV and 3 nA - were also applied, owing to the much finer pearlitic lamellar cementite microstructure compared to the spheroidised one.

When it comes to statistical analysis of cementite particles, the particle size was evaluated using ECD d_{ECD} describing

$$d_{\mathrm{ECD}} = 2\sqrt{\frac{A_\theta}{\pi}} \tag{3.3}$$

The apparent aspect ratio was evaluated using the ratio of the minor axis to the major axis of the best-fit ellipse.

3.4.2 High-resolution electron backscatter diffraction: HR-EBSD

EBSD patterns were captured using a Bruker e-Flash HR detector operated with Esprit 2.1 software, and recorded at 800 × 600 pixel resolution. SEM conditions used were 20 to 30 keV accelerating voltage and 10 to 15 nA probe current, and maps were collected at various step sizes up to 0.25 μm. Cementite has an orthorhombic unit cell [216], and lattice parameters for the cementite phase in this study are taken as a = 5.107 Å, b = 6.778 Å and c = 4.540 Å as applied in the software. As described in Section 2.3.1, the space group of cementite adopted in this research was *Pnma*.

To analyse local deformation around and inside cementite particles in the $\alpha + \theta$ microstructure, HR-EBSD cross-correlation analysis was applied. Wilkinson et al. [28, 29] have developed a precise method of evaluating lattice rotation and elastic strain with EBSD patterns at 0.01 ° angular sensitivity and 1×10^{-4} strain sensitivity, respectively. This method is to measure image shifts in the position of zone axes and other features in the EBSD patterns between a reference and testing points by cross-correlating many regions of interest (ROIs) in the diffraction pattern, generating a displacement gradient tensor between the two, then calculating elastic strain and lattice rotation tensors. More details of the procedure are described in the relevant references [217–219].

3.4.3 SEM-based transmission Kikuchi diffraction : TKD

For characterisation using transmission electron beam, thin foils were prepared from fractured tensile specimens by a ZEISS Crossbeam focused ion beam (FIB) method, allowing for observing a particular area of the microstructure. Specimens were lifted

out from the cross-sectional surface with about 2 μm in thickness, and then were thinned to less than 100 nm. Finishing ion milling was performed with a low voltage of 5 kV to minimise any damage caused by FIB to the foils.

For more localised and detailed characterisation of the $\alpha + P$ microstructure, a SEM-based on-axis TKD method was applied with the ZEISS Merlin FEG-SEM system [220]. In this study, on-axis TKD alignment was adopted. As shown in Figure 3.8, the TKD detector is aligned in line with the electron gun and specimen, which is advantageous to quicker acquisition speed, higher resolution, and better indexing rate [31]. The operating voltage was from 20 to 30 kV, and the probe current was from 0.8 to 2.0 nA. The step size ranged from 1 to 5 nm. TKD pattern resolution was 800×600 with 16 bits.

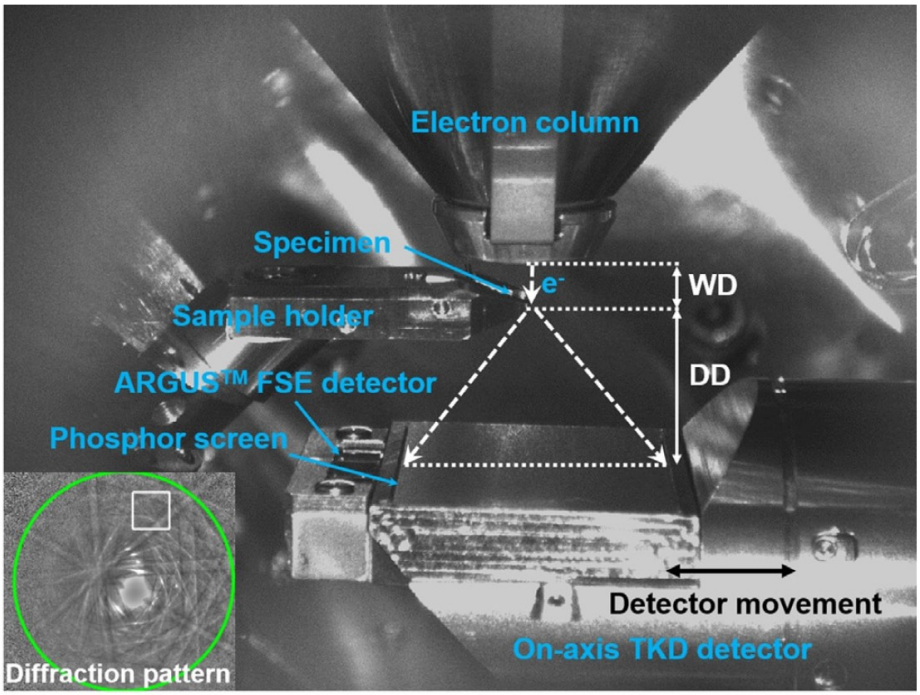


Fig. 3.8 The setup of on-axis TKD, and an example of a diffraction pattern acquired by using this technique [220].

Chapter 4

Ductile-Brittle Transition Behaviour in Steels with Identical Chemical Composition and Different Cementite Morphology

4.1 Introduction

A deeper understanding of the DBT in steels is required to improve the level of control of the mechanical properties. The literature survey in Chapter 2 revealed that metallurgical factors have significant effects on the DBT behaviour, in particular the grain size, which contributes to the stress concentration through dislocation pile-up. Embrittling secondary phases, which act as the initiation site of brittle cracks, are important factors too.

The effect of pearlite volume fraction on impact properties has been previously examined. For example, Pickering et al. [54, 221] evaluated the Charpy impact properties of pearlitic steels with different carbon contents and reported that an increase in pearlite fraction results in 1) a higher transition temperature, 2) a wider transition region, and 3) a lower upper shelf. The first result arises due to an increase in the amount of cementite phase, meaning the increase in the amount of embrittle secondary phase leads to more brittle initial cracks. In addition, from the perspective of macroscopic mechanical property, it can be understood that the strength of steel increased, and the toughness decreased with increasing carbon content. The second result appeared to be the consequence of energy absorption by deformation in pearlite, but the precise details are unknown. The decrease in the slope of the transition curves may be due to the increase in the pearlite fraction. Regarding the third result, it has been reported that the increase in pearlite increases both the flow stress and the work hardening rate at a certain strain [221–223]. Hence, the deformation around the crack formed in pearlite is suppressed compared to when it is formed in the ferrite phase.

A very limited number of systematic experimental works have been conducted about the effect of cementite morphology on deformation and fracture in carbon steels. When it comes to its effect on ductile fracture, Gladman and Pickering et al. [213, 222] investigated the true strain for ductile fracture in different morphologies (spheroidal and pearlitic) and showed that fracture strain became smaller in pearlitic cementite microstructure at a given cementite fraction. Nevertheless, the effect of the cementite morphology on the DBT has not been experimentally investigated. It seems not easy to transfer the indicated effect [213] of cementite morphology on the strain at ductile fracture into the one on the transition temperature region. This is because

the fracture strain includes all the processes from void (or crack) initiation, its growth and coalescence. Thus, it is difficult to separate the effect of only the local plastic deformation that occurs also in the transition region, especially in the lower region of the DBT.

The essence of the DBT behaviour is the high Peierls stress at low temperatures and its significant temperature-dependence, which affects the dislocation mobility [35, 36]. Hence, the DBT phenomenon is essentially a thermal activation process. The thermal activation process is the process by which a reaction or process is initiated or accelerated by the input of thermal energy. In the context here, the process is that dislocations overcome the Peierls barrier to move. It is known that the activation energy of the DBT process can be obtained from the transition temperatures with different strain rates [224]. By making use of the activation energies and inferring the rate-controlling step of the DBT in each cementite morphology, our understanding of the mechanism may be deepened. This strategy is adopted in this chapter.

Based on what is described in this section, the objectives of this chapter are as follows; (i) to correctly capture the DBT behaviour of test steels with different cementite morphology, (ii) to understand the deformation and fracture process in the transition region by observing thoroughly the fracture and the cross-sectional surfaces of tested steels using SEM, and (iii) to calculate the activation energies using Arrhenius plot analysis to grasp and compare the DBT behaviour.

To achieve this, the test is designed to evaluate the effect of only the cementite morphology, while minimising the influence of contributing factors as much as possible, as described in Chapter 3. To obtain and compare the DBT behaviour, tensile tests are performed over a wide range of temperatures and strain rates. The fracture surfaces

and cross sections after the tests were thoroughly investigated, and the deformation and fracture behaviour in the transition region are considered.

4.2 Experimental methods

4.2.1 Materials

Carefully designed test material was employed, of chemical composition as described in Table 3.1. Through well-designed and properly selected heat treatment conditions described in Figure 3.1, testing materials with almost the same apparent ferrite grain size but different cementite morphology were achieved. The cementite phase fraction in the test steels is kept constant. Furthermore, high-cleanliness steel, such that impurities such as phosphorus and sulfur and inclusions like oxide and sulfide are eliminated as much as possible, is used. The testing materials are termed the ferrite and spheroidised cementite ($\alpha+\theta$) microstructure and the ferrite and pearlitic lamellar cementite ($\alpha+P$) microstructure.

4.2.2 Mechanical testing

Uniaxial tensile tests were conducted over a wide range of temperatures and strain rates to evaluate the DBT behaviour in each microstructure. The details also should be referenced in Section 3.3.1. To measure strain, DIC method was applied. By spraying white and black paints, speckle patterns were drawn on the surface of the tensile specimens. Tensile tests were recorded by cameras, and DIC analysis was conducted thereafter for the recorded videos with software. A high-speed camera - PHOTRON - was used for recording the tests which were conducted under the strain

rate of 1×10^{-1}/s and higher with the camera frequency ranging from 250 Hz to 7000 Hz. The recorded video was analysed with GOM Collerate software. For the tests with slower strain rates, the video extensometry system by iMetrum Ltd. was applied with the acquisition frequency from 1 Hz to 17 Hz, and the data was analysed using Video Gauge software. The cameras were set outside the window of the environmental chamber (Figure 3.4 (c)).

4.2.3 Characterisation: SEM

Fracture and cross-sectional surfaces of tested specimens obtained at various temperatures and strain rates were observed by ZEISS Merlin FEG-SEM. The experimental procedure should also be referred to Section 3.4.1.

4.3 Results

4.3.1 Transition curve of fracture strain

Figure 4.1 illustrates a series of recorded images. As the same tendency was observed regardless of the test specimen's microstructure, here the data of the $\alpha+\theta$ microstructure is given as an example. Figure 4.1 (a) to (d) show the test at -25 °C and 1×10^{1}/s, and Figure 4.1 (e) to (h) are from the test at -75 °C and 1×10^{1}/s, illustrating ductile fracture and brittle fracture, respectively. The strain rate applied here was the fastest condition. In the first condition, corresponding to the upper region of the transition curve, the fracture strain was 40.5 %, and the testing duration was 0.051 s. In the latter condition - the lower shelf of the transition curve - the measured fracture strain was 2.1 %. The time from the test start to failure was only 0.026 s, which was

significantly short. Even though some tensile tests were conducted for such a short time, as shown in Figure 4.1, the deformation was reliably measured and recorded by using the high-performance high-speed camera. In addition, a substance thought to be ice was observed at low temperature testing, but, as shown in Figure 4.1 (e) to (h), the speckle pattern, which was necessary for measuring strain, was still clearly visible. As a result, the strain measurement was performed without any problems. In the ductile fracture condition, a reduction in the cross-sectional area of the gauge part can be observed, whereas it was not in the brittle fracture condition until the specimen broke suddenly.

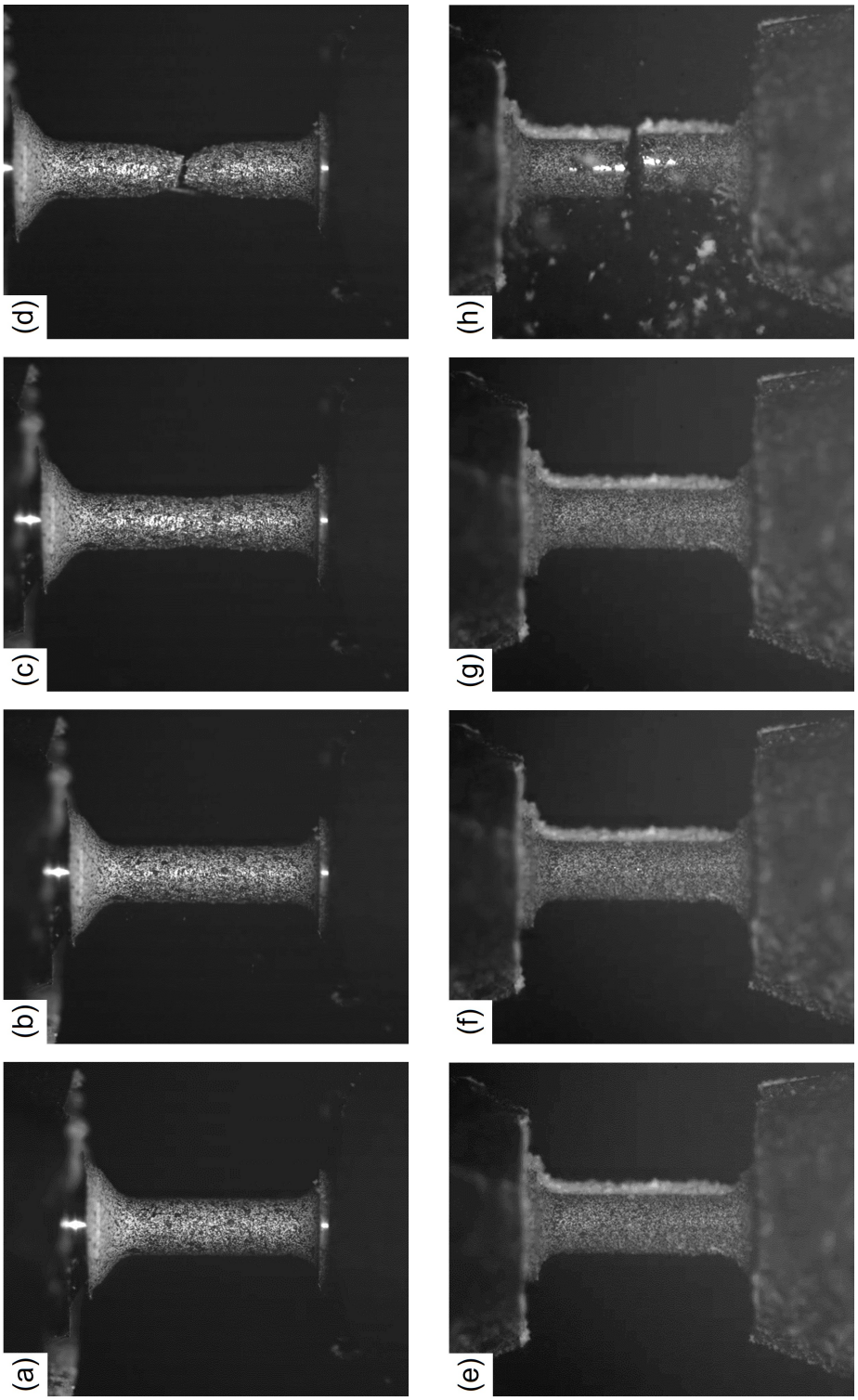


Fig. 4.1 A series of images of tensile tests captured by a high-speed camera; (a) to (d) the test at -25 °C and 1×10^1/s showing the ductile fracture with fracture strain of 40.5 %, (e) to (h) the test at -75 °C and 1×10^1/s representing the brittle fracture with fracture strain of 2.1 %. Test duration were 0.051 s and 0.026 s, respectively.

Figure 4.2 (a) and (b) show engineering fracture strain under various test temperatures and strain rates in the $\alpha + \theta$ and the $\alpha + P$ microstructures, respectively. DBT curve has been represented nicely by a hyperbolic tangent function [225, 226]. Here, given the same type of formula was assumed to fit a trend line for each transition curve, fracture strain S is represented

$$S = S_0 \left\{ 1 + \tanh \left[a(T - T_{\mathrm{DBT}}) \right] \right\} \tag{4.1}$$

where T is temperature, T_{DBT} is the DBTT, and S_0 and a are fitting constants. In the $\alpha + \theta$ microstructure, fracture strain decreased as temperature lowered and strain rate increased. Fitting the Equation 4.1 to the data and taking a temperature at which the upper shelf fracture strain halves as the DBTT, it varied from -83 °C in 1×10^{-2}/s to -35 °C in 1×10^{1}/s. The same trend of fracture strain to test temperature and strain rate can also be recognised in the $\alpha + P$ microstructure. The DBTT at 1×10^{-2}/s was estimated -102 °C, which changed to -79 °C at 1×10^{1}/s. Table 4.1 summarises the fitting constants to Equation 4.1 and the DBTTs of each microstructue and strain rate.

With respect to the comparison between the two microstructures, the $\alpha + \theta$ microstructure displays a clear trend in fracture strain with test temperature and strain rate. By contrast, in the $\alpha + P$ microstructure, fracture curves are relatively insensitive to temperature and strain rate. Specifically, assuming a straight line between 10 % and 90 % of the upper shelf of the transition curve, the slope of the line can be a way of representing how much drastic change the transition curve has in fracture strain against temperature. Table 4.2 indicates the slopes of the trend line from 10 to 90 % of the upper shelf strain for each curve. The slope ranged from 0.65 to 0.94 %/°C in the $\alpha + \theta$ microstructure, whereas the $\alpha + P$ microstructure experienced between 0.24

and 0.33 %/°C, which indicated the α+P microstructure has a wider transition range compared to its counterpart.

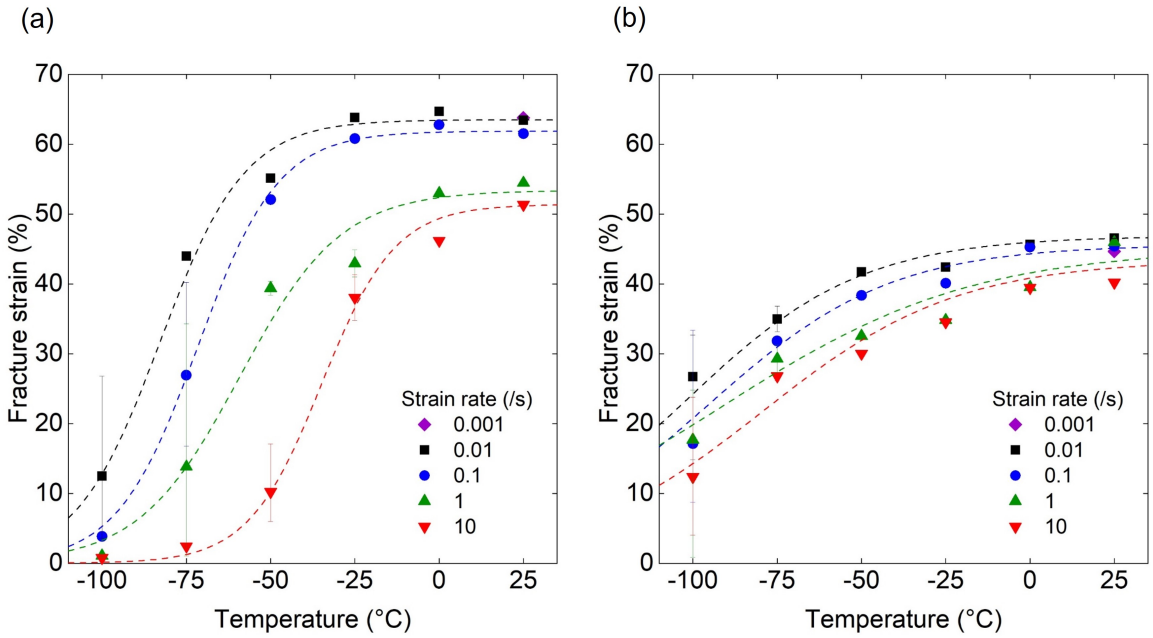


Fig. 4.2 Transition curves of fracture strain under various test temperatures and strain rates in (a) the $\alpha + \theta$ microstructure, and in (b) the $\alpha + P$ microstructure.

Table 4.1 The fitting constants to Equation 4.1 and the DBTTs of each microstructue and strain rate.

Strain rate (s^{-1})	$\alpha + \theta$			$\alpha + P$		
	S_0	a	T_{DBT} (°C)	S_0	a	T_{DBT} (°C)
0.01	31.7	0.0399	-83	23.4	0.0193	-102
0.1	30.9	0.0419	-72	22.8	0.0186	-95
1	26.7	0.0333	-59	22.6	0.0136	-91
10	25.7	0.0458	-35	21.7	0.0174	-79

Table 4.2 The slopes of trend lines from 10 to 90 % of upper shelf of the transition curves.

Strain rate (s^{-1})	Slope (%/°C) from 10 % to 90 % of the upper shelf of the curve	
	$\alpha + \theta$	$\alpha + P$
0.01	0.92	0.33
0.1	0.94	0.31
1	0.65	0.24
10	0.86	0.27

4.3.2 Fractography

Typical examples of ductile and brittle fracture surfaces observed in this study are shown. Figure 4.3 shows ductile fracture surfaces of the $\alpha + \theta$ microstructure with various magnifications, tested at 25 °C and 1×10^0/s. Typically, a so-called cup and cone fracture surface can be observed Figure 4.3 (a). Many dimples were detected in Figure 4.3 (b) and (c). Figure 4.3 (d), which is a magnified image of a rectangle in Figure 4.3 (c), indicates that cementite particles can be recognised in the bottom of such dimples as shown with an arrow. Figure 4.4 demonstrates brittle fracture surfaces of the $\alpha+\theta$ microstructure with various magnifications, tested at -100 °C and 1×10^0/s. By chasing the river patterns observed on the surface as shown in Figure 4.4 (b), their conversion point corresponded to an area indicated with a rectangle in Figure 4.4 (c). After slightly etching the surface, a cementite particle can be identified, as shown in Figure 4.4 (d).

In the $\alpha+P$ microstructure, ductile fracture surfaces, tested at 25 °C and 1×10^{-1}/s, had dimple-like structures as shown in Figure 4.5 (a) and (b). Figure 4.5 (c) shows one of the dimple-like structures on the surface. There were particular areas at the bottom of such dimple-like structures. Figure 4.5 (d) is a magnified image of a rectangle

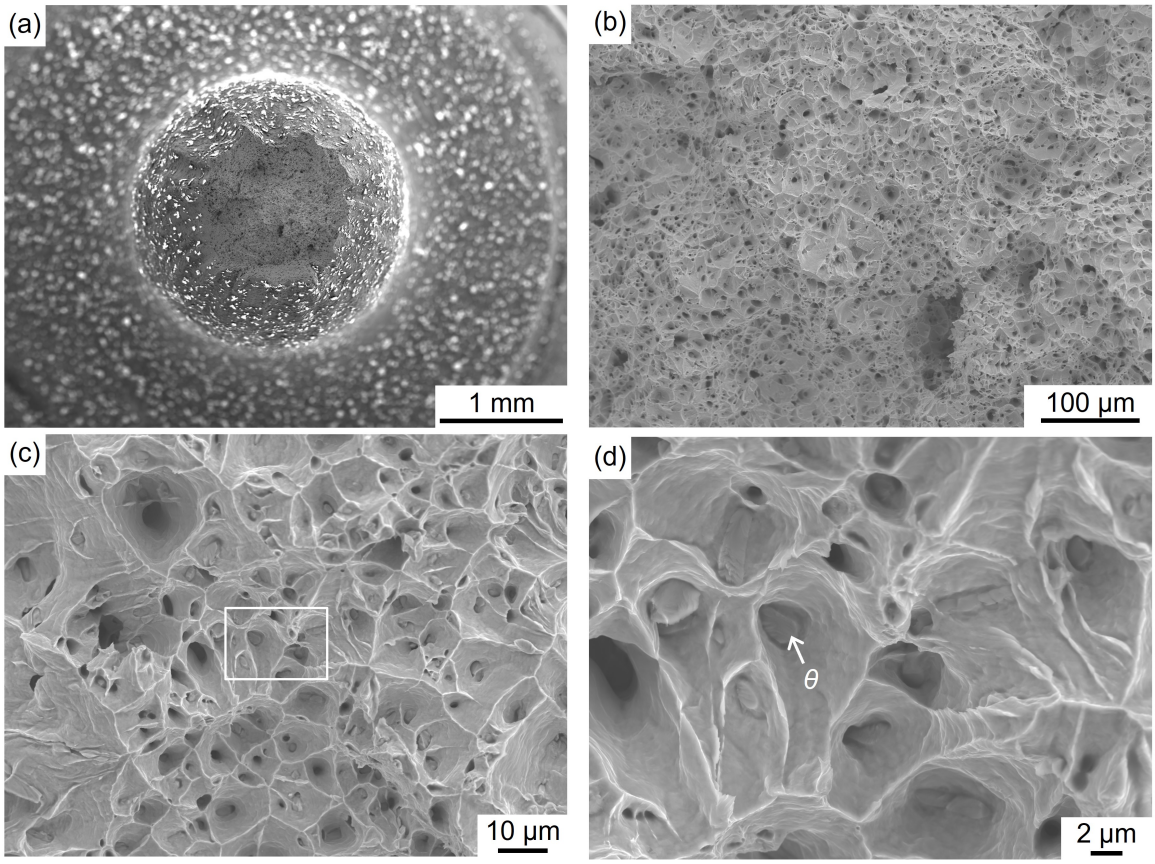


Fig. 4.3 An example of ductile fracture surface in the $\alpha+\theta$ microstructure with fracture strain of 56.1 %, tested at 25 °C and 1×10^0/s, taken by various magnifications, with cementite particles in the bottom of fine dimple structure on the fractured surface in (d), which is the magnified image of a rectangle in (c).

in Figure 4.5(c), showing fine ductile fracture surface. It was implied that this area was fractured pearlite. Figure 4.6 demonstrates brittle fracture surfaces of the $\alpha + P$ microstructure, tested at -100 °C and 1×10^{-1}/s. As shown with arrows in Figure 4.6 (b), the river patterns were traced to a particular area in the upper middle of the image. Figure 4.6 (c) is a magnified image of the area and shows that the river patterns on the surface initiated exactly from the interface between ferrite and the particular area as indicated by arrows in Figure 4.6 (c). Figure 4.6 (d) shows a magnified image of a rectangle in Figure 4.6 (c), indicating this area had a fine fractography.

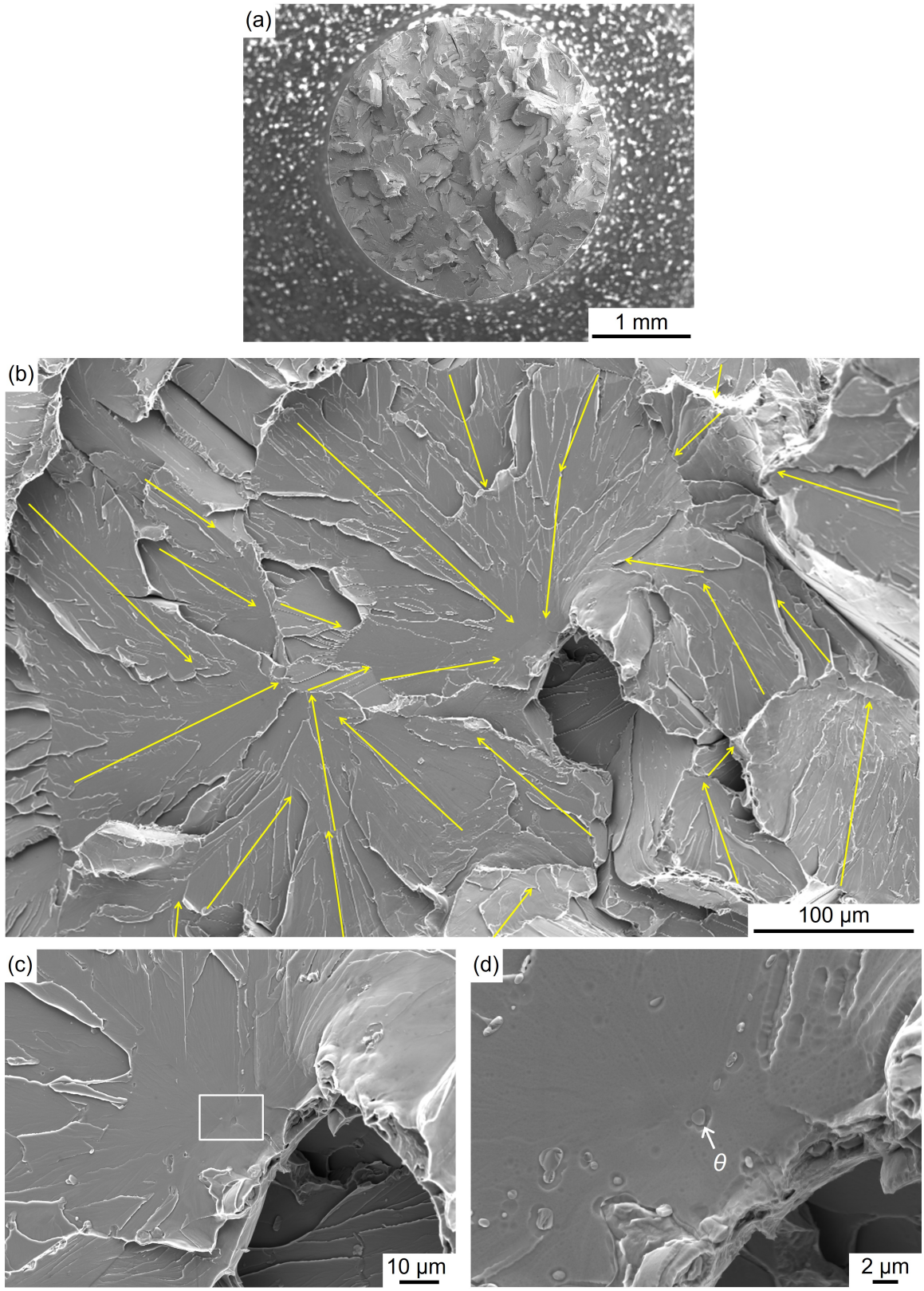


Fig. 4.4 An example of brittle fracture surface in the $\alpha + \theta$ microstructure with fracture strain of 0.9 %, tested at -100 °C and 1×10^0/s, taken by various magnifications, with arrows indicating flow of the river patterns on the surface in (b), with a cementite particle at a conversion point of the river patterns in (d).

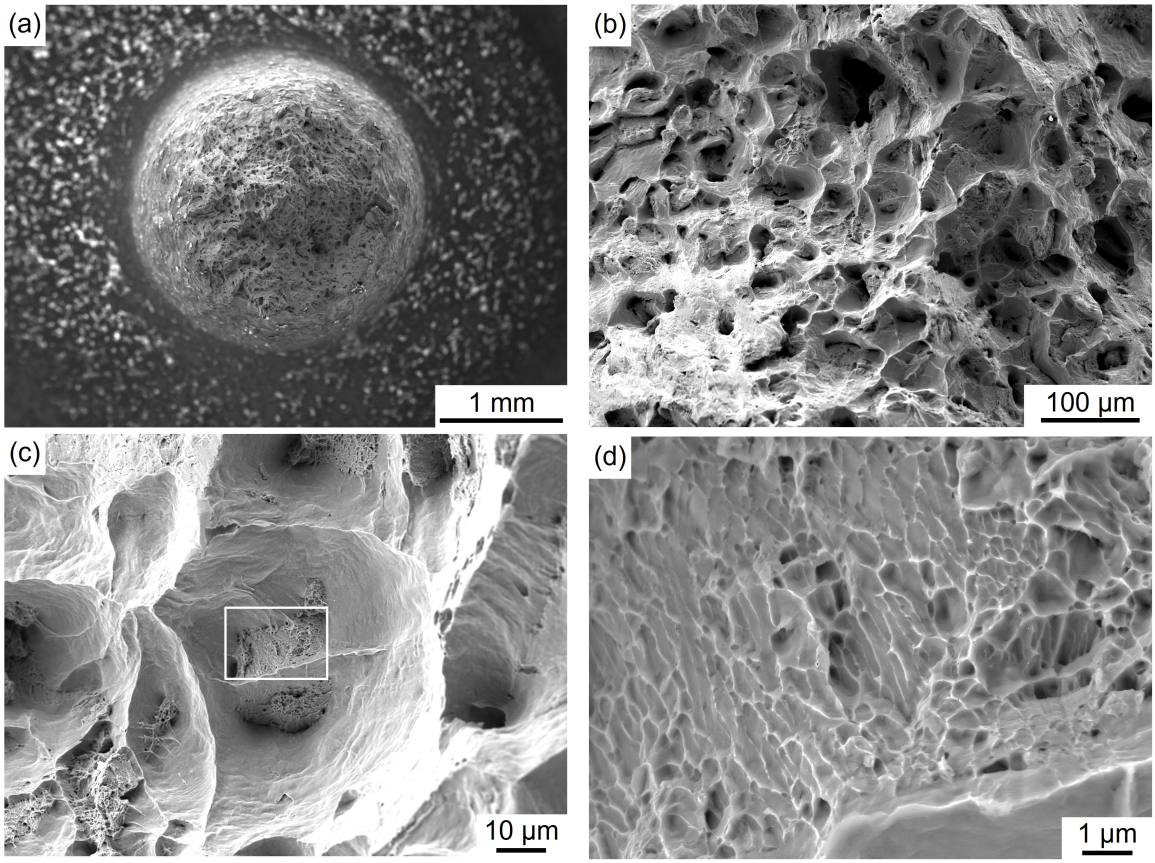


Fig. 4.5 An example of ductile fracture surface in the $\alpha+P$ microstructure with fracture strain of 45.4 %, tested at 25 °C and 1×10^{-1}/s, taken by various magnifications, with showing fine ductile fractured pearlite in (d), which is the magnified image of a rectangle in (c).

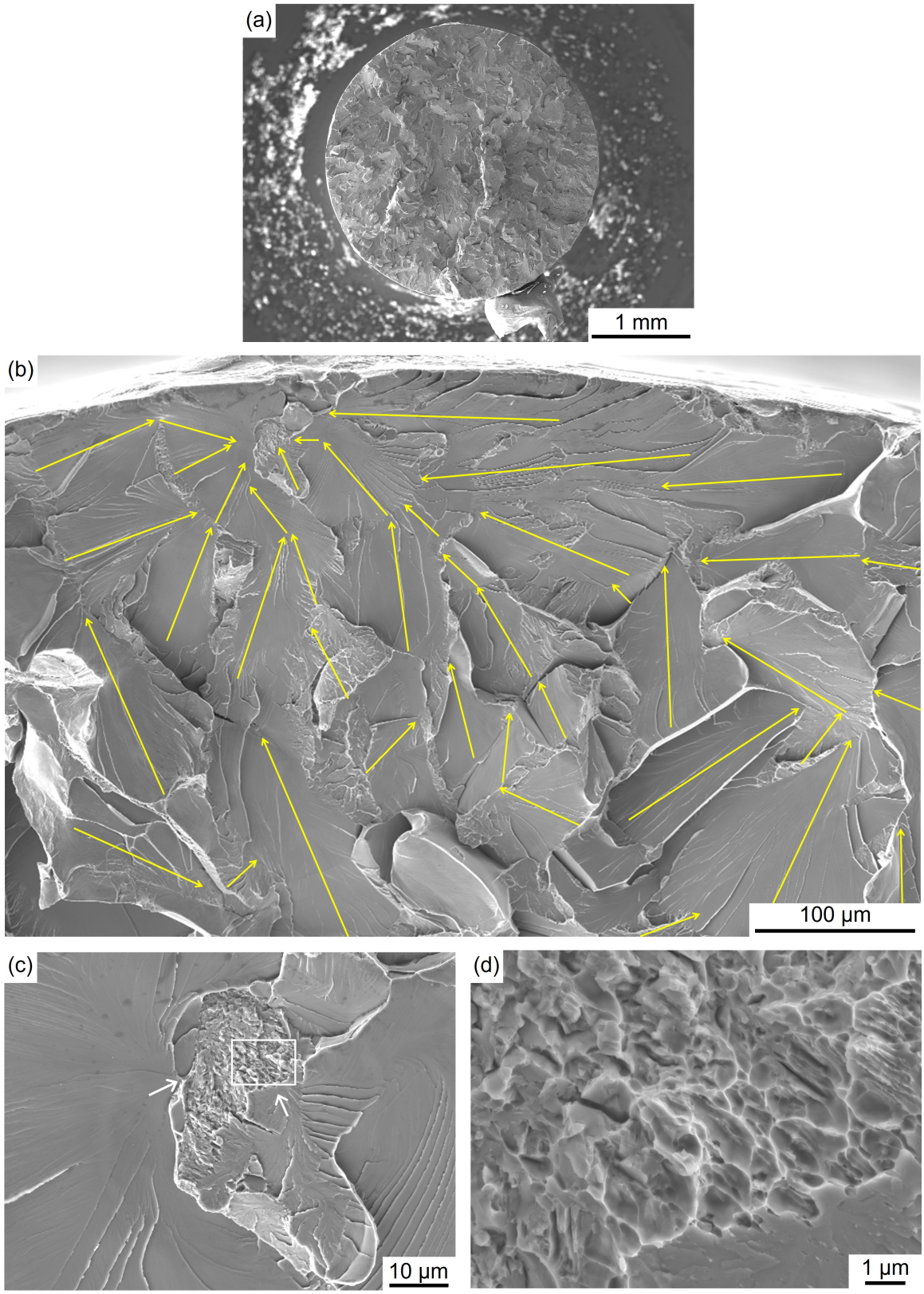


Fig. 4.6 An example of brittle fracture surface in the $\alpha + P$ microstructure, tested at -100 °C and 1×10^{-1}/s with fracture strain of 10.6 %, taken by various magnifications, with arrows indicating flow of the river patterns on the surface in (b). The river patterns on the surface are initiated exactly from the interface between ferrite and fine ductile fractured region in (c) and (d).

4.3.3 Cross-sectional observation

Figure 4.7 exhibits examples of cross-sectional observation for tested specimens with various fracture strains in ascending order of fracture strain. Here, the $\alpha+\theta$ microstructure was taken as an example because of the same tendency being recognised in the $\alpha + P$ microstructure too. Figure 4.7 (a) is the specimen with fracture strain of 1.6 %, tested at -100 °C and 1×10^0/s. Figure 4.7 (b) is the specimen with fracture strain of 7.6 %, tested at -50 °C and 1×10^{-1}/s. The first one can be thought of as the specimen in the lower shelf of the transition curve and the second in the lower region of the DBT, respectively. Almost no reduction in fracture surface area can be observed in either specimen. Figure 4.7 (c) is the image with fracture strain of 26.8 %, tested at -100 °C and 1×10^{-2}/s. Figure 4.7 (d) has fracture strain of 51.3 %, tested at 25 °C and 1×10^1/s. The specimen in Figure 4.7 (c) is in the upper region of the DBT, and the one in Figure 4.7 (d) is in the upper shelf of the transition curve. Reduction in area observed in Figure 4.7 (c) is much smaller than that in Figure 4.7 (d). However, unlike in the specimens with smaller fracture strain, gradual change in the diameter of the specimen's gauge part can be seen to some extent.

Figure 4.8 reveals cementite particles beneath fracture surfaces of tensile specimens tested in various conditions in the $\alpha + \theta$ microstructure, placed in ascending order of fracture strain. In the condition of complete brittle fracture, as shown in Figure 4.8 (a) - namely at the lower shelf of the transition curve - cracked cementite particles were hardly seen on the cross-sectional surfaces, as far as being observed. However, a number of cracked cementite were observed in the lower region of the DBT (fracture strain of 7.6 %), as shown in Figure 4.8 (b). As the testing temperature increased and became into the upper region of the DBT, such cementite cracks turned blocky, as

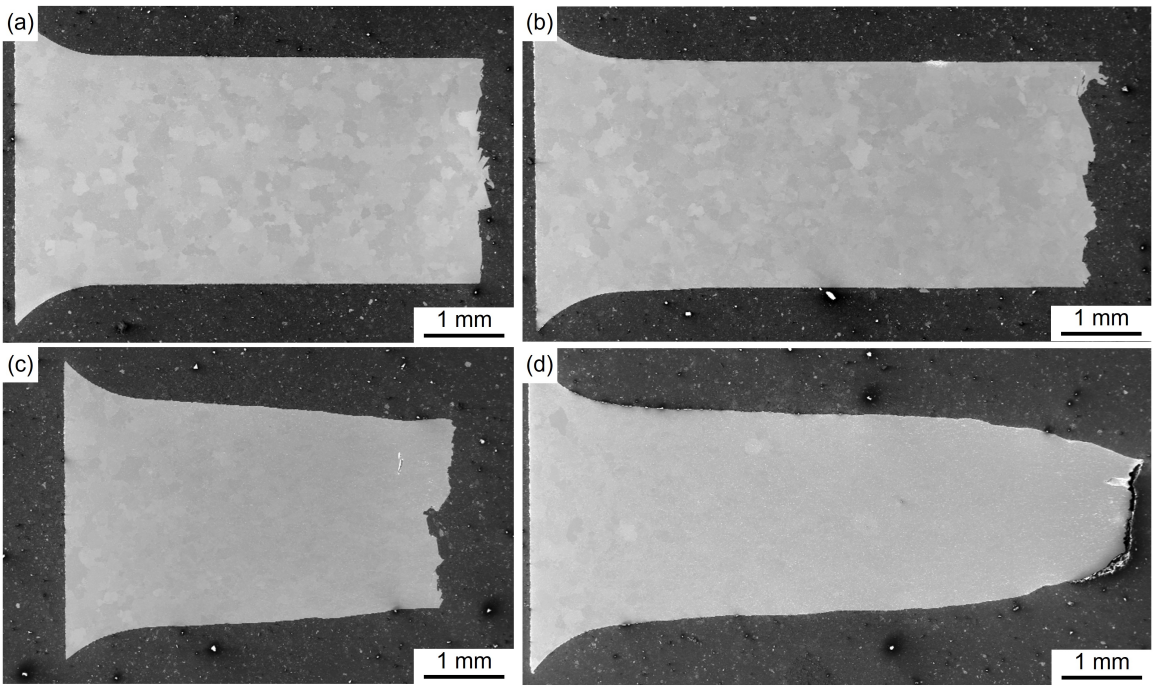


Fig. 4.7 Cross-sectional SEM images of tested specimens with low magnification in the $\alpha + \theta$ microstructure; (a) fracture strain of 1.6 %, tested at -100 °C and 1×10^0/s, (b) fracture strain of 7.6 %, tested at -50 °C and 1×10^1/s, (c) fracture strain of 26.8 %, tested at -100 °C and 1×10^{-2}/s, (d) fracture strain of 51.3 %, tested at 25 °C and 1×10^1/s. (a) is in the lower shelf, (b) is in the lower region of the DBT, (c) is in the upper region of the DBT, and (d) is in the upper shelf of the transition curve, respectively.

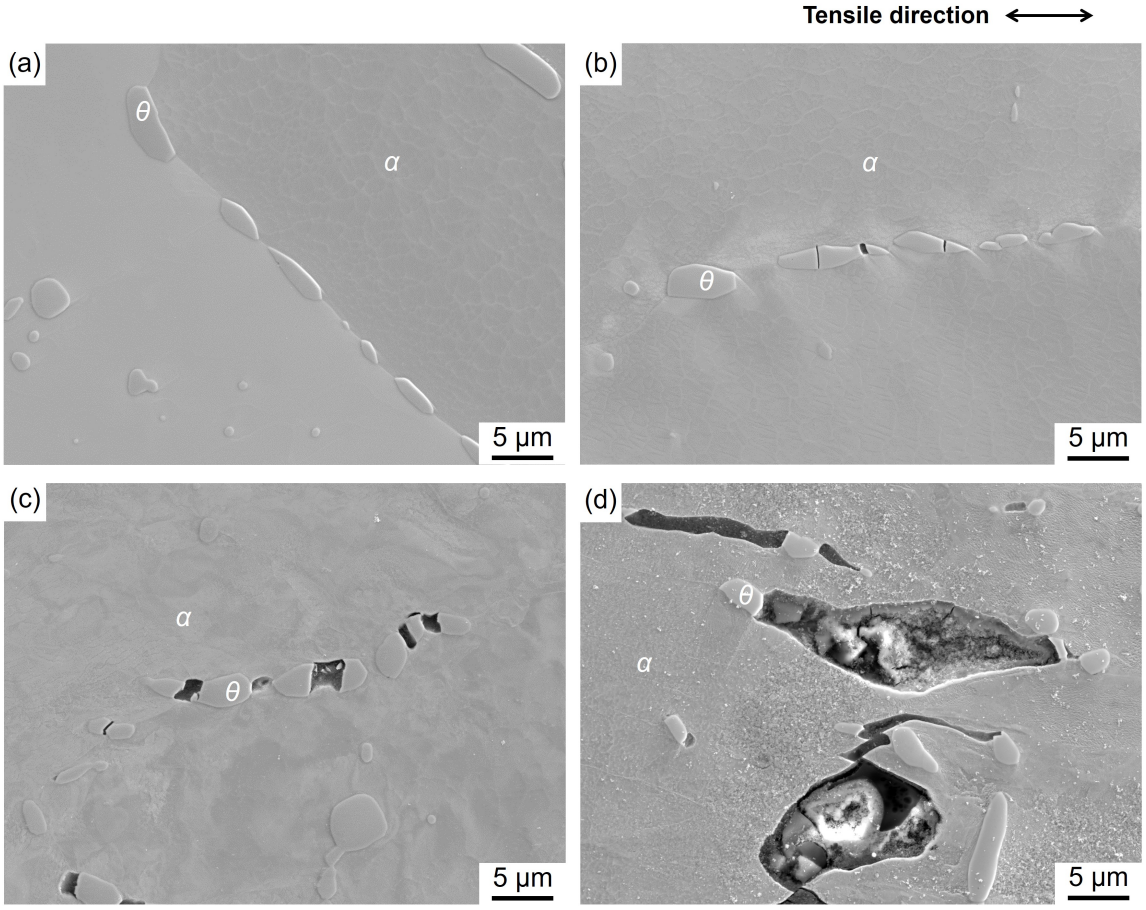


Fig. 4.8 Cross-sectional SEM images of cementite particles taken beneath the fracture surfaces of tested spesimens in the $\alpha + \theta$ microstructure; (a) fracture strain of 1.6 % with no crack in cementite, tested at -100 °C and 1×10^0/s, (b) fracture strain of 7.6 % with cracked cementite, tested at -50 °C and 1×10^1/s, (c) fracture strain of 26.8 % showing cracks looked blocky, tested at -100 °C and 1×10^{-2}/s, (d) fracture strain of 51.3 % indicating void growth and coalescence, tested at 25 °C and 1×10^1/s.

indicated in Figure 4.8 (c). Yet further deformation, void formation around cementite particles and its coalescence can be seen as shown in Figure 4.8 (d).

Figure 4.9 represents several ROIs in cross-sectional observation for the $\alpha + \theta$ microstructure. Figure 4.9 (a) shows arrested cracks with fracture strain of 1.6 %, tested at -100 °C and 1×10^0/s. The microcrack in the centre of the image seems to be arrested by grain boundary cementite particles. On the other hand, the cracks in the bottom right were arrested at ferrite grain boundaries, judging from surface

irregularities due to etching. Figure 4.9 (b) demonstrates another crack that was arrested at ferrite/cementite boundary. It appears that the crack has slightly entered the upper ferrite grain and was arrested, while it stopped at the boundary between the particle and the lower ferrite grain. Figure 4.9 (c) clearly shows how the three-dimensional structure of the fine dimpled structure, as shown in Figure 4.3 (d), manifests itself, meaning that the cementite particle is at the bottom of the dimple structure.

Figure 4.10 shows cross-sectional surfaces of ductile fracture specimens of the $\alpha + P$ microstructure tested at -100 °C and 1×10^{-2}/s with fracture strain of 46.6 % in (a), with fracture strain of 32.7 % in (b) (the same condition but different test), and tested at -100 °C and 1×10^{0}/s with fracture strain of 26.8 % in (c). Looking at the fracture surface in Figure 4.10 (a), elongated pearlite was found in the bottom of the "valleys" of the dimple-like structure, as indicated with arrows. This confirms the views that the fine ductile fracture surfaces found in Figure 4.5 (d) and Figure 4.6 (d) are the fractured pearlite phase. Figure 4.10 (b) and (c) captured just beneath the fracture surface. Some cracks were crossing over the pearlite area, and others stopped inside pearlite as shown by arrows in Figure 4.10 (b). In addition, cracks were observed along the interface between ferrite and pearlite as indicated by arrows in Figure 4.10 (c).

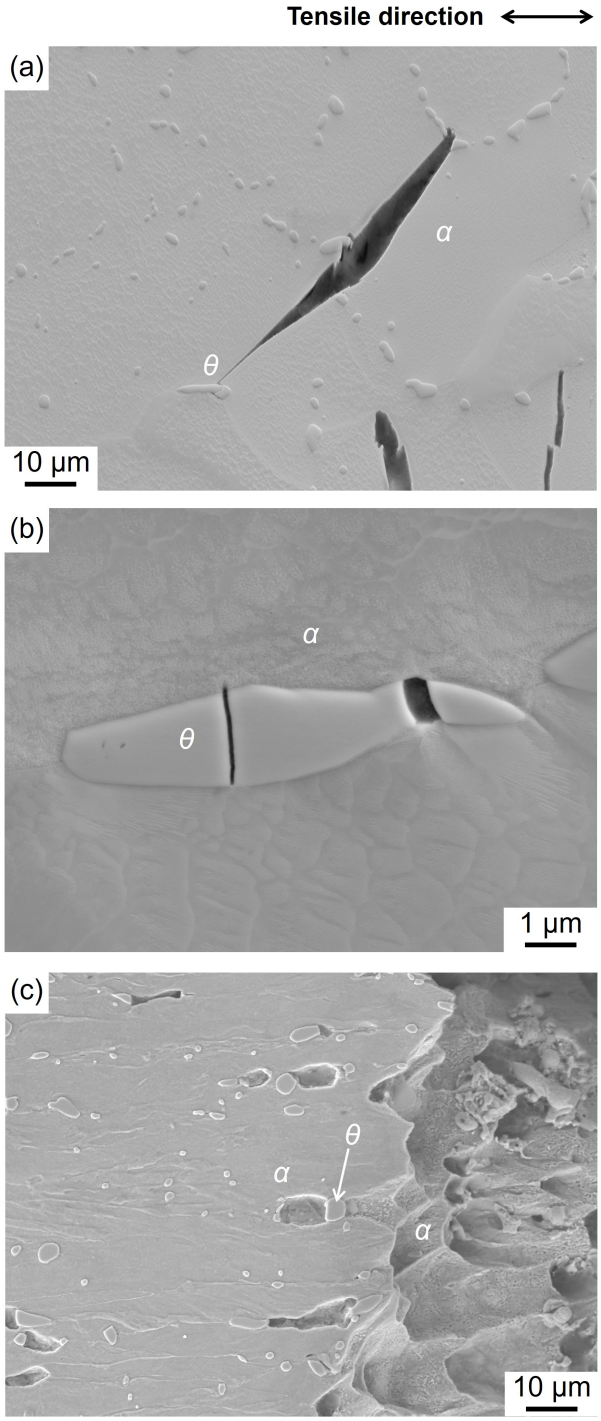


Fig. 4.9 Cross-sectional SEM images of ROIs in the $\alpha + \theta$ microstructure; (a) fracture strain of 1.6 % with crack arrest at grain boundary cementite, tested at -100 °C and 1×10^0/s, (b) fracture strain of 7.6 % with crack arrest at ferrite/cementite boundary, tested at -50 °C and 1×10^1/s, (c) fracture strain of 51.3 % with indicating how cementite particle is in the bottom of dimple on the ductile fracture surface, tested at 25 °C and 1×10^1/s.

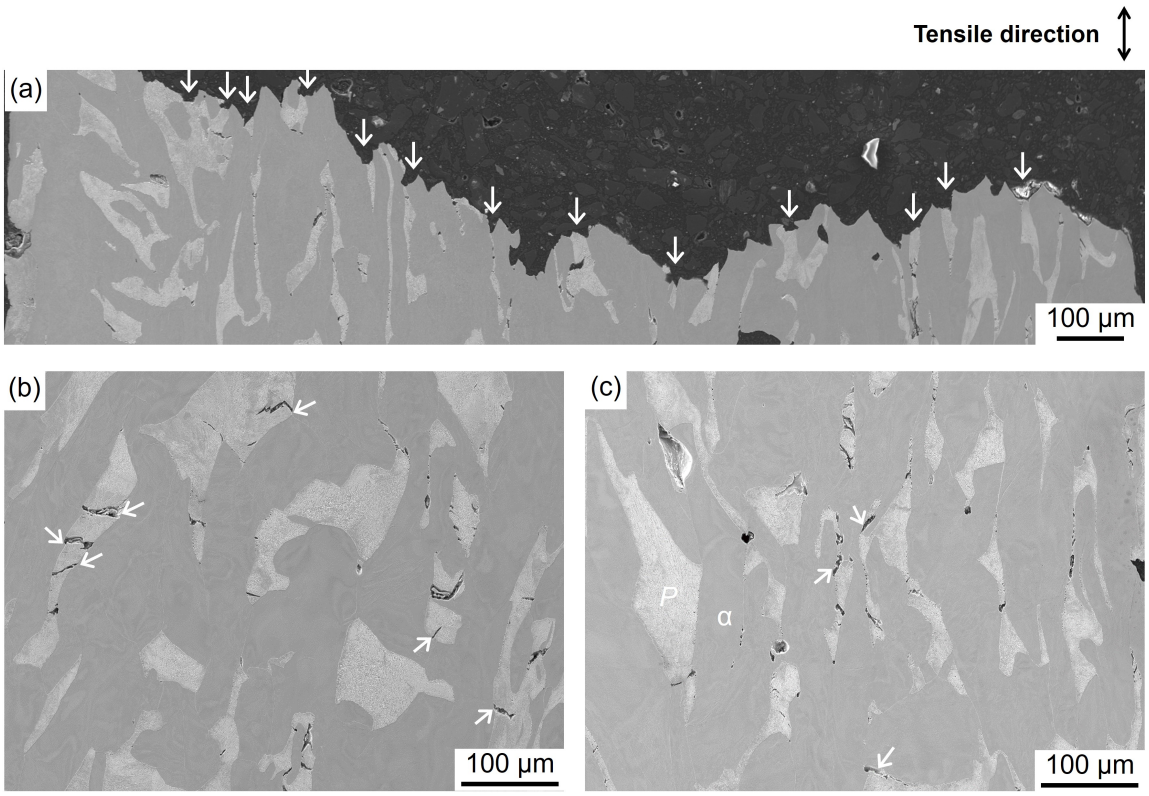


Fig. 4.10 Cross-sectional SEM images of ductile deformation and cracking in the $\alpha + P$ microstructure; (a) fracture strain of 46.6 %, tested at -100 °C and 1×10^{-2}/s, (b) fracture strain of 32.7 %, tested at -100 °C and 1×10^{-2}/s, (c) fracture strain of 26.8 %, tested at -100 °C and 1×10^{0}/s. As indicating with arrows, some cracks were ranging over pearlite, and others stopped inside pearlite in (b), and interfacial decohesion were also detected in (c).

Figure 4.11 demonstrates ROIs, especially deformed and fractured at the lower region of the DBT in the α+P microstructure. Figure 4.11 (a) shows arrested microcracks. The microcracks can be recognised in not only pearlite but also ferrite. Figure 4.11 (b) is a magnified image of a rectangle in (a), revealing that the crack propagated in a complex and zig-zag fashion in the pearlite. The crack changed its direction at the pearlite colony. Figure 4.11 (c) represents that microcracks are arrested at ferrite grain boundary. Figure 4.11 (d) indicates cracks ranging over pearlite colonies. Interestingly, in a particular pearlite colony where relatively clear and long cementite lamellae were observed, see in Figure 4.11 (e), voids were lined up in a straight. Figure 4.11 (f) is another image showing microcracks in a pearlite region. This image clearly shows that a crack can change its direction at the pearlite colony, with more straight cracks compared to Figure 4.11 (b) due to the lower fracture strain.

Figure 4.12 reveals cementite lamellae in the fracture surfaces tested in various conditions in the $\alpha + P$ microstructure. Figure 4.12 (a) shows neighbouring cracked cementite lamellae in the specimen fractured in the lower region of the DBT (fracture strain of 4.1 %). As shown in Figure 4.12 (b) with the specimen of fracture strain of 9.3 %, some cracked lamellae were shifted off each other, and micro-holes observed between lamellae appear to be etch-pits, implying the existence of a slip plane [227, 228]. A larger crack was observed in Figure 4.12 (c) in another area of the same specimen. In the specimen of fracture strain of 10.6 % shown in Figure 4.12 (d), cracks ranging over the pearlite colony were observed, and such pearlite cracks look more blocky in the upper region of the DBT.

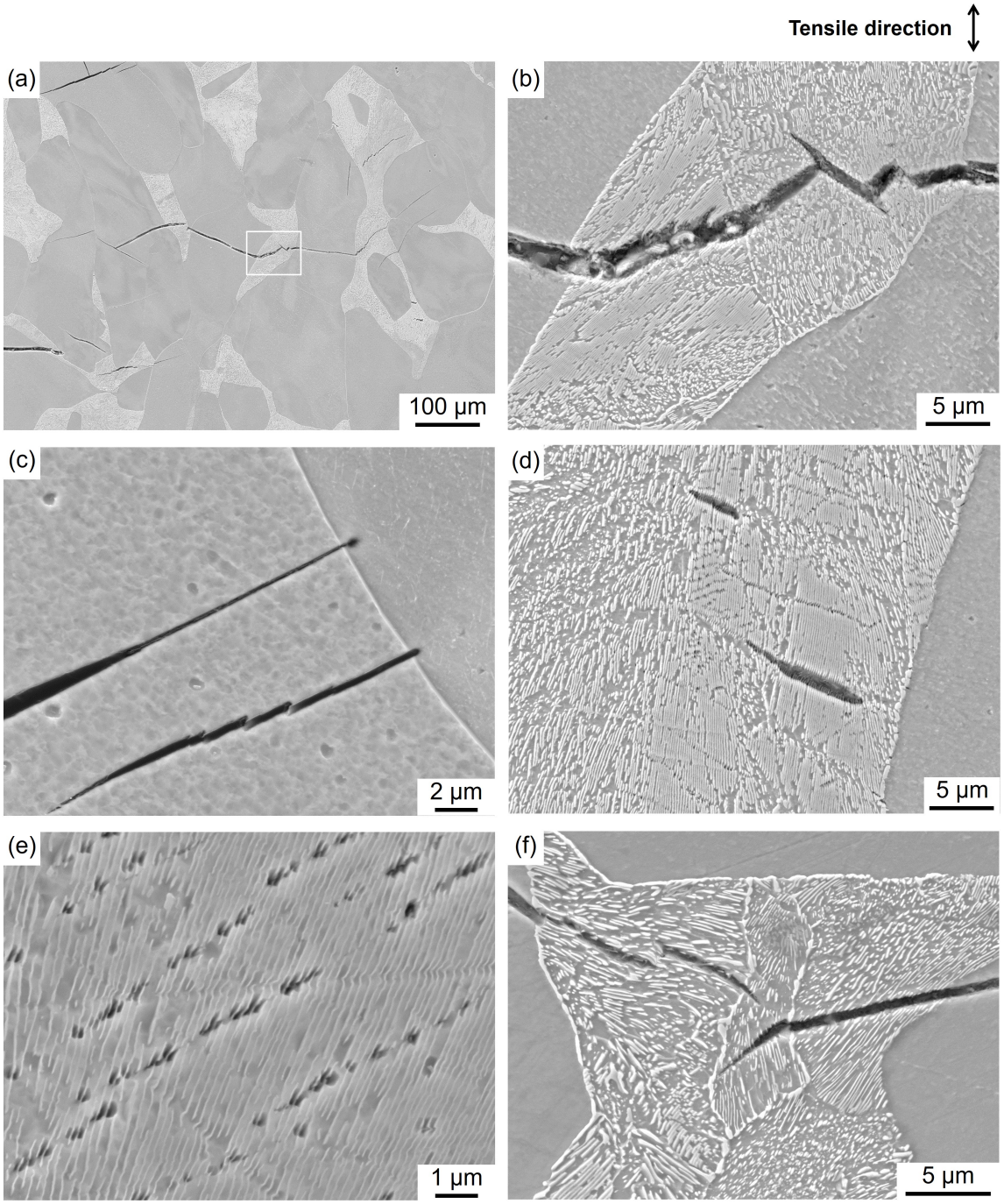


Fig. 4.11 Cross-sectional SEM images of ROIs in the $\alpha + P$ microstructure; (a), (b) and (c) fracture strain of 14.8 % with arrested microcracks in pearlite and ferrite, tested at -100 °C and 1×10^{-2}/s, (d) fracture strain of 10.6 % with cracks ranging over pearlite, tested at -100 °C and 1×10^{-1}/s, (e) fracture strain of 9.3 % with holes lined up in straight in particular pearlite area, tested at -100 °C and 1×10^{1}/s, (f) fracture strain of 3.2 %with microcracks in pearlite, tested at -100 °C and 1×10^{0}/s.

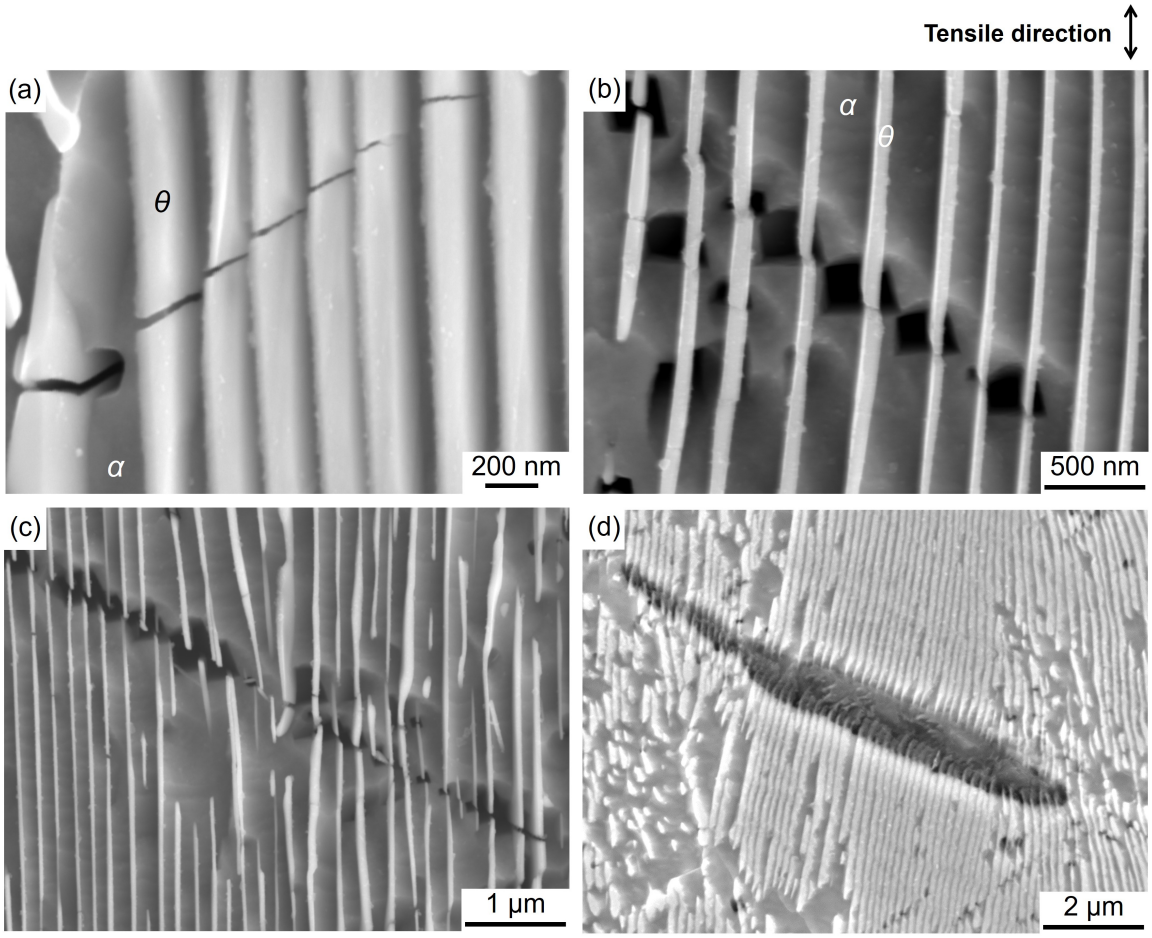


Fig. 4.12 Cross-sectional SEM images of cementite lamellae cracking, lamellae shifting, and formation of pearlitic cracking; (a) fracture strain of 4.1 % with neighbouring lamellae cracking, tested at -100 °C and 1×10^1/s, (b) fracture strain of 9.3 % with shifting off of the lamellae cracking, tested at -100 °C and 1×10^1/s, (c) fracture strain of 9.3 % with enlarged pearlite cracking, tested at -100 °C and 1×10^1/s, (d) fracture strain of 10.6 % showing pearlite colony-size cracking, tested at -100 °C and 1×10^{-1}/s.

4.4 Discussion

4.4.1 Deformation and fracture process in the lower region of the DBT in the $\alpha + \theta$ microstructure

The micromechanism of brittle fracture in the $\alpha+\theta$ microstructure has been investigated, and it is thought to be composed of three stages [21, 174, 175]. That is, stage 1: crack nucleation at cementite particles, stage 2: crack propagation into ferrite/cementite interface, stage 3: crack propagation into adjacent ferrite/ferrite interface. The findings presented in this chapter complement the proposed micromechanical process described above. As supported by Figure 4.4 (d), brittle fracture initiated from a cementite particle. In the test conditions where the specimen is completely brittle, once cementite is cracked, an unstable crack propagates all the way through the specimen. That is why cracked cementite particles were hardly observed in the cross-sectional surface as shown in Figure 4.8 (a). In contrast, in the lower region of the DBT, local plasticity was allowed to some extent before an unstable brittle crack propagates macroscopically. That is why cracks were arrested at ferrite/cementite interface (in Figure 4.8(b)) and at ferrite/ferrite interface (in Figure 4.9 (a)), corresponding to stop at stage 1 and at stage 2, respectively.

Regarding factors causing cementite cracking, it is revealed that macroscopic plastic strain plays a significant role [150–152]. The number of cracked cementite particles increased with increasing macroscopic plastic strain [22, 152]. Statistical analysis for the effect of particle size and morphology on cementite cracking is shown in Figure 4.13. Here, the cementite cracking ratio is defined as the ratio of the number of actually cracked cementite to the number of all cementite of a given size or aspect ratio. These

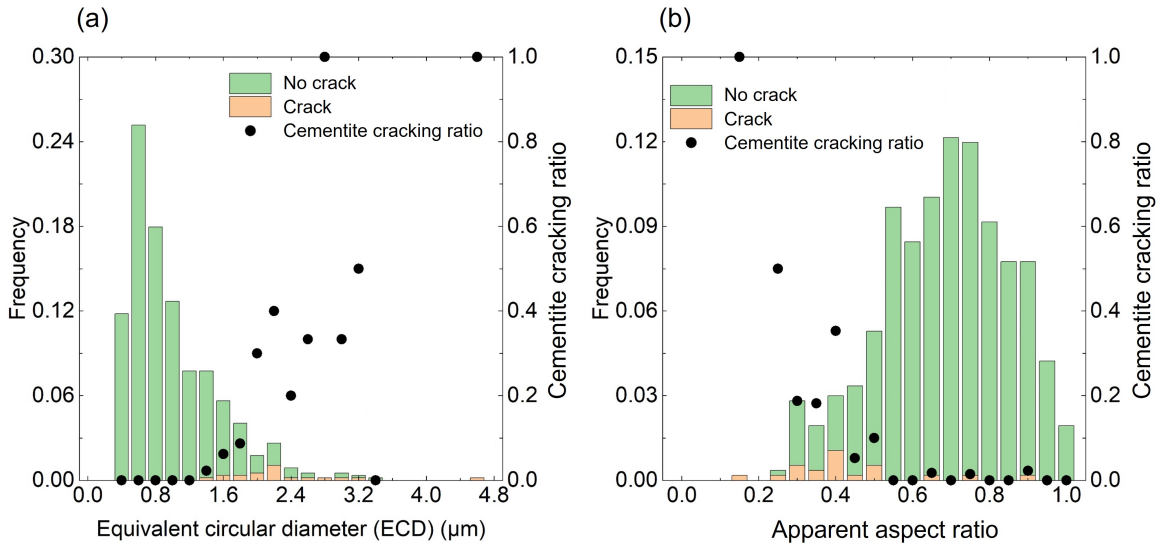


Fig. 4.13 The effect of apparent cementite particle size as equivalent circular diameter (a), and its morphology (apparent aspect ratio) (b) on cementite cracking rate. The cementite cracking ratio is defined here as the ratio of the number of actually cracked cementite to the number of all cementite of a given size or aspect ratio.

histograms reveal that larger cementites in size and more elongated ones in morphology are more likely to be cracked. This tendency of cementite cracking with particle size and morphology can be understood by the fibre loading mechanism [151]. According to this mechanism, the maximum stress applied in cementite particles becomes larger when its aspect ratio is bigger, which means more elongated morphology, and also when the shear stress in the ferrite matrix rises [151, 229, 230]. The reason for the crack ratio depending on particle size may be that larger particles tend to get much dislocation pile-up. Micromechanically, cementite cracking can occur when its internal stress exceeds its fracture stress. Hence, Figure 4.13 reveals that the internal stress of cementite becomes higher in larger and/or elongated cementite.

4.4.2 Deformation and fracture process in the lower region of the DBT in the $\alpha + P$ microstructure

Miller and Smith [159] proposed a mechanism for shear cracking in a pearlite colony based on optical microscopy; cementite lamella cracking is induced by ferrite slip followed by the development of shear zone causing further cracking in neighbour cementite lamellae, formation of micro-voids, its coalescence, and eventually a crack ranging over a pearlite colony. The set of images shown in Figure 4.12 seemingly supports this process.

A comparison between Figure 4.5 (d) and Figure 4.6 (d) gave an insight that in the $\alpha + P$ microstructure brittle fracture initiated from where pearlite failed in a ductile manner, at least, in the lower region of the DBT. In addition, as shown in Figure 4.10 (b) and (c) with the specimens fractured in the upper region of the DBT and the upper shelf of the transition curve, no cracks formed in the ferrite except for ferrite/cementite interface. On the contrary, arrested microcracks can be seen both in pearlite and ferrite in Figure 4.11. Taking these experimental results together with previous research, it is reasonable to conclude that pearlite fails first and forms cracks ranging over the region and next, unstable brittle cracks propagate to adjacent ferrite, resulting in macroscopic brittle fracture. Further characterisation with high-resolution electron microscope techniques, nevertheless, is required for confirmation of the deformation and fracture process of $\alpha + P$ microstructure in the DBT region.

4.4.3 Activation energy of the DBT in both microstructures

St. John [224] demonstrated that the DBTT and strain rate have a strong correlation, and that there is a relationship between strain rate and the DBTT. It is known

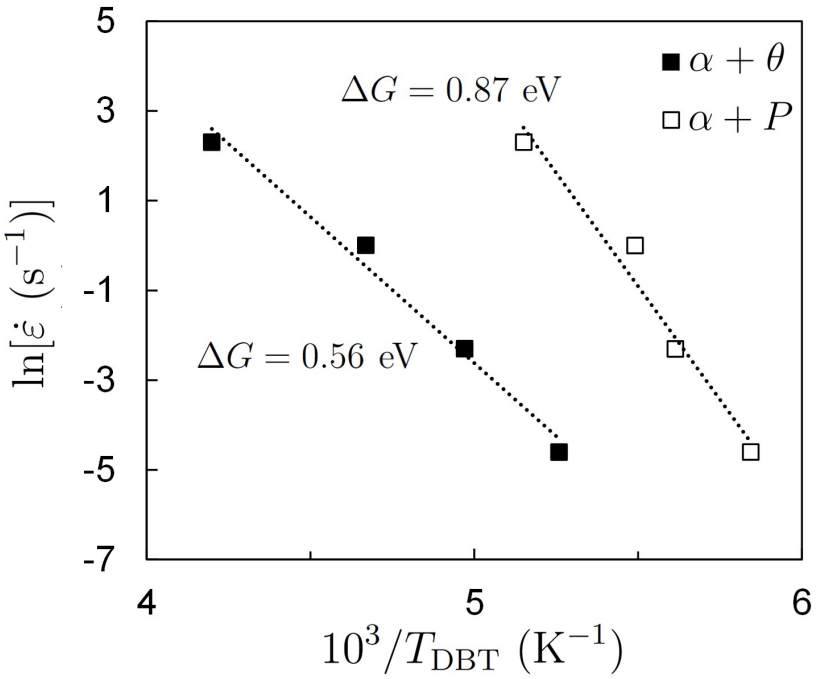


Fig. 4.14 Arrhenius plot of the strain rate versus the DBTT reciprocal for the two microstructures.

empirically that the following Arrhenius-type equation can express the DBTT T_{DBT};

$$\dot{\varepsilon} = \varepsilon_0 \exp\left(\frac{-\Delta G}{k_{\mathrm{B}} T_{\mathrm{DBT}}}\right) \tag{4.2}$$

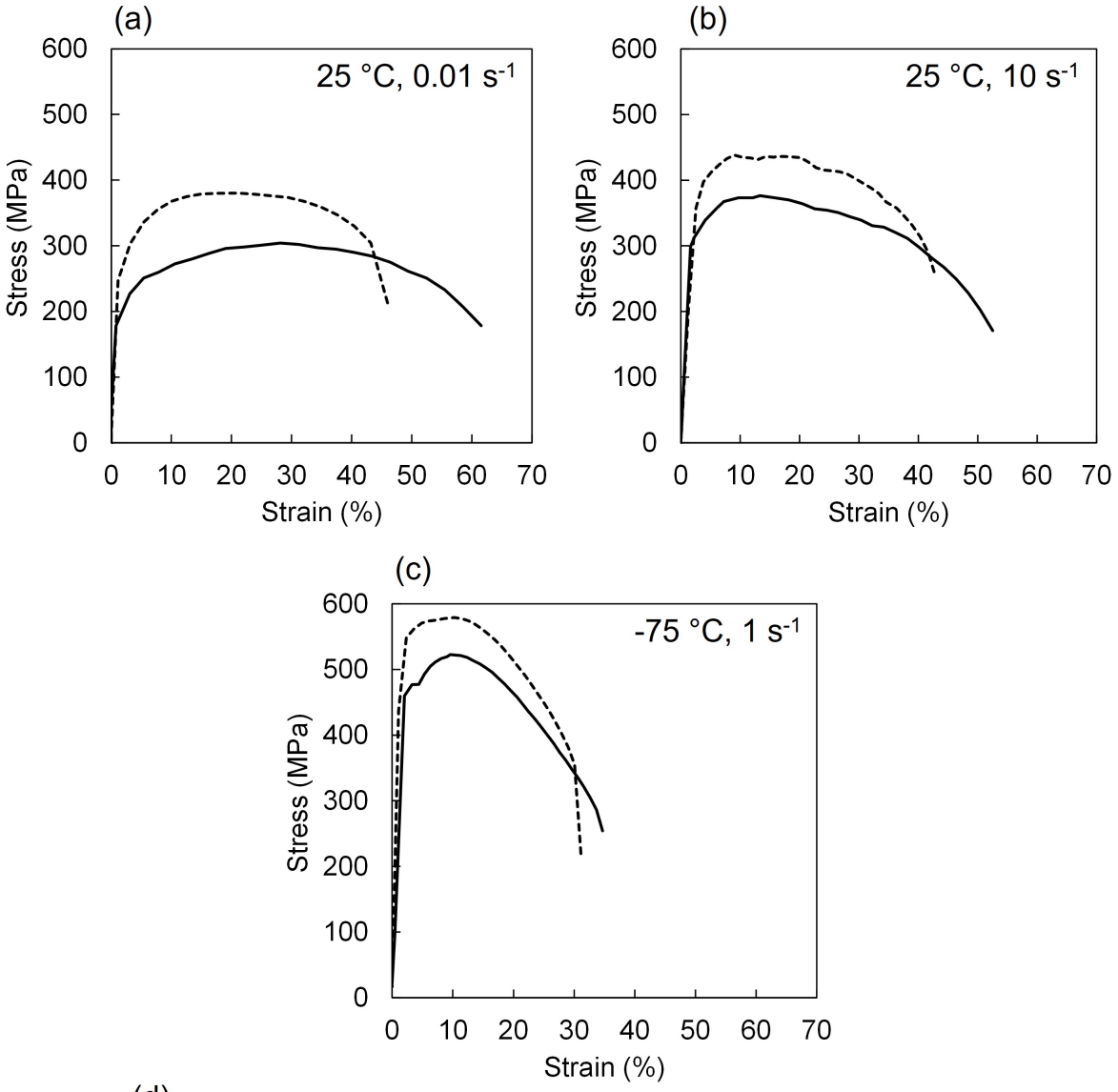
where $\dot{\varepsilon}$ is strain rate, ΔG is an activation energy of the DBT process, k_{B} is the Boltzmann constant, and ε_0 is a constant. This approach was first studied in a single crystal of silicon, sapphire, and BCC metals like tungsten and iron [231–234], but was later applied to polycrystalline BCC metals [235–237]. Figure 4.14 shows the Arrhenius plot of the DBTT reciprocal and logarithm of strain rate. From the relationship in Equation 4.2, the activation energy was calculated from the slope of the line in the graph, which is 0.56 eV (9.0×10^{-20} J) for the $\alpha + \theta$ microstructure and 0.87 eV (1.4×10^{-19} J) for the $\alpha + P$ microstructure, respectively.

Effectiveness of using fracture strain to define DBTT

In this study, the temperature at which the fracture strain of the upper shelf is half was defined as the DBTT. If the macroscopic ductility of the two tested microstructures, i.e., the ratio of uniform strain and non-uniform strain, are markedly different, it cannot be denied overestimating (underestimating) the DBTT. Therefore, the engineering stress-strain curves of tested specimens that ductile-fractured were compared. Figure 4.15 (a), (b), and (c) show examples of the stress-strain curves with several test conditions. Comparing the two microstructures, the $\alpha + \theta$ microstructure has lower yield strength and ultimate tensile strength and larger fracture strain in all conditions than those of the $\alpha + P$ microstructure's. Figure 4.15 (d) indicates total (fracture) strain, uniform strain, non-uniform strain, and their ratio to total strain. There was no significant difference in the ratio of uniform strain and non-uniform strain between the two microstructures. From this, it can be considered that the evaluation error described above is limited.

There are several ways to define the DBT. According to ISO148-1 [238], the standard for the Charpy impact testing method, there is no universal definition that can be applied to all cases, and one of the following methods is considered to be effective; the temperature at which the brittle fracture surface area ratio is 50 %, the temperature at which the absorbed energy is half that of the upper shelf, and the temperature at which the absorbed energy is 27 J.

Figure 4.16 shows the fracture surface of the specimen with $\alpha + \theta$ microstructure shown in Figure 4.15 (c). Although it is difficult to quantify the brittle fracture surface ratio, it can be determined from the result of the fracture strain curve that the fracture strain of this test condition is reduced by about 30 % from the upper



(d)

Test conditions			Total strain (%)	Uniform strain		Non-uniform strain	
				Value (%)	Ratio (%)	Value (%)	Ratio (%)
(a)	25 °C, 0.01 s^{-1}	$\alpha + \theta$	61.6	28.1	45.6	33.5	54.4
		$\alpha + P$	46.1	21.8	47.3	24.3	52.7
(b)	25 °C, 10 s^{-1}	$\alpha + \theta$	52.5	13.3	25.3	39.2	74.7
		$\alpha + P$	42.9	10.4	24.2	32.5	75.8
(c)	-75 °C, 1 s^{-1}	$\alpha + \theta$	34.7	9.6	27.7	25.1	72.3
		$\alpha + P$	31.3	10.2	32.6	21.1	67.4

Fig. 4.15 Examples of the engineering stress-strain curves with several test conditions; (a) tested at 25 °C and 1×10^{-2}/s, (b) tested at 25 °C and 1×10^{1}/s, (c) tested at -75 °C and 1×10^{0}/s. (d) is a summary of total (fracture) strain, uniform strain, non-uniform strain, and their ratio to total strain in each curve.

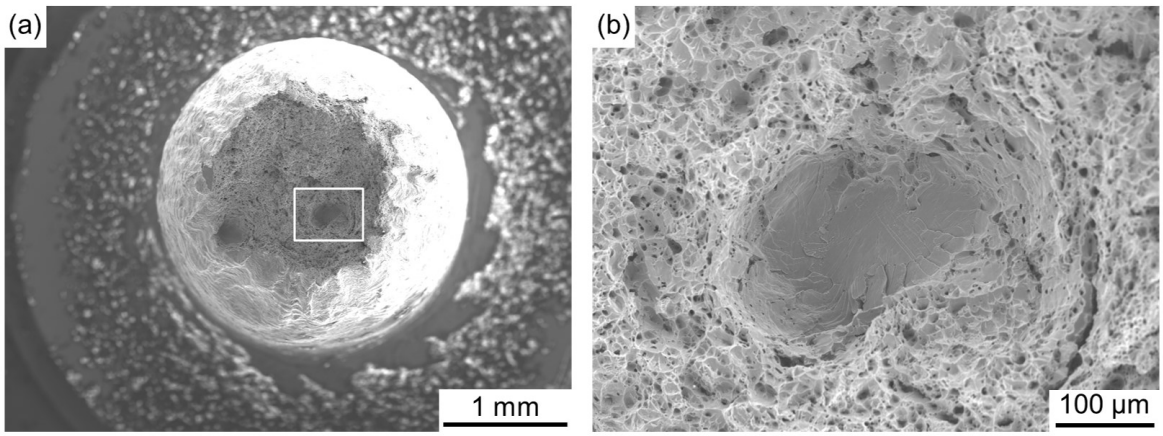


Fig. 4.16 The fracture surface of the specimen with $\alpha + \theta$ microstructure, tested at -75 °C and 1×10^0/s, as shown in Figure 4.15 (c). (b) is a magnified image of a rectangle in (a). It is obvious that the brittle fracture surface ratio to the initial cross-sectional area of the gauge part has not reached even 30 %. On the other hand, from the result of the fracture strain curve, the fracture strain of this test condition is reduced by about 30 % from the upper shelf (from 51.4 % to 34.7 %).

shelf of fracture strain (from 51.4 % to 34.7 %), but the brittle fracture surface ratio has not reached even 30 %. Therefore, it is suggested that if the transition curve is defined by the brittle fracture surface ratio, the transition curve may shift to the lower temperature side, resulting in a lower DBTT, at least $\alpha + \theta$ microstructure. As the property of "toughness" of steel, it should be better that the transition between ductility and brittleness is judged by a parameter related to energy. Evaluation using other definitions recommended in the standard above and improvement of the experimental methodology are future work.

Meaning of activation energy and its difference

Previous studies on Equation 4.2 have shown that the DBT activation energy is almost equal to the activation energy of dislocation motion at that temperature [236]. More specifically, it is known that the activation energy correlates well with the enthalpy of kink pair formation of screw dislocations [239]. From this, it was pointed out that

the DBT is rate-controlled by dislocation motion in metal. However, it should be noted that these experiments were all performed on single-crystal single-phase material. In that case, it can be said that the mobility of dislocations at the crack tip is the rate-controlling process of DBT. However, this type of analysis may be less accurate in polycrystalline practical steels. This is because there are grain boundaries and secondary phases. Grain boundaries and cementite could be barriers to dislocation motion, restricting the movement of dislocations [239]. The discussion should be made with this in mind.

Based on what is discussed in the previous subsection about the validity of the DBTT definition, it is not easy to compare the obtained DBTTs for the two microstructures with relating to activation energies. Having said that, here, the activation energy will be qualitatively discussed with the obtained DBTTs in the experiment.

Phenomenologically, a high activation energy for the transition means that the initiation and propagation of unstable cracks are relatively less likely to occur. It may be about the capability of plastic deformation guaranteed until macroscopic brittle fracture. Although detailed characterisation is needed, as shown in Figure 4.11 and Figure 4.12, it seems that cracks form with a certain degree of plastic deformation corresponding to the substructure of pearlite in the $\alpha + P$ microstructure. If this is the case, it can be regarded that the fine lamellar structure of the pearlite phase functions virtually to refine the microstructure in terms of resistance to brittle crack initiation and propagation. The macroscopic strength of $\alpha + P$ microstructure is higher due to the presence of pearlite phase compared to $\alpha + \theta$ microstructure. At the same time, the microscopic fracture stress of the pearlite part could also increase. As a result, it

could be explained that a certain degree of plastic deformation (fracture strain) is seen in the temperature range where cleavage fracture occurs in $\alpha + \theta$ microstructure.

The activation energy of the DBT in pure iron and 0.02 wt%C steel is reported to be 0.33 eV for single crystal iron and 0.21 eV for polycrystalline iron [235], and 0.2 to 0.25 eV for 0.02 wt%C steel, respectively [240]. In the previous study on 0.02 wt%C steel, the microstructure of the test specimen was not mentioned, but judging from the carbon content, the cementite fraction is extremely low compared to that of this study, and the primary phase is thought to be ferrite. In addition, since the activation energy value is almost in the same range as that of pure iron, the controlling step of the DBT is thought to be dislocation glide in ferrite.

On the other hand, the value of 0.56 eV obtained in this study for the $\alpha + \theta$ microstructure is about twice as high as those of pure iron. In this case, it might be considered that the activation energy for the DBT is no longer guaranteed to be equal to that of dislocation motion in ferrite but rather that to be the height of the transition barrier in the rate-controlling process corresponding to the deformation and fracture process of each microstructure. It is assumed that due to the presence of cementite equivalent to the amount of carbon of 0.2 wt% the transition is not determined solely by the dislocation motion at the crack tip in the ferrite phase, but with the influence of cementite such as the crack nucleation on cementite particles and its propagation into the ferrite matrix.

In the $\alpha + P$ microstructure, the activation energy value was even larger and was close to the value previously reported for full pearlite steel [241]. This suggests that the deformation of pearlite is influential to the process. This inference seems to be in good agreement with the experimental results we saw in the lower transition region, as shown

in Figure 4.6 and Figure 4.12. In other words, it is presumed that the deformation of cementite, which is less likely to occur, could also contribute.

A high activation energy means the barrier to the transition between brittleness and ductility is significant and is less likely to occur. Comparing the activation energies in both microstructures, $\alpha + P$ microstructure indicated a higher value than $\alpha + \theta$ microstructure. This might be due to the more complicated microstructure of pearlite and its restriction towards deformation compared to the spheroidised θ microstructure. However, an additional investigation using high-resolution characterisation techniques is required for further confirmation.

4.5 Summary and Conclusions

In this chapter, tensile tests and subsequent thorough post-mortem characterisation by SEM were presented, for a single steel but with two very different microstructural conditions across a wide range of temperatures and strain rates. The following specific conclusions can be drawn:

1. The $\alpha + \theta$ microstructure showed relatively clear and steep change in fracture strain with temperature and strain rate in the transition range, while the $\alpha + P$ microstructure was less sensitive to them, consistent with a gradual variation with the wider transition range.

2. For the $\alpha + \theta$ microstructure, what has been shown in this chapter complements the proposed micromechanism of deformation and fracture process. Brittle fracture initiated from cementite particles. In the test conditions where the specimen is completely brittle, once cementite is cracked, an unstable crack

propagates all the way through the specimens. On the contrary, in the lower region of the DBT, local plasticity occurs to some extent before an unstable brittle crack propagates.

3. In the $\alpha + P$ microstructure, brittle fracture initiated from where pearlite failed in a ductile manner, at least, in the lower DBT region. It is thought that pearlite fails first and forms cracks across the region, and then an unstable brittle crack propagates to the adjacent ferrite, resulting in macroscopic brittle fracture.

4. Statistical analysis for cracked cementite indicated that larger cementite in size and more elongated ones in morphology are likely to be cracked, and implied that the internal stress of cementite caused by local plasticity easily became higher in larger and/or elongated cementite.

5. The activation energy of DBT in the $\alpha + \theta$ microstructure is higher than that for pure iron or low carbon steel. This suggests that only simple dislocation glide in ferrite is not a decisive factor, but the effect of microstructure, the deformation and fracture of cementite particles and/or further crack propagation into adjacent ferrite grains strongly depends on the rate-controlling process. The activation energy of the DBT in the $\alpha + P$ microstructure is similar to the reported value in fully pearlitic steel. This probably indicates that the deformation of pearlite, including cementite plasticity, has a significant impact on the controlling process for the DBT even though there is much more ferrite phase in the tested steel than in fully pearlitic steel.

Chapter 5

Local Plasticity Preceding Macroscopic Fracture in the Lower Region of the DBT Detected by High-Resolution Characterisation Techniques

5.1 Introduction

The deformation and fracture process in the DBT region can be regarded as a process in which local plastic deformation proceeds to some extent before an unstable brittle crack initiates and propagates in a macroscopic scale. Under such circumstances, it is vital to clarify how the cementite morphology has an influence on local plasticity and, finally, the mechanical properties. Moreover, with an emphasis on the micromechanisms of

deformation and fracture themselves too in the DBT region of spheroidised cementite and pearlite, a fundamental study is required to obtain a more detailed and clear understanding of the effect of microstructures. Particularly, it is on the elastic and plastic deformation of cementite, its interaction with the ferrite matrix before crack initiation, and the fracture plane of cementite that we need to build up more empirical knowledge.

There are various types of techniques for measuring elastic strain fields [242–244]. However, the methodology making use of SEM-EBSD is advantageous in terms of high spatial resolution and high strain sensitivity, and, unlike TEM-based methods, it does not require thinning of specimens, which causes no relaxation of the elastic field due to the thinning process [24]. Wilkinson et al. [28, 29] have developed the precise method of evaluating lattice rotation and elastic strain rotations with EBSD patterns at 0.01 $^\circ$ angular sensitivity and 1×10^{-4} strain sensitivity, respectively. This method is to measure image shifts in the position of zone axes and other features in the EBSD patterns between a reference and testing points by cross-correlating many ROIs in the diffraction pattern, generating a displacement gradient tensor between the two, then calculating elastic strain and lattice rotation tensors. More details of the procedure should be referred to the related papers [217–219]. Furthermore, through Nye's work on dislocation tensor [245], GND density can be estimated with the lattice curvature derived from EBSD observations. Details of this procedure can be found in the work of Wilkinson et al. [246].

The research activity for the deformation and fracture process of ferrite and pearlite microstructure in the DBT region is not as intensive as that for ferrite and spheroidised cementite microstructure, which is a simpler microstructure. One reason for this is the

complex and hierarchical microstructure of pearlite. Very limited work has primarily focused on fully pearlitic steels, and studies on ferrite and pearlite dual-phase steels are even fewer. The difficulty in the characterisation of pearlite microstructure lies in the fact that it is required to deal with a broader length scale. It is necessary to observe from ferrite and pearlite grains of tens to hundreds of micrometres, pearlite blocks and colonies of the substructure being of a similar size, to the ferrite/cementite lamellar structure of submicrometre or nanometre-scale. To put another way, characterisation over a wide length scale from sub-milli to sub-micrometre-scale is considered to be effective in understanding its behaviour. Based on this perspective, the methodology used in this study is SEM-based TKD. Using a SEM and its equipment, including an EBSD detector, it is possible to observe the microstructure and acquire crystallographic information. Keller et al. [30] established the acquisition of EBSD patterns using a transmission electron beam in 2012. This is a relatively new characterisation technique named transmission Kikuchi diffraction (TKD) or transmission-electron backscatter diffraction (t-EBSD). This method is SEM-based and is thought to be suitable for observation on a wide length scale of pearlite microstructures. Since crystallographic orientation analysis is also possible at the same time, it can also be used to analyse the crystal orientation relationship of pearlite, which is still open to debate.

This chapter focuses on the lower part of the DBT region where a certain degree of plastic deformation occurs before the macroscopic cleavage fracture. The objectives are two-fold; (i) to clarify the elastic and plastic deformation of cementite, its interaction with the ferrite matrix before crack initiation, and the fracture plane of cementite experimentally, and (ii) to understand the deformation and fracture process of pearlite, which has a complicated and hierarchical microstructure and hence has not been well

characterised and modelled. For this, with test specimens obtained in a series of tensile tests in Chapter 4, HR-EBSD cross-correlation analysis is used to analyse the local deformation around and inside cementite particles with the $\alpha + \theta$ microstructure. TKD is performed to observe the initial deformation and analyse the crystallographic information in the $\alpha + P$ microstructure.

5.2 Experimental methods

5.2.1 Materials

The test specimens used in this chapter were carefully designed steels with the same chemical composition (Table 3.1) but different cementite morphology. They were used to investigate the DBT behaviour in Chapter 4, and termed the $\alpha + \theta$ microstructure and the $\alpha + P$ microstructure, respectively. For more details, see Chapter 3.

Uniaxial tensile tests were operated with various temperatures and strain rates to reveal the DBT behaviour in each microstructure. The details of the experimental procedure should also be referred to Section 3.3.1 and Section 4.2.2. Based on the DBT curves obtained in the series of tensile tests, test specimens corresponding to the lower region of the DBT were selected for subsequent characterisation.

5.2.2 Characterisation

SEM

The cross-sectional surfaces of the selected specimens were observed by ZEISS Merlin FEG-SEM. The details of the experimental procedures should be referred to Section 3.4.1.

HR-EBSD

In order to analyse local deformation around and inside cementite particles in the $\alpha+\theta$ microstructure, HR-EBSD cross-correlation analysis was applied [28, 29]. For more details, see also Section 3.4.2. Single crystal elastic constants are needed to separate the normal strains by imposing the condition that the normal stress perpendicular to the sample surface is zero [29]. For ferrite, elastic constants are well-established, but there is more uncertainty for cementite. The values used are given in Table 5.1 [123].

Table 5.1 Elastic constants of single crystal cementite adopted in this study [123].

(GPa)

C_{11}	C_{22}	C_{33}	C_{12}	C_{13}	C_{23}	C_{44}	C_{55}	C_{66}
385	341	316	157	162	167	13	131	131

Through Nye's work on dislocation tensor [245], GND density can be estimated with the lattice curvature derived from EBSD observation. Burgers vectors and line directions for dislocation types supporting the observed lattice curvature need to be specified. The analysis is more important for the ferrite where the well-established pure screw and edge dislocations described in the reference of [246] were used. Much less plasticity is expected in the cementite for which the dislocation types were assumed as (001)[100], (100)[010], (100)[001], (010)[001], and (010)[100] in the analysis [135, 216].

SEM-based on-axis TKD

For more localised and detailed characterisation of the $\alpha+P$ microstructure, SEM-based on-axis TKD method was applied with the ZEISS Merlin FEG-SEM system [220]. Thin foils for TKD analysis were prepared from the tensile specimens fractured

at the lower region of the DBT by the ZEISS Crossbeam FIB method, owing to the observation of a particular area of the microstructure. For more details, Section 3.4.3 should be referred to.

5.3 Results

5.3.1 HR-EBSD analysis for spheroidised cementite microstructure

Cementite cracking

EBSD investigated the directions of cracks in cementite particles. Figure 5.1 shows four cracked cementite particles as examples observed in the specimen of fracture strain of 7.6 %, tested at -50 °C and 1×10^1/s. Figure 5.1 (a1), (b1), (c1), and (d1) are SEM images. Figure 5.1 (a2), (b2), (c2), and (d2) are EBSD inverse pole figure (IPF) maps. Figure 5.1 (a3), (b3), (c3), and (d3) show EBSD pattern quality maps with $(010)_\theta$ (red) and $\{101\}_\theta$ (blue) plane traces of cementite. Out of nine cementite particles, the crack direction matched well with $(010)_\theta$ plane trace in five particles, with $\{101\}_\theta$ in two, and the other two were ambiguous between $(010)_\theta$ and $\{101\}_\theta$ so that these plane traces are very close to each other.

Elastic stress distribution

Elastic stress distribution in the ferrite matrix and cementite particles at the early stage of deformation and fracture processes were calculated by the cross-correlation analysis based on HR-EBSD measurement with the specimen of fracture strain of 1.6 %, tested at -100 °C and 1×10^0/s. For the HR-EBSD data, some uncertainty remains

on the absolute stress value due to the unknown stress at its reference point, but the analysis using its variation can be done. One way to dilute this issue is to calculate the mean stress for the region associated with each reference pattern (ie grain) and plot the maps as variations from these mean values. This gives insights into the range of stress variation over each ferrite or cementite grain, and such distributions can be comparable between grains. The results are shown in Figure 5.2 with elastic stress components of σ_{11}, σ_{22}, and σ_{12}. White lines indicate phase and grain boundaries. Elastic stress was accumulated in the matrix close to cementite particles. In cementite, the stress was not distributed homogeneously but exhibited significant variation, even within a particle. Some particles had much larger stress variations than others. This suggests that the local stresses were high there, which would come from the high rigidity of cementite.

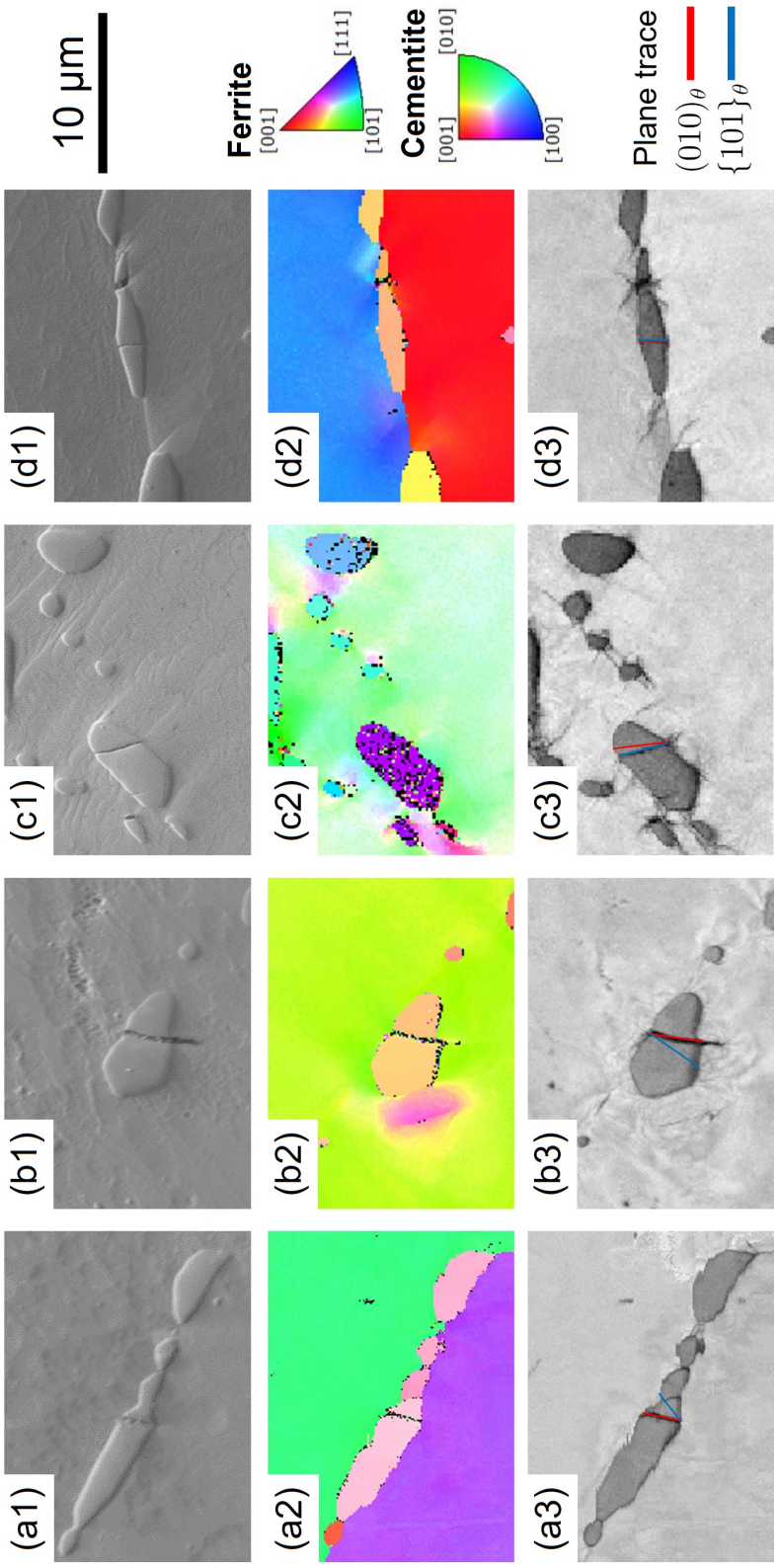


Fig. 5.1 Cracked cementite plane trace analysis with the specimen of fracture strain of 7.6 %, tested at -50 °C and 1×10^1/s; (a1) to (d1) SEM images, (a2) to (d2) EBSD IPF maps of the same region, (a3) to (d3) EBSD image quality maps with cementite $(010)_\theta$ plane trace by red line, and $\{101\}_\theta$ plane trace by blue line, respectively.

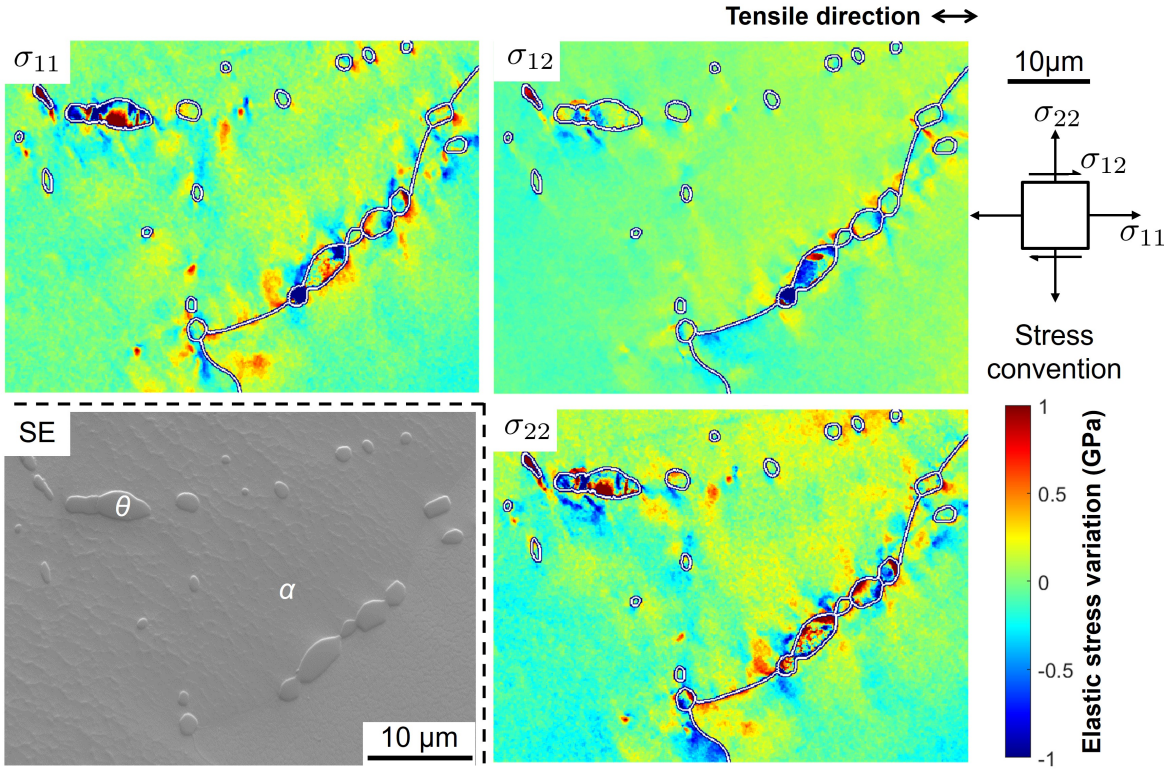


Fig. 5.2 The distribution of elastic stress variation in the ferrite matrix and cementite particles at the early stage of deformation calculated by the cross-correlation analysis based on HR-EBSD measurement with the specimen of fracture strain of 1.6 %, tested at -100 °C and 1×10^0/s. The results are shown with a corresponding SEM image, and stress components of σ_{11}, σ_{22} and σ_{12}.

GND density

GND density distributions, obtained from the cross-correlation analysis, in the ferrite matrix of different specimens are shown in Figure 5.3. No GND density concentration can be observed in the undeformed specimen as shown in Figure 5.3 (a). In contrast, once specimens were deformed, GND was accumulated around cementite, being indicated in Figure 5.3 (b) and (c) (fracture strain of 1.6 % tested at -100 °C and 1×10^0/s, and 7.6 % tested at -50 °C and 1×10^1/s, respectively). It can be seen that there are higher GND density lines with the direction from left-bottom to right-top in the

specimen shown in Figure 5.3 (c). This direction is almost parallel to the $\{110\}_\alpha$ plane trace of the ferrite matrix. Moreover, the lines are interfered with the cementite particles. This image clearly shows dislocation pile-up at cementite particles, which resulted in strain, hence stress, concentration in the ferrite matrix around cementite, and the increase of internal stress of cementite.

Average GND density around and away from cementite particles in different specimens is demonstrated in Figure 5.4. The value of average GND density around particles is calculated by averaging GND density over the ferrite matrix whose distance to any particle is within 1 μm. This graph indicates the relationship between macroscopic fracture strain and average GND density at each specimen. Average GND density away from cementite particles did not change drastically as macroscopic fracture strain increased. By contrast, the one around cementite experienced a significant increase as fracture strain increased. This trend clearly confirms the local dislocation accumulation in the vicinity of the matrix very close to cementite particles, which is needed to accommodate the large plastic strain gradients.

5.3.2 TKD analysis for pearlitic lamellar cementite microstructure

Microstructural evolution at the early stage of deformation and fracture

To pbtaom for further of the initial stage of the deformation process in pearlite region, SEM-based TKD analysis was conducted with the specimen fractured in the lower region of the DBT (fracture strain of 9.3 %, tested at -100 °C and 1×10^1/s).

A specimen for TKD was lifted out by FIB method from where etch-pits were found in lines like the area as shown in Figure 5.5 (a) with a rectangle, crossing some

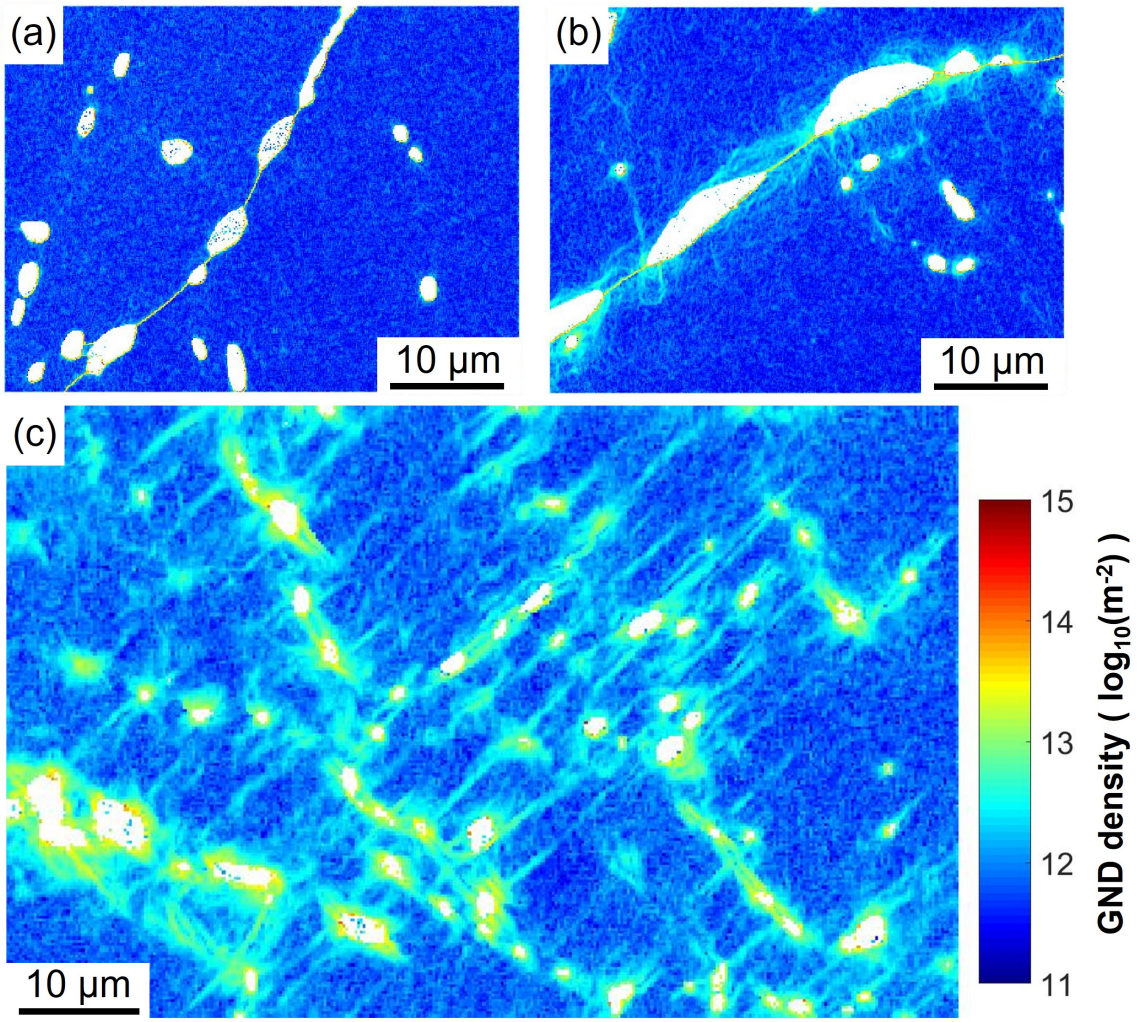


Fig. 5.3 GND density distributions in the ferrite matrix of different specimens, obtained from the HR-EBSD cross-correlation analysis. (a) No obvious GND density concentration can be observed in the undeformed specimen. (b) and (c) GND is accumulated around cementite as macroscopic fracture strain increased (fracture strain of 1.6 % tested at -100 °C and 1×10^0/s, and 7.6 % tested at -50 °C and 1×10^1/s, respectively). There are higher GND density lines with the direction from left-bottom to right-top in (c), which matched well with $\{110\}_\alpha$ plane trace.

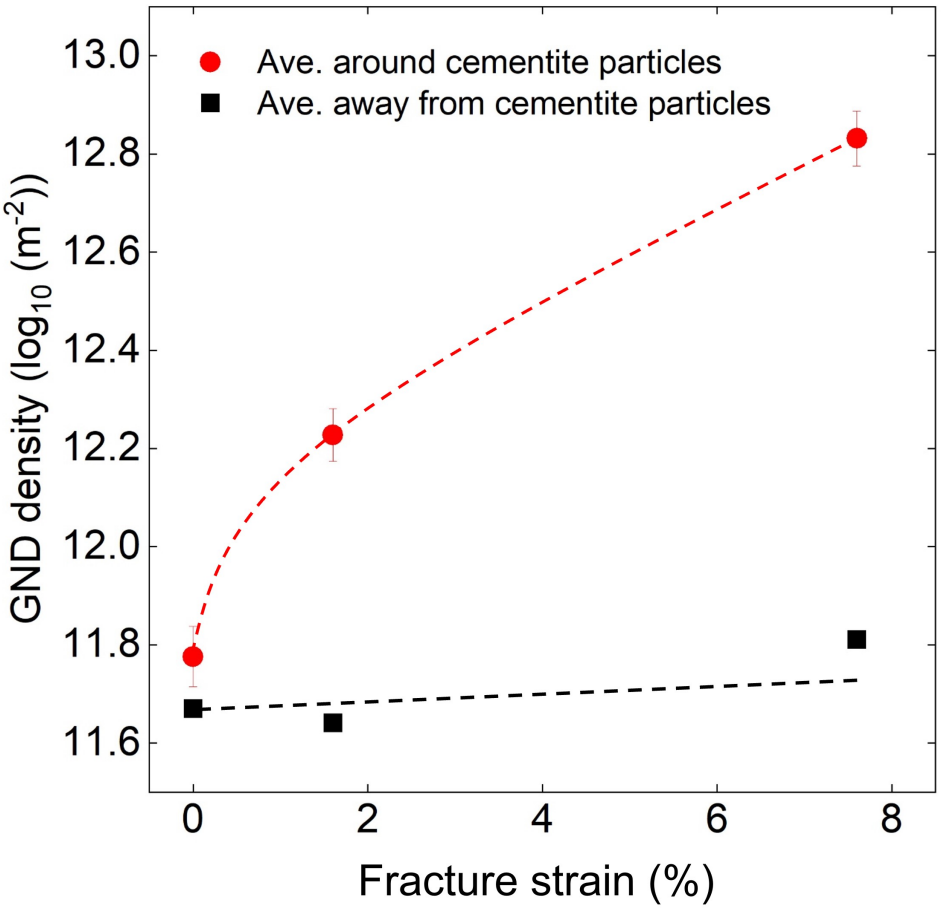


Fig. 5.4 Average GND density around and away from cementite particles in the early stage of deformation, indicating plastic deformation occurred preferentially and locally in the ferrite matrix very close to cementite particles.

lines of etch-pits. Figure 5.5 (b) is a stereographic projection map with $\{100\}_\alpha$ of the ferrite phase in the pearlite having the lines of etch-pits, indicating that the $\{100\}_\alpha$ plane normal is almost vertical to the observation surface. This means at least one of the $\{110\}_\alpha$ plane of ferrite matrix could be almost vertical to the specimen surface. When considered the experimental result that high GND density line corresponded well with the $\{110\}_\alpha$ plane trace as shown in Figure5.3 (C), it can be reasonable to think that what was observed in line is the evidence of slip plane, that is, one of $\{110\}_\alpha$. Figure 5.5 (c) is a SEM image showing the overall appearance of the TKD specimen after being extracted and thinned by FIB. Pearlitic lamellar structure can be detected, and some pits observed on the surface before extracting are recognised on the upper edge of the extracted specimen. Interestingly, there are lamellar discontinuities on the cross-sectional surface in line, which are positionally linked to the initial pits on the sample edge of the top side.

Figure 5.6 displays TKD bright field images of the specimen, focused on the vicinity of lamellar discontinuities. Figure 5.6 (a) is a magnified image of the solid rectangle in Figure 5.5 (c). It can be seen that there are neighbouring fractured cementite lamellae all the way through from the right top to the left bottom. Since all the neighbouring lamellae observed here had such discontinuity, they appeared to be due to deformation rather than lamellar growth during pearlite transformation. Dislocations can be observed just between such fractured cementite lamellae. The facet of lamellar discontinuity preferentially faces a particular direction. Figure 5.6 (b) is another magnified image of the dotted rectangle in Figure 5.5 (c), which reveals many dislocation was developed around such discontinuous lamellae. Figure 5.6 (c) is yet another magnified image of the dash-dotted rectangle in Figure 5.5 (c), showing holes

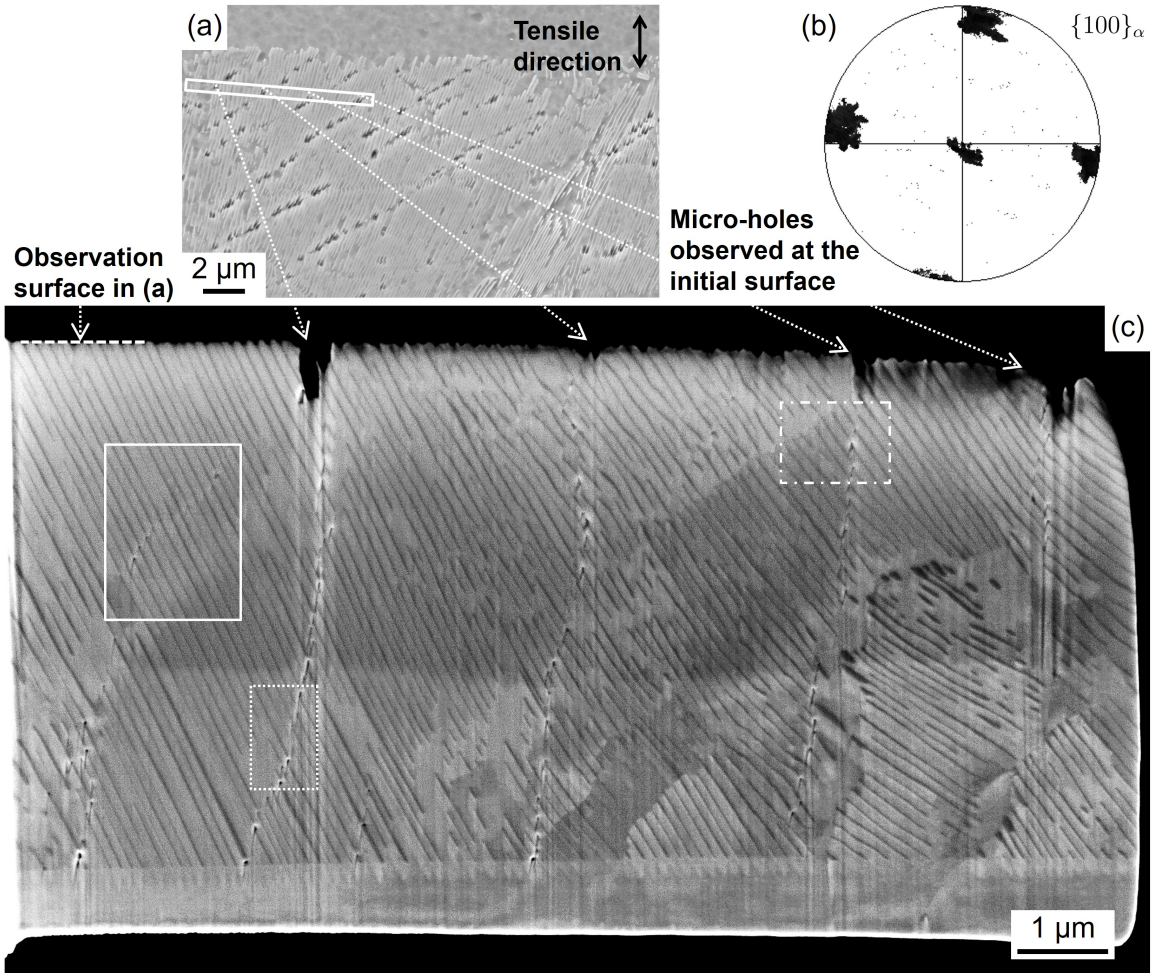


Fig. 5.5 The specimen of fracture strain of 9.3 %, tested at -100 °C and 1×10^1/s; (a) a SEM image of the area where FIB lifted out a thin foil for TKD, (b) a stereographic projection map with $\{100\}_\alpha$ of the ferrite phase in the pearlite having the lines of etch-pits, indicating that the plane normal of $\{100\}_\alpha$ is almost vertical to the observation surface shown in (a), (c) a SEM image showing the overall appearance of the TKD specimen after being extracted and thinned by FIB. Rectangular areas in this picture are to be enlarged in the following figures.

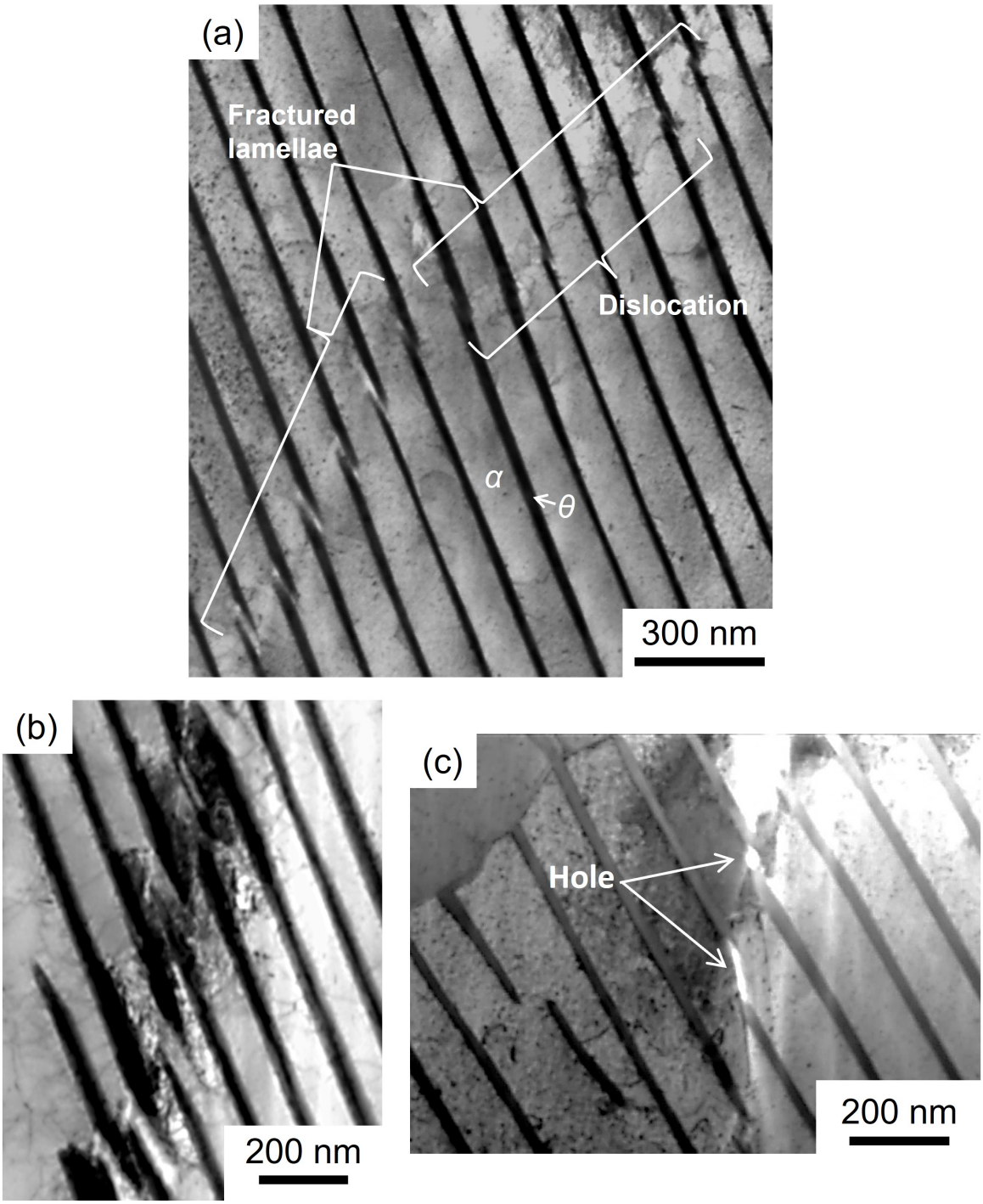


Fig. 5.6 TKD bright field images of the specimen of fracture strain of 9.3 %, tested at -100 °C and 1×10^1/s; (a) a magnified image of the solid rectangle in Figure 5.5 (c) showing neighbouring fractured cementite lamellae all the way through right top to left bottom and dislocations between such fractured cementite lamellae, (b) a magnified image of the dotted rectangle in Figure 5.5 (c) indicating many dislocations around discontinuous lamellae, (c) a magnified image of the dash-dotted rectangle in Figure 5.5 (c) showing micro-holes between such discontinuous lamellae.

between such discontinuous lamellae. Figure 5.6 (b) and (c) give enough implication that such an area is a preferable site for micro-voids to be developed, even if there might have been some influence of sample preparation by FIB thinning on generating such micro-holes shown in discontinuous lamellae.

Figure 5.7 and Figure 5.8 demonstrate another set of results of TKD observation with a specimen taken in the same procedure as previously but with the specimen direction now parallel to the tensile direction as shown in Figure 5.7 (a). Again, the TKD specimen was also taken from the vicinity where etch-pit lines were recognised. Figure 5.7 (b) is a SEM image during FIB thinning, indicating obviously that shear bands on the cross-sectional surface are positionally linked to the pits on the upper edge of the specimen, which were the line etch-pits observed on the surface before the TKD foil is lifted out.

Figure 5.8 (a) is a TKD pattern quality map, which is the area indicated by a rectangle in Figure 5.7 (b), including the shear bands. The line represents $\{110\}_\alpha$ plane trace of the ferrite matrix, which was almost parallel to the direction of the observed shear bands. Figure 5.8 (b) is a Kernel Average Misorientation (KAM) map. This represents the degree of crystallographic misorientation among adjacent pixels, with misorientation corresponding to local plasticity. There can be seen shear bands, with the degree of misorientation more considerable in the ferrite matrix between cementite lamellae. The TKD IPF map from the area surrounded by a rectangle in Figure 5.8 (a) is shown in Figure 5.8 (c). The dotted line indicates $\{101\}_\theta$ plane trace of cementite, which matched well with the direction of the divided cementite lamella. It is noted that this direction is also almost parallel to the $\{110\}_\alpha$ plane trace of the ferrite, forming the shear bands.

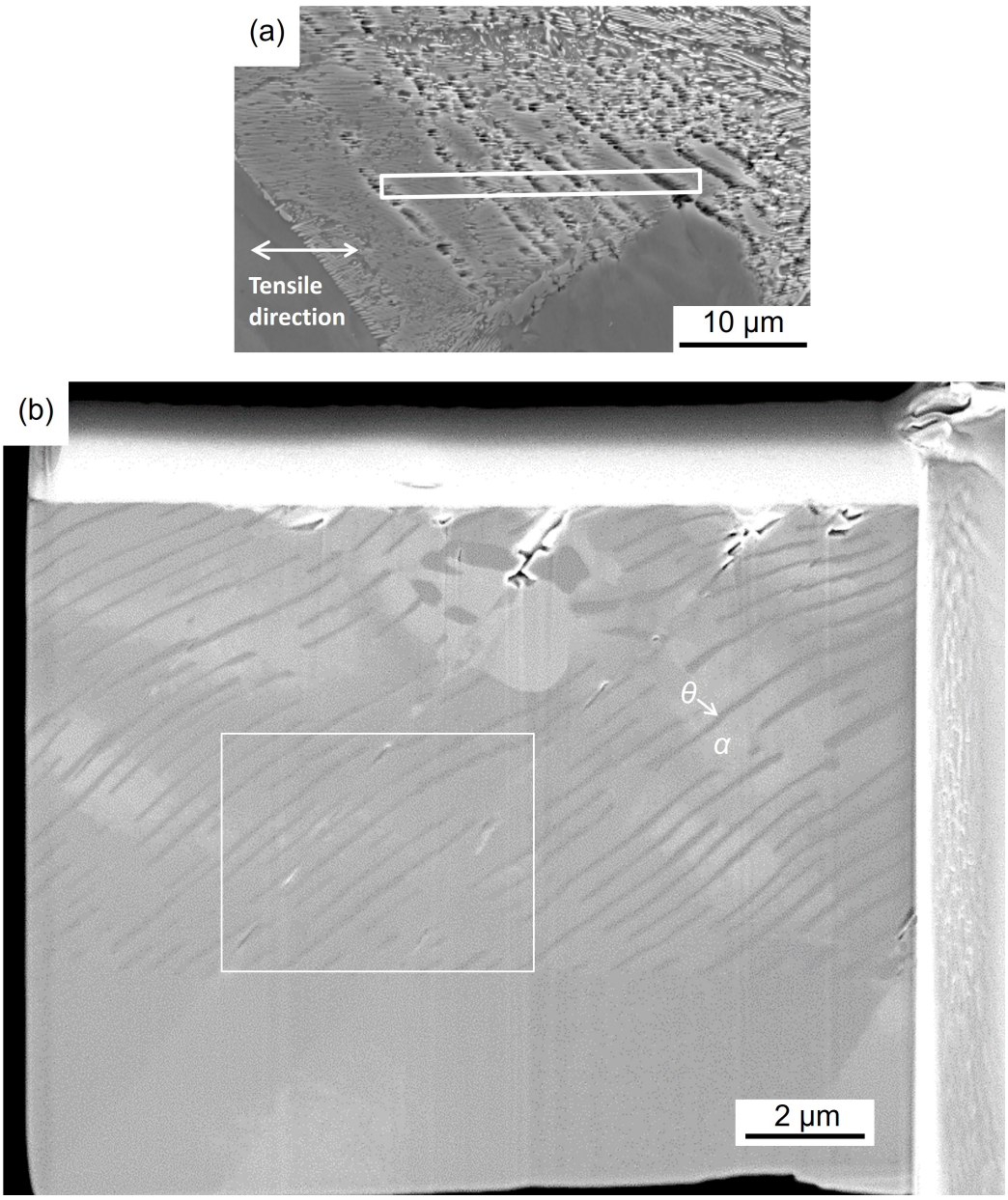


Fig. 5.7 The specimen of fracture strain of 9.3 %, tested at -100 °C and 1×10^1/s; (a) a SEM image of the area where FIB lifted out a thin foil for TKD, (b) a SEM image during FIB thinning indicating the shear bands on the cross-sectional surface are positionally linked to the pits on the upper edge of the specimen, which are the line etch-pits observed on the surface before TKD foil is lifted out in (a).

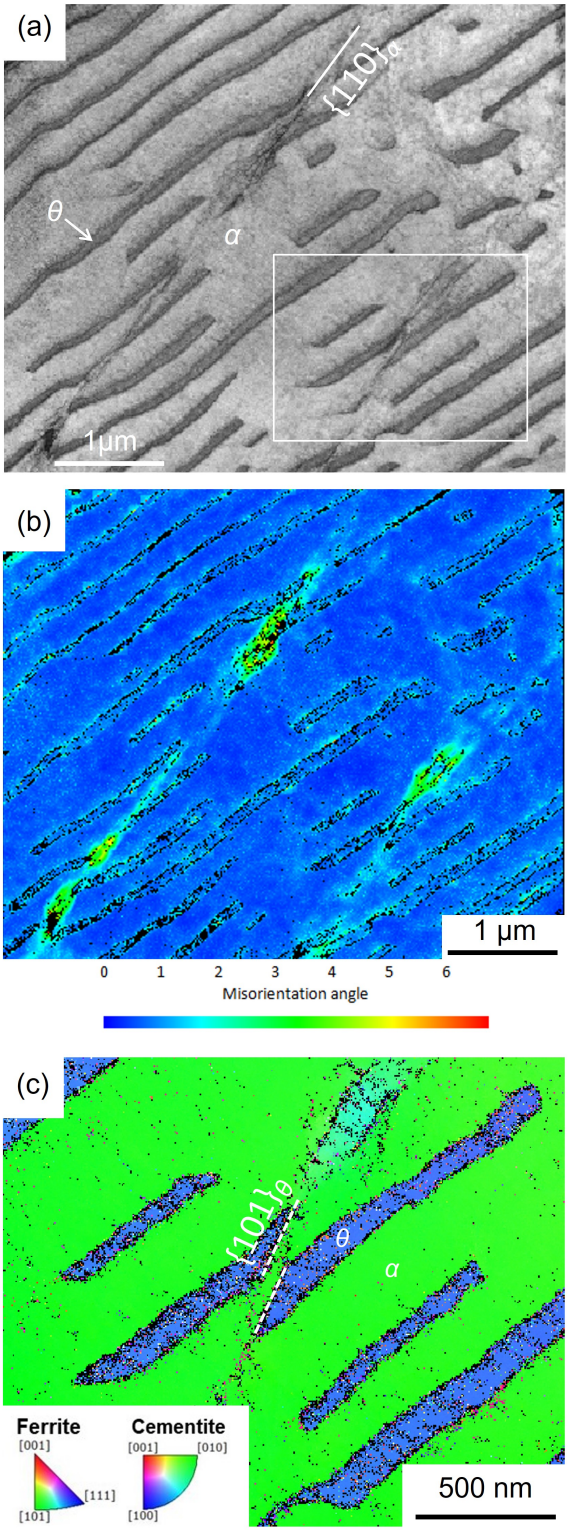


Fig. 5.8 The specimen of fracture strain of 9.3 %, tested at -100 °C and 1×10^1/s; (a) a TKD pattern quality map of the rectangle in Figure 5.7 (b) with a line showing ferrite $\{110\}_\alpha$ plane trace, (b) a TKD KAM map showing considarable misorientation in the ferrite between fractured cementite lamellae on the shear band, (c) a TKD IPF map from the rectangle in (a) with dotted lines indicating cementite $\{101\}_\theta$ plane traces.

Crystallographic orientation relationship in pearlite

Since pearlite has a fine lamellar structure of ferrite and cementite, cementite lamellae could have some influence on slip deformation in ferrite. With respect to local deformability in pearlite, understanding the crystal orientation relationship between ferrite and cementite is important, and if a specific orientation relationship exists, it should be understood. Figure 5.9 demonstrates another pearlite area from the same specimen of fracture strain of 9.3 %, with a TKD bright field image in (a), a phase map in (b), and an IPF map in (c). Zhou and Shiflet [247] pointed out that the crystal orientation relationships may exist between ferrite and cementite in pearlite based on the lattice correspondence of iron atoms in a habit plane, as shown in Table 5.2. The orientation relationships in the table have been reported in previous research [248–250]. Figure 5.10 indicates the crystal orientation of ferrite and cementite in Figure 5.9 (c). The measurement points circled on the left and right in each row are in almost the same position, which means $[001]_\theta$, $[100]_\theta$, and $(010)_\theta$ are almost parallel to $[\bar{3}1\bar{1}]_\alpha$, $[131]_\alpha$, and $[\bar{2}\bar{1}5]_\alpha$ respectively. This reveals that the orientation relationship between the ferrite and the lamellar cementite, observed here, is close to the Pitsch-Petch orientation relationship [251, 252]. Figure 5.11 shows pole figures to check Bagaryatsky orientation relationship [253] (Figure 5.11 (a)) and Isaichev orientation relationship [254] (Figure 5.11 (b)). The fact that all the rows do not match means that they do not have the specific orientation relationships in this case.

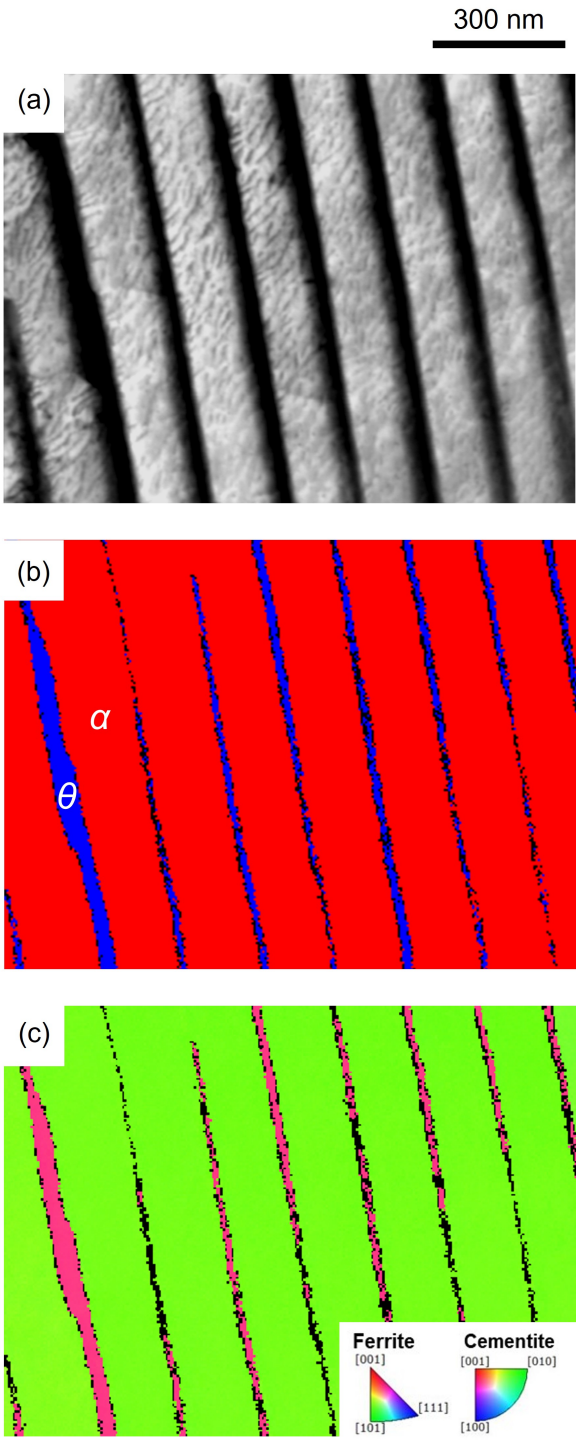


Fig. 5.9 Pearlite crystallographic orientation information obtaind from TKD with specimen of fracture strain of 9.3 %, tested at -100 °C and 1×10^1/s; (a) a TKD bright field image of pearlite, (b) a TKD phase map, (c) a TKD IPF map.

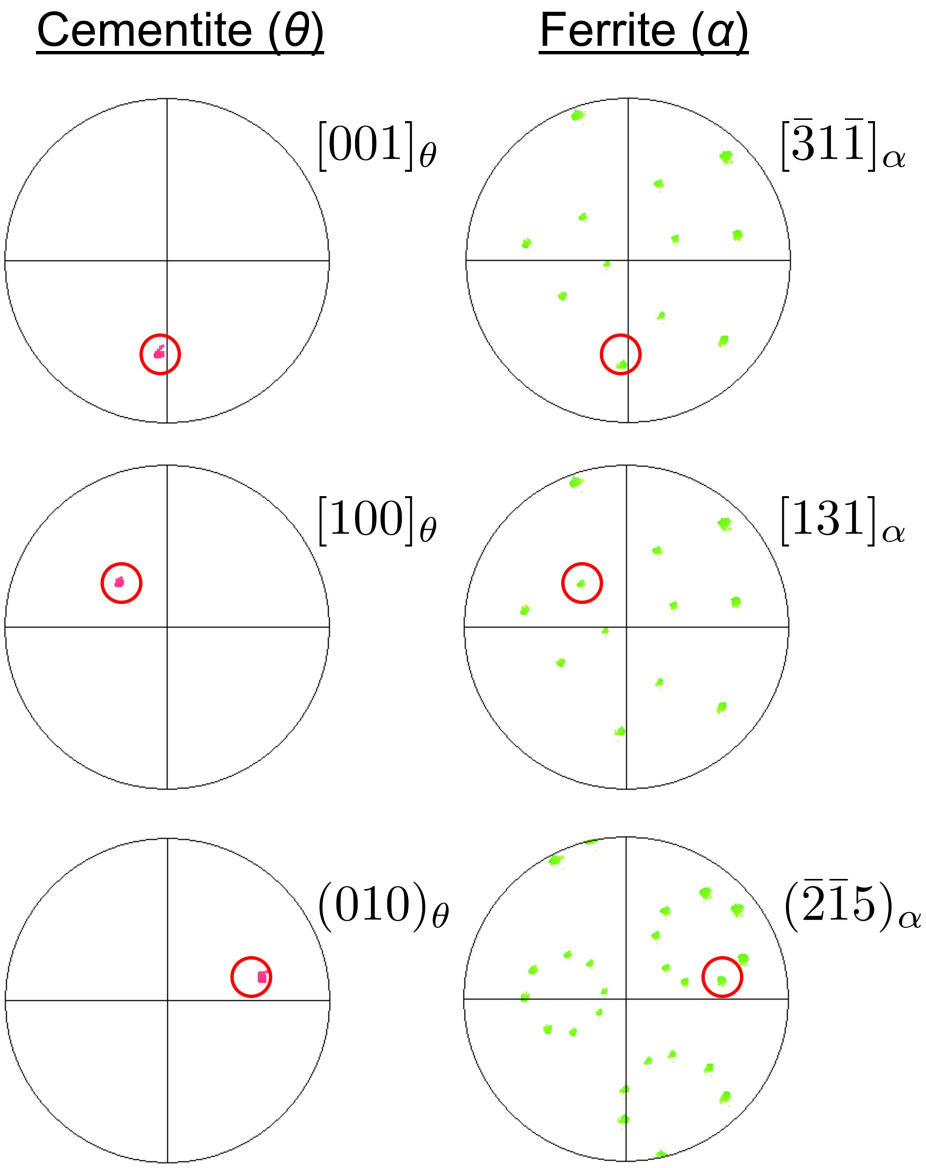


Fig. 5.10 A set of pole figures of ferrite and cementite from the TKD IPF map of Figure 5.9 (c), indicating Pitch-Petch orientation relationship between the ferrite and the cementite.

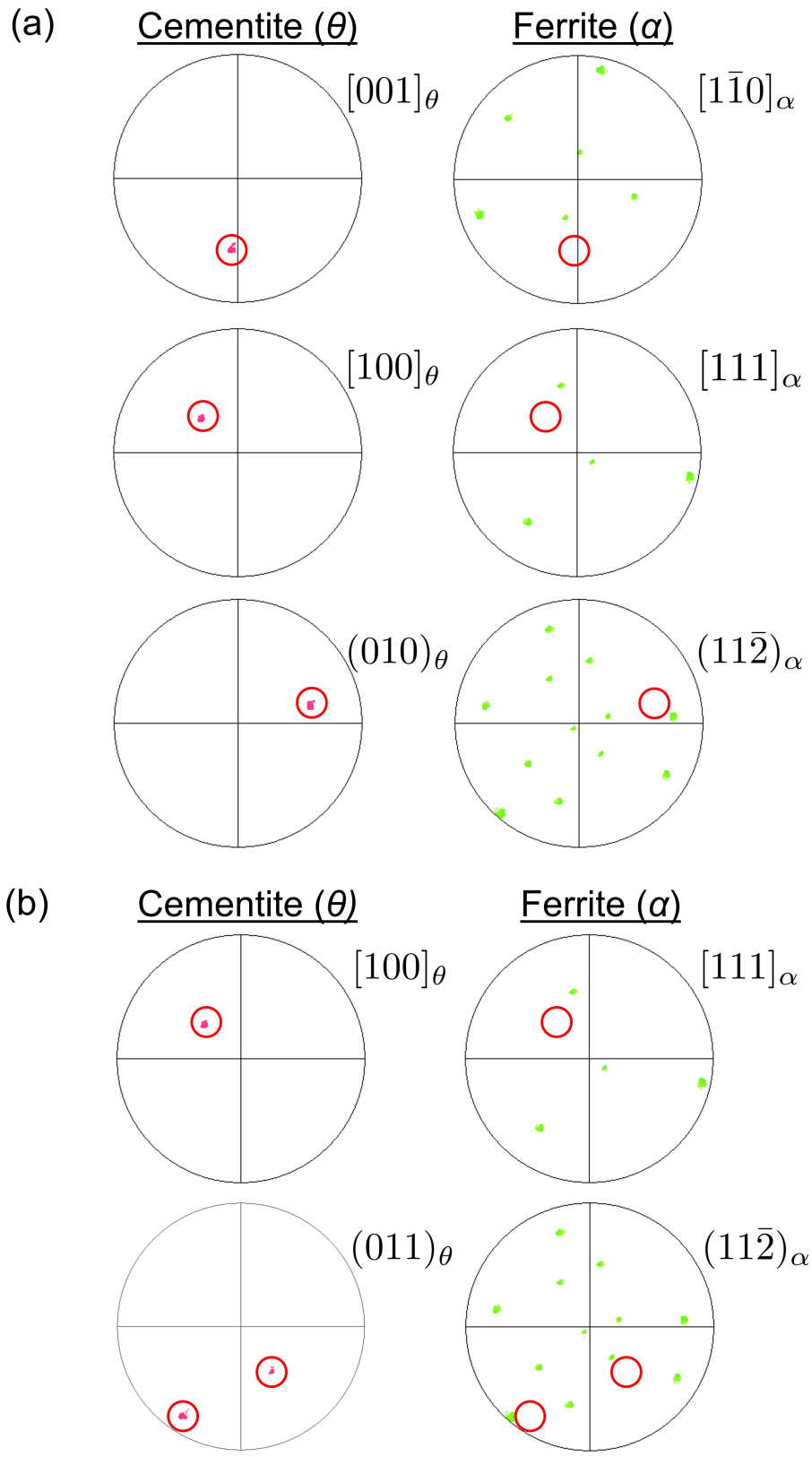


Fig. 5.11 A set of pole figures of ferrite and cementite from the TKD IPF map of Figure 5.9 (c) to check whether (a) Bagaryatsky, and (b) Isaichev orientation relationships between the ferrite and the cementite are satisfied with or not, respectively.

Table 5.2 Crystallographic orientation relationships reported between ferrite and cementite in pearlite [247].

Bagaryatsky	$[001]_\theta \parallel [1\bar{1}0]_\alpha$ $[100]_\theta \parallel [111]_\alpha$ $(010)_\theta \parallel (11\bar{2})_\alpha$
Isaichev	$[100]_\theta \parallel [111]_\alpha$ $(011)_\theta \parallel (11\bar{2})_\alpha$
Pitch-Petch	$[001]_\theta$ 2.6° from $[\bar{3}1\bar{1}]_\alpha$ $[100]_\theta$ 2.6° from $[131]_\alpha$ $(010)_\theta \parallel (\bar{2}\bar{1}5)_\alpha$

5.4 Discussion

The deformation and fracture process in each microstructure is considered, where necessary, with the comparison with what previous studies have reported. More focus should be placed on local deformation detected by the HR-EBSD and SEM-based TKD before macroscopic brittle fracture occurs. Finally, how cementite morphology affects DBT behaviour is discussed.

5.4.1 Internal stress of cementite particles

The micromechanism of brittle fracture process in the $\alpha + \theta$ microstructure is thought to be composed of three stages [21, 174, 175], that is, (i) crack nucleation at cementite particle, (ii) crack propagation into ferrite/cementite interface entering a ferrite grain, (iii) crack propagation into adjacent ferrite/ferrite grain boundary. Regarding factors causing cementite crack, it is revealed that macroscopic plastic strain plays a significant role [150–152]. The number of cracked cementite increased with increasing macroscopic plastic strain [152].

However, empirical datasets corresponding to the local deformation leading to cementite cracks are limited due to the difficulty of post-mortem analysis. Even though elastic strain and stress obtained from the HR-EBSD cross-correlation analysis are not absolutely correct due to the unknown stress at the reference point, the order of magnitude can be compared. In addition, plastic flow and local work hardening can be evaluated, at least qualitatively, through the GND density distribution. Here, the maximum in-plane shear stress τ_{max} is introduced to handle the magnitude of the stress inside cementite as a scalar;

$$\tau_{max} = \sqrt{\left(\frac{\sigma_{11} - \sigma_{22}}{2}\right)^2 + \sigma_{12}^2} \tag{5.1}$$

where σ_{11} and σ_{22} are normal stress, and σ_{12} is shear stress. Figure 5.12 (a) unveiled the distribution of stress variation with the same area as Figure 5.2. A large variation in the maximum in-plane shear stress was observed in some cementite particles. From a statistical viewpoint, cracking occurred preferentially in relatively large particles in size and those oriented with their longest axis parallel to the direction of the tensile direction according to the fibre loading mechanism [229]. Individually, however, crystallographic orientations both in cementite and adjacent ferrite, as well as their relationship, can have some influence on the internal stress of cementite (in addition that this is so-called 2D analysis), and these factors may contribute to such variation. Figure 5.12 (b) indicates the stress variation profile over the dotted line crossing a grain boundary cementite in Figure 5.12 (a). The value of each pixel in the cementite reaches 2.2 GPa. The variation in ferrite was much smaller than that in cementite. The fracture stress of this particular cementite is unclear. However, there have been some studies to report the fracture stress of bulk cementite under compression tests at room temperature. It

was about 2.8 GPa as shown in Figure 5.12 [142] or about 2.0 GPa in different research [255], and happened in elastic region. Assuming these values, it can be said that the range of maximum in-plane shear stress variation shown in Figure 5.12 (b) and the fracture stress of cementite lie in a similar magnitude. Therefore, it is not saying too much, even if I would say that the internal stress of cementite is raised to the extent that leads to the cracking of some particles.

5.4.2 Cementite particle cracking

Most frequently, the cementite cracking was consistent with the $(010)_\theta$ plane trace, but sometimes $\{101\}_\theta$, as shown in Figure 5.1. There is a very limited number of papers to report the cracking plane of cementite particles. However, the trend obtained in this study that $(010)_\theta$ plane trace was most frequently observed is consistent with previous work with cementite particles in Fe-0.1 wt%C steel [22]. As mentioned above, since crystallographic orientations should affect the internal stress of a cementite particle, the fracture plane of the particle can be changed because fracture stress is regarded as a tensile stress component normal to a particular plane. In fact, $\{101\}_\theta$ has been reported as one of the probable cleavage planes of cementite lamellae in Fe-1.23 wt%C hypereutectoid steel [137].

In this study, Figure 5.3 clearly shows that dislocation pile-up occurred at cementite particles. Furthermore, Figure 5.4 understandably indicates that plastic deformation was accumulated preferentially and locally in the ferrite matrix close to cementite particles, which resulted in stress concentration at cementite particles and eventually cementite cracking. Actually, the internal stress of the cementite was thought to be raised to a similar magnitude of fracture stress as shown in Figure 5.12 (b).

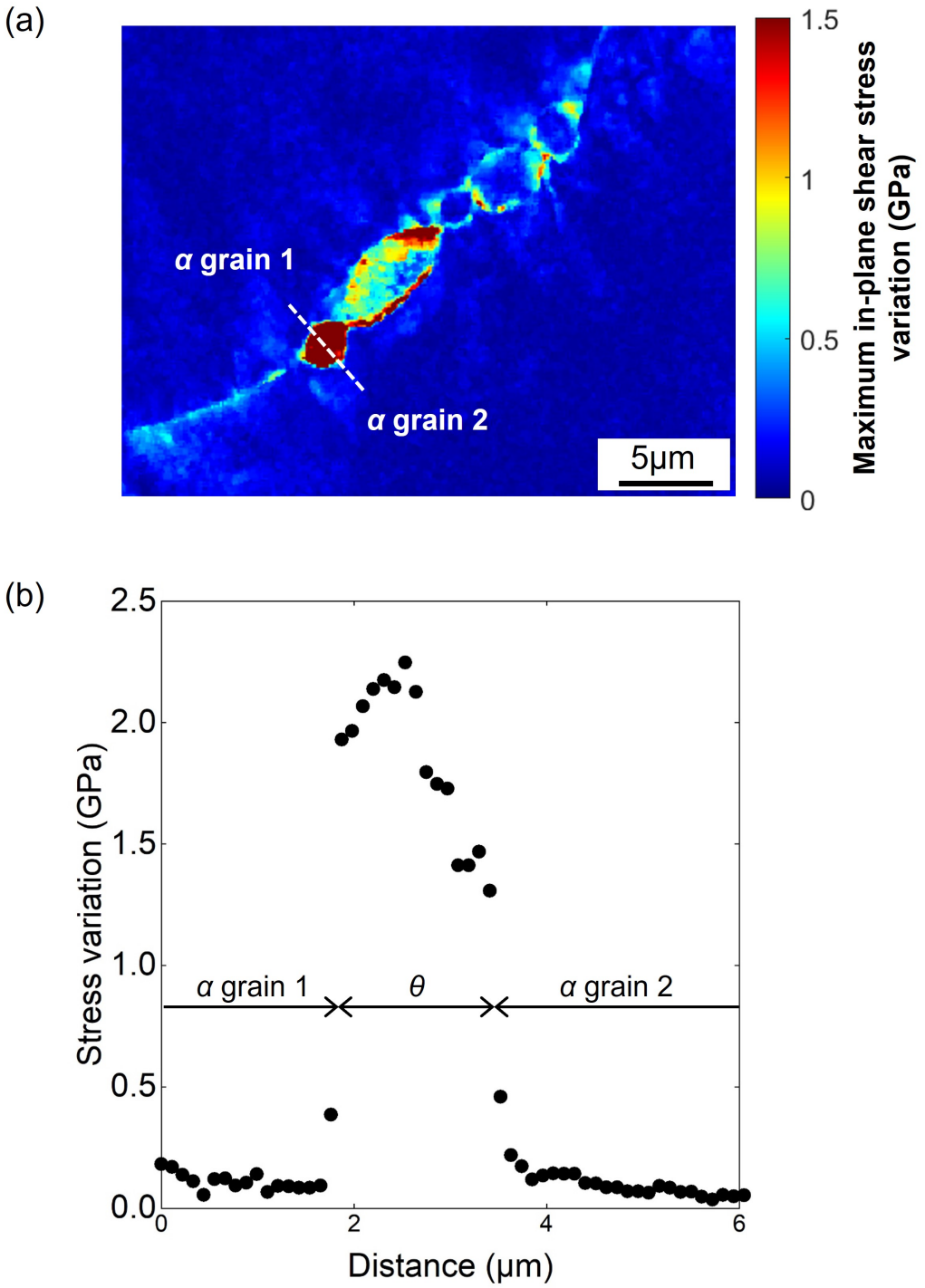


Fig. 5.12 (a) The distribution of maximum in-plane shear stress variation in the ferrite matrix and cementite particles with the specimen of fracture strain of 1.6 %, tested at -100 °C and 1×10^0/s. (b) The stress variation profile over the dotted line crossing a grain boundary cementite described in (a).

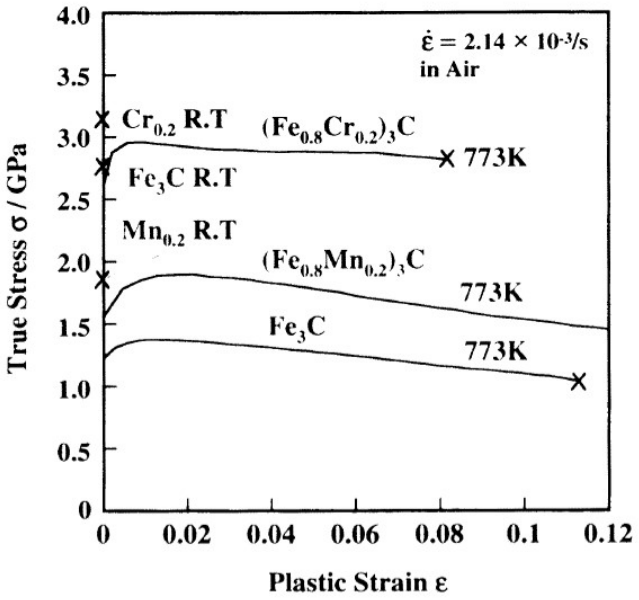


Fig. 5.13 Stress - strain curves of pure and alloyed bulk cementite at room temperature and 773 K [142].

5.4.3 Lamellae fracture at the early stage of the deformation process

In the present study with SEM-based TKD measurement, the trace of $\{101\}_\theta$ plane trace was well matched to the direction of the discontinuous lamellar facet. $\{101\}_\theta$ has been reported as one of the probable cleavage planes of lamellar cementite [138] as well as the slip planes [136]. Several studies have been conducted previously on the plane of the lamellar facet. Tagashira et al. [139] reported that the "slip-off" plane of lamellar cementite after heavily drawing deformation at room temperature was $(12\bar{1})_\theta$. They pointed out the possibility of multiple slip systems maintaining the compatibility of the ferrite matrix and cementite lamellae, and that the slip-off would happen in a ductile manner. Porter et al. [256] investigated pearlite deformation with changing lamellar thickness. They reported that crack initiation in lamellar cementite in relatively thick lamellae was observed to be mainly a low-energy process, though they did not mention

which plane it was, initially assisted by cementite yield to some extent. Whereas in thinner cementite lamellae after cold-drawn deformation showed a much larger plastic deformation. The deformation conditions in the reference of [136] - reporting that $\{101\}_\theta$ is a slip plane - were thought to be relatively easy for plastic deformation to occur because of room temperature and heavily drawn deformation, rather than in the condition with cryogenic and tensile deformation in the present study and in the reference of [138].

The plane trace of the lamella facet matched with $\{101\}_\theta$, which was reported as a cleavage plane of cementite. Moreover, Figure 5.14 is a SEM image showing lamellar cementite on the heavily etched cross-sectional surface of the specimen fractured in the lower region of the DBT. It seems that cementite lamellae include several cracks heading in different directions, and no deformation or reduction in area was observed. From these two experimental results, cementite lamellae were thought to be fractured in a brittle manner. However, it is also obvious from the TKD observation (Figure 5.7 and Figure 5.8) that slip activity on $\{110\}_\alpha$ induced such lamellae fracture. $\{101\}_\theta$ plane trace was almost parallel to the $\{110\}_\alpha$ plane trace. Considering all factors above, it can be concluded that cementite lamellae were fractured in a brittle manner but still plastic deformation in cementite on $\{101\}_\theta$ plane can contribute to the onset of brittle fracture.

5.4.4 Forming pearlitic cracking

Miller et al. [159] suggested the mechanism for shear cracking in a pearlite colony based on the observation with optical microscope, that is, lamellar cracking is induced by the ferrite slip followed by the development of shear zone causing another cracking

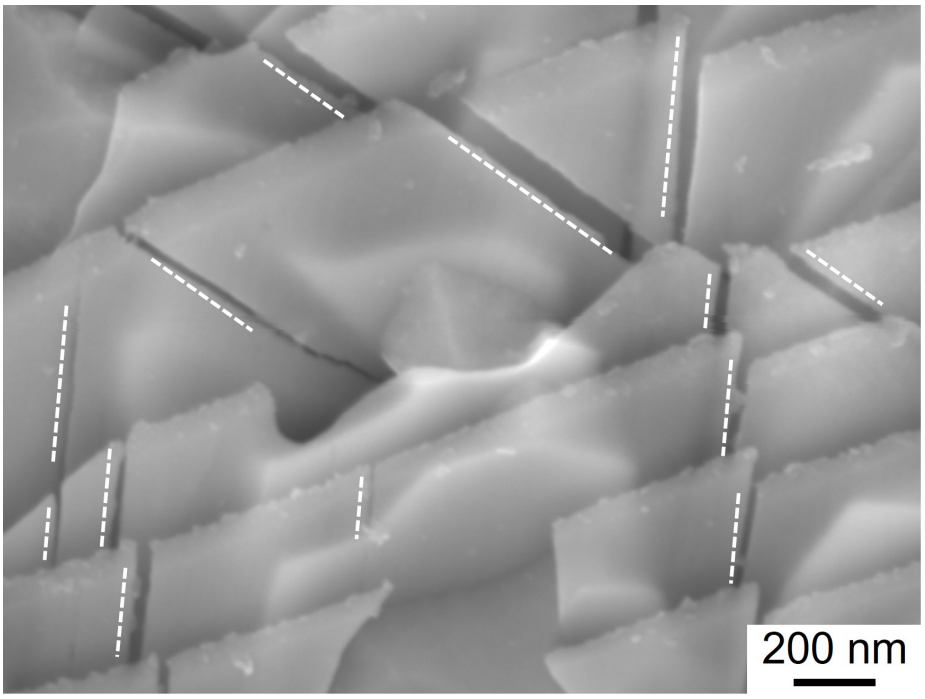


Fig. 5.14 Cracked cementite lamellae observed on the polished and heavily etched cross-sectional surface of the specimen of fracture strain of 9.3 %, tested at -100 °C and 1×10^1/s. Cementite lamellae include several cracks heading in different directions, and there seems to be no deformation and no reduction in area around the cracks.

in neighbour lamellae, forming micro-voids, its coalescence, and linking up to be a crack ranging over the pearlite colony. Figure 5.8 confirms that ferrite slip activity within pearlite caused lamella fracture, and subsequent local plasticity and void formation along with ferrite slip planes can be deduced by Figure 5.6 (b) and (c). These experimental results are strongly complementary, and reinforce the shear cracking mechanism [159]. In terms of the deformation and fracture process of the $\alpha + P$ microstructure in the DBT region, it is likely that an unstable brittle crack propagates, as shown in Figure 4.6, from such a crack ranging over a pearlite colony developed in line with the shear cracking mechanism.

5.4.5 Orientation relationship in pearlite

As mentioned in Section 5.3.2, various orientation relationships between ferrite and cementite in pearlite have been reported. It is thought that the orientation relationships might vary depending on the carbon content in steel [248]. Pitch-Petch orientation relationships tend to be observed in eutectoid steel, whereas Isaichev and Bagaryatsky orientation relationships are prominent in steel of hypoeutectoid and hypereutectoid compositions, respectively. The change of preferred relationship depending on the carbon content is explained by pearlite nucleation related to proeutectoid ferrite and cementite. In this study, the chemical composition of the tested material is Fe–0.2 wt%C hypoeutectoid steel. Crystallographic orientation relationship with TKD analysis was demonstrated in three different areas of three specimens, meaning nine datasets in total. They all indicated Pitch-Petch relationship between ferrite and cementite in the evaluated pearlite colonies, as shown Figure 5.10. This does not match what has been reported in Mangan's paper [248]. On the other hand, Amemiya et al. [257] showed

Bagaryatsky and Pitch-Petch orientation relationships in the same eutectoid steel. They analysed the lattice parameter of cementite in tested steel and internal stress of pearlite by EBSD and neutron diffraction technique, and suggested the possibility that various crystallographic orientation relationships can coexist regardless of the composition, that is, the presence of proeutectoid ferrite and cementite. Although internal stress accommodation during pearlite transformation seems to relate to the selection of orientation relationship between ferrite and cementite, further research shall be required. Hence, the result of the crystallographic orientation relationship in pearlite in this study is by no means surprising. More recently, the work of the same research group [258] introduced that different orientation relationships were simultaneously developed in pearlitic steel.

5.4.6 The effect of cementite morphology on the DBT behaviour

Once the internal stress of cementite reaches its fracture stress, a crack is generated in the $\alpha + \theta$ microstructure. Judged by Figure 5.3, the length for dislocation in ferrite to pile-up appears to reach, at least, tens of micrometres order. In contrast, the $\alpha + P$ microstructure has a sub-micrometre lamellar structure with the particular Pitch-Petch orientation relationship between ferrite and cementite (Figure 5.10), which restricts itself from deforming freely and significantly. Hence, lamellar cementite is cracked after ferrite slip occurs in pearlite. This type of crack is lamella-thickness-order in size, and the pile-up length for dislocation in ferrite is significantly tiny due to the lamellar structure, while its counterpart is a relatively "sharp" micrometre-order crack corresponding a particle.

Crack length and length of slip plane for dislocation to pile-up have an influence on local fracture stress for crack in cementite to propagate ferrite/cementite boundary [100]. The smaller the crack in size and the shorter the length of the slip plane for pile-up, the higher the local fracture stress for a crack to propagate at the ferrite/cementite boundary; that is, it should be much harder for a lamella-thickness-size crack formed in a cementite lamella to propagate to the ferrite/cementite boundary in a brittle manner compared to a micrometre-size crack initiated at grain boundary cementite particle in the $\alpha + \theta$ microstructure. Therefore, lamellar cracking seems less likely to propagate unstably throughout a colony and moreover, but rather, promotes further plastic deformation owing to stress and strain concentration caused by the cracking. Once a lamellar crack is formed, it enhances local plasticity much more as shown in Figure 5.6 (b) and (c) to produce additional defects like micro-void and/or another lamellar crack, forming a relatively "blunted" shear cracking over a pearlite colony in the end (Figure 4.12).

Combined with all the experimental findings by high-resolution characterisation techniques and a thorough SEM characterisation in Chapter 4, it can be understood that a wider transition temperature range of the DBT curves comes from the difference in the formation process of the crack and the sensitivity to macroscopic brittle fracture of the resultant crack.

5.5 Summary and Conclusions

In this chapter, post-mortem analysis using advanced characterisation techniques - HR-EBSD and SEM-based TKD - was employed to clarify the elastic and plastic deformation of cementite, its interaction with the ferrite matrix before crack initiation,

and the fracture plane of cementite experimentally, and to understand the deformation and fracture process of pearlite. The following specific conclusions can be drawn:

1. It has been proven possible that HR-EBSD can be used to characterise the cleavage fracture plane of cementite. For the cementite particle analyses, the cracking was consistent with the $(010)_\theta$ plane most frequently, and sometimes $\{101\}_\theta$, as shown by trace analysis.

2. In the $\alpha + \theta$ microstructure, HR-EBSD analysis has been used to quantify the extent to which localised plasticity accumulates around cementite particles, consistent with a cementite crack acting as a brittle fracture initiation point in the lower DBT region.

3. SEM-based TKD has been used to reveal the crystallographic orientation relationship between ferrite and cementite in pearlite, and shows that Pitch-Petch orientation relationship is prominent in all areas analysed.

4. In the $\alpha + P$ microstructure, TKD showed that ferrite slip in pearlite induces cracking of the lamellar cementite. The direction of the cracked lamellar facet fitted to $\{101\}_\theta$ plane trace. Such cracks ended up forming a larger crack over a pearlite colony, where an unstable brittle crack initiated in the DBT region.

5. Combined with all the experimental findings using high-resolution characterisation techniques and the thorough SEM characterisation in Chapter 4, it is proven that the wider transition temperature range of the DBT curves arises from the difference in the formation process of cracks and their sensitivity to macroscopic brittle fracture.

Chapter 6

In-situ Observation of Local Plasticity on Spheroidised and Pearlitic Lamellar Cementite Microstructures

6.1 Introduction

In the DBT region, localised plastic deformation occurs before macroscopic brittle fracture. Such deformation is very localised, especially in the lower region of the DBT. It is crucial that to understand the interaction between cementite and the ferrite matrix until the point that cementite cracks in the $\alpha + \theta$ microstructure. In the $\alpha + P$ microstructure, the interaction between ferrite and pearlite, as well as the localised plastic deformation behaviour within the pearlite, are considered important.

In addition, it is very important to have a global view of how the deformation progresses dynamically and how damage accumulates.

To capture strain distribution over dual-phase and trace its development, DIC method can be applied. DIC is an analysis method which captures patterns before and after deformation as digital images and calculates the displacement and strain for each element locally [259]. It is often used to observe the development of strain with deformation and its distribution in multi-phase steels because DIC has the advantage of corresponding directly to microstructures. DIC analysis for plastic deformation combined with *in-situ* observation has been applied to observations for the deformation and its mechanism in DP steel [260, 261], bainitic steel [86], and pearlitic steel [262–265]. For example, it is known that the deformation of fully pearlitic steel is affected by the cementite lamellae orientation [263, 264], and that the difference in the distribution of hard phase in DP steel affects the microscopic strain concentration and ductile crack initiation [260]. Nevertheless, there have been no empirical studies with *in-situ* test and DIC that compare plastic deformation using materials in which only the cementite morphology is changed as in this study.

The purpose of this chapter therefore is to observe directly and visualise the local plastic deformation in both microstructures using *in-situ* observations coupled with subsequent DIC analysis, and to deepen our understanding of the interaction between the ferrite matrix and cementite, the difference depending on their morphology, the cracking of cementite particles, and the deformation behaviour of the pearlitic microstructure itself. Although the deformation is under static tensile conditions at room temperature, it functions sufficiently when it comes to observing the local

plasticity and how it is developed and comparing the differences that may be caused by cementite morphology.

6.2 Experimental methods

6.2.1 Materials

As in previous chapters, carefully designed test material was employed. Chemical composition is given in Table 3.1. Through the heat treatment described in Figure 3.1, testing materials with almost the same apparent ferrite grain size distribution but different cementite morphology were achieved. Any other influencing factors, including ferrite grain size, on the DBT behaviour have not been changed. They are the $\alpha + \theta$ microstructure and the $\alpha + P$ microstructure, as shown in Figure 3.2.

6.2.2 *In-situ* tensile test

For the detailed conditions of sample preparation and tensile testing, Section 3.3.2 should be referred to. The key to the *in-situ* test is to obtain an appropriate speckle pattern for subsequent DIC analysis. As shown in Chapter 3, spheroidised cementite particles were about 2 μm in diameter, and cementite lamellae were of sub-micrometre order. These cementites play an important role in deformation. Hence, at least equal to or less than the order of sub-micrometre speckle pattern was thought to be required to detect very local plasticity in and around the particle and in pearlite. In addition, ferrite grain size ranged up to an order of 400 μm in ECD (see Figure 3.3), though the average diameter was about 80 μm. This meant a relatively large area should be captured in *in-situ* testing to recognise the interactions between ferrite grains, and

cementite particles or lamellae. To acquire information on local plasticity for these sub-micrometre scales of such ROIs with restrictions mentioned above, a high-resolution image with a considerably fine and homogeneous speckle pattern was thought to be proper. For this, gold spattering was performed for the specimen surface, followed by patterning by removing the surface gold with Ga ion beam in ZEISS Crossbeam FIB.

Figure 6.1 shows SEM images of tensile specimens in low magnification after gold spattering and FIB patterning. Figure 6.1 (a) and (c) are relatively low magnification images. Areas where FIB was applied turned black in each image. As shown in Figure 6.1 (b) and (d), the speckle pattern finally obtained was distributed in the scale of sub-micrometre order, which enabled to the analysis of local plasticity around cementite particles and lamellae.

6.2.3 Characterisation

SEM

The Zeiss Merlin FEG-SEM was used for the observation. During tensile deformation in the chamber, in-lens and SE images were captured at every step of 1 to 5 % increment of engineering strain until just after having recognised unstable deformation with macroscopic necking of the specimen. Low accelerating voltage of 5 kV and probe current of 1 nA were applied in both microstructures to be sensitive to the specimen's surface condition during deformation.

EBSD

EBSD was used to acquire crystal orientation information before tensile deformation. The detailed information should be referred to Section 3.4.2.

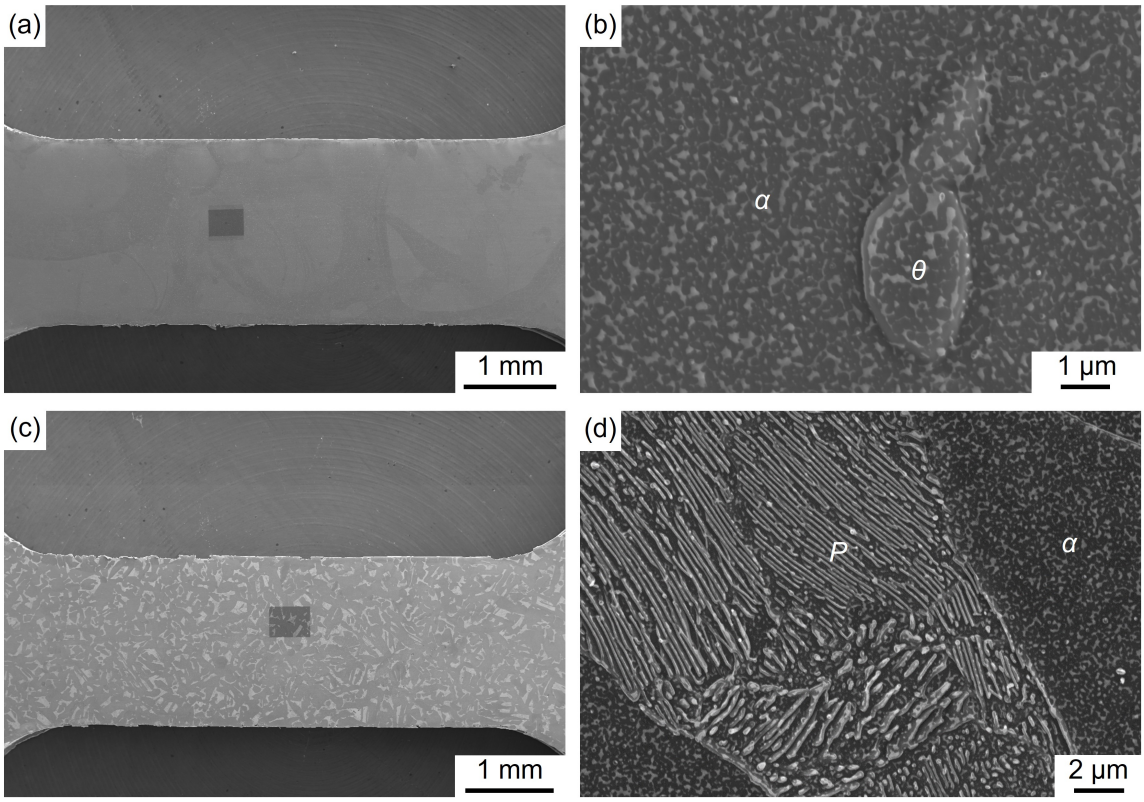


Fig. 6.1 *In-situ* tensile testing specimen after gold spattering followed by FIB patterning for the $\alpha + \theta$ microstructure ((a) and (b)) and the $\alpha + P$ microstructure ((c) and (d)) .

DIC

Post-processing for DIC analysis of the captured SEM images was carried out with Vic–2D software (Correlated Solutions) to quantify strain and its distribution. The subset and step sizes for DIC analysis were set at 29 × 29 and 5 × 5 pixels, respectively.

6.3 Results

6.3.1 *In-situ* tensile test

Figure 6.2 is the engineering stress-engineering strain curve of the tested specimens, where the solid line indicates the result from the $\alpha + \theta$ microstructure and the dotted line represents the result from the $\alpha + P$ microstructure. There can be found stress drop in every in-situ tensile step, but an overall smooth chart was obtained. The tested material was substantially ductile under the tensile condition, and the test was suspended before necking the gauge part. Although the macroscopic ductility and uniform elongation were not clearly exhibited, here we investigate plasticity on the microstructural scale. Besides, ultimate tensile strength can be estimated from the data, which is 250 MPa in the $\alpha + \theta$ microstructure and 340 MPa in the $\alpha + P$ microstructure, respectively.

6.3.2 Microstructural evolution with spheroidised cementite

Overall deformation behaviour

Firstly, strain maps with relatively low magnification are demonstrated with the related EBSD IPF map to show the overall deformation process. Figure 6.3 (a) is an EBSD

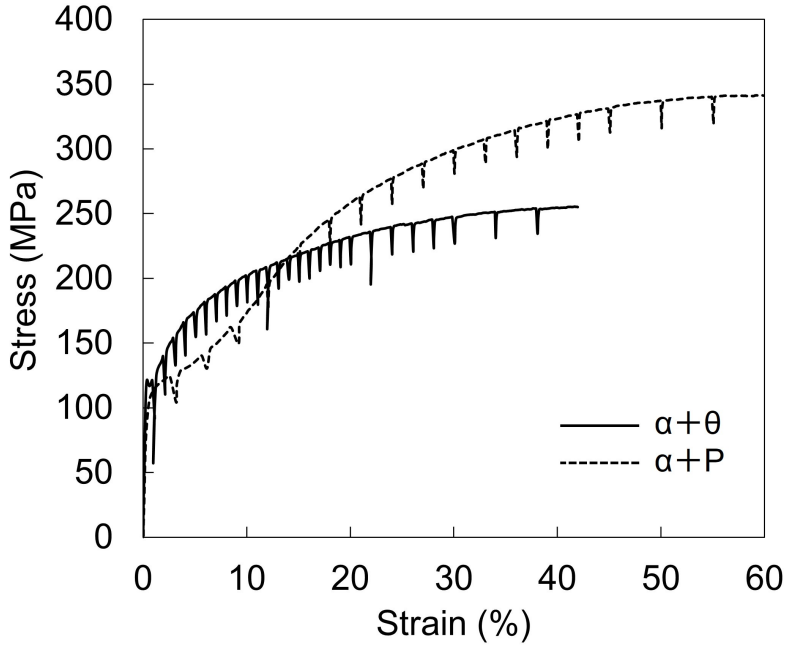


Fig. 6.2 Stress-strain curve obtained from *in-situ* tensile test.

pattern quality map, where cementite particles are coloured black. Figure 6.3 (b) is an EBSD IPF map of the same area. Figure 6.3 (c) to (h) represent equivalent strain maps from DIC post-analysis. The tensile direction is the left-right of the images, and the strain in that direction is displayed as macroscopic tensile strain ε_{xx}. The local strain distribution hereafter is expressed by the equivalent strain ε_{eqv} defined by the following equation:

$$\varepsilon_{eqv} = \sqrt{\varepsilon_1^2 - \varepsilon_1\varepsilon_2 + \varepsilon_2^2} \tag{6.1}$$

where ε_1 and ε_2 are the maximum and minimum principal strains, respectively. It is noted that the plane strain condition is applied as a premise for the equation. As shown in Figure 6.3 (d), when macroscopic tensile strain reached 6 %, rather straight slip lines can be recognised. $\{110\}_\alpha$ and $\{112\}_\alpha$ plane traces are drawn in the figure by solid and dotted lines, respectively. The directions of the slip plane traces were

matched well to high-strain straight lines. Figure 6.3 (e) illustrates the strain map after macroscopic tensile strain reached 12 %. The point of this map is that strain became more intense in some areas, both at grain boundary and inside grain, and that not very much of the ferrite grain boundary experienced strain concentration. Grain 1 had several concentration sites, however, most of which were intragranular. Figure 6.3 (f) is the strain map after reaching 20 % macroscopic tensile strain. Most of the ferrite experienced some strain. In contrast, the strain in cementite particles remained low to the extent that the difference in contour colour can tell where the particles are. The strain in the vicinity of ferrite around cementite particles was also found to be relatively low due to constraints from cementite particles. When the macroscopic tensile strain was equal to and above 30 %, as shown in Figure 6.3 (g) and (h), the plasticity in ferrite became more intense. Cementite cracking was successfully detected even at low magnification by the arrows in Figure 6.3 (h). Several specific regions in Figure 6.3 are to be described in the following figures.

Figure 6.4 indicates a cementite cracking at a ferrite grain boundary, identified in the solid rectangle in Figure 6.3 (f). No cracking was found at 26 % macroscopic tensile strain. Slip lines were observed in both the upper and lower ferrite grains, and these were continuous but changed their orientation across the grains (Figure 6.4 (c)). There are two relatively large cementite particles at the centre of the image, and the ferrite matrix between the particles experienced substantially high strain concentration. The cracking occurred at 28 % of macroscopic tensile strain (Figure 6.4 (d)). After cracking, it can be seen that the right-hand side of the cracked cementite experienced strain increase. At 30 % of macroscopic strain, the cracking was observed more clearly. After being cracked, as with the cracked cementite particle in Figure 6.4, the development of

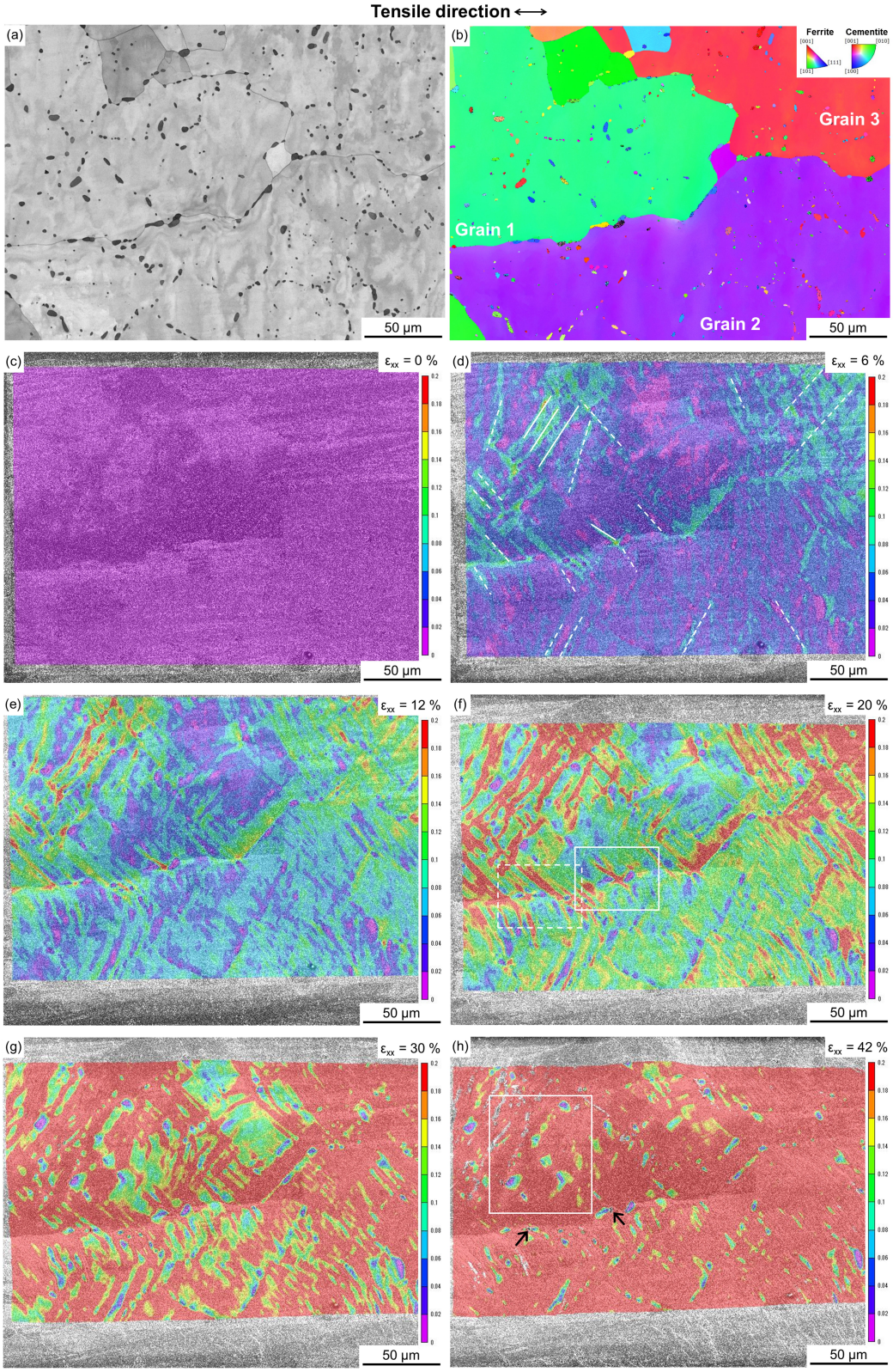


Fig. 6.3 The sequential DIC strain maps for the $\alpha + \theta$ microstructure; (a) an EBSD pattern quality map, (b) an EBSD IPF map of the same area, (c) to (h) represent equivalent strain maps at each macroscopic tensile strain.

a slip line across the upper and lower ferrite grains through the separated particle was observed. Judging from the IPF map, the crystal orientation of the cracked cementite is identical, meaning that the cementite particle was a single crystal, and that cracking had indeed occurred. By contrast, another cementite particle cracked at the grain boundary is shown in Figure 6.5, located where the dotted rectangle is in Figure 6.3 (f). The crack was detected at 16 % of macroscopic tensile strain (Figure 6.5 (d)). Comparing SEM images with the corresponding EBSD phase map and IPF map, one can see that the particle was composed of two different cementite grains, and the crack is at the cementite grain boundary.

Figure 6.6 represents ferrite and cementite particles after further deformation of 42 % macroscopic tensile strain. Figure 6.6 (a) and (b) are an in-lens SEM image and a strain map, respectively. Decohesion at ferrite/cementite boundary was observed in the area surrounded by circles. Figure 6.6 (c) shows the equivalent strain profile in the tensile direction. Like other boundaries, there was a steep strain gradient at the ferrite and cementite phase boundary, where the decohesion occurred in the end. This is because keeping cohesion at the boundary was difficult due to the rigidity of cementite, as deformation progressed.

Cementite particle cracking

The direction of cracking in cementite particles was investigated by EBSD. Figure 6.7 shows all four examples of single-grain cracked cementite. Figure 6.7 (a1), (b1), (c1), and (d1) are SEM images that captured for the first time cementite cracking in a set of pictures. To compensate for the displacement after deformation, the amount of rotation of particles was calculated, assuming that the change in shape of the rigid

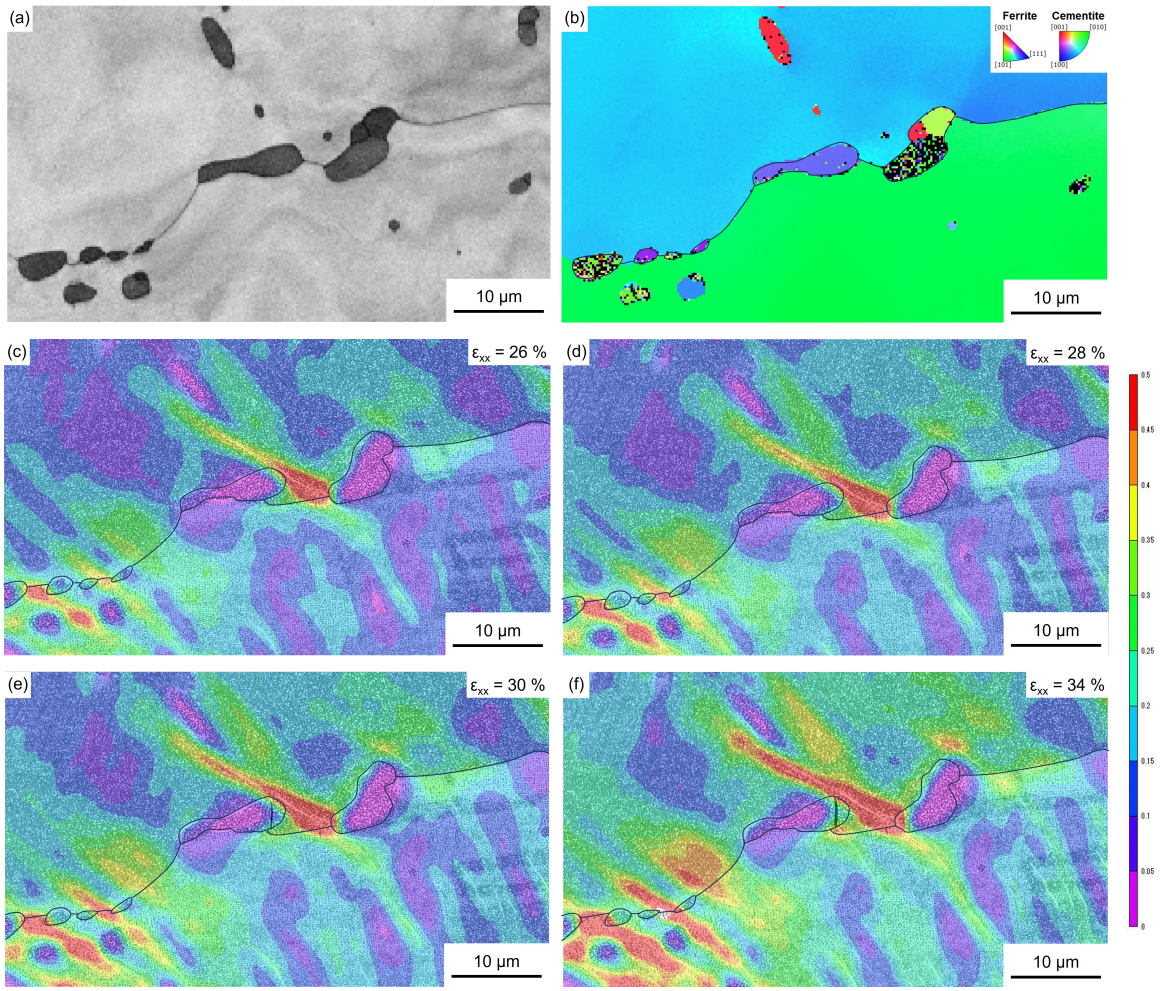


Fig. 6.4 A grain boundary cementite cracking related to ferrite slip activity; (a) an EBSD pattern quality map before tensile testing, (b) an EBSD IPF map of the same area, (c) to (f) demonstrate equivalent strain maps at each macroscopic tensile strain and its change before and after the cementite cracking.

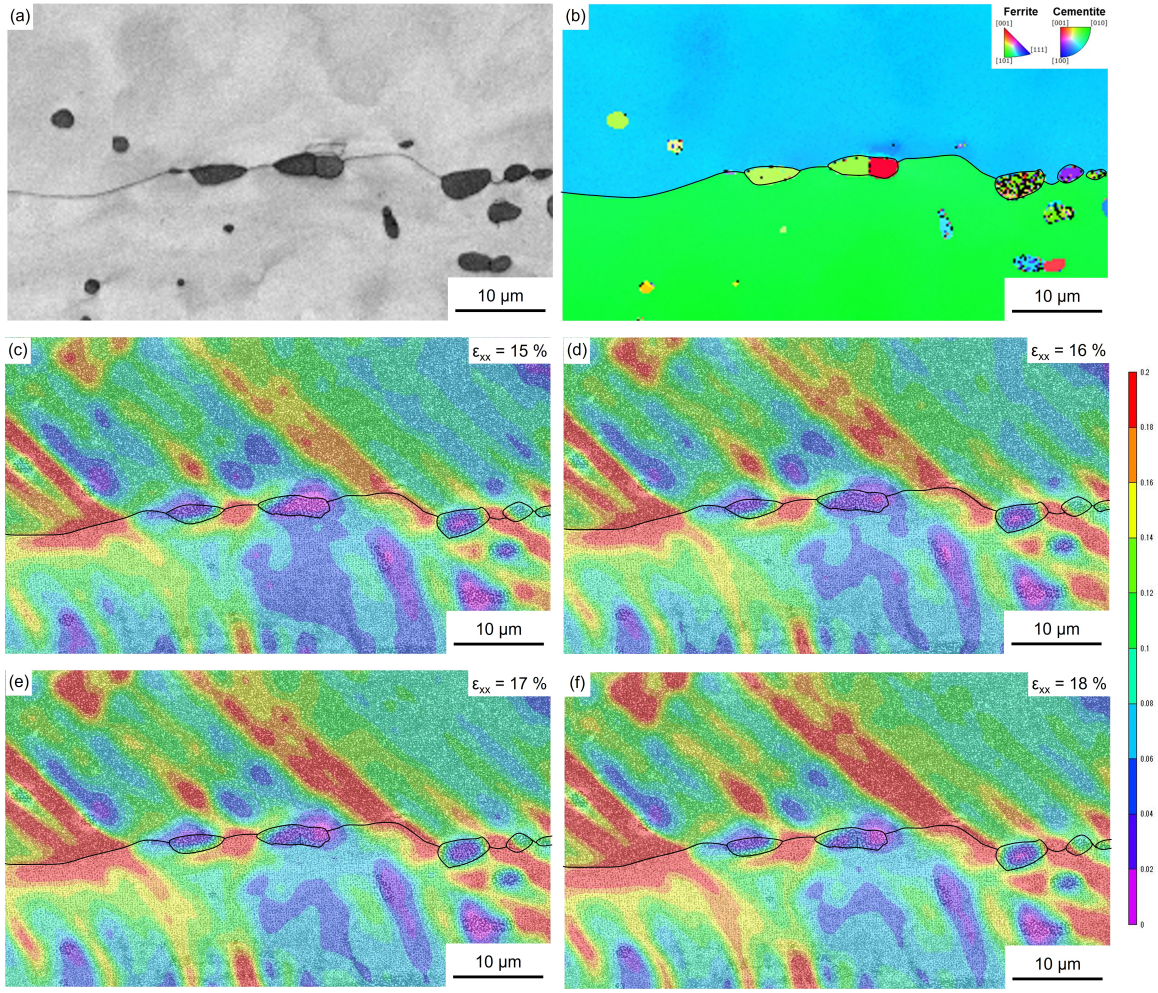


Fig. 6.5 Intergranular fracture of two-grain-combined cementite particle; (a) is an EBSD pattern quality map showing cementite particles coloured black. (b) is an EBSD IPF map of the same area. (c) to (f) show equivalent strain maps at each macroscopic tensile strain and its change before and after the cementite cracking.

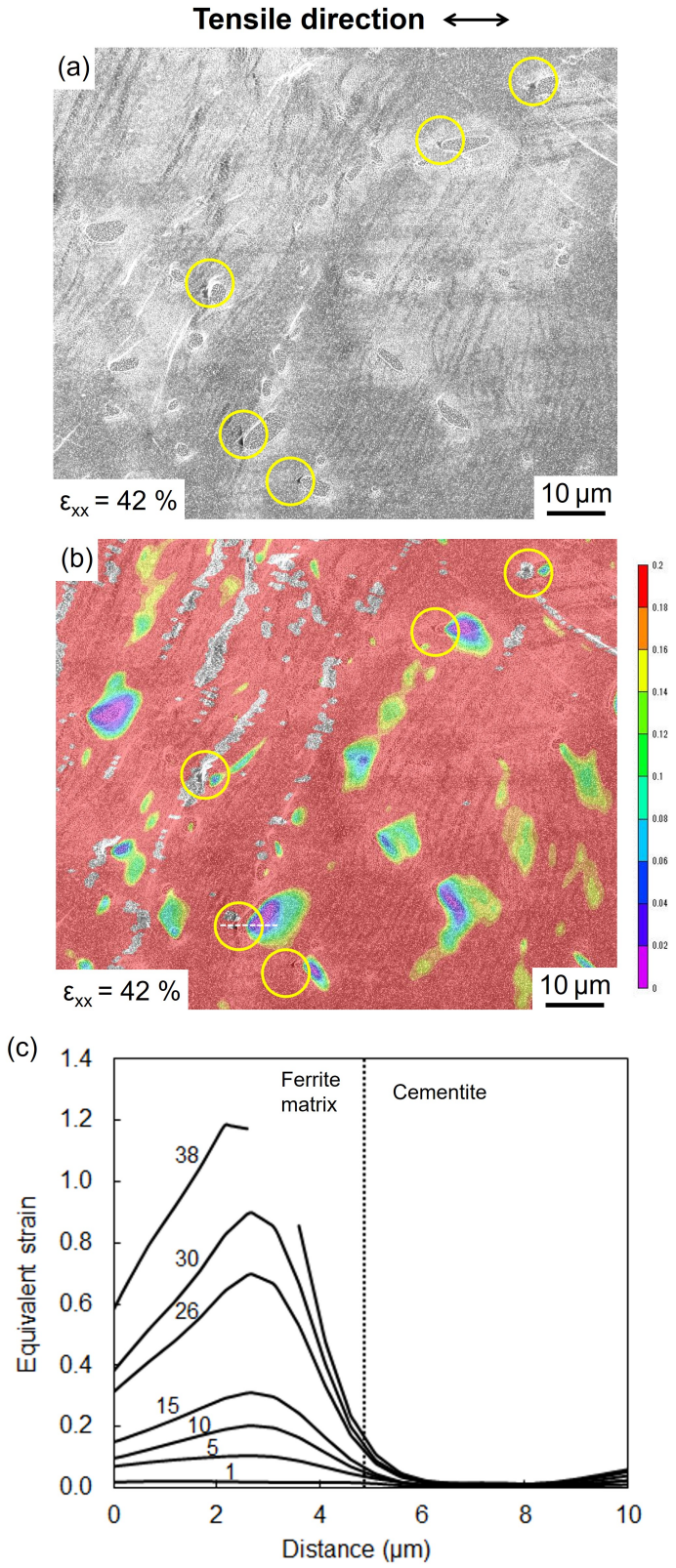


Fig. 6.6 Decohesion at ferrite and cementite interphase boundary; (a) is a SEM image showing the decohesion with circles, (b) is an equivalent strain map of the area, (c) display the strain profile along with the dotted line in (b).

cementite particles before and after deformation is negligible. Figure 6.7 (a2), (b2), (c2), and (d2) illustrate that processing. Red dotted lines were obtained after tilting to the degree that blue dotted lines, representing the initial cementite particles, came to fit best. The direction of the crack was rotated by the angle obtained and compared with the trace of the crystallographic plane of the initial cementite particles. Figure 6.7 (a3), (b3), (c3), and (d3) confirm that the plane trace of $\{101\}_\theta$ is fitted best to crack direction in all cases.

This result could be understood, too, as different from the results obtained in the post-mortem characterisation with HR-EBSD as shown in Figure 5.1, which indicated that fracture planes of cementite particles was matched well with $(010)_\theta$ most frequently followed by $\{101\}_\theta$. The former result was obtained under the cryogenic and high-strain rate conditions, whereas the current was performed at room temperature and with a slower strain rate. The preferred fracture plane of cementite may change due to the influence of deformation conditions, but this is an interesting topic for future work.

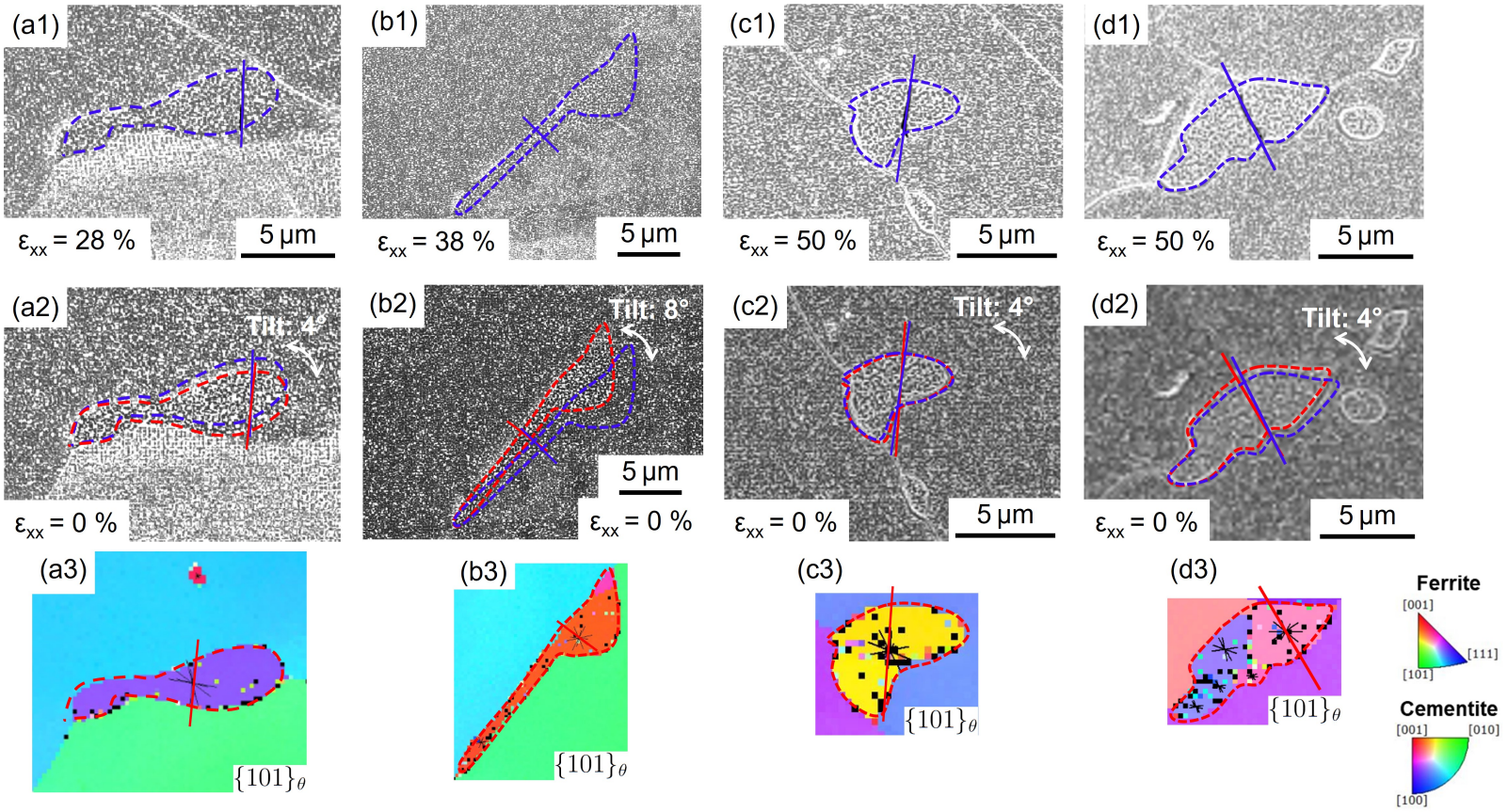


Fig. 6.7 The plane trace analysis with EBSD for cracked cementite particles; (a1), (b1), (c1), and (d1) are SEM images that captured first cementite cracking in a set of pictures for each particle, (a2), (b2), (c2), and (d2) show the amount of rotation of the particles through the deformation, (a3), (b3), (c3), and (d3) represent EBSD IPF map with cementite $\{101\}_\theta$ plane trace and the rotated crack directions.

6.3.3 Microstructural evolution with lamellar cementite

Figure 6.8 illustrates equivalent strain development in the $\alpha + P$ microstructure. Figure 6.8 (a) is an EBSD pattern quality map, where the pearlite phase can be recognised with its pattern, although cementite lamellae were not detected due to its spatial resolution. Figure 6.8 (b) is an EBSD IPF map of the same area. Figure 6.8 (c) to (h) demonstrate equivalent strain maps from DIC post-analysis. The tensile direction is left-right in the images, and the strain in that direction is displayed as ε_{xx}. When looking at the image after the macroscopic strain of 6 % (Figure 6.8 (d)), the earliest strain concentration was found at ferrite/pearlite phase boundaries. In addition to this, some areas in the pearlite, indicated by arrows in the image, experienced significantly localised high strain. As shown in Figure 6.8 (e), a wider area of the ferrite matrix has become deformed. Figure 6.8 (f) indicates that the strain is heterogeneous and thus widely distributed. Ferrite and its phase boundary to pearlite experienced relatively higher strain concentration, while the strain in pearlite remained low. However, the area in the middle of the pearlite at the centre of the image shows strain development to some extent. This may be caused by the interaction between the severely deformed ferrite just beneath the pearlite area. Going further, deformation above 30 %, deformation in ferrite became more intensive but still inhomogeneous, compared to the strain maps in the $\alpha + \theta$ microstructure under the same macroscopic tensile strain (Figure 6.3 (g) and (h)). That is, there was ferrite with a low strain level in this microstructure, while it was more evenly deformed in the counterpart. Strain concentration was mainly observed at the ferrite/pearlite interphase boundary, ferrite/ferrite boundary, in the ferrite surrounded by pearlite, and slip lines in ferrite grains. In the pearlite at the right-bottom of Figure 6.8 (g), there were high strain

areas crossing over the pearlite region. This is clear evidence that pearlite can be influenced by the surrounding ferrite matrix. In Figure 6.8 (h), deformation in pearlite has also progressed, but the high and low strain areas were still unevenly distributed.

To identify where strain accumulates preferentially, the DIC strain map after significant deformation was compared to its microstructure. Figure 6.9 (a) is a SEM image before tensile deformation with solid lines corresponding to pearlite block boundaries. Figure 6.9 (b) is a SEM image of the same area after heavy deformation to 60 % of macroscopic tensile strain. The pearlite block boundaries after deformation were carefully drawn by corresponding to the pattern of cementite lamellae before and after the deformation. Figure 6.9 (c) is a DIC equivalent strain map superimposed on the same SEM image as (b). The dotted lines represent colony boundaries, even though they are not perfectly drawn due to ambiguity from the 2D images, and to avoid overcomplexity when considering the magnification of the SEM image. From this figure, even when the specimen's macroscopic strain reached 60 %, pearlite had a significant deviation in strain. Strain concentration was observed preferentially at some block and colony boundaries.

6.4 Discussion

6.4.1 The effect of microstructural factors on cementite cracking

Particle size

In this study, the four cracked cementite particles were observed in total within several *in-situ* tensile test specimens. Figure 6.10 represents a statistical distribution of particle

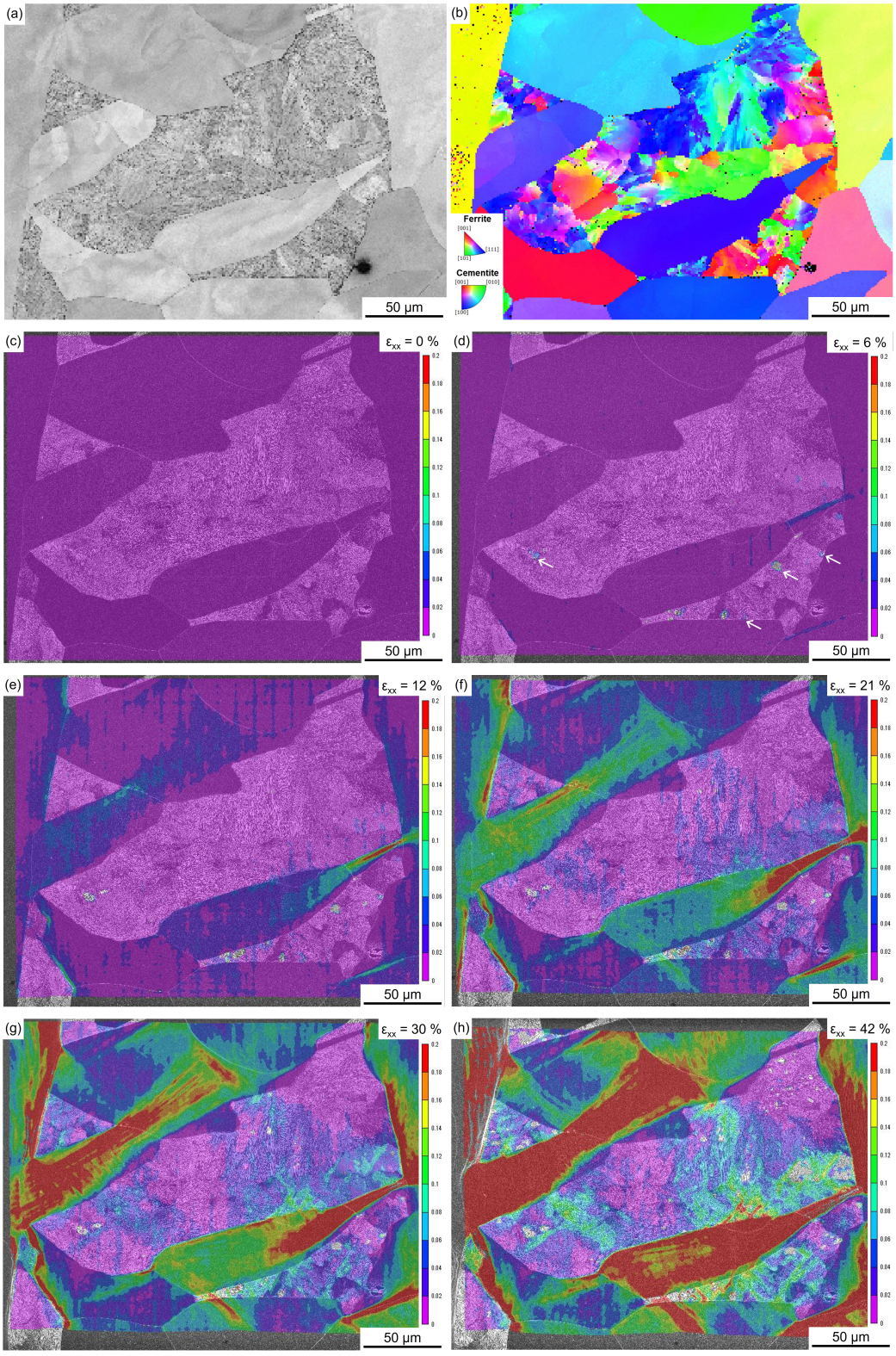


Fig. 6.8 The sequential DIC strain maps for the $\alpha + P$ microstructure; (a) an EBSD pattern quality map, (b) an EBSD IPF map of the same area, (c) to (h) demonstrate equivalent strain maps at each macroscopic tensile strain.

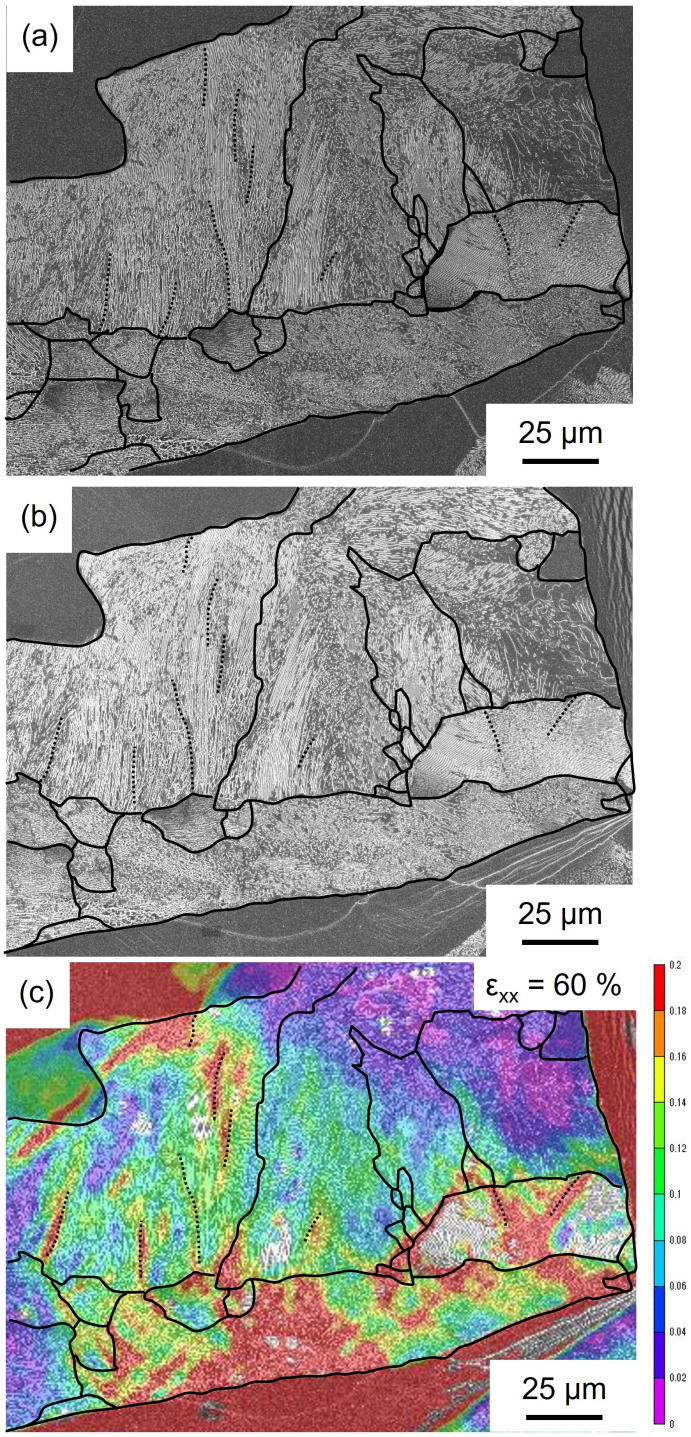


Fig. 6.9 Preferred strain concentration sites in pearlite microstructure; (a) a SEM image before tensile deformation with solid lines indicating pearlite block boundaries, (b) a SEM image of the same area after heavy deformation to 60 % of macroscopic tensile strain, (c) a DIC equivalent strain map superimposed on the image (b), showing strain concentration preferentially occurred not only at block boundaries (the solid lines) but also at colony boundaries (the dotted lines).

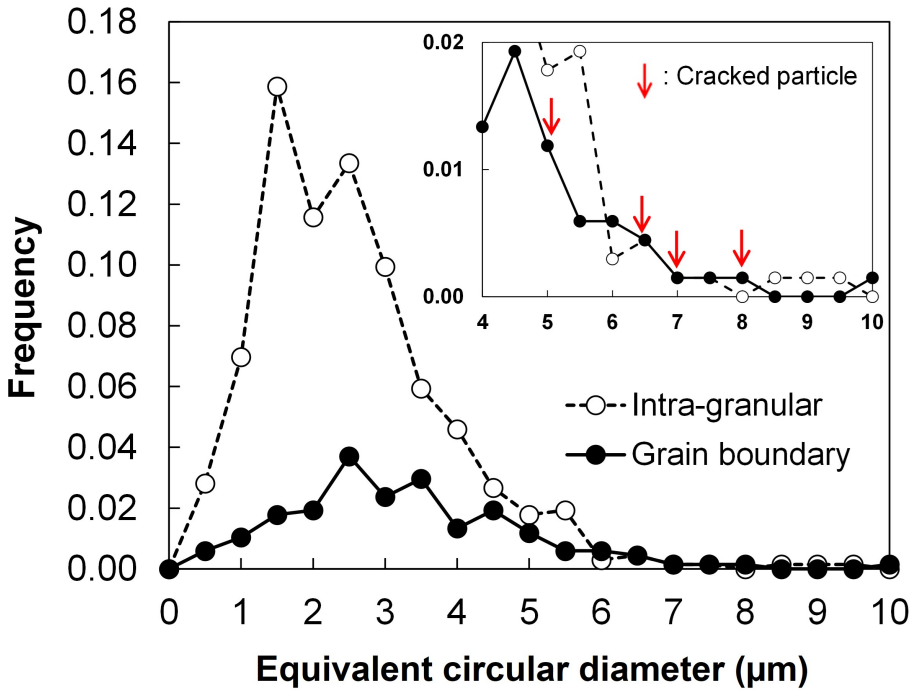


Fig. 6.10 A statistical distribution of apparent cementite particle size as equivalent circular diameter from areal intercept, and its location information. Arrows indicate the particles cracked in the end.

size with the information on where they are. Arrows indicate the particles cracked in the end. Although some intragranular cementite was larger than the ones in the ferrite grain boundary, all of the cracked cementite particles were located at ferrite grain boundaries. In terms of particle size, they were not necessarily the largest particles, although the cracked particles were not small among the range of detected cementite particle sizes. The trend that larger particles are likely to crack was the same as what the post-mortem analysis observed as shown in Figure 4.13. One possible reason for this may be that dislocation pile-up is easier close to larger particles.

Location of particles: Intragranular or at a grain boundary

Figure 6.11 shows the strain changes in the ferrite matrix and several cementite particles, including the one cracked in the end. Figure 6.11 (a) is an EBSD phase map showing the points as P1 to P6 being measured strain. Figure 6.11 (b) is a SEM image taken just after the cementite crack was detected. Figure 6.11 (c) shows the change in equivalent strain. The ferrite matrix (P6) experienced strain with almost the same degree as the macroscopic tensile strain. Meanwhile, the strain within cementite particles stayed low. However, there were some differences in strain development. Relatively, intragranular cementite particles (P3, P4, P5) were exposed to higher strain compared to the ones at a grain boundary (P1, P2). In the first place, although cementite is known to be very rigid and hard to deform plastically, the surrounding ferrite matrix may have led to the deformation in the cementite. Thus, cementite may be deformed to some extent when surrounded and constrained by a soft and deformable matrix. The deformability of cementite in such circumstances has been reported [262]. The smaller the intragranular cementite particles were, the more significant the strain they were exposed to. Although the influence of the free surface on the particle's strain detected cannot be completely eliminated, this tendency that the larger the particle the smaller the strain is intuitively reasonable. On the other hand, the strain of the grain boundary cementite remained low and stable even when the macroscopic tensile strain exceeded 20 %. The reason for the relatively low level of strain in grain boundary cementite can be understood in terms of constraint, in addition to the size. When the degree of constraint is high, the practical yield stress becomes high, which in turn leads to less deformation.

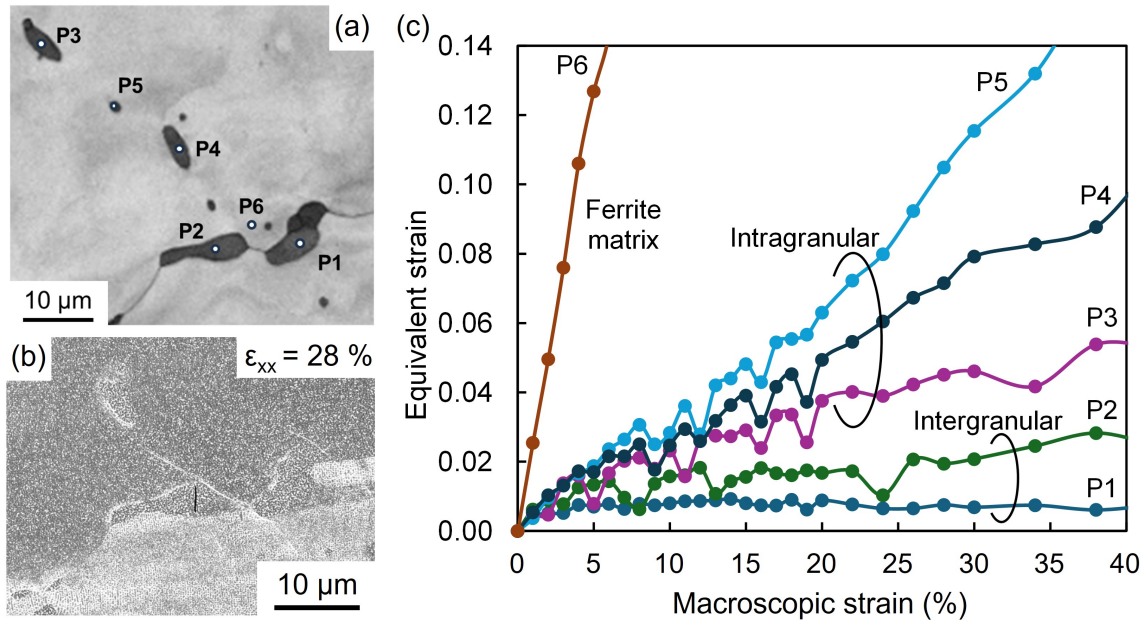
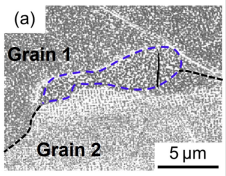
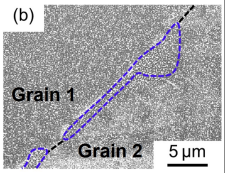
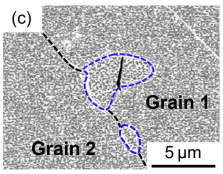
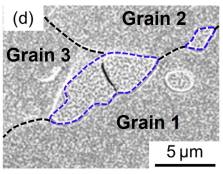


Fig. 6.11 The variations of equivalent strain at each measurement point in the $\alpha + \theta$ microstructure; (a) is an EBSD phase map showing the point as P1 to P6 being recorded strains, (b) a SEM image taken just after the cementite crack was detected, (c) the changes in equivalent strain at the each point.

Table 6.1 The Schmid factors of the ferrite grains adjacent cracked cementite particles

Maximum Schmid factor Grain 1 / Grain 2 or Grain 1 / Grain 2 / Grain 3	Specimen 1		Specimen 2	
	Particle 1	Particle 2	Particle 1	Particle 2
				
	0.50 / 0.45	0.50 / 0.44	0.50 / 0.50	0.48 / 0.46 / 0.40

Schmid factor of ferrite matrix

Table 6.1 shows the maximum Schmid factors of the adjacent ferrite grains for each cracked cementite. In this study, since slip lines visualised by the DIC high-strain pattern were fitted well to the plane trace of $\{110\}_\alpha$ and $\{112\}_\alpha$, these two slip systems were considered. It should be noted that at least one adjacent ferrite grain had the highest Schmid factor when a cementite particle was surrounded by two ferrite grains. This means dislocations can glide easily and pile-up at the grain boundary cementite particle due to slip deformation.

Combining this with the discussion in "Location of particles" of Section 6.4.1, from the perspectives of stress concentration due to dislocation pile-up and the relaxation of internal stress depending on a constraint, the grain boundary cementite can be understood to have lied in the preferable condition of being cracked. The cracked cementite particles are thought to be affected by the constraint from surrounding ferrite grains, and this could help internal stress coming from dislocation pile-up in the ferrite grain with the highest Schmid factor increase, which may have caused crack initiation.

6.4.2 The effect of lamellar orientation on local plasticity in pearlite

According to DIC analysis on the $\alpha + P$ microstructure, deformation occurred preferentially in ferrite rather than pearlite. As the degree of plastic deformation increased in the latter stages of deformation, strain distribution corresponding to the substructure of pearlite was observed. Specifically, strain concentration was observed along block boundaries and colony boundaries. This result is important and consistent with what has been reported [263, 264]. When considering the DBT behaviour, understanding the plastic deformation in pearlite in the early stage is equally vital. Therefore, focusing on the early stages of deformation, the local deformation behaviour in pearlite from microstructural perspectives is considered here.

Figure 6.12 shows equivalent strain distribution when the macroscopic tensile strain reached 9 %. Figure 6.12 (a) is a low magnification image to capture overall. Strain concentration is observed at certain ferrite grain boundaries as well as ferrite/pearlite phase boundaries, as indicated by arrows in the image. Still, at the same time, several areas were exposed to high strain values in the pearlite. Figure 6.12 (b) and (c) are magnified images of the two areas indicated by rectangles in (a). These figures show the ferrite/pearlite phase boundaries as black lines, pearlite block boundaries as blue lines, and pearlite colony boundaries as yellow lines, respectively. Strain is high in certain colonies in Figure 6.12 (b) and (c). While the strain in the surrounding pearlite is close to zero, the strain in the region is locally high, reaching 0.05.

The experimental result that strain concentration was observed not only at block boundaries but also at colony boundaries strongly suggests that the orientation of pearlite lamellae has an impact on local plasticity in pearlite. Figure 6.13 (a) shows the

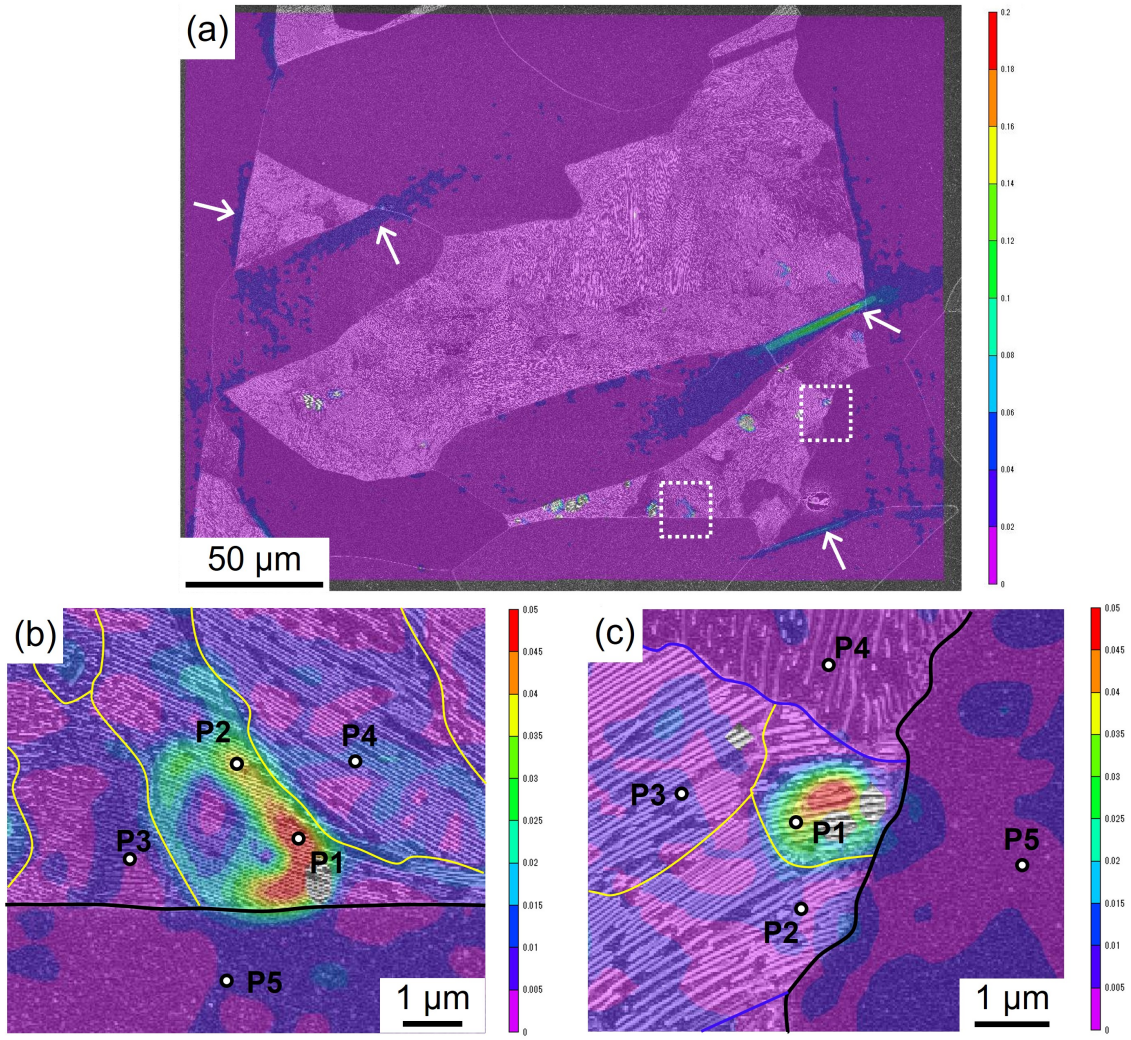


Fig. 6.12 Equivalent strain distribution when the macroscopic tensile strain reached 9 %; (a) is a low magnification image showing several areas in pearlite are exposed to high strain values, (b) and (C) are magnified images of the two areas indicated by the rectangles in (a), indicating strain is locally high in certain colonies.

variation of strain at each measurement point corresponding to Figure 6.12 (b). When looking at the early stage of the deformation until 10 % of macroscopic tensile strain, the strain of P1 and P2 in a specific colony reached the degree of 0.03 to 0.05 from the beginning. It increased continuously thereafter as deformation progressed. By way of comparison, the strain in the surrounding colonies stayed low and at most about 0.01. It should be noted that the strain level in the vicinity of the pearlite colony was higher than that in the ferrite adjacent to the pearlite containing the particular colony.

Figure 6.13 (b) represents the strain changes at each point corresponding to Figure 6.12 (c). The strain also reached about 0.04 at P1 in a specific colony, but the strain of the surrounding colonies and blocks remained low. In particular, the left and lower colonies had lamellae orientations similar to that of the colony of interest, but the Schmid factors were slightly lower (0.45 against 0.48). While the upper colony had the Schmid factor larger than that of interest, reaching 0.49, the lamellae orientation was significantly different. This result suggests that even if the Schmid factor is high enough, localised plastic deformation does not occur in the early stage unless the lamellae orientation is favourable for deformation at the same time.

As shown so far for the individual cases, Figure 6.14 summarises the relationship between the Schmid factors, the alignment of cementite lamellae, and the equivalent strain in many colonies when the macroscopic tensile strain reached 9 %. The alignment of cementite lamellae was defined here by the inclination angle ϕ of the lamellae with respect to the tensile axis. The figure clearly reveals that the strain concentration occurred in specific colonies where the conditions that the Schmid factor is high enough and that lamellae orientation is close to parallel to the tensile direction are both

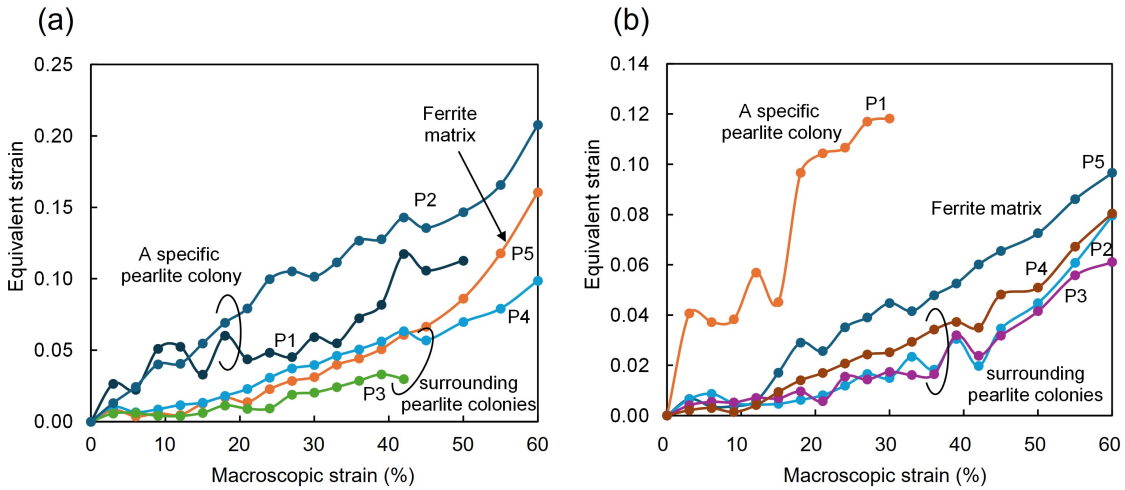


Fig. 6.13 The variations of equivalent strain at each measurement point in the $\alpha + P$ microstructure; (a) and (b) correspond to Figure 6.12 (b) and (c), respectively.

satisfied. This is why localised deformation was observed in the specific pearlite regions (colonies).

This is in accordance with the results shown in Figure 2.19. They reported that most pearlitic cracks were found where the cementite lamellae were parallel to the tensile axis ,and that the cracks were inclined to 45° against the tensile axis. In this *in-situ* tensile test, cracked lamellae were not observed. This may have been affected by ambient testing temperature rather than cryogenic one, and *in-situ* test under cryogenic conditions can be pursued as a future work. However, considering these two results - Figure 6.14 and Figure 2.19 - together, it is reasonable to think that deformation occurs preferentially in such specific colonies even from the early stage and forms pearlitic cracks over the colonies in the end.

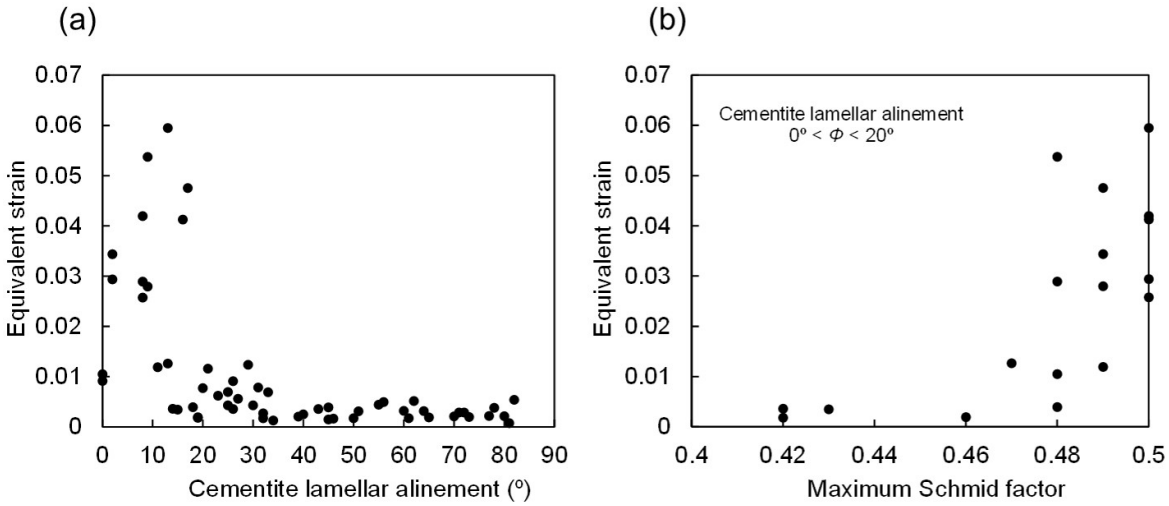


Fig. 6.14 The relationship between the Schmid factors, the alignment of cementite lamellae to the tensile axis, and equivalent strain of the colonies.

6.4.3 Comparison with two microstructures

A detailed investigation of plastic deformation behaviour in both microstructures has been done so far in this chapter. Here, statistical analysis is added to compare the plastic deformation in each microstructure and to discuss the development process of the local plasticity, coupled with the microstructural insights obtained. For this, DIC analysis was conducted separately in ferrite and cementite particles or pearlite. Figure 6.15 (a1) to (a5) and (b1) to (b5) show histograms of the strain distribution in the $\alpha + \theta$ and the $\alpha + P$ microstructures in almost the same condition in macroscopic tensile strain, respectively.

In the $\alpha + \theta$ microstructure, almost all of the ferrite is already deformed at the early stage of deformation of 6 % macroscopic tensile strain (Figure 6.15 (a1)). The average value of the strain of ferrite does not match the macroscopic tensile strain, which is thought to be due to the observation field being chosen randomly. As the macroscopic deformation progressed, the strain of ferrite became larger and its distribution broader

(Figure 6.15 (a2) and (a3)). Cementite particles also underwent strain of about 0.02, and the strain distribution in the particles became broader as deformation progressed. The increase in strain of cementite particles slowed down in the latter stage of deformation (Figure 6.15 (a4) and (a5)).

In the $\alpha + P$ microstructure, the deformation of ferrite was suppressed drastically compared to the $\alpha + \theta$ microstructure at equivalent macroscopic strain (Figure 6.15 (b1)). This is thought to be because the presence of the pearlite phase constrained plastic deformation in ferrite. Then, only slip deformation under quite favourable conditions occurred at the beginning. There were still areas of strain concentration that depended on its microstructure, such as the ferrite/pearlite phase boundary. Hence, the strain distribution of ferrite has a certain spread toward the higher strain side (Figure 6.15 (b1) and (b2)). As the deformation progressed, the strain in pearlite developed and became broadly distributed. Unlike the $\alpha + \theta$ microstructure, it was not stable at around 0.10 or less, and the strain in pearlite also increased as the macroscopic deformation progresses (Figure 6.15 (b2) to (b5)). Notably, in the very early stage of deformation, pearlite was subjected to the same level of strain of ferrite. At 6 % of macroscopic tensile strain (Figure 6.15 (b1)), almost all strains, both in the ferrite and pearlite, were less than 0.01, so the histogram is shown with the strain axes enlarged. The strain levels were about the same for both ferrite and pearlite, which was a distinct feature of this microstructure that was not seen in the $\alpha + \theta$ microstructure.

In summary, the $\alpha + \theta$ microstructure showed relatively uniform deformation behaviour throughout testing. In contrast, the $\alpha + P$ microstructure demonstrates non-uniform deformation behaviour that is more dependent on its microstructure. These characteristics of the $\alpha + P$ microstructure are thought to be due to the fact that

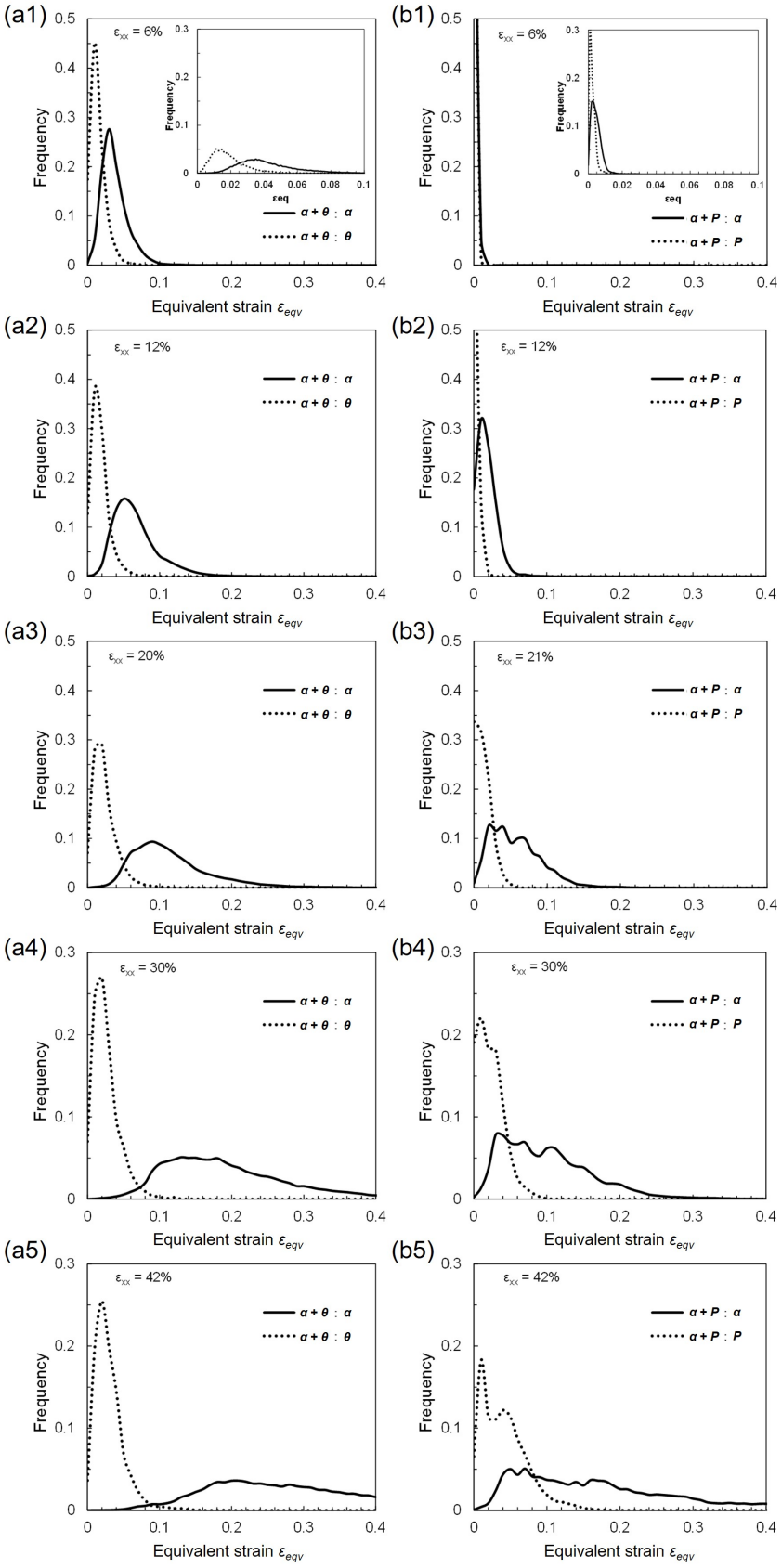


Fig. 6.15 Comparison of strain distribution with two different microstructures in a series of tensile test; (a) the $\alpha + \theta$ microstructure, (b) the $\alpha + P$ microstructure.

pearlite has a complex hierarchical microstructure. It is difficult to deform generally, but still, the development of strain in local regions that satisfy conditions such as the Schmid factor and lamellar orientation in pearlite is able to progress depending on the microstructure.

6.5 Summary and Conclusions

In this chapter, an *in-situ* observation technique was employed for the purpose of detecting and visualising local plasticity before cracking formation and comparing its development in the $\alpha + \theta$ and the $\alpha + P$ microstructures. The following specific conclusions can be drawn:

1. The $\alpha + \theta$ microstructure showed relatively uniform deformation behaviour throughout, whereas the $\alpha + P$ microstructure experienced non-uniform deformation behaviour that exhibited a greater microstructure dependence. This is thought to be due to the fact that pearlite has a complex hierarchical microstructure.

2. A statistical analysis for strain distribution found that the $\alpha + P$ microstructure has the following features compared to the $\alpha + \theta$ microstructure: (i) the deformation of ferrite phase is more limited, (ii) pearlite is subjected to a strain level equivalent to that of ferrite in the early stage of deformation, (iii) as the deformation progressed, the strain in pearlite continuously increases while the strain in cementite particle saturated.

3. As plastic deformation progressed, two types of fracture were observed in the $\alpha + \theta$ microstructure: (i) cracks in single crystal particles, and (ii) cracks at grain

boundaries in combined two cementite particles. Interface decohesion was also recognised within ferrite grains. A combination of *in-situ* observation and EBSD orientation analysis indicated that the fracture plane of all cracks in single crystal particles in this study is consistent with the $\{101\}_\theta$ plane trace.

4. From DIC and EBSD analyses, the cracked cementite particles were thought to be affected by the constraint from surrounding ferrite grains and the increase of internal stress arising from dislocation pile-up in the ferrite grain with the highest Schmid factor.

5. In the early stage of deformation, certain regions in pearlite were observed to experience high strains of several per cent, which are equivalent to or greater than those in ferrite at the same instant. Specifically, they were colonies where the Schmid factor was large enough and the lamellar orientations were close to parallel to the tensile direction.

Chapter 7

Conclusions and Future Work

7.1 Conclusion remarks

This research has aimed to improve our fundamental understanding of the relationship between the DBT behaviour of steel and its microstructure. To achieve this, with carefully designed test steels and cutting-edge high-resolution characterisation techniques, much attention has been paid to elucidating the effect of cementite morphology on the DBT behaviour of structural steel, focusing on local plasticity before a macroscopic brittle fracture occurs and how the microstructure affects it.

In Chapter 4, the DBT behaviour of the two microstructures - the $\alpha + \theta$ and the $\alpha + P$ - was investigated by tensile tests for a wide range of temperatures and strain rates, and the deformation and fracture behaviour of the DBT region was considered by thorough SEM observation. The activation energy of the DBT was calculated, and the controlling steps of the transition process were compared.

In Chapter 5, the characterisation conducted in Chapter 4 was further developed, and the local plastic deformation of cementite particles and in their vicinity was quanti-

fied using HR-EBSD. In addition, the early stage of the deformation process in pearlite was clarified by SEM-based TKD, which enables it to couple with crystallographic orientation information.

In Chapter 6, *in-situ* observation was conducted to visualise and analyse quantitatively the plastic deformation in the two microstructures. The strain distribution and its development were clearly stated. The effect of ferrite deformability on the cracking of cementite particles as well as the development of local plasticity in pearlite microstructure, and their influencing factors were clarified.

The temperature range of the DBT region was considerably wider for the $\alpha + P$ microstructure than for the $\alpha + \theta$ microstructure (Figure 4.2 and Table 4.2). The transition curves under the condition of 1×10^1/s in the strain rate are shown again in Figure 7.1 (a). Figure 7.1 (b) and (c) illustrate the summary of the deformation and fracture process in the DBT region derived from the experimental findings in this research. The significant difference is that pearlitic crack initiation can proceed in a ductile manner, as discussed in sections 5.4.3 and 5.4.4. This step should help pearlite have the ability to undergo continuous local plastic deformation rather than unstable crack initiation and its propagation unless tensile tests are conducted under completely brittle conditions.

In the $\alpha + \theta$ microstructure, the ferrite matrix can deform more freely than in the $\alpha + P$ microstructure around cementite particles to the extent of keeping compatibility between ferrite and cementite (Figure 5.3). From the perspectives of stress concentration due to dislocation pile-up and the relaxation of internal stress depending on a constraint, the grain boundary cementite lies in the preferable condition of being cracked rather than intragranular cementite. The constraint from surrounding ferrite grains affects

grain boundary cementite, and this could help internal stress arising from dislocation pile-up in the ferrite grain (Figure 5.12) with the highest Schmid factor increase (Figure 6.4 and Table 6.1). Once the internal stress of cementite reaches its fracture stress, a micrometre-order crack is generated. The fracture planes of the cementite particles observed in this study were $(010)_\theta$ and $\{101\}_\theta$ (Figure 5.1 and Figure 6.7). When under completely brittle conditions, the rate-controlling step is to generate cementite cracking (Figure 4.4 and Figure 4.8 (a)). However, in the lower region of the DBT, such a step is propagation of cementite crack (Figure 4.8 (b), Figure 4.9 (a) and (b)). The microstructure experiences relatively uniform deformation (Figure 6.3). When in the upper region of the DBT or more ductile conditions, voids nucleate at cementite crack or interfacial decohesion, then follow its growth and coalescence (Figure 4.3, Figure 4.8 (c) and (d), Figure 4.9 (c), and Figure 6.6).

In the $\alpha + P$ microstructure, a pearlite colony, with the cementite lamellae nearly parallel to the tensile axis and the highest Schmid factors, can deform from the beginning of the process (Figure 6.12 and Figure 6.14). Dislocation pile-up causes stress concentration on the slip planes of the ferrite in the colonies (Figure 5.7 and Figure 5.8). In this case, the fibre loading mechanism may be superimposed on the increase in the internal stress of cementite lamellae.The fracture surface of the cementite lamellae observed in this study was $\{101\}_\theta$ plane (Figure 5.8 (c)) This process seems to proceed in a brittle manner (Figure 5.14). Deformation is promoted by the cracked cementite lamellae (Figure 5.8 (b)). Dislocation increases around the fragmented lamellae (Figure 5.6 (a) and (b)), which leads to a void formation (Figure 5.6 (c)). The formation and coalescence of voids along the ferrite slip planes progresses (Figure 5.5 (c), Figure 4.12 (a) and (b)), eventually forming a shear crack corresponding to a

pearlite colonies (Figure 4.12 (c) and (d)). When the macroscopic fracture conditions are satifaied, brittle fracture occurs from such shearing cracks (Figure 4.6).

Once the internal stress of cementite reaches its fracture stress, a crack is generated in the $\alpha + \theta$ microstructure. Judged by Figure 5.3, the length for dislocations in ferrite to pile-up appears to reach, at least, tens of micrometre order. In contrast, the $\alpha + P$ microstructure has a sub-micrometre lamellar structure with the particular Pitch-Petch orientation relationship between ferrite and cementite (Figure 5.10), which restricts it from deforming freely and significantly. Hence, lamellar cementite is cracked after ferrite slip occurs in pearlite. This type of crack is lamella-thickness-order in size, and the pile-up length for dislocation in ferrite is significantly small due to the lamellar structure, while its counterpart is a relatively "sharp" micrometre-order crack corresponding a particle.

Crack length and length of slip plane for dislocation to pile-up have an influence on local fracture stress for crack in cementite to propagate ferrite/cementite boundary. The smaller the crack in size and the shorter the length of the slip plane for pile-up, the higher the local fracture stress for a crack to propagate at the ferrite/cementite boundary; that is, it should be much harder for a lamella-thickness-size crack formed in a cementite lamella to propagate the ferrite/cementite boundary in a brittle manner compared to a micrometre-size crack initiated at grain boundary cementite particle in the $\alpha+\theta$ microstructure. The micrometre-size sharp cracks are more likely to satisfy the local fracture stress condition. Once satisfied, brittle cracks propagate throughout the steel, resulting in a relatively steep ductile-brittle transition. By contrast in the $\alpha + P$ microstructure, lamellar cracking is less likely to propagate unstably throughout a colony and more, but rather, promotes further plastic deformation owing to stress and strain

concentration caused by the cracking. Once a lamellar crack formed, it enhances local plasticity much more (Figure 5.6 (b) and (c)) to produce additional defects like micro-void and/or another lamellar crack, forming a relatively "blunted" shear cracking over a pearlite colony in the end (Figure 4.12). Until a critical shearing crack is generated, this microstructure can experience a gradual and continuous deformation that occurs simultaneously in the specimen, resulting in a broader transition temperature range.

Furthermore, the root cause of pearlitic cracks formed in a ductile manner is the hierarchical microstructure of pearlite itself. As shown in Figure 6.14, in addition to the crystallographic orientation of ferrite (Schmid factor), the lamellae orientation to the tensile axis also affects the deformability of the pearlite colony. The degree of plastic deformation varies in units of pearlite colonies, which are the substructures of pearlite blocks. This means that some pearlite regions have relatively high deformability. At the same time, it prevents deformation from concentrating in one spot, which is all about a high anti-brittle fracture property. For this reason, while the deformation and fracture process in the $\alpha + \theta$ microstructure is relatively uniform, the process in the $\alpha + P$ microstructure is more dependent on its microstructure. In short, the process helps avoid significant strain and stress concentration, suppresses unstable crack nucleation and growth on the one hand, and thus fosters simultaneous and continuous local plastic deformation on the other hand, as long as it is not under completely brittle conditions. This explains why the $\alpha + P$ microstructure has a broader and more gradual transition range. The findings of this research are of significance because they can help design the microstructure of engineering steels better. Although it is difficult to state clear guidelines for microstructural control based on only what has been uncovered from this study, and further work is necessary, it is noteworthy that introducing cementite in a

lamellar form results in a wider DBT, which may ensure plastic deformation at lower temperatures than if the carbon were introduced in a spherical form. One of the most important things to avoid in steel structures under low-temperature circumstances is sudden and unstable fracture. In addition, from the perspective of countermeasures to earthquakes, having a certain degree of energy absorption capacity is desirable. In these senses, it is suggested that lamellar microstructures such as pearlite should be selected for the purpose.

As concluded in this chapter, the deformation and fracture mechanisms strongly depend on the microstructure (the morphology of cementite in this study). For the $\alpha + \theta$ microstructure, what has been found reinforces the reliability of the multiscale synthesis model approach proposed so far. For the $\alpha + P$ microstructure, it was succeeded to be clearly demonstrated that brittle fracture nucleation occurs in a ductile manner and is the factor that causes the difference in DBT behaviour. This strongly reinforces the model proposed by Miller and Smith. The influence of other factors on the pearlitic crack nucleation remains in future work, as will be described in the next section. However, it is important to keep combining the micromechanisms obtained from reliable microstructural characterisation into the multiscale synthesis model approach to improve the models.

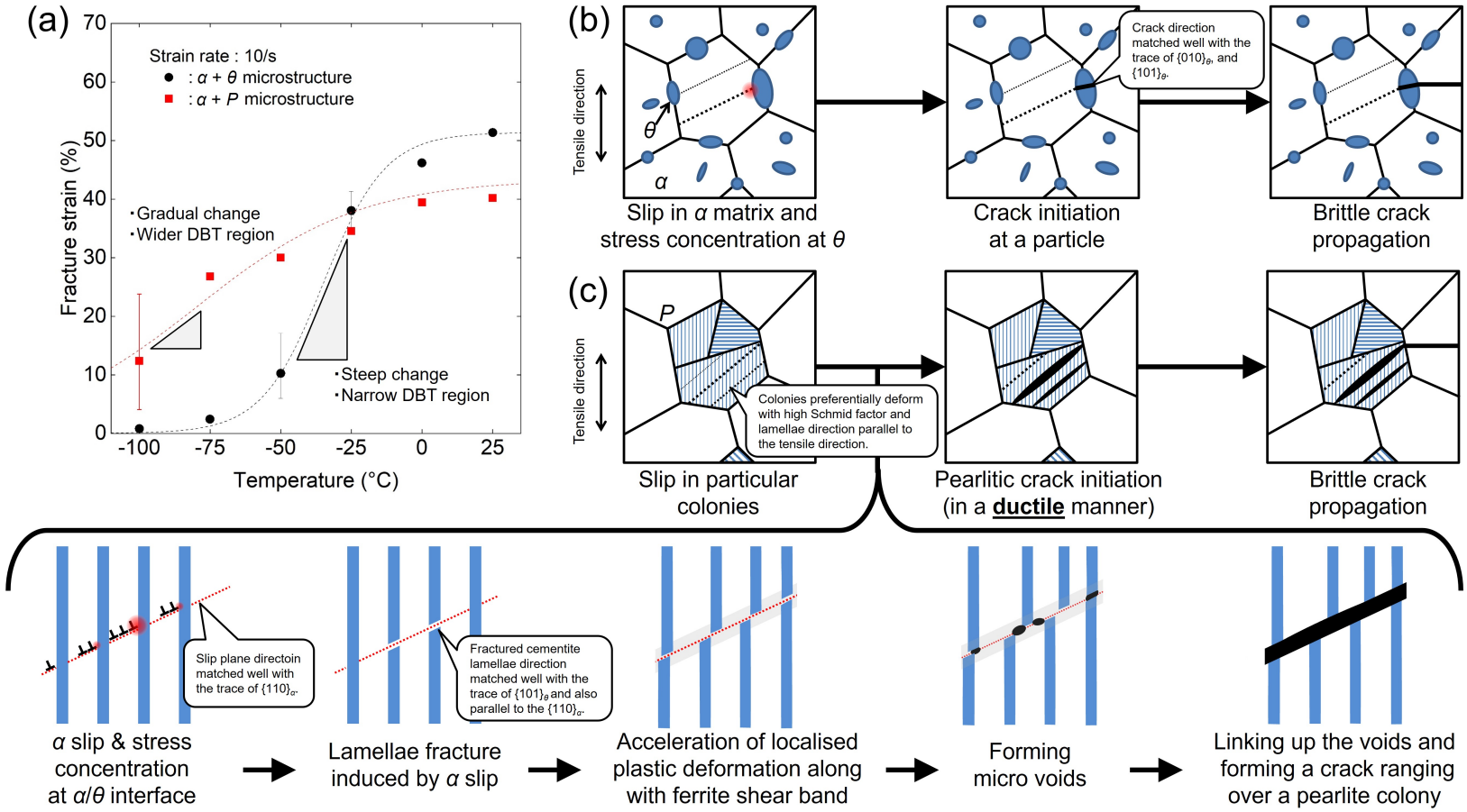


Fig. 7.1 The summary on how different the DBT behaviour is in the two cementite morphologies, the deformation and fracture process in the DBT region, and how the cementite morphology affected them. (a) is the transition curve of macroscopic fracture strain under the strain rate of 1×10^1/s as an example. (b) and (c) describe the process in the $\alpha + \theta$ and in the $\alpha + P$ microstructure, respectively.

7.2 Future Work

As mentioned in Chapter 1, the ultimate goal of the research is to fully understand the relationship between mechanical properties, microstructures, and manufacturing processes, and to design and utilise them on an industrial and commercial scale. With this ultimate goal in mind, this research of body has clarified the effect of cementite morphology on the DBT behaviour of structural steel using carefully designed tested steels and high-resolution characterisation techniques, with the aim of improving the basic understanding of the first relationship, between properties (the DBT behaviour) and microstructures (cementite morphology). This series of studies is expected to extend from the following point of view in the future.

7.2.1 Improvement of the experimental methodology to determin and consider T_{DBT}

As discussed in Section 4.4.3, the evaluation of the validity of T_{DBT} by using other definitions and improvement of the experimental methodology, followed by examining potential influencing factors for the activation energy.

7.2.2 Examination of the effects of other metallurgical factors

It is important to clarify the effects of other metallurgical factors that were not included in the current research in order to further expand the basic knowledge obtained in this study. Specifically, cementite fraction (carbon content), ferrite grain size, and stress triaxiality can be examined in the $\alpha + \theta$ and the $\alpha + P$ microstructures.

Cementite fraction: The cementite particles and fraction (thus, the number of

particles) in the $\alpha + \theta$ microstructure and the pearlite phase fraction in the $\alpha + P$ microstructure can be altered by changing the carbon content of tested steel. It is particularly interesting to study a large change in the pearlite fraction. If the carbon content is below 0.2 wt%, for example, the DBT behaviour is estimated to approach that of the $\alpha + \theta$ microstructure in principle, based on the findings obtained in the current study. On the other hand, if the carbon content is getting close to the eutectoid composition, i.e., under 100 % of pearlite microstructure, the transition curve is expected to become even broader. What about the $\alpha + \theta$ microstructure?

Ferrite grain size: What would happen if the ferrite grain size distribution changes to a level that is consistent with the engineering practice of common steels? Usually, cementite size becomes smaller as ferrite grain is refined. A further set of experiments might allow for more practical effects to be confirmed.

Stress triaxiality: It is considered meaningful to introduce a mechanical notch into the test specimen as in the Charpy impact test and investigate the transition behaviour under various mechanical conditions with different stress concentration. A set of mechanical tests were conducted without a mechanical notch in the current study. Adding a notch increases the tendency for brittle fracture, so the influence of the microstructure may be less likely to be observed. It is predicted that the transition temperature range of the $\alpha + P$ microstructure would narrow, and that a temperature range would emerge in which macroscopic brittle fracture occurs before pearlitic lamellar cracks form. However, this is a future work.

7.2.3 Extension to other microstructures

In addition to ferrite and pearlite, bainite and martensite are other important microstructures of steels in practical use. It is also crucial and valuable from an industrial point of view to expand fundamental knowledge of the DBT behaviour acquired in this study to such microstructures. Martensite is displacively transformed by quenching from austenite. Tempered martensite should be included, which is quenched and then tempered to precipitate cementites. Bainite is a low-temperature transformation product that is transformed in the intermediate region between ferrite and pearlite (diffusive transformation products) and martensite (displacive transformation products). Both martensite and bainite are systems consisting of BCC iron and cementites, which are the same as the microstructure scoped in the current study. However, since they transform at lower temperatures than the phases currently handled, the BCC phase becomes finer and tends to have substructures with specific crystal orientation relationships. Cementite also becomes finer. These things are the expected changes, and the subject of study becomes more complex. In addition, because the strength of steels with martensite and bainite is high, it may be necessary to consider not only cleavage fracture but also intergranular fracture as brittle failure. In such systems, it may be worthwhile to consider the effects of embrittlement elements such as phosphorus.

7.2.4 Generalisation by modelling of the DBT behaviour

From the two perspectives mentioned above, the influence of metallurgical factors, as well as stress concentration, will be fundamentally understood. Besides, modelling the DBT is also worth tackling. As a first step, the deformation and fracture process in each microstructure under each mechanical condition should be understood. Then,

based on a macroscopic model in which the DBT transition is determined by the relationship between yield stress and fracture stress, it may be possible to predict the transition temperature by utilising model or theoretical formulas for each stress that has been reported so far and in some cases by using improved formulas that reflect new insights obtained from upcoming experiments. It is surely important for industrial use to build a model that can predict the transition temperature and transition behaviour.

References

[1] M. L. Williams, G. A. Ellinger, Investigation of structural failures of welded ships, Welding Journal 32 (1953) 498–528.

[2] S. Garwood, Investigation of the MV *Kurdistan* casualty, Engineering Failure Analysis 4 (1) (1997) 3–24. doi:https://doi.org/10.1016/S1350-6307(96)00030-1.

[3] H. I. McHenry, Examination of a pressure vessel that ruptured at the Chicago refinery of the Union Oil Company on July 23 1984, Tech. rep., U.S. Department of Commerce, National Bureau of Standard (1986).

[4] J. F. Knott, Brittle fracture in structural steels: Perspectives at different size-scales, Philosophical Transactions of the Royal Society A: Mathematical, Physical and Engineering Sciences 373 (2015) 2038. doi:10.1098/rsta.2014.0126.

[5] B. Hayes, R. Phaal, Catastrophic failures of steel structure in industry: Case histories, TWI Report Summary 632/1998.

[6] I. Kawata, Numerical modeling of cleavage brittle fracture initiation in bainitic steel, Ph.D. thesis, The University of Tokyo (2017).

[7] K. Ushioda, M. Yoshimura, H. Kaidoh, K. Kimura, History of utilization of alloying elements in steels and its future perspectives (*in Japanese*), *Tetsu-To-Hagane* 100 (6) (2014) 716–727. doi:10.2355/tetsutohagane.100.716.

[8] Net zero by 2050: A roadmap for the global energy sector, Tech. rep., International Energy Agency, Paris. doi:https://www.iea.org/reports/net-zero-by-2050.

[9] Y. Liu, P. Zhou, B. Jeong, H. Wang, Design and optimization of a type-C tank for liquid hydrogen marine transport, International Journal of Hydrogen Energy 48 (89) (2023) 34885–34896. doi:https://doi.org/10.1016/j.ijhydene.2023.05.102.

[10] G. Notaro, J. Belgaroui, K. Marak, R. Tverra, S. Burthom, E. M. Sorhaug, CETO: Technology qualification of low-pressure CO_2 ship transport, Tech. rep., DNV (2022). doi:http://dx.doi.org/10.2139/ssrn.4272083.

[11] A. Valera-Medina, R. Banares-Alcantara, Techno-Economic Challenges of Green Ammonia as an Energy Vector, Academic Press, 2020. doi:https://doi.org/10.1016/C2019-0-01417-3.

[12] A. Pineau, A. Benzerga, T. Pardoen, Failure of metals I: Brittle and ductile fracture, Acta Materialia 107 (2016) 424–483. doi:https://doi.org/10.1016/j.actamat.2015.12.034.

[13] C. Zener, The micro-mechanism of fracture, in: Fracturing of metals, American Society of Metals, Cleaveland, Ohio, 1948, pp. 3–31.

[14] A. N. Stroh, The formation of cracks as a result of plastic flow, Proceedings of the Royal Society A; Mathematical, Physical and Engineering Sciences 223 (1954) 404–414. doi:doi.org/10.1098/rspa.1954.0124.

[15] A. H. Cottrell, Theory of brittle fracture in steel and similar metals, Transactions of The Metallurgial Society of AIME 212 (1958) 192–203.

[16] E. Smith, The nucleation and growth of cleavage microcracks in mild steel, Proceedings of Physical Basis of Yield and Fracture, 1966.

[17] J. A. Rinebolt, W. J. Harris, Effect of alloying elements on notch toughness of pearlitic steels, Transactions of America Society for Metals 43 (1951) 1175–1214.

[18] H. M. Banta, R. H. Frazier, C. H. Lorig, Some metallurgical aspects of ship steel quality, The Welding Journal Research Supplement 30 (2) (1951) 79–90.

[19] T. Gladman, I. D. McIvor, F. B. Pickering, Some aspects of the structure-property relationships in high-carbon ferrite-pearlite steels, Journal of The Iron and Steel Institute 210 (12) (1972) 916 – 930.

[20] G. T. Hahn, B. L. Averbach, W. S. Owen, M. Cohen, Initiation of cleavage microcracks in polycrystalline iron and steel, in: B. L. Averbach, D. K. Fekbeck, G. T. Hahn, D. A. Thomas (Eds.), Fracture, Proceedings of an international conference on the atomic mechanisms of fracture, MIT, MIT press, Swampscott, Massachusetts, 1959, p. 91.

[21] T. Lin, A. G. Evans, R. O. Ritchie, Stochastic modeling of the independent roles of particle size and grain size in transgranular cleavage fracture, Metallurgical and Materials Transactions A 18 (4) (1987) 641–651. doi:10.1007/BF02649480.

[22] K. Shibanuma, S. Aihara, S. Ohtsuka, Observation and quantification of crack nucleation in ferrite-cementite steel, ISIJ International 54 (7) (2014) 1719–1728. doi:10.2355/isijinternational.54.1719.

[23] J. R. Low, The relation of microstructure to brittle fracture, Transactions of American Society for Metals 46A (9) (1954) 163–179.

[24] A. J. Wilkinson, D. J. Dingley, G. Meaden, Strain mapping using electron backscatter diffraction, in: Electron Backscatter Diffraction in Materials Science, Springer, Boston, 2009, pp. 231–249.

[25] D. Curry, J. Knott, Effects of microstructure on cleavage fracture stress in steel, Metal Science 12 (11) (1978) 511–514. doi:10.1179/msc.1978.12.11.511.

[26] R. Ritchie, J. Knott, J. Rice, On the relationship between critical tensile stress and fracture toughness in mild steel, Journal of the Mechanics and Physics of Solids 21 (6) (1973) 395–410. doi:https://doi.org/10.1016/0022-5096(73)90008-2.

[27] F. M. Beremin, A. Pineau, F. Mudry, J. Devaux, Y. D'Escatha, P. Ledermann, A local criterion for cleavage fracture of a nuclear pressure vessel steel, Metallurgical Transactions A 14 (11) (1983) 2277–2287. doi:10.1007/BF02663302.

[28] A. J. Wilkinson, G. Meaden, D. J. Dingley, High-resolution elastic strain measurement from electron backscatter diffraction patterns: New levels of sensitivity, Ultramicroscopy 106 (4) (2006) 307–313. doi:https://doi.org/10.1016/j.ultramic.2005.10.001.

[29] A. J. Wilkinson, G. Meaden, D. J. Dingley, High resolution mapping of strains and rotations using electron backscatter diffraction, Materials Science and Technology 22 (11) (2006) 1271–1278. doi:10.1179/174328406X130966.

[30] R. Keller, R. Geiss, Transmission EBSD from 10 nm domains in a scanning electron microscope, Journal of Microscopy 245 (3) (2012) 245–251. doi:https://doi.org/10.1111/j.1365-2818.2011.03566.x.

[31] J. Liu, S. Lozano-Perez, A. J. Wilkinson, C. R. Grovenor, On the depth resolution of transmission Kikuchi diffraction (TKD) analysis, Ultramicroscopy 205 (2019) 5–12. doi:https://doi.org/10.1016/j.ultramic.2019.06.003.

[32] T. L. Anderson, Fracture Mechanics: Fundamentals and Applications, Fourth Edition, CRC Press, 2017. doi:https://doi.org/10.1201/9781315370293.

[33] K. Wallin, W. Baer, Evaluation of Charpy-V transition curve fitting based on distribution-free statistical assessment, International Journal of Pressure Vessels and Piping 206 (2023) 105079. doi:https://doi.org/10.1016/j.ijpvp.2023.105079.

[34] M. Karlík, P. Haušild, C. Prioul, M. Stöger-Pollach, Microstructure of low alloyed steel close to the fracture surface, Materials Science and Engineering: A 462 (1) (2007) 183–188, International Symposium on Physics of Materials, 2005. doi:https://doi.org/10.1016/j.msea.2006.04.149.

[35] T. L. Altshuler, J. W. Christian, W. Hume-Rothery, The mechanical properties of pure iron tested in compression over the temperature range 2 to 293 °K, Philosophical Transactions of the Royal Society of London. Series A, Mathematical and Physical Sciences 261 (1121) (1967) 253–287. doi:10.1098/rsta.1967.0004.

[36] Y. Kamimura, K. Edagawa, S. Takeuchi, Experimental evaluation of the Peierls stresses in a variety of crystals and their relation to the crystal structure, Acta Materialia 61 (1) (2013) 294–309. doi:https://doi.org/10.1016/j.actamat.2012.09.059.

[37] J. F. Knott, Fundamentals of Fracture Mechanics, Butterworth & Co Ltd., London, 1973.

[38] J. F. Knott, Micro-mechanisms of fracture and the fracture toughness of engineering alloys, in: D. M. R. Taplin (Ed.), Fracture 1977, Advances in research on the strength and fracture of materials, International Conference on Fracture, Pergamon Press, New York, 1978, pp. 61–92.

[39] T. Miyata, A. Otsuka, M. Mitsubayashi, T. Haze, S. Aihara, Prediction of fracture toughness of steels by local fracture criterion (*in Japanese*), *Zairyo* 37 (419) (1988) 897–903. doi:10.2472/jsms.37.897.

[40] A. A. Griffith, VI. The phenomena of rupture and flow in solids, Philosophical Transactions of the Royal Society of London. Series A, Containing Papers of a Mathematical or Physical Character 221 (1921) 163–198. doi:http://doi.org/10.1098/rsta.1921.0006.

[41] G. R. Irwin, Fracture dynamics, in: Fracturing of metals, American Society of Metals symposium, 1948, p. 143.

[42] E. Orowan, Fundamentals of brittle behavior in metals, in: Fatigue and Fracture of Metals, MIT symposium, New York, 1952, pp. 139–154.

[43] A. Needleman, V. Tvergaard, Numerical modeling of the ductile-brittle transition, International Journal of Fracture 101 (2000) 73–97. doi:https://doi.org/10.1023/A:1007520917244.

[44] J. M. Barsom, Development of the AASHTO fracture-toughness requirements for bridge steels, Engineering Fracture Mechanics 7 (3) (1975) 605–618. doi:https://doi.org/10.1016/0013-7944(75)90060-0.

[45] N. Petch, The influence of some substitutional alloys on the cleavage of ferritic steels, Acta Metallurgica 35 (8) (1987) 2027–2034. doi:https://doi.org/10.1016/0001-6160(87)90031-9.

[46] H. Li, R. H. Jones, J. P. Hirth, D. S. Gelles, Effect of loading mode on the fracture toughness of a ferritic/martensitic stainless steel, Metallurgical and Materials Transactions A 26 (9) (1995) 2259–2267. doi:10.1007/BF02671241.

[47] J. G. Schroth, J. P. Hirth, R. G. Hoagland, A. R. Rosenfield, Effect of loading mode on the fracture toughness of a ferritic/martensitic stainless steel, Metallurgical Transactions A 18 (6) (1987) 1061–1072. doi:10.1007/BF02668555.

[48] M. Manoharan, J. P. Hirth, A. Rosenfield, Combined mode I - mode III fracture toughness of a high carbon steel, Scripta Metallurgica 23 (5) (1989) 763–766. doi:https://doi.org/10.1016/0036-9748(89)90527-9.

[49] S. Raghavachary, A. R. Rosenfield, J. P. Hirth, Mixed mode I/III fracture toughness of an experimental rotor steel, Metallurgical Transactions A 21 (9) (1990) 2539–2545. doi:10.1007/BF02646999.

[50] M. Manoharan, On the relationship between mode I fracture toughness and susceptibility to mixed-mode fracture, Scripta Metallurgica et Materialia 26 (8) (1992) 1187–1192. doi:https://doi.org/10.1016/0956-716X(92)90561-R.

[51] J. F. Knott, Second-phase particles and the toughness of structural steels, in: Effect of Second-Phase Particles on the Mechanical Properties of Steel, the Iron and Steel Institute., 1971, pp. 44–53.

[52] J. F. Knott, Some effects of hydrostatic tension on the fracture behavior of mild steel, Journal of The Iron and Steel Institute 204 (1966) 104–111.

[53] F. B. Pickering, T. Gladman, Metallurgical developments in carbon steels, in: Spec. Rep. No.81, The Iron and Steel Institute, London, 1963, p. 10.

[54] F. B. Pickering, Physical Metallurgy and The Design of Steels, Applied Science Publishiers Ltd., London, 1978.

[55] M. Tanaka, K. Matsuo, N. Yoshimura, G. Shigesato, M. Hoshino, K. Ushioda, K. Higashida, Effects of Ni and Mn on brittle-to-ductile transition in ultralow-carbon steels, Materials Science and Engineering: A 682 (2017) 370–375. doi:https://doi.org/10.1016/j.msea.2016.11.045.

[56] W. Spitzig, W. Leslie, Solid-solution softening and thermally activated flow in alloys of Fe with 3at.% Co, Ni or Si, Acta Metallurgica 19 (11) (1971) 1143–1152. doi:https://doi.org/10.1016/0001-6160(71)90046-0.

[57] W. Gerberich, Y. Chen, D. Atteridge, T. Johnson, Plastic flow of Fe-binary alloys - II. Application of the description to the ductile-brittle transition, Acta Metallurgica 29 (6) (1981) 1187–1201. doi:https://doi.org/10.1016/0001-6160(81)90069-9.

[58] M. Tanaka, K. Maeno, K. Higashida, M. Fujikura, K. Ushioda, The increase in a brittle-to-ductile transition temperature in Fe-Al single crystals, ISIJ International 51 (6) (2011) 999–1004. doi:10.2355/isijinternational.51.999.

[59] J. Syarif, T. Tsuchiyama, S. Takaki, Mechanism of toughening in ferritic iron by solute copper at low temperature, ISIJ International 43 (7) (2003) 1100–1104. doi:10.2355/isijinternational.43.1100.

[60] E. O. Hall, The deformation and ageing of mild steel: III Discussion of results, Proceedings of the Physical Society. Section B 64 (9) (1951) 747–753. doi:10.1088/0370-1301/64/9/303.

[61] N. J. Petch, The cleavage strength of polycrystals, Journal of the Iron and Steel Institute 174 (1953) 25–28.

[62] J. Heslop, N. J. Petch, The ductile-brittle transition in the fracture of α-iron: 2, The Philosophical Magazine: A Journal of Theoretical Experimental and Applied Physics 3 (34) (1958) 1128–1136. doi:10.1080/14786435808237043.

[63] W. Jolley, Effect of Mn and Ni on impact properties of Fe and Fe-C alloys, Journal of The Iron and Steel Institute 206 (1968) 170–173.

[64] A. Takahashi, M. Iino, Improvement of yield strength-transition temperature balance by microstructural refinement, ISIJ International 36 (3) (1996) 341–346. doi:10.2355/isijinternational.36.341.

[65] S. Morito, H. Tanaka, R. Konishi, T. Furuhara, T. Maki, The morphology and crystallography of lath martensite in Fe-C alloys, Acta Materialia 51 (6) (2003) 1789–1799. doi:https://doi.org/10.1016/S1359-6454(02)00577-3.

[66] S. Morito, Y. Adachi, T. Ohba, Morphology and crystallography of sub-blocks in ultra-low carbon lath martensite steel, Materials Transactoins 50 (8) (2009) 1919–1923. doi:10.2320/matertrans.MRA2008409.

[67] Y. Ohmori, The crystallography of the bainite in a low-carbon low-alloy high strength steel, Transactions of the Iron and Steel Institute of Japan 13 (1) (1973) 56–62. doi:10.2355/isijinternational1966.13.56.

[68] T. Furuhara, H. Kawata, S. Morito, T. Maki, Crystallography of upper bainite in Fe–Ni–C alloys, Materials Science and Engineering: A 431 (1) (2006) 228–236. doi:https://doi.org/10.1016/j.msea.2006.06.032.

[69] N. Takayama, G. Miyamoto, T. Furuhara, Effects of transformation temperature on variant pairing of bainitic ferrite in low carbon steel, Acta Materialia 60 (5) (2012) 2387–2396. doi:https://doi.org/10.1016/j.actamat.2011.12.018.

[70] H. S.Matsuda, T.Inoue, Y.Okamura, Toughness and effective grain size in heat-treated low-alloy high-strength steels, in: Toward Improved Ductility and Toughness, Climax Molybdenum Development Company (Japan) Ltd., Tokyo, 1971, pp. 47–66.

[71] A. Kamada, N. Koshizuka, T. Funakoshi, Effect of austenite grain size and C content on the substructure and toughness of tempered martensite and bainite, Transactions of the Iron and Steel Institute of Japan 16 (8) (1976) 407–416. doi:10.2355/isijinternational1966.16.407.

[72] P. Brozzo, G. Buzzichelli, A. Mascanzoni, M. Mirabile, Microstructure and cleavage resistance of low-carbon bainitic steels, Metal Science 11 (4) (1977) 123–130. doi:10.1179/msc.1977.11.4.123.

[73] H. Ohtani, F. Terasaki, T. Kunitake, The microstructure and toughness of high tensile strength steels, Transactions of the Iron and Steel Institute of Japan 12 (2) (1972) 118–127. doi:10.2355/isijinternational1966.12.118.

[74] R. Dolby, J. F. Knott, Toughness of martensitic and maartensitic-bainitic microstructures with paticular reference to heat-affected zones in welded low alloy steel, Journal of The Iron and Steel Institute 210 (11) (1972) 857–865.

[75] J. John William Morris, On the ductile-brittle transition in lath martensitic steel, ISIJ International 51 (10) (2011) 1569–1575. doi:10.2355/isijinternational.51.1569.

[76] D. Hull, Twinning and fracture of single crystals of 3% silicon iron, Acta Metallurgica 8 (1) (1960) 11–18. doi:https://doi.org/10.1016/0001-6160(60)90133-4.

[77] R. Honda, Cleavage fracture in single crystals of silicon iron, Journal of the Physical Society of Japan 16 (7) (1961) 1309–1321. doi:10.1143/JPSJ.16.1309.

[78] A. Gilbert, G. Hahn, C. Reid, B. Wilcox, Twin-induced grain boundary cracking in b.c.c. metals, Acta Metallurgica 12 (6) (1964) 754–755. doi:doi.org/10.1016/0001-6160(64)90230-5.

[79] J. M. Berry, Cleavage step formation in brittle fracture propagation, Transactions of American Society for Metals 51 (9) (1959) 556–588.

[80] C. F. Tipper, The fracture of metals, Metallurgia 39 (231) (1949) 133–137.

[81] B. Marino, F. Mudry, A. Pineau, Experimental study of cavity growth in ductile rupture, Engineering Fracture Mechanics 22 (6) (1985) 989–996. doi:https://doi.org/10.1016/0013-7944(85)90038-4.

[82] L. Babout, W. Ludwig, E. Maire, J. Buffière, Damage assessment in metallic structural materials using high resolution synchrotron X-ray tomography, Nuclear Instruments and Methods in Physics Research Section B: Beam Interactions with Materials and Atoms 200 (2003) 303–307, Proceedings of the E-MRS 2002 Symposium I on Synchrotron Radiation and Materials Science. doi:https://doi.org/10.1016/S0168-583X(02)01692-0.

[83] L. Babout, Y. Brechet, E. Maire, R. Fougères, On the competition between particle fracture and particle decohesion in metal matrix composites, Acta Materialia 52 (15) (2004) 4517–4525. doi:https://doi.org/10.1016/j.actamat.2004.06.009.

[84] M. F. Ashby, Work hardening of dispersion-hardened crystals, The Philosophical Magazine: A Journal of Theoretical Experimental and Applied Physics 14 (132) (1966) 1157–1178. doi:10.1080/14786436608224282.

[85] C. Tasan, J. Hoefnagels, M. Diehl, D. Yan, F. Roters, D. Raabe, Strain localization and damage in dual phase steels investigated by coupled in-situ deformation experiments and crystal plasticity simulations, International Journal of Plasticity 63 (2014) 198–210. doi:https://doi.org/10.1016/j.ijplas.2014.06.004.

[86] N. Fujita, N. Ishikawa, F. Roters, C. C. Tasan, D. Raabe, Experimental–numerical study on strain and stress partitioning in bainitic steels with martensite–austenite constituents, International Journal of Plasticity 104 (2018) 39–53. doi:https://doi.org/10.1016/j.ijplas.2018.01.012.

[87] G. Lacroix, T. Pardoen, P. Jacques, The fracture toughness of TRIP-assisted multiphase steels, Acta Materialia 56 (15) (2008) 3900–3913. doi:https://doi.org/10.1016/j.actamat.2008.04.035.

[88] D. P. Fairchild, D. G. Howden, W. A. T. Clark, The mechanism of brittle fracture in a microalloyed steel: Part I. Inclusion-induced cleavage, Metallurgical and Materials Transactions A 31 (3) (2000) 641–652. doi:10.1007/s11661-000-0007-4.

[89] Y. Li, T. N. Baker, Effect of morphology of martensite–austenite phase on fracture of weld heat affected zone in vanadium and niobium microalloyed steels, Materials Science and Technology 26 (9) (2010) 1029–1040. doi:10.1179/026708309X12512744154360.

[90] D. Curry, J. Knott, The relationship between fracture toughness and microstructure in the cleavage fracture of mild steel, Metal Science 10 (1) (1976) 1–6. doi:10.1179/030634576790431453.

[91] D. Curry, Influence of microstructure on yield stress and cleavage fracture stress at -196°C of SA 508 class 2 pressure vessel steel, Metal science 18 (2) (1984) 67–76. doi:10.1179/030634584790420276.

[92] P. Bowen, S. Druce, J. Knott, Effects of microstructure on cleavage fracture in pressure vessel steel, Acta Metallurgica 34 (6) (1986) 1121–1131. doi:https://doi.org/10.1016/0001-6160(86)90222-1.

[93] C. McMahon Jr, M. Cohen, Initiation of cleavage in polycrystalline iron, Acta Metallurgica 13 (6) (1965) 591–604. doi:https://doi.org/10.1016/0001-6160(65)90121-5.

[94] M. Holzmann, J. Man, B. Vlach, J. Krumpos, Degradation of mechanical properties of cast Cr-Mo-V and Cr-W-V steam turbine casings after long-term service at elevated temperatures. part I: Tensile properties, brittle fracture strength and charpy impact properties, International Journal of Pressure Vessels and Piping 57 (2) (1994) 141–152. doi:https://doi.org/10.1016/0308-0161(94)90048-5.

[95] T. Lin, A. Evans, R. Ritchie, A statistical model of brittle fracture by transgranular cleavage, Journal of the Mechanics and Physics of Solids 34 (5) (1986) 477–497. doi:https://doi.org/10.1016/0022-5096(86)90013-X.

[96] T. Lin, A. Evans, R. Ritchie, Statistical analysis of cleavage fracture ahead of sharp cracks and rounded notches, Acta Metallurgica 34 (11) (1986) 2205–2216. doi:https://doi.org/10.1016/0001-6160(86)90166-5.

[97] A. R. Rosenfield, D. K. Shetty, A. J. Skidmore, Fractographic observations of cleavage initiation in the ductile-brittle transition region of a reactor-pressure-vessel steel, Metallurgical Transactions A 14 (9) (1983) 1934–1937. doi:10.1007/BF02645567.

[98] T. Wilshaw, C. Rau, A. Tetelman, A general model to predict the elastic-plastic stress distribution and fracture strength of notched bars in plane strain bending, Engineering Fracture Mechanics 1 (1) (1968) 191–211. doi:https://doi.org/10.1016/0013-7944(68)90025-8.

[99] A. G. Evans, Statistical aspects of cleavage fracture in steel, Metallurgical Transactions A 14 (7) (1983) 1349–1355. doi:10.1007/BF02664818.

[100] N. Petch, The influence of grain boundary carbide and grain size on the cleavage strength and impact transition temperature of steel, Acta Metallurgica 34 (7) (1986) 1387–1393. doi:https://doi.org/10.1016/0001-6160(86)90026-X.

[101] N. P. Allen, W. P. Regs, B. E. Hopkins, H. R. Tipler, Tensile and impact properties of high-purity iron-carbon-manganese alloys of low cabon content, Journal of the Iron and Steel Institute 174 (1953) 108–121.

[102] T. Takahashi, M. Nagumo, Y. Asano, Microstructures dominating the ductility of eutectoid pearlitic steels (*in Japanese*), Journal of the Japan Institute of Metals 42 (7) (1978) 708–715. doi:10.2320/jinstmet1952.42.7_708.

[103] J. Embury, R. Fisher, The structure and properties of drawn pearlite, Acta Metallurgica 14 (2) (1966) 147–159. doi:https://doi.org/10.1016/0001-6160(66)90296-3.

[104] A. Marder, B. Bramfitt, The effect of morphology on the strength of pearlite, Metallurgical Transactions A 7 (3) (1976) 365–372. doi:10.1007/BF02642832.

[105] G. Langford, Deformation of pearlite, Metallurgical Transactions A 8 (6) (1977) 861–875. doi:10.1007/BF02661567.

[106] J. M. Hyzak, I. M. Bernstein, The role of microstructure on the strength and toughness of fully pearlitic steels, Metallurgical Transactions A 7 (1976) 1217–1224. doi:doi.org/10.1016/j.matchar.2016.07.023.

[107] A. N. Turkalo, The morphology of brittle fracture in pearlite, bainite and martensite, Transactoins of the American Institute of Mining and Metallurgical Engineers 218 (1) (1960) 24–30.

[108] L. Miller, G. C. Smith, The process of crack initiation and effective grain size for cleavage fracture in pearlitic eutectoid steel, Metallurgical Transactions A 10 (11) (1979) 1653–1664. doi:10.1007/BF02811698.

[109] B. Garbarz, F. B. Pickering, Effect of pearlite morphology on impact toughness of eutectoid steel containing vanadium, Materials Science and Technology 4 (4) (1988) 328–334. doi:10.1179/mst.1988.4.4.328.

[110] V. N. Khiratkar, K. Mishra, P. Srinivasulu, A. Singh, Effect of inter-lamellar spacing and test temperature on the Charpy impact energy of extremely fine pearlite, Materials Science and Engineering: A 754 (2019) 622–627. doi:https://doi.org/10.1016/j.msea.2019.03.121.

[111] J. J. Lewandowski, A. W. Thompson, Effects of the prior austenite grain size on the ductility of fully pearlitic eutectoid steel, Metallurgical Transactions A 17 (3) (1986) 461–472. doi:10.1007/BF02643953.

[112] S. N. Doi, H. J. Kestenbach, Determination of the pearlite nodule size in eutectoid steels, Metallography 23 (2) (1989) 135–146. doi:https://doi.org/10.1016/0026-0800(89)90015-3.

[113] S. Zhou, Y. Zuo, Z. Li, X. Wang, Q. Yong, Microstructural analysis on cleavage fracture in pearlitic steels, Materials Characterization 119 (2016) 110–113. doi:https://doi.org/10.1016/j.matchar.2016.07.023.

[114] M. Umemoto, H. Ohtsuka, Mechanical properties of cementite, ISIJ International 62 (7) (2022) 1313–1333. doi:10.2355/isijinternational.ISIJINT-2022-048.

[115] E. J. Fasiska, G. A. Jeffrey, On the cementite structure, Acta Crystallographica 19 (3) (1965) 463–471. doi:10.1107/S0365110X65003602.

[116] A. Kagawa, T. Okamoto, Lattice parameters of cementite in Fe-C-X (X=Cr, Mn, Mo, and Ni) alloys, Transactions of the Japan Institute of Metals 20 (11) (1979) 659–666. doi:10.2320/matertrans1960.20.659.

[117] K. D. Litasov, S. V. Rashchenko, A. N. Shmakov, Y. N. Palyanov, A. G. Sokol, Thermal expansion of iron carbides, Fe_7C_3 and Fe_3C, at 297–911 K determined by in situ X-ray diffraction, Journal of Alloys and Compounds 628 (2015) 102–106. doi:https://doi.org/10.1016/j.jallcom.2014.12.138.

[118] M. Umemoto, S. E. Kruger, H. Ohtsuka, Ultrasonic study on the change in elastic properties of cementite with temperature and Mn content using nearly full density polycrystalline bulk samples, Materials Science and Engineering: A 742 (2019) 162–168. doi:https://doi.org/10.1016/j.msea.2018.10.115.

[119] B. Koo, Y. J. Chang, S. P. Hong, C. S. Kang, S. W. Jeong, W. Nam, I. Park, Y. Lee, K. H. Oh, Y. Kim, Experimental measurement of Young's modulus from a single crystalline cementite, Scripta Materialia 82 (2014) 25–28. doi:https://doi.org/10.1016/j.scriptamat.2014.03.013.

[120] J. Alkorta, J. G. Sevillano, Assessment of elastic anisotropy and incipient plasticity in Fe_3C by nanoindentation, Journal of Materials Research 27 (2012) 45–52. doi:10.1557/jmr.2011.284.

[121] S. A. Kim, W. L. Johnson, Elastic constants and internal friction of martensitic steel, ferritic-pearlitic steel, and α-iron, Materials Science and Engineering: A 452-453 (2007) 633–639. doi:https://doi.org/10.1016/j.msea.2006.11.147.

[122] C. Jiang, S. G. Srinivasan, A. Caro, S. A. Maloy, Structural, elastic, and electronic properties of Fe_3C from first principles, Journal of Applied Physics 103 (4) (2008) 043502. doi:10.1063/1.2884529.

[123] M. Nikolussi, S. Shang, T. Gressmann, A. Leineweber, E. Mittemeijer, Y. Wang, Z.-K. Liu, Extreme elastic anisotropy of cementite, Fe_3C: First-principles calculations and experimental evidence, Scripta Materialia 59 (8) (2008) 814–817. doi:https://doi.org/10.1016/j.scriptamat.2008.06.015.

[124] G. Ghosh, A first-principles study of cementite (Fe_3C) and its alloyed counterparts: Elastic constants, elastic anisotropies, and isotropic elastic moduli, AIP Advances 5 (8) (2015) 087102. doi:10.1063/1.4928208.

[125] K. O. E. Henriksson, N. Sandberg, J. Wallenius, Carbides in stainless steels: Results from *ab initio* investigations, Applied Physics Letters 93 (19) (2008) 191912. doi:10.1063/1.3026175.

[126] L. Huang, Y. Tu, X. Wang, X. Zhou, F. Fang, J. Jiang, Site preference of manganese in Mn-alloyed cementite, physica status solidi (b) 253 (8) (2016) 1623–1628. doi:https://doi.org/10.1002/pssb.201552675.

[127] L. Mauger, J. E. Herriman, O. Hellman, S. J. Tracy, M. S. Lucas, J. A. Muñoz, Y. Xiao, J. Li, B. Fultz, Phonons and elasticity of cementite through the Curie temperature, Physical Review B 95 (2017) 024308. doi:10.1103/PhysRevB.95.024308.

[128] S. K. R. Patil, S. V. Khare, B. R. Tuttle, J. K. Bording, S. Kodambaka, Mechanical stability of possible structures of PtN investigated using first-principles calculations, Physical Review B 73 (2006) 104118. doi:10.1103/PhysRevB.73.104118.

[129] J. J. Adams, D. S. Agosta, R. G. Leisure, H. Ledbetter, Elastic constants of monocrystal iron from 3 to 500 K, Journal of Applied Physics 100 (11) (2006) 113530. doi:10.1063/1.2365714.

[130] A. Keh, Imperfections and plastic deformation of cementite in steel, Acta Metallurgica 11 (9) (1963) 1101–1103. doi:https://doi.org/10.1016/0001-6160(63)90201-3.

[131] Z. Nishiyama, A. Kore'eda, S. Katagiri, Study of plane defects in the cementite by transmission electron microscopy, Transactions of the Japan Institute of Metals 5 (2) (1964) 115–121. doi:10.2320/matertrans1960.5.115.

[132] A. Koréeda, K. Shimizu, Dislocations in cementite, The Philosophical Magazine: A Journal of Theoretical Experimental and Applied Physics 17 (149) (1968) 1083–1086. doi:10.1080/14786436808223185.

[133] A. Inoue, T. Ogura, K. Masumoto, Lattice defects and deformation and fracture behavior of cementite in steel (*in Japanese*), Bulletin of the Japan Institute of Metals 13 (9) (1974) 653–664. doi:10.2320/materia1962.13.653.

[134] A. Inoue, T. Ogura, T. Masumoto, Transmission electron microscope study on deformation and fracture of cementite in cold-rolled steels, Transactions of the Japan Institute of Metals 17 (3) (1976) 149–157. doi:10.2320/matertrans1960.17.149.

[135] A. Inoue, T. Ogura, T. Masumoto, Burgers vectors of dislocations in cementite crystal, Scripta Metallurgica 11 (1) (1977) 1–5. doi:https://doi.org/10.1016/0036-9748(77)90002-3.

[136] J. Sevillano, Room temperature plastic deformation of pearlitic cementite, Materials Science and Engineering 21 (1975) 221–225. doi:https://doi.org/10.1016/0025-5416(75)90218-9.

[137] A. Inoue, T. Ogura, T. Masumoto, Deformation and fracture behaviours of cementite, Transactions of the Japan Institute of Metals 17 (10) (1976) 663–672. doi:10.2320/matertrans1960.17.663.

[138] A. Inoue, T. Ogura, T. Masumoto, Microstructures of deformation and fracture of cementite in pearlitic carbon steels strained at various temperatures, Metallurgical Transactions A 8 (11) (1977) 1689–1695. doi:10.1007/BF02646871.

[139] S. Tagashira, K. Sakai, T. Furuhara, T. Maki, Deformation microstructure and tensile strength of cold rolled pearlitic steel sheets, ISIJ International 40 (11) (2000) 1149–1156. doi:10.2355/isijinternational.40.1149.

[140] L. E. Kar'kina, T. A. Zubkova, I. L. Yakovleva, Dislocation structure of cementite in granular pearlite after cold plastic deformation, The Physics of Metals and Metallography 114 (3) (2013) 234–241. doi:10.1134/S0031918X13030095.

[141] A. Mussi, P. Cordier, S. Ghosh, N. Garvik, B. C. Nzogang, P. Carrez, S. Garruchet, Transmission electron microscopy of dislocations in cementite deformed at high pressure and high temperature, Philosophical Magazine 96 (17) (2016) 1773–1789. doi:10.1080/14786435.2016.1177670.

[142] M. Umemoto, K. Tuchiya, Fundamental properties of cementite and their present understanding (*in Japanese*), *Tetsu-To-Hagane* 88 (3) (2002) 117–128. doi:10.2355/tetsutohagane1955.88.3_117.

[143] T. Sato, T. Nishizawa, J. Ishihara, A study on hardness of carbides in iron and steel (*in Japanese*), Transactions of the Japan Institute of Metals 23 (7) (1959) 403–407. doi:10.2320/jinstmet1952.23.7_403.

[144] K. B. Gove, J. A. Charles, The high-temperature hardness of various phases in steel, Metals Technology 1 (1) (1974) 279–283. doi:10.1179/030716974803287834.

[145] M. Yakushiji, Y. Kondo, H. Matsumoto, T. Okamoto, The hardness of cementite at elevated temparatures (*in Japanese*), Transactions of the Japan Institute of Metals 39 (6) (1975) 606–608. doi:10.2320/jinstmet1952.39.6_606.

[146] A. Kagawa, T. Okamoto, Hot hardness of cementite, Journal of Materials Science 18 (1) (1983) 225–230. doi:10.1007/BF00543829.

[147] M. Umemoto, Z. Liu, K. Masuyama, K. Tsuchiya, Influence of alloy additions on production and properties of bulk cementite, Scripta Materialia 45 (4) (2001) 391–397. doi:https://doi.org/10.1016/S1359-6462(01)01016-8.

[148] J. J. Coronado, S. A. Rodríguez, Cementite characterization with chromium and vanadium contents using indentation technique, Journal of Iron and Steel Research International 22 (4) (2015) 366–370. doi:10.1016/S1006-706X(15)30013-3.

[149] A. Fernández-Vicente, M. Pellizzari, J. Arias, Feasibility of laser surface treatment of pearlitic and bainitic ductile irons for hot rolls, Journal of Materials Processing Technology 212 (5) (2012) 989–1002. doi:https://doi.org/10.1016/j.jmatprotec.2011.11.013.

[150] L. Kaeghele, A. Tetelman, A statistical investigation of microcrack formation, Acta Metallurgica 17 (4) (1969) 463–475. doi:https://doi.org/10.1016/0001-6160(69)90028-5.

[151] T. Lindley, G. Oates, C. Richards, A critical of carbide cracking mechanisms in ferride/carbide aggregates, Acta Metallurgica 18 (11) (1970) 1127–1136. doi:https://doi.org/10.1016/0001-6160(70)90103-3.

[152] J. Gurland, Observations on the fracture of cementite particles in a spheroidized 1.05%C steel deformed at room temperature, Acta Metallurgica 20 (5) (1972) 735–741. doi:https://doi.org/10.1016/0001-6160(72)90102-2.

[153] A. S. Argon, J. Im, A. Needleman, Distribution of plastic strain and negative pressure in necked steel and copper bars, Metallurgical Transactions A 6 (4) (1975) 815–824. doi:10.1007/BF02672305.

[154] A. S. Argon, J. Im, Separation of second phase particles in spheroidized 1045 steel, Cu-0.6pct Cr alloy, and maraging steel in plastic straining, Metallurgical Transactions A 6 (4) (1975) 839–851. doi:10.1007/BF02672307.

[155] A. H. Cottrell, A theory of cementite, Materials Science and Technology 9 (4) (1993) 277–280. doi:10.1179/mst.1993.9.4.277.

[156] S. Lee, S. Kim, B. Hwang, B. Lee, C. Lee, Effect of carbide distribution on the fracture toughness in the transition temperature region of an SA 508 steel, Acta Materialia 50 (19) (2002) 4755–4762. doi:https://doi.org/10.1016/S1359-6454(02)00313-0.

[157] W. H. Bruckner, The micro-mechanism of fracture in the tension-impact test, The Welding Journal 29 (1950) 467.

[158] A. R. Rosenfield, E. Votava, G. T. Hahn, Slip-induced crack formation in mild steel, Transactions of American Society for Metals 61 (4) (1968) 807–815.

[159] L. Miller, G. C. Smith, Tensile fractures in carbon steels, Journal of the Iron and Steel Institute 208 (1970) 998–1005.

[160] Y. Ohmori, F. Terasaki, Effects of nickel and manganese on cleavage fracture of ferritic-pearlitic steels, Transactions of the Iron and Steel Institute of Japan 16 (10) (1976) 561–568. doi:10.2355/isijinternational1966.16.561.

[161] K. Shibanuma, Y. Nemoto, T. Hiraide, K. Suzuki, S. Aihara, Investigation of micro-crack initiation as a trigger of cleavage fracture in ferrite-pearlite steels, ISIJ International 57 (2) (2017) 365–373. doi:10.2355/isijinternational.ISIJINT-2016-396.

[162] Y. Nemoto, K. Shibanuma, K. Suzuki, S. Sadamatsu, Y. Adachi, S. Aihara, 3D observation of micro-cracks as cleavage fracture initiation site in ferrite-pearlite steel, ISIJ International 57 (4) (2017) 746–754. doi:10.2355/isijinternational.ISIJINT-2016-607.

[163] D. M. Alexander, I. M. Bermstein, The cleavage plane of pearlite, Metallurgical Transactions A 13 (10) (1982) 1865–1868. doi:10.1007/BF02647843.

[164] P. Błoński, A. Kiejna, Calculation of surface properties of bcc iron, Vacuum 74 (2) (2004) 179–183, Proceedings of the International Workshop on Surface Physics: Metals on Solid Surfaces. doi:https://doi.org/10.1016/j.vacuum.2003.12.118.

[165] P. Błoński, A. Kiejna, Structural, electronic, and magnetic properties of bcc iron surfaces, Surface Science 601 (1) (2007) 123–133. doi:https://doi.org/10.1016/j.susc.2006.09.013.

[166] P. Mohseni, J. K. Solberg, M. Karlsen, O. M. Akselsen, E. Østby, Application of combined EBSD and 3D-SEM technique on crystallographic facet analysis of steel at low temperature, Journal of Microscopy 251 (1) (2013) 45–56. doi:https://doi.org/10.1111/jmi.12041.

[167] J. Nohava, P. Haušild, M. Karlík, P. Bompard, Electron backscattering diffraction analysis of secondary cleavage cracks in a reactor pressure vessel steel, Materials Characterization 49 (3) (2002) 211–217. doi:https://doi.org/10.1016/S1044-5803(02)00360-1.

[168] I. R. Vatne, A. Stukowski, C. Thaulow, E. Østby, J. Marian, Three-dimensional crack initiation mechanisms in bcc-Fe under loading modes I, II and III, Materials Science and Engineering: A 560 (2013) 306–314. doi:https://doi.org/10.1016/j.msea.2012.09.071.

[169] C. H. Ersland, I. R. Vatne, C. Thaulow, Atomistic modeling of penny-shaped and through-thickness cracks in bcc iron, Modelling and Simulation in Materials Science and Engineering 20 (7) (2012) 075004. doi:10.1088/0965-0393/20/7/075004.

[170] R. K. Barik, A. Ghosh, Md. Basiruddin Sk, S. Biswal, A. Dutta, D. Chakrabarti, Bridging microstructure and crystallography with the micromechanics of cleavage fracture in a lamellar pearlitic steel, Acta Materialia 214 (2021) 116988. doi:https://doi.org/10.1016/j.actamat.2021.116988.

[171] F. P. L. Kavishe, T. J. Baker, Micromechanism of cleavage fracture in fully pearlitic steels, Materials Science and Technology 2 (6) (1986) 583–588. doi:10.1179/mst.1986.2.6.583.

[172] J. J. Lewandowski, A. W. Thompson, Microstructural effects on the cleavage fracture stress of fully pearlitic eutectoid steel, Metallurgical Transactions A 17 (610) (1986) 1769–1786. doi:10.1007/BF02817275.

[173] A. W. Thompson, J. F. Knott, Micromechanisms of brittle fracture, Metallurgical Transactions A 24 (3) (1993) 524–534. doi:10.1007/BF02656622.

[174] M. A. Linaza, J. M. Rodriguez-Ibabe, J. J. Urcola, Determination of the energetic parameters controlling cleavage fracture initiation in steels, Fatigue & Fracture of Engineering Materials & Structures 20 (5) (1997) 619–632. doi:https://doi.org/10.1111/j.1460-2695.1997.tb00296.x.

[175] J. San Martin, J. M. Rodriguez-Ibabe, Determination of energetic parameters controlling cleavage fracture in a Ti-V microalloyed ferrite-pearlite steel, Scripta Materialia 40 (4) (1999) 459–464. doi:https://doi.org/10.1016/S1359-6462(98)00467-9.

[176] K. Shibanuma, S. Aihara, Quantitative prediction of cleavage fracture toughness of ferrite steel without adjustable parameters, Procedia Materials Science 3 (2014) 1238–1243, 20th European Conference on Fracture. doi:https://doi.org/10.1016/j.mspro.2014.06.201.

[177] E. Bouyne, H. Flower, T. Lindley, A. Pineau, Use of EBSD technique to examine microstructure and cracking in a bainitic steel, Scripta Materialia 39 (3) (1998) 295–300. doi:https://doi.org/10.1016/S1359-6462(98)00170-5.

[178] A. Gourgues, H. F. adn T. Kindley, Electron backscattering diffraction study of acicular ferrite, bainite, and martensite steel microstructures, Materials Science and Technology 16 (1) (2000) 26–40. doi:doi:10.1179/026708300773002636.

[179] A. Lambert-Perlade, A. Gourgues, J. Besson, T. Sturel, A. Pineau, Mechanisms and modeling of cleavage fracture in simulated heat-affected zone microstructures of a high-strength low alloy steel, Metallurgical and Materials Transactions A: Physical Metallurgy and Materials Science 35 (13) (2004) 1039 – 1053. doi:10.1007/s11661-004-1007-6.

[180] M. Gell, E. Smith, The propagation of cracks through grain boundaries in polycrystalline 3% silicon-iron, Acta Metallurgica 15 (2) (1967) 253–258. doi:https://doi.org/10.1016/0001-6160(67)90200-3.

[181] Y. Qiao, A. Argon, Cleavage crack-growth-resistance of grain boundaries in polycrystalline Fe–2%Si alloy: experiments and modeling, Mechanics of Materials 35 (1) (2003) 129–154. doi:https://doi.org/10.1016/S0167-6636(02)00194-1.

[182] Y. Qiao, A. Argon, Cleavage cracking resistance of high angle grain boundaries in Fe–3%Si alloy, Mechanics of Materials 35 (3) (2003) 313–331. doi:https://doi.org/10.1016/S0167-6636(02)00284-3.

[183] Y. Qiao, X. Kong, An energy analysis of the grain boundary behavior in cleavage cracking in Fe–3wt.%si alloy, Materials Letters 58 (25) (2004) 3156–3160. doi:https://doi.org/10.1016/j.matlet.2004.05.063.

[184] A. Pineau, Crossing grain boundaries in metals by slip bands, cleavage and fatigue cracks, Philosophical Transactions of the Royal Society of London. Series A, Mathematical, Physical and Engineering Scieces 373 (2015) 0131. doi:https://doi.org/10.1016/j.matlet.2004.05.063.

[185] J. Chen, R. Cao, Micromechanism of cleavage fracture of metals: A comprehensive microphysical model for cleavage cracking in metals, Butterworth-Heinemann, 2014. doi:https://doi.org/10.1016/C2013-0-18727-2.

[186] J. Chen, G. Wang, H. Wang, A statistical model for cleavage fracture of low alloy steel, Acta Materialia 44 (10) (1996) 3979–3989. doi:https://doi.org/10.1016/S1359-6454(96)00041-9.

[187] J. Hutchinson, Singular behaviour at the end of a tensile crack in a hardening material, Journal of the Mechanics and Physics of Solids 16 (1) (1968) 13–31. doi:https://doi.org/10.1016/0022-5096(68)90014-8.

[188] J. Rice, G. Rosengren, Plane strain deformation near a crack tip in a power-law hardening material, Journal of the Mechanics and Physics of Solids 16 (1) (1968) 1–12. doi:https://doi.org/10.1016/0022-5096(68)90013-6.

[189] J. Watanabe, T. Iwadate, Y. Tanaka, T. Yokobori, K. Ando, Fracture toughness in the transition region, Engineering Fracture Mechanics 28 (5) (1987) 589–600. doi:https://doi.org/10.1016/0013-7944(87)90055-5.

[190] R. O. Ritchie, A. W. Thompson, On macroscopic and microscopic analyses for crack initiation and crack growth toughness in ductile alloys, Metallurgical Transactions A 16 (1) (1985) 233–248. doi:10.1007/BF02815305.

[191] T. L. Anderson, D. Stienstra, A model to predict the sources and magnitude of scatter in toughness data in the transition region, Journal of Testing and Evaluation 17 (1) (1989) 46–53. doi:doi.org/10.1520/JTE11532J.

[192] T. S. K. Wallin, K. Törrönen, Statistical model for carbide induced brittle fracture in steel, Metal Science 18 (1) (1984) 13–16. doi:10.1179/030634584790420384.

[193] W. Weibull, A statistical distribution function of wide applicability, ASME Journal of Applied Mechanics 18 (3) (1951) 293–297. doi:10.1115/1.4010337.

[194] F. Minami, A. Brückner-Foit, D. Munz, B. Trolldenier, Estimation procedure for the Weibull parameters used in the local approach, International Journal of Fracture 54 (3) (1992) 197–210. doi:10.1007/BF00035355.

[195] A. Pineau, Development of the local approach to fracture over the past 25 years: Theory and applications, International Journal of Fracture 138 (1) (2006) 139–166. doi:10.1007/s10704-006-0035-1.

[196] ISO27306:2016, Metallic materials - Method of constraint loss correction of CTOD fracture toughness for fracture assessment of steel components, Standard, International Organization for Standardization (2016).

[197] ASTM E1921-19, Standard test method for determination of reference temperature, T_0, for ferritic steels in the transition range, Standard, American Society for Testing and Materials (2019).

[198] K. Shibanuma, S. Aihara, K. Suzuki, Prediction model on cleavage fracture initiation in steels having ferrite–cementite microstructures – part I: Model presentation, Engineering Fracture Mechanics 151 (2016) 161–180. doi:https://doi.org/10.1016/j.engfracmech.2015.03.048.

[199] K. Shibanuma, S. Aihara, K. Suzuki, Prediction model on cleavage fracture initiation in steels having ferrite–cementite microstructures – part II: Model validation and discussions, Engineering Fracture Mechanics 151 (2016) 181–202. doi:https://doi.org/10.1016/j.engfracmech.2015.03.049.

[200] K. Shibanuma, Y. Nemoto, T. Hiraide, K. Suzuki, S. Sadamatsu, Y. Adachi, S. Aihara, A strategy to predict the fracture toughness of steels with a banded ferrite–pearlite structure based on the micromechanics of brittle fracture initiation, Acta Materialia 144 (2018) 386–399. doi:https://doi.org/10.1016/j.actamat.2017.10.046.

[201] BS 7448:1991 Part 1, Fracture mechanics toughness tests - Method for determination of K, critical CTOD and critical J values of metallic materials, Standard, British Standard Institution (1991).

[202] S. Bordet, A. Karstensen, D. Knowles, C. Wiesner, A new statistical local criterion for cleavage fracture in steel. Part I: Model presentation, Engineering Fracture Mechanics 72 (3) (2005) 435–452. doi:https://doi.org/10.1016/j.engfracmech.2004.02.009.

[203] S. Bordet, A. Karstensen, D. Knowles, C. Wiesner, A new statistical local criterion for cleavage fracture in steel. Part II: Application to an offshore structural steel, Engineering Fracture Mechanics 72 (3) (2005) 453–474. doi:https://doi.org/10.1016/j.engfracmech.2004.02.010.

[204] G. Bernauer, W. Brocks, W. Schmitt, Modifications of the Beremin model for cleavage fracture in the transition region of a ferritic steel, Engineering Fracture Mechanics 64 (3) (1999) 305–325. doi:https://doi.org/10.1016/S0013-7944(99)00076-4.

[205] J. P. Petti, R. H. Dodds, Ductile tearing and discrete void effects on cleavage fracture under small-scale yielding conditions, International Journal of Solids and Structures 42 (13) (2005) 3655–3676. doi:https://doi.org/10.1016/j.ijsolstr.2004.11.015.

[206] M. Kroon, J. Faleskog, Micromechanics of cleavage fracture initiation in ferritic steels by carbide cracking, Journal of the Mechanics and Physics of Solids 53 (1) (2005) 171–196. doi:https://doi.org/10.1016/j.jmps.2004.05.008.

[207] M. Kroon, J. Faleskog, Influence of crack deflection into the carbide/ferrite interface on cleavage fracture initiation in ferritic steels, Mechanics of Materials 40 (9) (2008) 695–707. doi:https://doi.org/10.1016/j.mechmat.2008.03.006.

[208] M. Stec, J. Faleskog, Micromechanical modeling of grain boundary resistance to cleavage crack propagation in ferritic steels, International Journal of Fracture 160 (2) (2009) 151–167. doi:10.1007/s10704-009-9415-7.

[209] N. Giang, M. Kuna, G. Hütter, Influence of carbide particles on crack initiation and propagation with competing ductile-brittle transition in ferritic steel, Theoretical and Applied Fracture Mechanics 92 (2017) 89–98. doi:https://doi.org/10.1016/j.tafmec.2017.05.015.

[210] G. Hütter, L. Zybell, M. Kuna, Micromechanical modeling of crack propagation in nodular cast iron with competing ductile and cleavage failure, Engineering Fracture Mechanics 147 (2015) 388–397. doi:https://doi.org/10.1016/j.engfracmech.2015.06.039.

[211] N. Giang, M. Kuna, G. Hütter, Effect of gradient plasticity on crack initiation and propagation in the ductile-brittle transition region of ferritic steel, Procedia Structural Integrity 13 (2018) 45–50, ECF22 - Loading and Environmental effects on Structural Integrity. doi:https://doi.org/10.1016/j.prostr.2018.12.008.

[212] N. Giang, A. Seupel, M. Kuna, G. Hütter, Dislocation pile-up and cleavage: Effects of strain gradient plasticity on micro-crack initiation in ferritic steel, International Journal of Fracture 214 (2018) 1–15. doi:10.1007/s10704-018-0313-8.

[213] T. Gladman, B. Holmes, I. D. McIvor, Effects of second-phase particles on strength, toughness and ductility, in: Effect of Second-Phase Particles on the Mechanical Properties of Steel, the Iron and Steel Institute, 1971, pp. 68–78.

[214] R. T. Dehoff, F. N. Rhines (Eds.), Quantitative Microscopy, McGraw-Hill, 1968.

[215] K. Sakuma, T. Nishizawa, Quantitative microscopy (*in Japanese*), Bulletin of the Japan Institute of Metals 10 (5) (1971) 279–289. doi:10.2320/materia1962.10.279.

[216] H. K. D. H. Bhadeshia, Cementite, International Materials Reviews 65 (1) (2020) 1–27. doi:10.1080/09506608.2018.1560984.

[217] D. J. Dingley, A. J. Wilkinson, G. Meaden, P. S. Karamched, Elastic strain tensor measurement using electron backscatter diffraction in the SEM, Journal of Electron Microscopy 59 (S1) (2010) S155–S163. doi:10.1093/jmicro/dfq043.

[218] P. S. Karamched, A. J. Wilkinson, High resolution electron back-scatter diffraction analysis of thermally and mechanically induced strains near carbide inclusions in a superalloy, Acta Materialia 59 (1) (2011) 263–272. doi:https://doi.org/10.1016/j.actamat.2010.09.030.

[219] T. B. Britton, J. Jiang, P. S. Karamched, A. J. Wilkinson, Probing deformation and revealing microstructural mechanisms with cross-correlation-based, high-resolution electron backscatter diffraction, JOM 65 (9) (2013) 1245–1253. doi:10.1007/s11837-013-0680-6.

[220] Y. T. Tang, P. Karamched, J. Liu, J. C. Haley, R. C. Reed, A. J. Wilkinson, Grain boundary serration in nickel alloy inconel 600: Quantification and mechanisms, Acta Materialia 181 (2019) 352–366. doi:https://doi.org/10.1016/j.actamat.2019.09.037.

[221] K. W. Burns, F. B. Pickering, Deformation and fracture of ferrite-pearlite structures, Journal of the Iron and Steel Institute 202 (1964) 899–906.

[222] F. B. Pickering, The effect of composition and microstructure on ductile and toughness, in: Toward Improved Ductility and Toughness, Climax Molybdenum Development Company (Japan) Ltd., Tokyo, 1971, pp. 9–31.

[223] T. Gladman, B. Holmes, F. B. Pickering, Work-hardening of low-carbon steels, Journal of the Iron and Steel Institute 208 (1970) 172–183.

[224] C. S. John, The brittle-to-ductile transition in pre-cleaved silicon single crystals, The Philosophical Magazine: A Journal of Theoretical Experimental and Applied Physics 32 (6) (1975) 1193–1212. doi:10.1080/14786437508228099.

[225] W. Oldfield, Curve fitting impact test data: a statistical procedure, ASTM Standard News 3 (11) (1975) 24–29.

[226] L. Cao, S. Wu, P. Flewitt, Comparison of ductile-to-brittle transition curve fitting approaches, International Journal of Pressure Vessels and Piping 93-94 (2012) 12–16. doi:https://doi.org/10.1016/j.ijpvp.2012.02.001.

[227] T. Tanaka, M. Kosugi, Crystallographic study of the fatigue crack nucleation mechanism in pure iron, in: Basic Questions in Fatigue: Volume I, 1988, pp. 98–119, ASTM Special Technical Publicatoin (STP) 924.

[228] K. Higashida, J. Takamura, N. Narita, The formation of deformation bands in f.c.c. crystals, Materials Science and Engineering 81 (1986) 239–258, Proceedings of the International Conference on Low Energy Dislocation Structures. doi:https://doi.org/10.1016/0025-5416(86)90266-1.

[229] T. Lindley, G. Oates, C. Richards, Fibre-loading mechanism for the fracture of cementite films in ferrite, Nature 226 (5241) (1970) 145–146. doi:https://doi.org/10.1038/226145a0.

[230] A. Kelly, D. J. Davies, The principles of the fibre reinforcement of metals, Metallurgical Reviews 10 (1) (1965) 1–77. doi:10.1179/mtlr.1965.10.1.1.

[231] P. B. Hirsch, S. G. Roberts, J. Samuels, The brittle-ductile transition in silicon. II. Interpretation, Proceedings of the Royal Society A; Mathematical, Physical and Engineering Sciences 421 (1989) 25–53. doi:10.1098/rspa.1989.0002.

[232] M. Brede, P. Haasen, The brittle-to-ductile transition in doped silicon as a model substance, Acta Metallurgica 36 (8) (1988) 2003–2018. doi:https://doi.org/10.1016/0001-6160(88)90302-1.

[233] H.-S. Kim, S. Roberts, Brittle–ductile transition and dislocation mobility in sapphire, Journal of the American Ceramic Society 77 (12) (1994) 3099–3104. doi:https://doi.org/10.1111/j.1151-2916.1994.tb04555.x.

[234] M. Tanaka, E. Tarleton, S. Roberts, The brittle–ductile transition in single-crystal iron, Acta Materialia 56 (18) (2008) 5123–5129. doi:https://doi.org/10.1016/j.actamat.2008.06.025.

[235] A. Giannattasio, M. Tanaka, T. D. Joseph, S. G. Roberts, An empirical correlation between temperature and activation energy for brittle-to-ductile transitions in single-phase materials, Physica Scripta 2007 (T128) (2007) 87. doi:10.1088/0031-8949/2007/T128/017.

[236] M. Tanaka, T. Onomoto, T. Tsuchiyama, K. Higashida, Brittle-to-ductile transition in nickel-free austenitic stainless steels with high nitrogen, ISIJ International 52 (5) (2012) 915–921. doi:10.2355/isijinternational.52.915.

[237] M. Tanaka, S. Takano, K. Higashida, Enhancement of low temperature toughness in bulk nanostructured metals, Materials Transactoins 54 (9) (2013) 1624–1628. doi:10.2320/matertrans.MH201319.

[238] ISO148-1:2016 Metallic materials - Charpy pendulum impact test - Part 1: Test method, Standard, The International Organization for Standardization (2016).

[239] R. K. Barik, A. Ghosh, D. Chakrabarti, Fundamental insights on ductile to brittle transition phenomenon in ferritic steel, Materialia 27 (2023) 101667. doi:https://doi.org/10.1016/j.mtla.2022.101667.

[240] M. Tanaka, K. Higashida, T. Shimokawa, T. Morikawa, Brittle-ductile transition in low carbon steel deformed by the accumulative roll bonding process, Materials Transactoins 50 (1) (2009) 56–63. doi:10.2320/matertrans.MD200817.

[241] T. Sirithanakorn, M. Tanaka, K. Higashida, Brittle-to-ductile transitions and its relation to the deformability of cementite in fully pearlitic steels, Materials Science and Engineering: A 611 (2014) 383–387. doi:https://doi.org/10.1016/j.msea.2014.06.007.

[242] D. K. Bowen, B. K. Tanner, A method for the accurate comparison of lattice parameters, Journal of Applied Crystallography 28 (6) (1995) 753–760. doi:https://doi.org/10.1107/S0021889895006297.

[243] H. J. Maier, R. R. Keller, H. Renner, H. Mughrabi, A. Preston, On the unique evaluation of local lattice parameters by convergent-beam electron diffraction, Philosophical Magazine A 74 (1) (1996) 23–43. doi:10.1080/01418619608239688.

[244] M. Yamaguchi, M. Tachikawa, M. Sugo, S. Kondo, Y. Itoh, Analysis for dislocation density reduction in selective area grown GaAs films on si substrates, Applied Physics Letters 56 (1) (1990) 27–29. doi:10.1063/1.102636.

[245] J. Nye, Some geometrical relations in dislocated crystals, Acta Metallurgica 1 (2) (1953) 153 – 162. doi:https://doi.org/10.1016/0001-6160(53)90054-6.

[246] A. J. Wilkinson, D. Randman, Determination of elastic strain fields and geometrically necessary dislocation distributions near nanoindents using electron back scatter diffraction, Philosophical Magazine 90 (9) (2010) 1159–1177. doi:10.1080/14786430903304145.

[247] D. S. Zhou, G. J. Shiflet, Ferrite: Cementite crystallography in pearlite, Metallurgical Transactions A 23A (1992) 1259–1269. doi:https://doi.org/10.1007/BF02665057.

[248] M. A. Mangan, G. J. Shiflet, The Pitsch-Petch orientation relationship in ferrous pearlite at small undercooling, Metallurgical and Materials Transactions A 30 (1999) 2767–2781. doi:10.1007/s11661-999-0114-9.

[249] D. S. Zhou, G. J. Shiflet, Interfacial steps and growth mechanism in ferrous pearlites, Metallurgical Transactions A 22A (1991) 1349–1365. doi:10.1007/BF02660668.

[250] M.-X. Zhang, P. Kelly, The morphology and formation mechanism of pearlite in steels, Materials Characterization 60 (6) (2009) 545–554. doi:https://doi.org/10.1016/j.matchar.2009.01.001.

[251] W. Pitsch, The orientation relationship between cementite and ferrite in perlite (*in German*), Acta metallurgica 10 (1) (1962) 79–80.

[252] N. J. Petch, The orientation relationships between cementite and α-iron, Acta Crystallographica 6 (1) (1953) 96. doi:10.1107/S0365110X53000260.

[253] Y. A. Bagayartsky, Probable mechanism of martensite decomposition (*in Russian*), Dokl. Akad. Nauk. SSSR 73 (1950) 1161–1164.

[254] I. V. Isaichev, Orientation of cementite in tempered carbon steel (*in Russian*), Zh. Tekh. Fiz. 17 (7) (1947) 835–838.

[255] M. Umemoto, Y. Todaka, Y. Tsuchiya, Mechanical properties of cementite and fabrication of artificial pearlite, Material Science Forum 426-432 (2003) 859–864. doi:https://doi.org/10.4028/www.scientific.net/msf.426-432.859.

[256] D. Porter, K. Easterling, G. Smith, Dynamic studies of the tensile deformation and fracture of pearlite, Acta Metallurgica 26 (9) (1978) 1405–1422. doi:https://doi.org/10.1016/0001-6160(78)90156-6.

[257] Y. Amemiya, N. Nakada, S. Morooka, M. Kosaka, M. Kato, Dynamic accomodation of internal stress and selection of crystallographic orientation relationship in pearlite (*in Japanese*), *Tetsu-to-Hagane* 105 (2) (2019) 314–323. doi:10.2355/tetsutohagane.TETSU-2018-086.

[258] S. Endo, N. Miyazawa, N. Nakada, S. Onaka, T. Teshima, M. Kosaka, Formation mechanism of pearlite colony by multiple orientation relationships between ferrite and cementite, ISIJ International 62 (2) (2022) 291–298. doi:10.2355/isijinternational.ISIJINT-2021-332.

[259] H. Ghadbeigi, C. Pinna, S. Celotto, J. Yates, Local plastic strain evolution in a high strength dual-phase steel, Materials Science and Engineering: A 527 (18) (2010) 5026–5032. doi:https://doi.org/10.1016/j.msea.2010.04.052.

[260] K. Park, M. Nishiyama, N. Nakada, T. Tsuchiyama, S. Takaki, Effect of the martensite distribution on the strain hardening and ductile fracture behaviors in dual-phase steel, Materials Science and Engineering: A 604 (2014) 135–141. doi:https://doi.org/10.1016/j.msea.2014.02.058.

[261] D. Yan, C. C. Tasan, D. Raabe, High resolution in situ mapping of microstrain and microstructure evolution reveals damage resistance criteria in dual phase steels, Acta Materialia 96 (2015) 399–409. doi:https://doi.org/10.1016/j.actamat.2015.05.038.

[262] M. Tanaka, Y. Yoshimi, K. Higashida, T. Shimokawa, T. Ohashi, A multiscale approach for the deformation mechanism in pearlite microstructure: Experimental measurements of strain distribution using a novel technique of precision markers,

Materials Science and Engineering: A 590 (2014) 37–43. doi:https://doi.org/10.1016/j.msea.2013.09.072.

[263] T. Teshima, M. Kosaka, K. Ushioda, N. Koga, N. Nakada, Local cementite cracking induced by heterogeneous plastic deformation in lamellar pearlite, Materials Science and Engineering: A 679 (2017) 223–229. doi:https://doi.org/10.1016/j.msea.2016.10.018.

[264] Y. Yajima, N. Koga, C. Watanabe, Influential factors on the deformability of colonies in pearlitic steel, Materials Characterization 177 (2021) 111197. doi:https://doi.org/10.1016/j.matchar.2021.111197.

[265] T. Vermeij, J. Hoefnagels, Plasticity, localization, and damage in ferritic-pearlitic steel studied by nanoscale digital image correlation, Scripta Materialia 208 (2022) 114327. doi:https://doi.org/10.1016/j.scriptamat.2021.114327.